2014-12-19

Digital Image Correlation and Edge Detection: Applications in Materials Testing

Shan Yuan
University of Miami, yuans82@yahoo.com

UNIVERSITY OF MIAMI

DIGITAL IMAGE CORRELATION AND EDGE DETECTION: APPLICATIONS IN MATERIALS TESTING

By

Shan Yuan

A DISSERTATION

Submitted to the Faculty
of the University of Miami
in partial fulfillment of the requirements for
the degree of Doctor of Philosophy

Coral Gables, Florida

December 2014

UNIVERSITY OF MIAMI

A dissertation submitted in partial fulfillment of
the requirements for the degree of
Doctor of Philosophy

DIGITAL IMAGE CORRELATION AND EDGE DETECTION: APPLICATIONS IN MATERIALS TESTING

Shan Yuan

Approved:

_____
James Giancaspro, Ph.D.
Associate Professor of Civil, Architectural,
and Environmental Engineering

_____
Carol Hays, Ph.D.
Professor-of-Practice of Civil,
Architectural, and Environmental
Engineering

_____
Antonio Nanni, Ph.D.
Professor and Chair of Civil, Architectural,
and Environmental Engineering

_____
M. Brian Blake, Ph.D.
Dean of the Graduate School

_____
Qingda Yang, Ph.D.
Associate Professor of Mechanical
and Aerospace Engineering

YUAN, SHAN (Ph.D., Civil Engineering)
Digital Image Correlation and Edge Detection: Applications in Materials Testing (December 2014)

Abstract of a dissertation at the University of Miami

Dissertation supervised by Professor James Giancaspro
No. of pages in text. (218)

Digital image processing (DIP) methods have been applied in civil engineering for many years. In this dissertation, DIP methods are applied to (1) quantify the mechanical properties of metallic and cementitious composites loaded in uni-axial tension, and (2) evaluate the effectiveness of removing paint from concrete surfaces. DIP is an optical method to characterize the behavior of the visible domain on the surface of the specimen.

Strain, an important measurement in mechanics of materials, can be measured by a digital image processing method known as Digital Image Correlation (DIC). Traditional DIC tracks the change in position of speckles on the surface of a specimen to determine the surface strain. In this dissertation, a novel pattern, a painted rectangle on the specimen surface, is developed to measure strain. This approach uses an edge detection method to track changes in the length of the rectangle. It is a target-based deformation method, which explicitly considers the deformation of the target (rectangle) to calculate strain. By computing the change in length of the rectangle in successive images, the strains are determined.

Both pixel-level and subpixel-level accuracy levels for different accuracy requirements are studied. The pixel-level is implemented using ImageJ software, while the subpixel-level is accomplished using two algorithms: Gaussian fitting and spline

interpolation, both implemented using Matlab. The two digital image methods (DIC speckles and rectangle edge detection) are compared with laser extensometry and strain gage measurements for uni-axial tension tests of A36 steel specimens. The strain measurement results are comparable to the laser extensomety and strain gages if high quality images are captured.

DIP methods only characterize the behavior of the visible domain on the surface of the specimen. A combination of technologies (both traditional and emerging) may be necessary to fully characterize the mechanical response of a material or structure subjected to loading.

Two digital image processing methods are established to evaluate the effectiveness of cleaning paint from concrete surfaces. The principle of this evaluation is to select a suitable gray intensity threshold value for each paint color to distinguish it from the concrete color. One method is histogram-based and selects the threshold value based on the histograms of the pixel values of the paint and concrete. The other method is an edge-based method, which selects the gray intensity of the edge as the threshold value. Based on the results from the binarized images produced by these two methods, the histogram-based method is more suitable for the darker paints and the edge-based method is more suitable for the white paint. These methods could also be applied to evaluate the removal of corrosion by-products from steel or even stains from teeth.

Five strain measurement methods are applied to measure the deformation of fabric reinforced cementitious matrix (FRCM) composites tested in uniaxial tension. The five methods include: laser extensometry, clip-on extensometry, strain gages, and two digital image methods (DIC speckle and rectangle edge detection). The strain gages

failed prematurely due to cracking of the FRCM. The two digital image methods can only analyze in-plane displacement. For out-of-plane displacement, a 3-D DIC method must be used.

Acknowledgements

It would not have been possible to complete this dissertation without the help and support of many kind people. Above all, I would like to take this opportunity to extend my deepest appreciation and gratitude to my advisor Dr. James Giancaspro, for his constant instruction, support and encouragement. His enthusiasm, optimism and persistence towards science have been instrumental in my progression as a scientist. He makes his support available in every aspect of my graduate life, for which I will always be grateful.

I would like to thank my committee members: Dr. Antonio Nanni, Dr. Carol Hays and Dr. Qingda Yang, for their immense input into this project. Their rigorous attitudes towards science and high expectations have encouraged me to strive to do my best.

I want to acknowledge and state my gratitude to all the students that have assisted in my research and dissertation: Kimberley Mac Donald, thank you for your support in research and this thesis and Lauren Millman and Diana Arboleda..

I would like to acknowledge the financial, academic and technical support of the University of Miami. Thank you to the entire faculty in the department of Civil, Architectural, and Environmental Engineering. This material is based upon work supported by the National Science Foundation under Grants No. EEC-0926794 and No. CMMI-0922825. Any opinions, findings, conclusions, or recommendations expressed herein are those of the author and do not necessarily reflect the views of the National Science Foundation; NSF has not reviewed, approved, or endorsed this content.

I would like to thank my family: My parents, husband and daughter. My parents are always supporting me and encouraging me. My husband, Zedong Wang, is always there cheering me up and stood by me through the good times and bad.

Table of Contents

Page

List of Figures

List of Tables

Chapter 1 Introduction

The application of digital image processing (DIP) in civil engineering has grown rapidly in recent years. Digital image technology can help engineers and scientists characterize the properties of materials, both at the micro- and macro-scopic levels. Through digital image processing, enormous information can be extracted from a digital image.

Digital image correlation (DIC) was introduced as an optical strain measurement method as early as the 1970s. Different from other optical methods such as holography and speckle interferometry, DIC uses white light as a lighting source. By using a Charge-Coupled Device (CCD) camera to acquire images for different levels of stress, the in-plane displacement field can be obtained. The correlation is determined by comparing the gray intensity changes of the object surface before and after deformation. With advances in computer technology and digital camera, the accuracy of the DIC method increases quickly. Compared with traditional strain measurement methods, the DIP method is a non-contact optical technique, having large dimension ranges for specimens, and able to provide full-field strain measurement.

The correlation pattern used in the DIC method is typically either the natural texture of the material or painted speckles. In this dissertation, a rectangle is used as a novel pattern for surface strain measurement. In this case, strain is measured by tracking the length changes of the painted rectangle on the specimen surface. This is an edge detection based method and is called rectangle edge detection. Subpixel-level accuracy can be accomplished by locating the subpixel edge position of the rectangle.

Rectangle edge detection is a target-based deformation method. In other words, the deformation of the rectangle is the study target. For other strain measurement methods, such as laser extensometry or DIC, the strain of a specimen is measured using reflective tape or speckles as the target. The relative movements of these targets are used to calculate strain. However, the deformations of the target, such as tape or speckles, are neglected.

DIP methods only characterize the behavior of the visible domain on the surface of the specimen. A combination of technologies (both traditional and emerging) may be necessary to fully characterize the mechanical response of a material or structure subjected to loading.

This dissertation includes four main chapters:

Chapter 2: Review of several strain measurement methods, including strain gages, laser extensometry, clip-on extensometry and DIC methods. This chapter also introduces the principle of the edge detection method.

Chapter 3: The rectangle strain measurement method is introduced with two accuracy levels: pixel-level and subpixel-level. To achieve subpixel accuracy, two algorithms (Gaussian fitting and spline interpolation) are studied. Three tests are studied to compare the strain measurement methods. Test 1 used a Nikon D3000 to record images of the rectangle; Test 2 used an iPhone 4S to capture images of the rectangle; Test 3 used a Nikon D3000 to record images of speckles.

Chapter 4: Two digital image processing methods (histogram-based and edge-based) are established to quantify the extent of paint removed from a concrete substrate during abrasive blasting. The histogram-based method selects the threshold value by

statistical analysis of the gray level intensities of the images. The edge-based method takes the gray intensity of the edge of the paint as the threshold value. The effect of varying the threshold values on the cleaning effectiveness is compared.

Chapter 5: Five strain measurement techniques for a fabric reinforced cementitious matrix (FRCM) composite are compared. These five strain measurement techniques include laser extensometry, clip-on extensometry, strain gages, and two DIC (speckle and rectangle) methods. A comprehensive comparison of these five strain measurement methods is given.

Chapter 6: Overall conclusions and suggestions for future research are discussed.

Chapter 2 Literature review

2.1 Strain measurement methods

Testing of mechanical properties of metals, composites, and ceramics has become widespread in collecting engineering design data. These data are essential for design applications with various types of materials. Strain and displacement measurements are major parts of material testing.

When external forces are applied to a material, deformations and displacements occur. Strain reflects the deformation of the material under loading, and is defined as elongation per unit length (Gere, 2001). Several methods are used to describe the amount of strain.

2.1.1 Resistance strain gage

A strain gage is a strain measurement device invented by Arthur Ruge and Edward Simmons (Hannah & Reed, 1992) in the late 1930s. The strain gage measures strain of a material by tightly bonding the material with a gage. The strain gage has a sensing element: a thin metallic resistive foil. When the material deforms, the metallic resistive foil deforms with it. This deformation of the metallic foil causes a change in its electrical resistance. The rate of change of the foil's resistance is proportional to the strain in the material by some constant called the gage factor. The gage factor (F_s) reflects the metal's sensitivity to strain, and is defined by Equation (2-1):

$$F_s = \frac{\Delta R / R_0}{\varepsilon} \tag{2-1}$$

Where F_s is the Gage factor (unitless), ΔR is the resistance change of the strain gage, Ω (ohms), R_0 is the Initial resistance of strain gage, Ω (ohms), and ε is the strain.

Table 2-1 Gage factors of metals and alloy (Hannah & Reed, 1992)

Metal or alloy	Trade name	Typical gage factor F_s
Iron	−	+4.0
Copper	−	+2.6
Silver	−	+3.0
Nickel	−	-12.0
Plantinum	−	+6.0
Titanium(commercially pure)	−	-1.1
Titanium(6AL4V alloy)	−	-0.2
Aluminum	−	+0.85
Copper-nickel 55-45 (constanta)	Advance,Cupron, Copel, etc.	+2.1
Nickel-chromium 80-20	Nichrome V, Tophet A	+2.2
Copper-nickel-manganese (manganin)	Manganin	+0.6
Iron-nickel-chromium	18-8 Stainless	+2.6
Iron-chromium-molybdenum	Iso-elastic	+3.5
Platinum-tungsten 92-8	Alloy 479	+4.1

The gage factor, F_s, depends on the metallic material used. By selecting different metals or alloys, a wide range of strains can be measured by strain gages. Table 2-1 (Hannah & Reed, 1992) shows gage factors of some commonly used metals and alloys.

In order to measure the change in resistance of a strain gage, the strain gage is connected to an electric circuit (Omega, 2014). When the material deforms, the change in resistance, which corresponds to strain (Figliola & Beasley, 2011), causes a change in

electric current. Therefore, strain is obtained by measuring this change in electric current. The Wheatstone bridge is one type of electric circuit used to detect changes in resistance (Kyowa Electronic Instruments, 2010). A Wheatstone bridge is suitable for detection of minute resistance changes. Figure 2-1 shows a schematic of a Wheatstone bridge circuit.

In a Wheatstone circuit, there are four resistances R_1, R_2, R_3, and R_4 as shown in Figure 2-1, and $R_1=R_2=R_3=R_4$ or $R_1 \times R_3=R_2 \times R_4$. Initially, the circuit requires an input voltage V_{in}, and the output $V_{out}=0$. This status is called a balanced bridge. Then a strain gage is connected to the circuit in place of R_4. When the strain gage bears strain and resistance changes ΔR, the bridge becomes unbalanced. The circuit outputs a nonzero value of V_{out}, which corresponds to the resistance change of the strain gage. Equation (2-2) shows the linear relationship between voltage and strain.

$$V_{out} = \frac{1}{4} \times \frac{\Delta R}{R} \times V_{in} = \frac{1}{4} \times F_s \times \varepsilon \times V_{in} \qquad (2\text{-}2)$$

Depending on the number of active strain gages in the bridge circuit, the circuit can be separated into quarter-bridge, half- bridge and full bridge configurations (National Instruments, 2006). The quarter-bridge has only one active strain gage. The resistance change of the circuit is $R_g+\Delta R$. In order to double the sensitivity of the bridge, a half-bridge uses two active strain gages: one in tension with resistance $R_g+\Delta R$, and the other in compression with resistance $R_g-\Delta R$. The output is approximately double that of a quarter bridge circuit. A full bridge has four active strain gages with two gages in tension and two gages in compression. It also has the highest sensitivity. Figure 2-2 shows the schematic of these three bridge circuits.

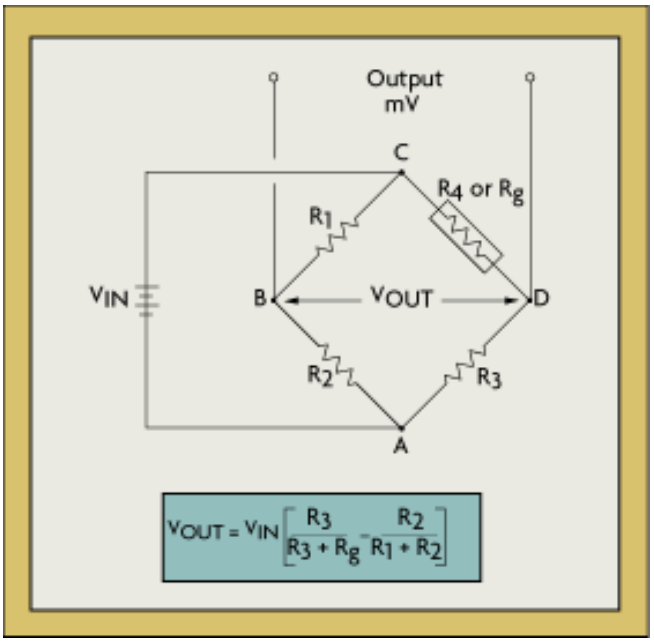

Figure 2-1 Wheatstone bridge circuit schematic (Omega, 2014)

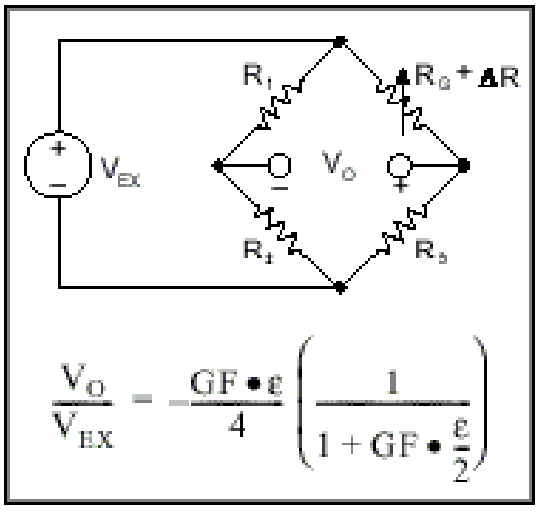

(a) Quarter-Bridge circuit

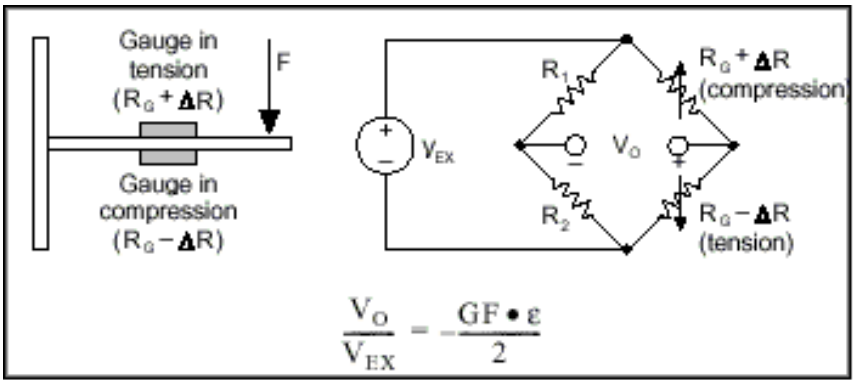

(b) Half-Bridge circuit

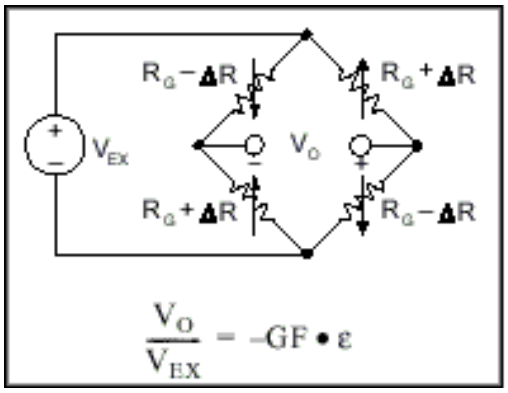

(c) Full-Bridge circuit

Figure 2-2 Bridge circuits (National Instruments, 2006)

Strain gages are very sensitive to ambient temperature since the metallic foil's resistance varies when temperature changes. To reduce the effect of temperature, two perpendicular strain gages are used (National Instruments, 2011).

To fulfill all the different requirements of various strain measurement experiments, numerous strain gages are available. To select the most suitable gage for a specific requirement, the following items (Hoffmann, 1989) must be considered:

— Mechanical conditions: principal measurement direction (uniaxial or biaxial) and type of loading (static or dynamic)

- Dimension and arrangement of the measuring grid: number of strain gages and their arrangement (the dimensions of the strain gage must fit the measuring grid)
- Strain measurement range: gage factor
- Electrical conditions: measurement circuit and voltage type (direct voltage, alternating voltage, voltage with respect to ground etc.)
- Environmental temperature: thermal expansion coefficients of the alloy used in the strain gage and the service temperature range of strain gage

2.1.2 Optical strain measurement method

Optical strain measurement is known as a non-contact and non-destructive technique. Laser technology has been used to measure displacement since the 1970s. The two most widely used technologies are holographic interferometry and speckle photography (Dandliker, 1980).

Holographic interferometry and speckle photography are both based on electronic speckle pattern interferometry (ESPI), which produces fringe patterns by superposition of multiple speckle images. In the early 1970s, Archbold (1970) discovered that double exposure speckles in combination with forthcoming optical Fourier transformation using an illuminated laser beam can be used to measure surface displacement. Digital fringe analysis is easily achieved by using mirror surfaces (Schwider, 1990). However, for diffusely reflecting surfaces, speckle noise arises. The cross-correlation function of the intensity distribution (Yamaguchi, 1981) is applied in evaluating the speckle displacement and correlation. In holographic and speckle interferometry, object deformations are observed as fringe patterns. The orientation and spacing of fringes are related to the orientation and magnitude of the speckle displacement (Yamaguchi, 2003).

Advances in computing and image sensing offer a simple and fast technique to measure speckle displacement. Speckle patterns are recorded with a charge coupled device (CCD) in matrix form which is used by a computer to calculate 2D cross-correlation of the sub-images. These calculations are used to obtain the distribution of speckle displacement (Yamaguchi, 1981; Noh & Yamaguchi, 1993; Wojciechowski, Pisarek, & Kityk, 2010).

Holography can record objects in three dimensions, unlike conventional photography, which is in two dimensions only. It is applicable to a wide range of scales, from a car to a small particle on the micrometer scale. In the holography process, a laser produces two coherent lights with the same wavelength. Coherence means that these two lights have the same frequency and wave direction, and have the same phase separation. One light is reflected from the object to a photosensitive surface. At the same time, the other light illuminates the same photosensitive surface from a different angle. The two lights cause interference fringes on the photosensitive surface (Martin, 1977; Wernicke, et al., 2001). When the laser illuminates the surface, a three dimensional image of the object, which is identical to the original object, is produced. If a small deformation is applied to object, the interference fringes alter. Thus, information about the deformation information can be obtained.

The principle of laser speckle photography is similar to that of conventional photography (Martin, 1977). The difference is that laser speckle photography uses a coherent light source in place of daylight. When laser coherent light illuminates an object, the speckles appear. The size of the speckle is related to the laser's wavelength, the distance between the observation point and the laser light and the grain size of the object. If there are displacements applied to the object, the grain size will change (Kihm,

1997). Therefore, the size of the speckles is changed (Schneider, J., Rupitsch, & Zagar, 2007; Du & Chiang, 1998; Tay, Yap, Shang, & Tay, 1995). A schematic of the laser speckle method is shown in Figure 2-3.

Laser holography interferometry and speckle photography are both highly sensitive to deformation with high accuracy, but they are also very expensive.

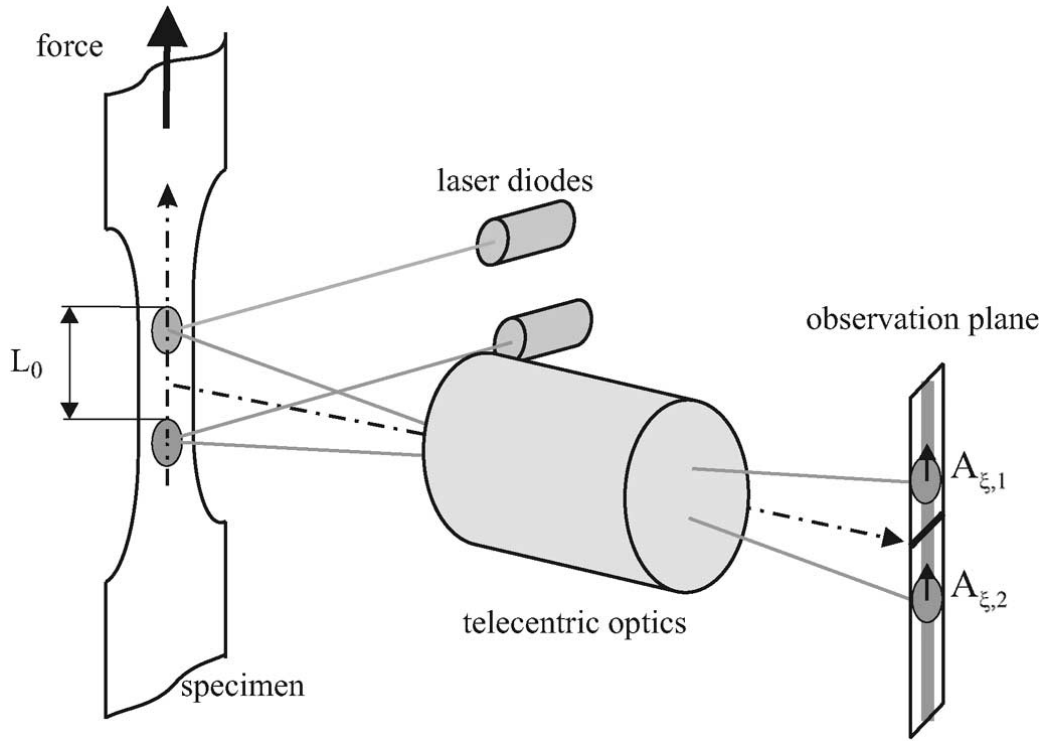

Figure 2-3 Schematic of the laser speckle method (Schneider, J., Rupitsch, & Zagar, 2007)

2.1.3 Extensometry

By definition, strain can be directly measured by the change in dimensions of the specimen. An extensometer is a device used to directly measure elongation of an object under axial loading. By determining the displacement between two points, which are the bounds of the specific gage length, the strain measurement is obtained. Compared to

other methods, the extensometer is the most direct method of strain measurement. Extensometry can be divided into contacting and non-contacting methods.

2.1.3.1 Contacting

A clip-on extensometer is a contacting, mechanical strain measurement device mounted directly onto the specimen. It uses knife-edges to track the extension of the specimen (Dripke & GmbH, 2009). The measurement of the clip-on extensometer can be as high as a few micrometers.

Sensor arm extensometers, another type of contacting extensometers, have the advantages of automatic operation and a large measurement range while maintaining high accuracy. Sensor arm extensometers apply minimum loading to the specimen, which minimizes damage to the specimen. Since the sensor arms are in contact with specimen on both sides, bending strains are mostly counterbalanced (Becker & Dripke, 2011).

Figure 2-4 shows a schematic of two types of contacting extensometers: clip-on and sensor arm extensometers. Both the clip-on extensometer and sensor arm extensometer measure strain with knife-edges, which are perpendicular to the gage length. Since these contacting extensometers directly contact the specimens, the knife-edges can easily damage a fragile specimen.

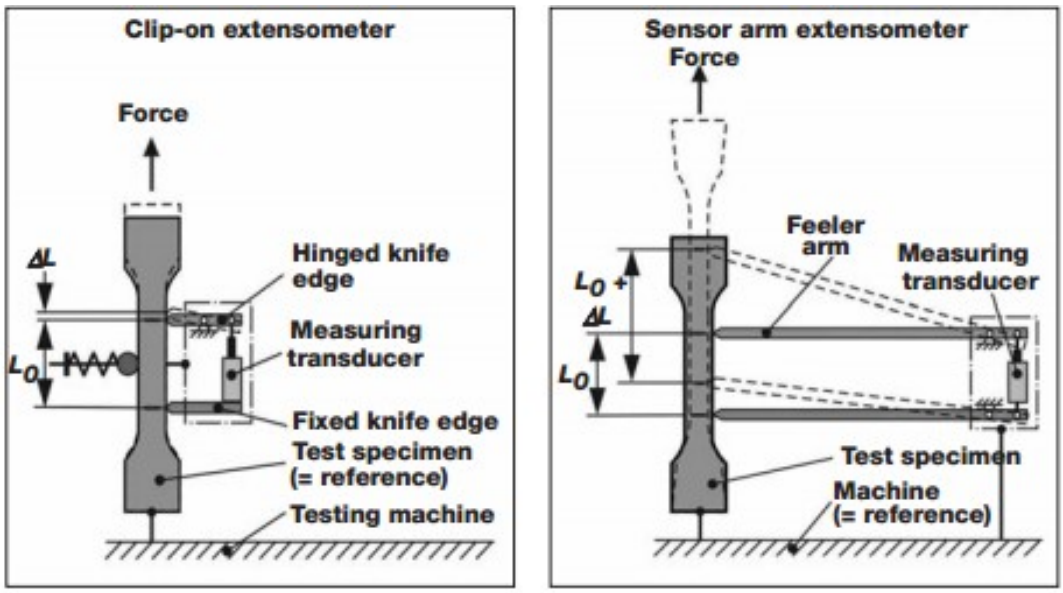

Figure 2-4 Two kinds of contacting extensometers (Dripke & GmbH, 2009)

Based on the measurement purpose, different mechanical extensometers with various gage lengths made from various materials are available. Liu and Ding (1993) designed a simple mechanical extensometer for ceramic testing at temperatures of 1400°C. The extensometer uses its own weight for contacting and uses a capacitive transducer as the sensing element. Fu *et al*. (1997) studied three kinds of axial extensometers: overhanging beam structure, bow-like structure with stiff arms, and bow–like structure with flexible arms. They found that the relationships between the strain, displacement, and the optimum structure parameters for ideal linearity could be inferred. Motoie *et al*. (1983) presented information about the design and construction of a compact extensometer, which utilizes a linear variable differential transformer (LVDT). In addition, this extensometer can be used to investigate the behaviors of metals at temperatures as high as 800°C. Bulut (2009) designed a LVDT extensometer to measure strain with minimal controller synthesis (MCS) load control. Mechanical extensometers have many applications, not only in mechanical and civil engineering, but also to

biomedical engineering and biomechanics. Perusek *et al.* (2001) used paired sensors to measure global bone strain due to combined bending, compression, and tension. In this paper, he provided air gap change calculations and angular displacements with error analysis and coordinate analysis for the sensor.

2.1.3.2 Non-contacting

In some cases, the specimen may be very small, restricting its fit into the grips of the loading device, or preventing a uniform loading rate in the loading direction. In addition, some materials are very brittle and can be easily fractured by a traditional clip-on extensometer. In these cases, it can be difficult to measure strain using a contacting extensometer. Therefore, a non-contacting extensometer may be used to avoid these problems. Non-contacting extensometry has the capability of operating under high temperature (Yonekawa, et al., 2002), is easy to operate, is insensitive to electro-magnetic interference, and is suitable for brittle materials (Zhu, Mobasher, & Rajan, 2012).

- Laser extensometry is the most common non-contacting optical strain measurement method. A laser extensometer illuminates the object along the loading direction by the laser. The reflections on the object surface produce diffuse scatterings, which are received by a camera and converted into electrical signals. The distance of the reflecting fringes changes when the object is under tensile loading, allowing change in length to be measured (Grellmann, C., & Konig, 1997).
- Video extensometry is a non-contacting method used to measure the strain by capturing continuous images of the specimen during loading, via a digital video

camera. It requires two markers attached to the specimen to serve as the gage length. The movement of the markers is used to measure the extension of the specimen. The distance between the camera and specimen should remain constant (Coimbra & Greenwood, 2000). Changes in gray intensity, shadows, and reflections can cause significant errors in the results (Wolverton, Bhattacharyya, & Kannarpady, 2009).

Noh *et al.* (2003) developed an optical laser extensometer using a position sensitive detector (PSD), which is different from the conventional time based laser extensometer. The time-based extensometer requires that the laser beam maintains a constant scanning linear velocity on the specimen. The time is calculated by an abrupt signal detected when a laser beam scans a specimen with reflective tapes. The distance is obtained by multiplying the time and linear velocity. With PSD, the laser extensometer can give direct information on the position and the diffused reflection type of the specimen.

- Digital image processing

Digital image processing measures deformation of the specimen by tracking digital images of the specimen. A high-resolution and high-speed digital camera can record the motion of the specimen under loading. By using digital image analysis software to analyze the pictures of the specimen before and after loading, the deformation of the specimen can be determined.

The digital image method records the process of the specimen throughout loading. It is useful in analyzing the failure mechanism. In addition, since it does not contact the specimen, it eliminates many sources of error. Digital image

processing uses pixels as the unit of measurement. With advanced imaging technology, the measurement accuracy of this method is as high as 10^{-4} pixel.

2.2 Digital Image Correlation

Digital Image Correlation (DIC) is a non-destructive measurement technique. It is an optical metrology designed to measure surface deformation. It is also a full-field image analysis method, which is used to evaluate the mechanical properties of a specimen by directly measuring displacement. By correlating a series of images taken before, during, and after loading, the displacement of the specimen is measured.

The DIC method is also known as the Digital Speckle Correlation Method (DSCM). It is a non-interferometry optical measurement method. The "speckle" implies that this technique is based on diffraction (Lagattu, Bridier, Villechaise, & Brillaud, 2006) of the surface, which is similar to the laser speckle method. Instead of a coherent light source, DSCM uses non-interference light sources. White-light is the most widely used light source in DSCM. For this reason, it is also called the white-light digital speckle correlation method. Since a white light source cannot cause speckles due to interference, virtual speckles have to be created. DSCM uses optical textures of the surface (e.g. Figure 2-5 (a)) or surface can be sprayed with speckles (e.g. Figure 2-5 (b)). DSCM measures the displacement of a solid by comparing the gray intensity changes of the solid (Pan, Qian, Xie, & Asundi, 2009) before and after deformation.

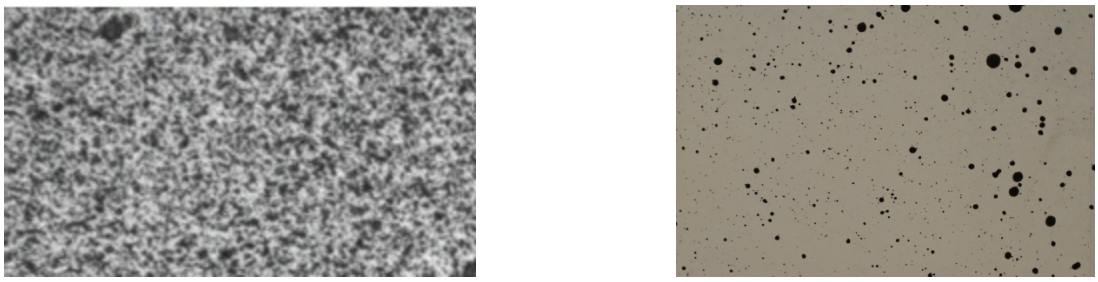

(a) Natural speckle pattern on the concrete surface

(b) Painted speckle on the steel surface

Figure 2-5 Speckle pattern

In the 1960's, Burch and Tokarski (1968) discovered the phenomena that a series of speckles appears when an object is illuminated by a coherent light source such as a laser. Later, Leendertz (1970) applied this technique on metrological measurements. The laser speckle method is widely used in strain measurements. As an interference method, however, the laser speckle method has some limitations: the laser speckle method requires a high stability (vibration-free) testing environment, and has a high cost. Chiang and Asundi (1979) developed a new technique that uses white-light instead of a laser. This is called the white light digital speckle method. After many years of experimentation and investigation, the DIC method has become well developed. DIC has many applications, including measuring displacement (Asundi & North, 1998), velocity, predicting failure (Guo, Sun, He, & Xu, 2008) and analyzing fatigue analysis. Strain measurement is one of the most useful applications of this technology because it achieves high accuracy (5×10^{-6}) for a wide range of materials.

The measurement process of DIC can be divided into three steps (Lagattu, Brillaud, & Lafarie-Frenot, 2004):

1. Experimental setup (including specimen preparation),

2. Data acquisition,

3. Computational analysis.

The data analysis can also be separated into the following steps: The first step is to locate the region of interest (ROI) in the image, followed by overlaying a fixed grid as a reference image (as shown in Figure 2-6). The location of the ROI can be extracted from the grid. Then, the location change of the ROI after loading is tracked by image correlation using pattern recognition. The corresponding ROI is matched to the reference image by superimposing the later images on the reference image. Displacement is calculated by measuring the location change of the ROI.

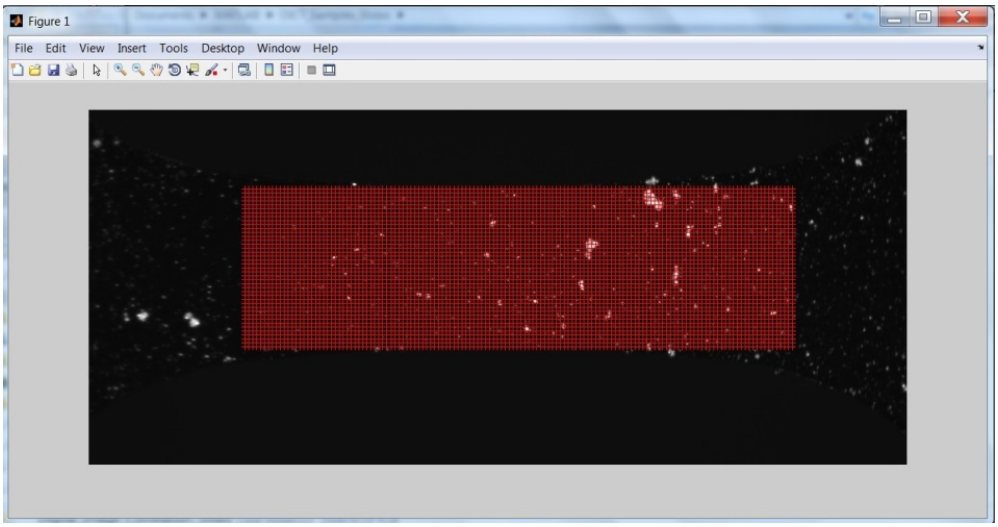

Figure 2-6 A grid on a reference image (Eberl, Thompson, Gianola, & Bundschuh, 2010)

Digital images employed in the DIC method can be recorded by various digital image acquisition devices with different resolutions and accuracy. From macro to micro scale, from full field measurement to specific areas, the DIC method can realize various measurement scales by using a variety of optical devices. The devices includes charge coupled device (CCD) camera, scanning electron microscopy (SEM) ((Paciornik, Martinho, de Mauricio, & d'Almeida, 2003; Canal, González, Molina-Aldareguía, Segurado, & LLorca, 2012), atomic force microscopy (AFM) (Chasiotis & Knauss, 2001;

Cho, Chasiotis, Friedmann, & Sullivan, 2005), and a computed tomography (CT) scan device (Verhulp, Rietbergen, & Huiskes, 2004).

Based on the measurement dimensions of the specimen, DIC can be divided into two general categories: 2D DIC and 3D DIC. Two-dimensional (2D) DIC is used to obtain in-plane deformation measurement. Out-of-plane deformation measurement requires three-dimensional (3D) DIC. Rather than tracking in-plane point movement, 3D DIC tracks the movement of a unit volume within the specimen (Pan, Qian, Xie, & Asundi, 2009). The 2D DIC method uses a single digital image acquisition device to track the deformation. The 3D method requires two digital image acquisition devices that are calibrated (Helm, McNeill, & Sutton, 1996). This system of two cameras is called stereo vision system, and can provide valuable three-dimensional information about the object (Sutton, Yan, Tiwari, Schreier, & Orteu, 2008). The schematic diagram of 3D-DIC is shown in Figure 2-7.

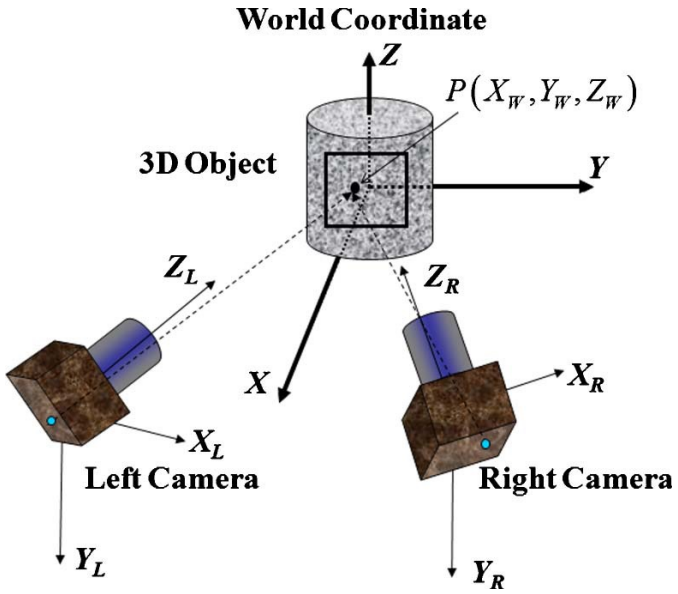

Figure 2-7 Schematic of 3D-DIC system (Hu, Xie, Lu, Hua, & Zhu, 2010)

2.2.1 Theoretical background

The principle of 2D DIC is to track the motion of specific points between a reference image and deformed images as shown in Figure 2–8. In order to compute the displacement of the region of interest, ROI, a grid is generated to locate the position. After loading, the change in location of the ROI is tracked by image correlation using a pattern matching technique. In the pattern, a subset with the pixel in the center is used for the correlation. The subset is an N×N pixel square. A schematic of a subset is shown in Figure 2-9. Usually, the sizes of the subsets range from 7×7 to 21×21 pixels. Using these subsets to match instead of individual pixels is desirable because each subset contains a wider variation in gray levels that can be uniquely identified (Pan, Qian, Xie, & Asundi, 2009). To find the similarity between the reference subset and the deformed subset, correlation criteria are involved. Correlation is based on matching each pixel within a neighborhood and calculating the disparity. The correlation criteria are the algorithms to achieve this. The procedure maximizes the correlation coefficient, which is determined by evaluating the pixel intensity array of the two images.

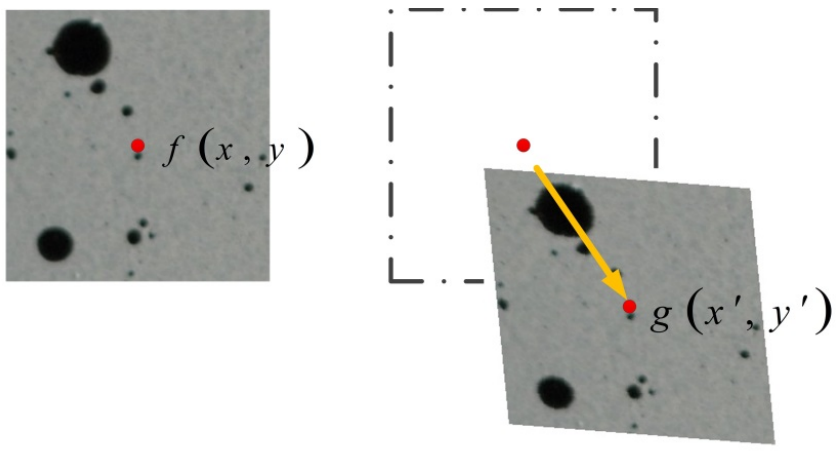

Figure 2-8 Correlation of pixel displacement by DIC (adapted from Pan 2009

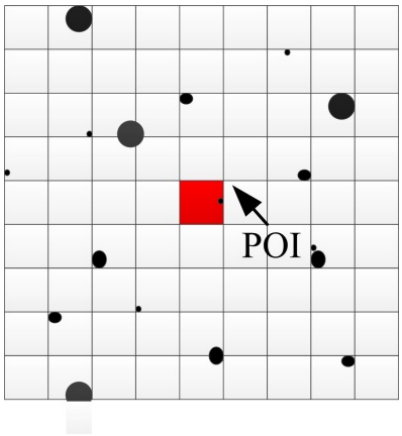

Figure 2-9 Schematic of a 9×9 pixel subset

For a small strain, deformation of the specimen may be within the subset or on the sub-pixel accuracy level. Thus, before the subsets of two images are correlated, locations of pixels with intensities that fall within the subset must be defined. The interpolation scheme, which provides sub-pixel accuracy, should be utilized. For a homogeneous material, a lower order (zero or first order) interpolation (e.g. bilinear interpolation) is enough to approximate the variation of displacement (Jin & Bruck, 2005). For a nonhomogeneous material, higher-order interpolation schemes (e.g. bicubic interpolation) are necessary. Higher-order interpolation schemes involve more terms and provide higher registration accuracy and better convergence character (Schreier, Braasch, & Sutton, 2000; Knauss, Chasiotis, & Huang, 2003; Cheng, Sutton, Schreier, & McNeill, 2002).

2.2.2 Displacement measurement in 2D DIC

The correlation is achieved by using a subset of a predetermined size surrounding the pixel of interest in the reference image and corresponding deformed image. The accuracy of subpixel-level is achieved by sub-pixel registration algorithms and robust

correlation criteria. Although the principle of DIC is straightforward, there are two main challenges in practical applications: accuracy and computational efficiency, which are usually contradictory. Higher accuracy requires longer computational time using the same computer configuration.

2.2.2.1 Correlation criteria

The principle of image correlation for deformation measurement is to map a local displacement. In the DIC method, the displacements are presented in terms of pixels. For a square subset containing n pixels, f_i and g_i are defined as the gray intensity of the reference image and the deformed image of the pixel, respectively.

Various correlation criteria have been proposed and used in displacement measurement, including cross-correlation (CC), sum of absolute difference (SAD), sum of squared difference (SSD), parametric sum of squared difference (PSSD), sum of Hamming distances (SHD), and least-squares correlation criteria (Vendroux & Knauss, 1998). In order to decrease the error caused by the change of intensity of the subsets, the above criteria are modified to zero-mean cross-correlation (ZNCC) criterion, zero-mean normalized sum of squared difference (ZNSSD) criterion and parametric sum of squared difference ($PSSD_{ab}$) criterion with two additional parameters. According to Tong (2005) and Pan *et al.* (2010), if the intensity of a pixel remains unchanged in the images during the deformation, using different correlation criteria do not affect the result of the displacement measurement. However, in real tests, this condition is rarely satisfied. To avoid significant error in displacement measurements caused by a mismatch of the intensity change model (Schreier, Braasch, & Sutton, 2000), a suitable correlation criterion must be selected to deal with the variations of intensity.

1) Cross-Correlation (CC) criteria

The CC criteria can be divided into four types, according to the accuracy of possible intensity changes: direct CC, zero-mean cross-correlation (ZCC), normalized cross-correlation (NCC), and zero-mean normalized cross-correlation (ZNCC). The principle of all CC criteria is to maximize the cross-correlation coefficients.

The coefficient of direct CC is shown in Equation (2-3)

$$C_{CC} = \sum f_i g_i \tag{2-3}$$

The coefficient of zero-mean cross-correlation (ZCC) involves subtracting the mean value of the subset intensity in Equation (2-4),

$$C_{ZCC} = \sum [(f_i - \overline{f}) \times (g_i - \overline{g})] \tag{2-4}$$

Where $\overline{f} = \frac{1}{n} \sum_{i=1}^{n} f_i$: the mean intensity value of the reference subset,

$\overline{g} = \frac{1}{n} \sum_{i=1}^{n} g_i$: the mean intensity value of the deformed subset.

By subtracting the mean value of the subset intensity, the ZCC criterion reflects the tolerance of the subset's offset change between the deformed image and the reference image. ZCC reduces the sensitivity of the DIC method to the offset change of the subset.

The coefficient of normalized cross-correlation (NCC) uses the root-sum-square of the subset intensity, as shown in Equation (2-5),

$$C_{NCC} = \frac{\sum f_i g_i}{\sqrt{\sum f_i^2 \sum g_i^2}} \tag{2-5}$$

NCC reduces the effect of differing lighting in two images by dividing by the root-sum-square of subset intensity (Watman, Austin, Barnes, Overett, & Thompson, 2004).

The coefficient of zero-mean normalized cross-correlation (ZNCC) combines the advantages of ZCC and NCC as defined by Equation (2-6).

$$C_{ZNCC} = \frac{\sum \overline{f}_i \overline{g}_i}{\sqrt{\sum \overline{f}_i^2 \sum \overline{g}_i^2}} \tag{2-6}$$

Where $\overline{f}_i = f_i - \overline{f}$ and $\overline{g}_i = g_i - \overline{g}$.

By combining the advantages of ZCC and NCC, the ZNCC criterion is the most robust and reliable criterion for processing images. The combination minimizes the influence of intensity change (Tong, 2005; Pan, Wang, & Xie, 2009).

2) Sum of absolute difference (SAD) criterion

The SAD is calculated by subtracting pixels within a square neighborhood between the reference image and deformed image. It is often used for motion estimation by means of landmark detection. A landmark is a visual feature that is relatively unique within an image and is stable over time (Watman, Austin, Barnes, Overett, & Thompson, 2004). Unlike NCC and ZNCC, the SAD correlation criteria can identify areas within the same image that exhibit local differences. The correlation is achieved by minimizing the coefficient of SAD. Equations (2-7) and (2-8) give the correlation coefficients for direct SAD and ZNCC respectively.

Direct SAD:

$$C_{SAD} = \sum |f_i - g_i| \tag{2-7}$$

Zero-mean sum of absolute differences:

$$C_{ZSAD} = \sum \left| (f_i - \overline{f_i}) - (g_i - \overline{g_i}) \right| \tag{2-8}$$

3) Sum of squared difference criteria (SSD)

The CC coefficients are closely related to the SSD coefficients (Tong, 2005). Maximization of the CC criteria coefficient is equivalent to minimization of the SSD criterion coefficient. The sum of squared difference criteria can be divided into four types as the cross-correlation criteria was also divided.

Direct SSD criterion:

$$C_{SSD} = \sum (f_i - g_i)^2 \tag{2-9}$$

Zero-mean sum of squared difference criterion (ZSSD), which corresponds to ZCC,

$$C_{ZSSD} = \sum \left[(f_i - \overline{f}) \times (g_i - \overline{g}) \right]^2 \tag{2-10}$$

Normalized sum of squared difference criterion (NSSD), which corresponds to NCC,

$$C_{NSSD} = \sum \left(\frac{f_i}{\sqrt{\sum f_i^2}} - \frac{g_i}{\sqrt{\sum g_i^2}} \right)^2 \tag{2-11}$$

Zero-normalized sum of squared difference criterion (ZNSSD), which corresponds to ZNCC

$$C_{ZNSSD} = \sum \left(\frac{\overline{f_i}}{\sqrt{\sum \overline{f_i}^2}} - \frac{\overline{g_i}}{\sqrt{\sum \overline{g_i}^2}} \right)^2 \tag{2-12}$$

4) Least-square correlation (LSC)

Least-square correlation is used in image matching. The basic equation for the correlation coefficient is based on a statistical modeling (Gruen, 1985) by least squares estimation as shown in Equation (2-13).

$$C = \frac{\sum [f_i - g_i]^2}{\sum f_i^2} \tag{2-13}$$

2.2.2.2 Sub-pixel registration algorithms

For micro scale strains, the displacement may be within several pixels. Therefore, the location must be determined at the subpixel-level using one of two available methods. One is the direct method, which uses an appropriate model to represent the location of the pixel, such as Gaussian or interpolation models. The details of these models are introduced in the next chapter. This method directly affects the performance of a correlation algorithm (Hild & Roux, 2006). The second method involves applying an optimization algorithm in order to determine accurate displacements. Some widely used sub-pixel registration algorithms are introduced next.

1) Newton-Raphson algorithm

The Newton-Raphson (NR) algorithm (Bruck, McNeill, Sutton, & Peters, 1989) is the most widely used subpixel registration algorithms since it has a relatively high measurement accuracy and computational efficiency.

The NR algorithm takes into account the deformation of a subset between the reference and the deformed image (Pan, Xie, Xu, & Dai, 2006). An assumed subset point (x, y) in the reference image is mapped into the deformed image as (x', y') by using Equation (2-14) and (2-15).

$$x' = x + u + \frac{\partial u}{\partial x}\Delta x + \frac{\partial u}{\partial y}\Delta y \quad (2\text{-}14)$$

$$y' = y + v + \frac{\partial v}{\partial x}\Delta x + \frac{\partial v}{\partial y}\Delta y \quad (2\text{-}15)$$

Where u and v are displacement components for the subset centers in the x and y directions respectively, Δx and Δy are the distances from the subset center to the point (x, y).

The above equation employs the first-order shape function. For some applications, the NR algorithm involves second-order derivatives of the correlation function, which increases the computational complexity (Lu & Cary, 2000). Increasing the order of algorithm greatly increases the required computation time. Thus, unless special high sub-pixel registration accuracy is required, using a linear shape function in the NR algorithm is appropriate.

The NR algorithm is a non-linear numerical optimization algorithm that requires an accurate initial guess of the location. Pan and Li (2011) improved the NR algorithm by effectively eliminating the repetitive and redundant calculations required for the conventional NR algorithm. They proposed a reliability-guided displacement scanning strategy to obtain a reliable and accurate initial guess. A pre-computed global interpolation coefficient look-up table is given to avoid the repetitive interpolation calculations at sub-pixel locations.

2) Gradient-based method

The gradient-based method was first developed as an optical flow method by Davis and Freeman (Davis & Freeman, 1998). The fundamental assumption of the gradient-based method is that the gray level intensity of a point in a reference image is

same in the deformed image (Pan, Asundi, Xie, & Gao, 2009). Assume $f(x, y)$ and $g(x', y')$ are the gray level intensity of a point in a reference image and a deformed image, respectively. Then,

$$f(x, y) = g(x', y') \tag{2-16}$$

Where $x' = x + u + \Delta x$, $y' = y + v + \Delta y$.

u and v are displacement components for the subset centers in the x and y directions, respectively. Δx and Δy are the distances from the subset center to the point (x, y).

Using a Taylor expansion of $g(x', y')$ to determine derivatives in terms of u, v, Δx and Δy, the system can be solved using the least squares method.

Zhou and Goodson (2001) applied an iterative spatial-gradient-based method to reduce the computational complexity of this method. Bing Pan *et al.* (2009) modified the iterative spatial-gradient-based method proposed by Zhou and Goodson by introducing a linear intensity-change model. This can reduce the sensitivity of changing lighting and gray intensity.

3) Genetic Algorithm

The Genetic Algorithm (GA) is an optimization method inspired by natural evolution: the Darwinian principle of survival and reproduction of the fittest (Mitchell, 1998). It is used for the 2D DIC method to optimize the correlation criterion to determine the deformation parameters.

GA was first explored by Holland in the 1960s. It is very different from classical optimization algorithms and can be easily applied to a variety of fields (Hwang, Horn, & Wang, 2008). GA creates an initial population of random individuals, and then applies

crossover and mutation to generate new individuals. Individuals are picked by some quality criteria to find the fittest, which is known as a fitness-proportionate selection (Wang & Hou, 2010; Pilch, Mahajan, & Chu, 2004). Thus, the new generation has better individuals. Repeat the process until the stop criteria is satisfied. The best individual in the last generation is the approximate optimal solution.

For the 2D DIC, an initial deformation vector map is randomly generated within a possible range. The correlation criterion functions as a quality criterion. When the convergence is met, the deformation vector is considered to be found.

4) Other algorithms

With the development of modern mathematics, new mathematical theories and recognition methods have been developed and applied to the DIC method to achieve subpixel accuracy.

Artificial neural networks (ANNs) are introduced to estimate sub-pixel displacements for digital image correlation by Pitter *et al*. (2001). The algorithm has been applied to thermally-stressed microelectronic devices. Pan *et al*. (Pan, Asundi, Xie, & Gao, 2009) investigated the iterative least squares algorithm (ILS) and pointwise least squares algorithm (PLS) to calculate displacement and strain, respectively. The goal of these new algorithms was to increase computational efficiency without sacrificing the sub-pixel measurement accuracy.

2.2.3 Error in DIC

The accuracy of DIC is affected by two major sources of error: experimental and numerical. Experimental errors result from experimental devices, testing environment and test setup parameters. Typical 2D DIC experimental devices consist of a digital

image acquisition device, a lighting source, and a loading device. The noise of the optical device is directly related to the quality of the digital image, which can influence the accuracy of the correlation. High resolution image acquisition devices produce high resolution images. The light intensity is related to gray levels of the specimen (Haddadi & Belhabib, 2008), which influences the accuracy of the correlation. Since overexposure and underexposure decrease accuracy, stable and suitable lighting is required to minimize the error associated with lighting. Jerabek *et al.* (2010) found that the lighting intensity just below overexposure can provide the best result. Overexposure will lose the detail in the information from the brightest parts of an image. The environment of the test contributes to errors in displacement measurements. Environmental errors are primarily due to vibrations caused by operation of the loading devices (Jerabek, Major, & Lang, 2010). These vibrations induce noise in the optical devices and desynchronize the timing between the photography and the ROI position (Haddadi & Belhabib, 2008).

Numerical errors include subset (also known as sub-window) size, speckle pattern of the specimen, and correlation algorithm. The DIC method divides the image into small sub-windows of N pixels or $N \times N$ pixels. The center of each window box is considered as a "point" (Lagattu, Bridier, Villechaise, & Brillaud, 2006) to correlate. The size of the subset is defined by pixels. By discretizing the image into subsets, correlation of images can be realized. The subset size selection is very important in the DIC method since it affects the accuracy significantly. The subset size depends on the speckle pattern of the specimen. Both too large and too small subset sizes induce inaccuracies. While larger subsets decrease the errors (Haddadi & Belhabib, 2008), they also smooth the real localized displacement (Lecompte, et al., 2006), increasing the computation time.

Smaller subsets simplify the computation, but may not contain enough characteristics to achieve reliable displacement measurement (Pan, Xie, Wang, Qian, & Wang, 2008), thus, increasing errors (Haddadi & Belhabib, 2008). To optimize the subset size, many studies have been undertaken. Sun & Pang (2007) introduced the concept of subset entropy to quantify the subset image pattern quality. They also proved the effects of subset size on homogeneous and nonhomogeneous displacement areas. For homogeneous displacement, the subset size has a lower boundary to decrease random errors. A subset size below the lower boundary may induce significant errors. Similarly, nonhomogeneous displacement, subset size has an upper boundary due to increased systematic errors. Bing Pan *et al.* (2008) developed the concept of subset entropy by using Sum of Square of Subset Intensity Gradients (SSSIG) as mathematical support.

As mentioned earlier, the DIC method uses "artificial" speckles. If the natural texture of the specimen surface has a random gray intensity distribution, DIC uses the natural texture as the speckle pattern. If the natural texture of the specimen surface does not have a random gray intensity distribution, speckles must be spray painted onto the surface. In this case, DIC uses the sprayed paint as the speckle pattern. The quality of the speckle pattern has a significant effect on accuracy of displacement measurement (Lecompte, et al., 2006; Haddadi & Belhabib, 2008; Sun & Pang, 2007; Pan, Xie, Wang, Qian, & Wang, 2008). Lecompte (2006) studied the influence of the mean speckle size and subset size on accuracy of DIC. Mean speckle size was determined by an image morphology method. Bing Pan *et al*. (2010) introduced a parameter called mean intensity gradient, which is another quality assessment of the speckle patterns. Mean intensity gradient of speckle patterns is closely connected to systematic errors (mean bias error)

and random errors (standard deviation) of displacement measurement. Larger mean intensity gradients corresponded to smaller mean bias and standard deviation errors.

2.3 Edge detection

2.3.1 Introduction to edge detection

The edge of an image is detected by variation in intensity or brightness. Edge detection in image processing refers to the process of identifying this change in an image. The CCD camera detects light and converts the incoming photons into electrical signal. In image acquisition, the CCD sensitive pixels receive light from both the local and the neighboring photosensitive pixel causing a gradual change based on the response signal, especially at edge points (Li & Xu, 2009). Figure 2-10 (a) illustrates an ideal edge signal, which has a straight edge of signal change. However, the real edge signal looks more like Figure 2-10 (b). The edge pixel is not a single point, but a gradual transition between phases. The subpixel edge is located within this transition.

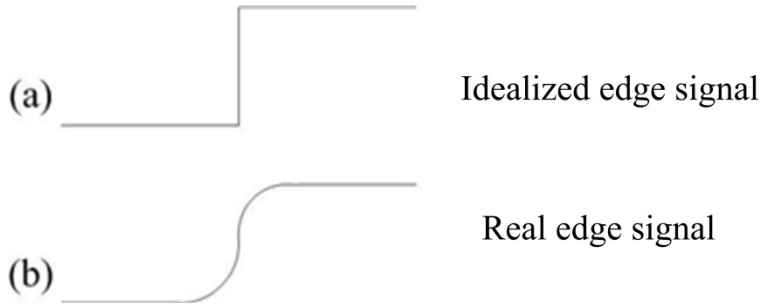

Figure 2-10 Edge signal of a one-dimensional image

2.3.2 Edge detection methods

There are many methods to detect edges, such as Canny edge detection (Canny, 1983& 1986), Sobel operator (Oskoei & Hu, 2010), and Prewitt's operator (Maini & Sggarwal, 2009).

Usually, a complete edge detection process involves smoothing, edge detection, and thresholding. Smoothing is like a 2-D filter to convolve the image. The procedure of the "convolve image" is to multiply the image singal function by a filter function. The filter function is called the convolution kernel. The aims of the smoothing is to remove the noise while keeping the image structure. Here, the image signal (*f*) multiples the smoothing function (kernel *h*) to produce a modified image signal. After smoothing, the signal is sensitive to large gradients and is flat in uniform areas. In addition, because differentiation is applied directly, the edge detection algorithms often have problems, as shown in Figure 2-11 (Oskoei & Hu, 2010), such as no real solution, no unique solution, or a lack of stability. By convolution of the raw image with kernel *h*, as shown in Figure 2-12, regularized differentiation can be accomplished. To reduce computations, a derivative of the kernel can be used in convolution to achieve a similar result. The Gaussian filter is one of the most widely used smoothing filters since it was first proposed by Marr and Hilderth (1980) in 1980. The second derivative of the Gaussian is called the Laplacian of a Gaussian (LOG), an orientation-independent operator used as a filter for edge detection (Basu, 2002).

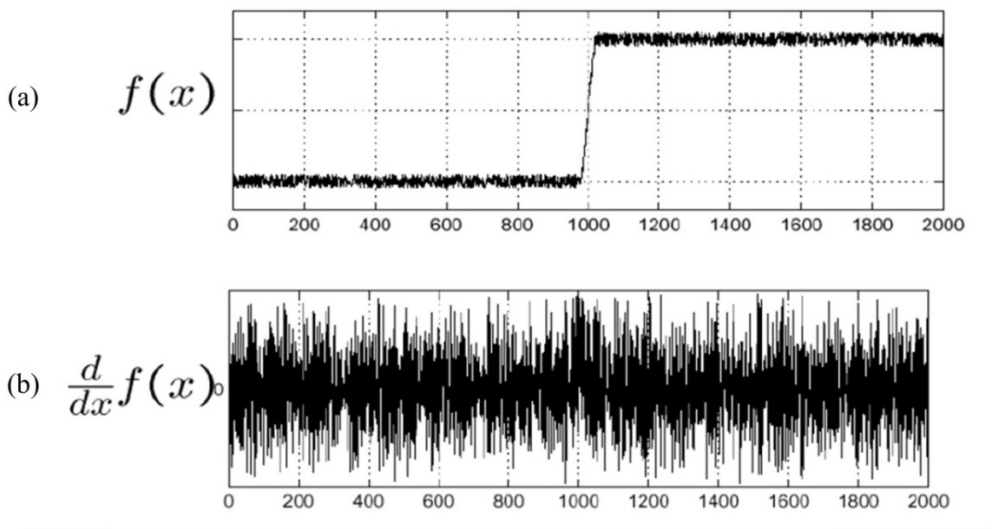

(a) Signal function; (b) First derivative of the signal function

Figure 2-11 The direct first derivative of a signal function that is affected by noise is not enough to localize a step change within it (Oskoei & Hu, 2010)

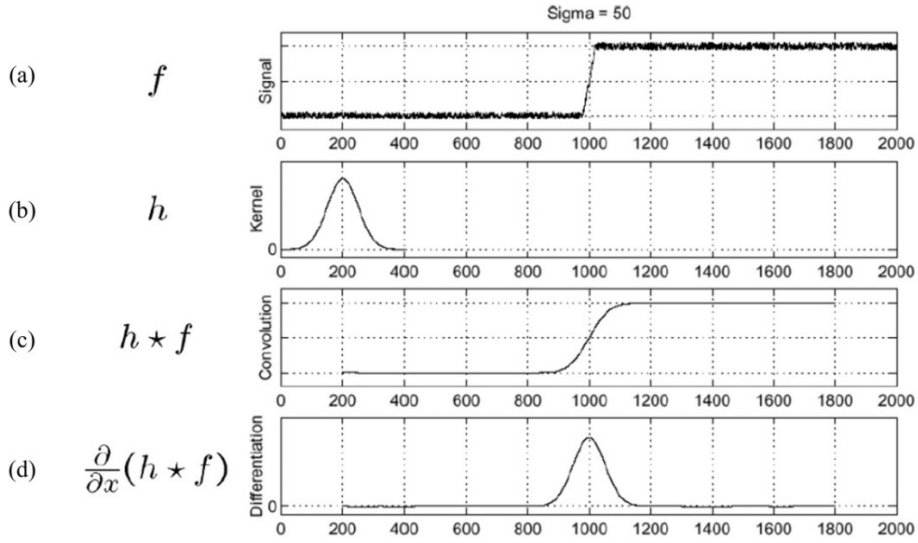

(a) Signal function *f*; (b) Kernel *h*; (c) Modified function by convolution ($h \times f$); (d) First derivative of the modified function

Figure 2-12 By applying convolution, the first derivative of modified function reaches the local maximum (Oskoei & Hu, 2010)

There are many methods to achieve edge detection, which can be collected into two categories, as shown in Figure 2-13:

- Gradient: the gradient method uses the maximum and minimum of the first derivative to find the edges.
- Laplacian: the Laplacian method looks for the zero crossings in the second derivative to detect the edges.

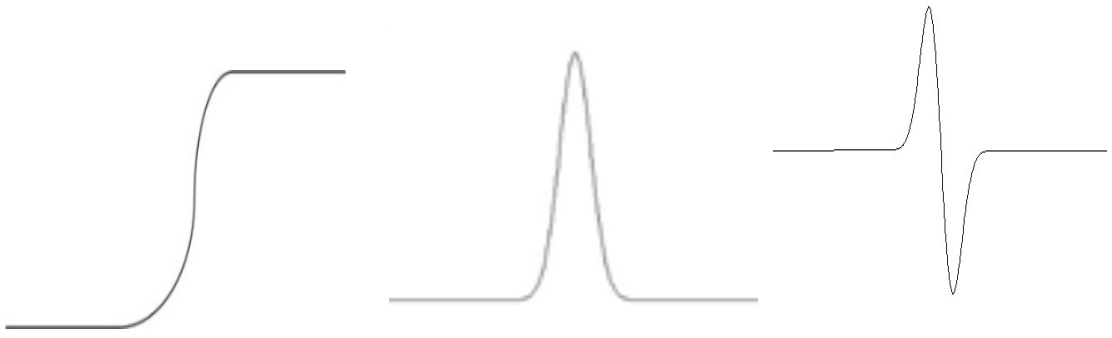

(a) (b) (c)

(a) Edge signal; (b) Detecting the local extreme by the 1st derivative of edge signal; (c) Detecting the zero-crossing by the 2nd derivative of edge signal

Figure 2-13 The first derivative and second derivative methods to detect the edge

Essentially, these two methods are the same. The location where the first derivative of the edge signal reaches the maximum (or minimum) is the same as the location where the second derivative at this point will equal zero.

2.3.2.1 Sobel operator

The Sobel operator is based on a discrete derivative. It consists of a pair of convolution kernels (3×3 matrix), which are perpendicular to each other. These two kernels are designed to compute the gradient of gray intensity of an image in the vertical

and horizontal directions. The gradient (G) at each point is a vector, which has both magnitude and direction. The gradient components are known as G_x and G_y, which can be calculated by two kernels (Equation (2-17) and Equation (2-18), respectively). The absolute magnitude of G is given by Equation (2-19) and its direction is calculated using Equation (2-20).

$$G_x \rightarrow \begin{bmatrix} -1 & 0 & +1 \\ -2 & 0 & +2 \\ -1 & 0 & +1 \end{bmatrix} \tag{2-17}$$

$$G_y \rightarrow \begin{bmatrix} +1 & +2 & +1 \\ 0 & 0 & 0 \\ -1 & -2 & -1 \end{bmatrix} \tag{2-18}$$

$$|G| = \sqrt{G_x{}^2 + G_y{}^2} \approx |G_x| + |G_y| \tag{2-19}$$

$$\theta = \tan^{-1}\left(\frac{G_y}{G_x}\right) \tag{2-20}$$

The Sobel operator is a fast and easy approach to detect edges. However, since it does not involve smoothing the source image, it is sensitive to noise (Oskoei & Hu, 2010). Therefore, the Sobel operator is used as an intermediate step to calculate the gradient of a pixel in the other edge detection methods.

2.3.2.2 Canny edge detection

The Canny edge detection algorithm is the most common and widely used edge detection algorithm, especially in industry. Canny (1986) proposed three criteria to improve the performance of edge detection algorithms to achieve an optimal result. The optimal edge detector should satisfy the following conditions:

- Good detection: the algorithm should mark many more real edge points than non-edge points, maximizing the signal-to-noise ratio.

- Good localization: the edge marks should be as close to the true edge as possible.
- Only one response to a single edge: multiple responses should be eliminated and the edge should be marked only once.

Based on the above criteria, Canny edge detection can be summarized into four steps (Oskoei & Hu, 2010; Maini & Sggarwal, 2009):

Step 1: Noise reduction. Before detection and localization of edges, a Gaussian smoothing filter is applied to the image to reduce the noise.

Step 2: Gradient computation. The gradient of the image is computed by the Sobel operator. The direction of the edge is calculated using the gradient in the x (G_x) and y (G_y) directions. There are only four traceable directions in an image for a pixel. The edge directions must be categorized by one of the four closest possible directions. The four possible directions (as shown in Figure 2-14) are: 0 degrees (in horizontal direction); 45 degrees (along the positive diagonal); 90 degrees (in vertical direction); 135 degrees (along the negative diagonal).

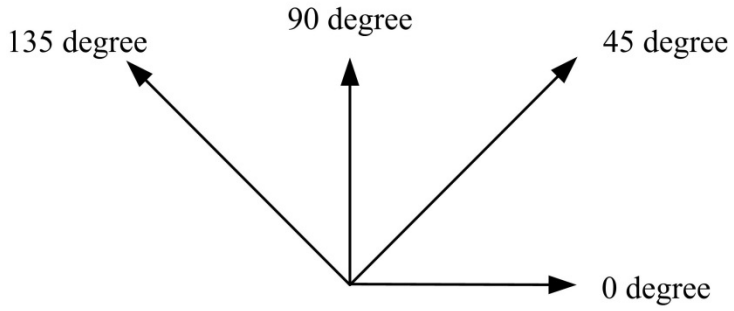

Figure 2-14 Four possible directions

Step 3: Non-maximum suppression. After estimating the direction of the edge gradient, non-maximum suppression is applied to trace along the edge. In the direction of

the edge, set the pixel values that are not considered to be an edge equal to zero. If a pixel meets one of the following conditions, the point can be assumed to be an edge:

- The rounded gradient angle is 0 degrees and the gradient magnitude is greater than the magnitude in the horizontal direction.
- The rounded gradient angle is 45 degrees and the gradient magnitude is greater than the magnitude in the positive diagonal direction.
- The rounded gradient angle is 90 degrees and the gradient magnitude is greater than the magnitude in the vertical direction.
- The rounded gradient angle is 135 degrees and the gradient magnitude is greater than the magnitude in the negative diagonal direction.

Step 4: Hysteresis thresholding. Canny edge detection uses adaptive thresholding with hysteresis to eliminate streaking. Hysteresis uses both an upper and a lower threshold. First, the upper threshold is applied to select a genuine edge. Then the lower threshold is used to thin the edge. After thresholding, a binary image with only edge and non-edge pixel is obtained.

2.3.3 Subpixel edge detection

Subpixel edge detection is extremely important in the digital image correlation method. Traditional edge detection methods like the Sobel operator and the Canny edge detector can only achieve pixel-level precision. With increasing precision requirements in digital image processing techniques, subpixel edge detection is needed (Hyde & Davis, 1983; Jensen & Anastassiou, 1995). This technique breaks the limitation of resolution of the CCD image.

Most sub-pixel edge detection algorithms can be divided into three groups: fitting methods, interpolation methods, and moment-based methods.

- Fitting methods use continuous functions to fit gray scales of the image. The sub-pixel edge location is at the inflection point of the continuous function. The published fitting functions include the B-spline (Bouchara, Bertrand, Ramdani, & Haydar, 2007; Breder, Estrela, & de Assis, 2009), the Gaussian function (Shang, Chen, & Tian, 2010), the hyperbolic tangent (Wei, Tan, Liu, & Xiong, 2010), and the Erf function (Hagara & Kulla, 2011).
- Interpolation methods use the traditional edge detection method to find a coarse edge, and then reach the subpixel accuracy by interpolating the image data to attain a finer grid of pixels. The interpolation method can recover a high resolution image from a low resolution image (Wang & Ling, 2010). By using the pixels in the neighborhood of the objective pixel of the original image, the pixel value is computed by interpolation based on the interpolation function. The interpolation method includes nearest neighbor interpolation, bilinear interpolation (Chen, Huang, & Lee, 2005; Press, Teukolsky, Vetterling, & Flannery, 2007), and bicubic interpolation (Thévenaz, Blu, & Unser, 2000).
- The Moment-based method formulates the edge detection as a statistical inference. By applying several moment-templates, the subpixel edge location is determined (Da & Zhang, 2010). There are many proposed moment-based methods, including Gray level moment (Tabatabai & Mitchell, 1984), Spatial-gray moment (SGM) (Lyvers & Mitchell, 1988), Zernike orthogonal moment (ZOM) (Cheng &

Wu, 2005; Yang & Pei, 2011), and Orthogonal Fourier-Mellin moment (OFMM) (Bin, Lei, Cui, Kang, & Liu, 2008).

2.3.3.1 Gaussian curve fitting algorithm

For the Gaussian curve fitting method, the gradient distribution curve of edge points is required. This is achieved by sampling some edge points, and determining their gray intensity. The gradient values of these points are obtained by measuring gray intensity. A Gaussian curve is used to fit the gradient curve of the edge points. The real edge is located at the extreme point of the curve, the zero-cross point of the first derivative or the zero-cross point of the second derivative (Shang, Chen, & Tian, 2010).

The Gaussian curve expression in one dimension is expressed as Equation (2-21)

$$y = \frac{1}{\sqrt{2\pi}} e^{-\frac{(x-\mu)^2}{2\sigma^2}} \tag{2-21}$$

Where μ- the mean and σ-standard deviation

In the Gaussian curve, the extreme point is the mean. In other words, the mean is the location of the edge point. Usually, the edge point is not located exactly on one pixel. Instead, it is located between pixels, as shown in Figure 2-15. A precise Gaussian curve is important to achieve subpixel accuracy.

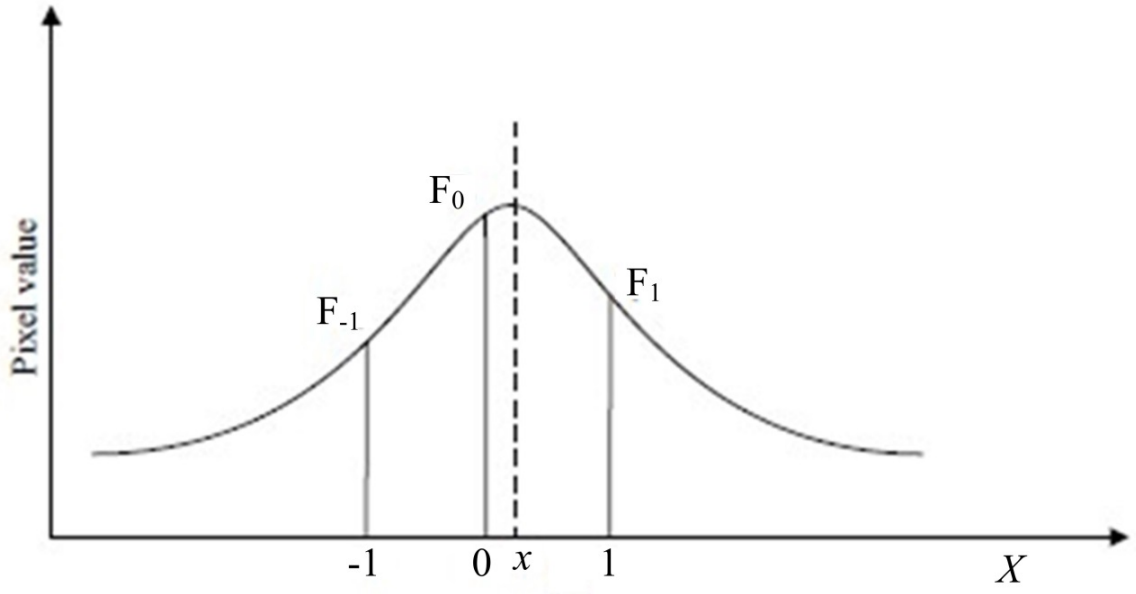

Figure 2-15 Gaussian curve for sub-pixel accuracy

For ease of calculation, the above Gaussian function is transformed as follows:

$$\ln y = -\frac{(x-\mu)^2}{2\sigma^2} + \ln\frac{1}{\sqrt{2\pi}\sigma} \tag{2-22}$$

This function is similar to the quadratic polynomial equation $y = ax^2 + bx + c$. To evaluate the parameters *a, b* and *c*, the least square method is used.

$$\Pi = \sum_{i=1}^{n} (y_i - ax_i^2 - bx_i - c)^2 \tag{2-23}$$

To minimize Π, the partial derivative of Π with respect to *a, b* and *c* is found:

$$a = \frac{d \times e - f \times g}{h \times d - g \times g} \tag{2-24}$$

$$b = \frac{f - g \times a}{d} \tag{2-25}$$

$$c = \frac{1}{n}\left(\sum_{i=1}^{n} y_i - a \times \sum_{i=1}^{n} x_i^2 - b \times \sum_{i=1}^{n} x_i\right) \tag{2-26}$$

Then the partial differential equation is set equal to zero, resulting in:

$$d = n\sum_{i=1}^{n} x_i^2 - \left(\sum_{i=1}^{n} x_i\right)^2 \tag{2-27}$$

$$e = n\sum_{i=1}^{n} x_i^2 y_i - \sum_{i=1}^{n} x_i^2 \sum_{i=1}^{n} y_i \tag{2-28}$$

$$f = n\sum_{i=1}^{n} x_i y_i - \sum_{i=1}^{n} x_i \sum_{i=1}^{n} y_i \tag{2-29}$$

$$g = n\sum_{i=1}^{n} x_i^3 - \sum_{i=1}^{n} x_i^2 \sum_{i=1}^{n} x_i \tag{2-30}$$

$$h = n\sum_{i=1}^{n} x_i^4 - \left(\sum_{i=1}^{n} x_i^2\right)^2 \tag{2-31}$$

Using Equations (2-27) to (2-31), the μ and σ of the Gaussian equation can be calculated as follows:

$$\mu = -\frac{b}{2 \times a} \tag{2-32}$$

$$\sigma = \sqrt{\frac{-1}{2 \times a}} \tag{2-33}$$

Where the subpixel edge location is at μ.

2.3.3.2 Quadratic Polynomial Interpolation

The edge in this investigation is a simple rectangle, which has only vertical and horizontal directions. Given that the gradient distribution of a pixel is similar in the

vertical and horizontal directions, the same 1-dimensional algorithm is used in both directions.

The process of subpixel edge detection by quadratic polynomial interpolation is:

1. Use Canny edge detection to obtain the coarse edge location at the pixel-level, (*m,n*).

2. Based on the edge coordinates obtained from Canny edge detection, the Sobel operator (2-34) is used to calculate the gradient by surrounding a pixel's gray value (Figure 2-16).

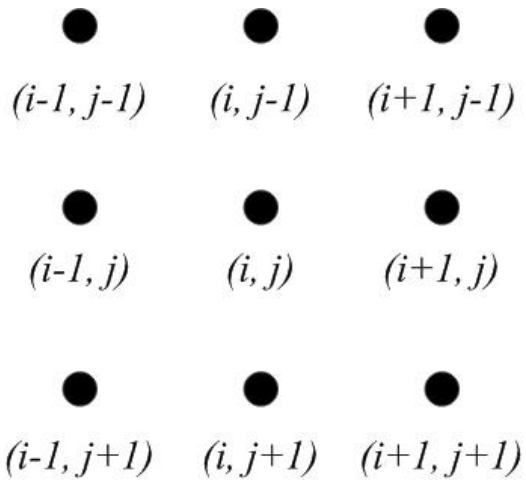

Figure 2-16 Pixel (*i, j*) and surrounding pixels

$$
\begin{aligned}
R(i,j) &= |G_x| + |G_y| \\
&= \left| \begin{matrix} f(i+1,j+1) + 2f(i,j+1) + f(i-1,j+1) \\ -f(i-1,j-1) - 2f(i,j-1) - f(i+1,j-1) \end{matrix} \right| \\
&+ \left| \begin{matrix} f(i-1,j-1) + 2f(i-1,j) + f(i-1,j+1) \\ -f(i+1,j+1) - 2f(i+1,j) - f(i+1,j-1) \end{matrix} \right|
\end{aligned} \tag{2-34}
$$

The gradient of three points in the *x* direction (*m-1*, *n*), (*m*, *n*), (*m+1*, *n*) is used to fit the quadratic polynomial $G(x) = ax^2 + bx + c$

$$R(m-1,n) = a(m-1)^2 + b(m-1) + c \tag{2-35}$$

$$R(m,n) = am^2 + bm + c \tag{2-36}$$

$$R(m+1,n) = a(m+1)^2 + b(m+1) + c \tag{2-37}$$

Solving the above system of equations, gives

$$a = \frac{R(m+1,n) + R(m-1,n) - 2R(m,n)}{2} \tag{2-38}$$

$$b = -[R(m+1,n) + R(m-1,n) - 2R(m,n)]m + \frac{R(m+1,n) - R(m-1,n)}{2} \tag{2-39}$$

$$c = \frac{R(m+1,n) + R(m-1,n) - 2R(m,n)}{2} m^2 - \frac{R(m+1,n) - R(m-1,n)}{2} m + R(m,n) \tag{2-40}$$

3. The parameters *a, b* and *c* are used in the polynomial function. The edge should be located at the extreme value of the gradient polynomial function, given by

$$\frac{\partial G(x)}{\partial x} = 0 \tag{2-41}$$

Solving the above equation, finds the horizontal subpixel edge as

$$x = m - \frac{R(m+1,n) - R(m-1,n)}{2[R(m+1,n) + R(m-1,n) - 2R(m,n)]} \tag{2-42}$$

Since Equation (2-42) is based on (*m*, *n*), the coarse edge point determined by the extreme gradient, Equations (2-43-A) and (2-43-B) have to satisfy:

$$R(m,n) > R(m-1,n) \tag{2-43-A}$$

$$R(m,n) > R(m+1,n) \tag{2-43-B}$$

Similarly, by using three points in the *y* direction (*m*, *n-1*), (*m*, *n*), (*m, n+1*), the vertical subpxiel edge is given by:

$$y = n - \frac{R(m,n+1) - R(m,n-1)}{2[R(m,n+1) + R(m,n-1) - 2R(m,n)]} \quad (2\text{-}44)$$

where Equations (2-45-A) and (2-45-B) must be satisfied:

$$R(m,n) > R(m,n-1) \quad (2\text{-}45\text{-A})$$

$$R(m,n) > R(m,n+1) \quad (2\text{-}45\text{-B})$$

The above polynomial interpolation is very easy and quick for computation. However, since only the nearest points to the edge point are involved, the result can include significant error. In addition, by neglecting the orientations of gradients of points, the conditions in (2-43-A) and (2-45-A) are difficult to satisfy. Many edge points will be lost based on the above equation.

2.4 Camera calibration

Camera calibration is an essential step in image analysis. The goal of calibration is to determine the intrinsic and extrinsic parameters, such as the camera's position and orientation, which affect the accuracy of measurements extracted from the images. It is necessary in various applications including photogrammetry, remote sensing, motion planning, virtual reality, robot navigation, and object recognition. After calibration, 3D computer vision can be extracted from 2D images. Calibrated cameras can also be used to make real measurements since pixels and real dimensions are related by the camera calibration parameters.

2.4.1 Camera calibration parameters

2.4.1.1 Coordinate system

To understand camera calibration parameters, three coordinate systems need to be defined: world coordinates (global coordinates), camera coordinates, and image coordinates.

The world coordinates are used to describe the position and orientation of 3D points. For a multi-camera system, the world coordinates are also used to locate the cameras. They are expressed as (X_w, Y_w, Z_w) by adding a subscript w.

The camera coordinates are expressed as (X_c, Y_c, Z_c) by adding a subscript c. The origin (0, 0, 0) of the camera coordinates is in the center of the camera and is projected at (X_{w0}, Y_{w0}, Z_{w0}) in the world coordinates. The Z_c-axis is perpendicular to the image plane.

The image coordinates are expressed with (x, y), which are 2D coordinates. In the image coordinates, the origin (0, 0) is in the upper left pixel of the image. The relationship between these coordinates is shown in Figure 2-17.

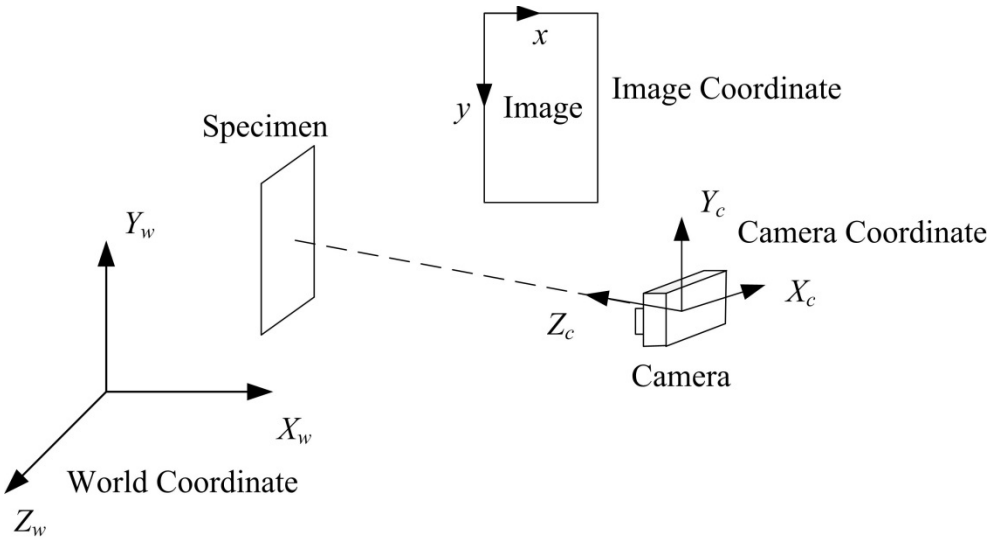

Figure 2-17 Coordinate systems

2.4.1.2 Intrinsic parameters

Focal length, f (α,β): the focal length of the lens is expressed in a 2×1 vector. The ratio $k=\beta/\alpha$ is called the aspect ratio, which is not equal to 1 if the pixels in the CCD array are not square.

Principal point (μ_0, v_0): the principal point is the image center.

Skew coefficient (s): the skew coefficient is the angle between the x and y pixel axes.

Distortions (kc): the image distortion coefficients include 3 numbers that describe radial distortion (expressed as $kc(1)$, $kc(2)$ and $kc(3)$) and 2 numbers that describe tangential distortion (expressed as $kc(4)$, $kc(5)$).

To estimate the intrinsic parameters, camera matrix C is needed. Camera matrix C is a 3×3 matrix describing the projection of the camera from a 3D point in the world to a 2D point in an image.

$$C = \begin{bmatrix} \alpha & s & \mu_0 \\ 0 & \beta & v_0 \\ 0 & 0 & 1 \end{bmatrix} \tag{2-46}$$

The 3D point in the camera coordinates (X_{ci}, Y_{ci}, Z_{ci}) is projected by the camera to 2D point in the image by means of the following changes:

The projection of the point (X_{ci}, Y_{ci}, Z_{ci}) to the image plane uses the pinhole model to find (x_n, y_n):

$$\begin{bmatrix} x_n \\ y_n \end{bmatrix} = f \begin{bmatrix} X_{ic} / Z_{ic} \\ Y_{ic} / Z_{ic} \end{bmatrix} \tag{2-47}$$

The pinhole model simply describes the mathematical relationship between a 3D point and its projection in the image coordinates.

Considering the displacement caused by lens distortion of the image point, the corrected point after lens distortion becomes (x_d, y_d):

$$\begin{bmatrix} x_d \\ y_d \end{bmatrix} = (1 + kc(1)r^2 + kc(2)r^4 + kc(5)r^6)\begin{bmatrix} x_n \\ y_n \end{bmatrix} + \begin{bmatrix} 2kc(3)x_n y_n + kc(4)(r^2 + 2x_n^2) \\ kc(3)(r^2 + 2y_n^2) + 2kc(4)x_n y_n \end{bmatrix} \quad (2\text{-}48)$$

The image coordinates (distorted) are used to find the image point (x_i, y_i):

$$\begin{bmatrix} x_i \\ y_i \\ 1 \end{bmatrix} = C\begin{bmatrix} x_d \\ y_d \\ 1 \end{bmatrix} \quad (2\text{-}49)$$

2.4.1.3 Extrinsic parameters

Extrinsic parameters can transform the world coordinates to a camera coordinate. In addition, in the multi-camera system, the extrinsic parameters also describe the relationship between the cameras.

Rotations (R): rotations reflect the orientation of the camera in the real world. R is a 3×3 matrix, which relates the world coordinates to the camera coordinate system. The rotation can be represented by ω, φ and κ, which is defined as three elementary rotations around X_c, Y_c, and Z_c-axes, respectively.

Translations (T): translations represent the position of the camera in the real world. T is a 3×1 coordinate vector.

The point in the world coordinates (X_w, Y_w, Z_w) and camera coordinates (X_{ci}, Y_{ci}, Z_{ci}) can be related by following rigid body motion equation:

$$\begin{bmatrix} X_{ic} \\ Y_{Ic} \\ Z_{ic} \end{bmatrix} = R\begin{bmatrix} X_w \\ Y_w \\ Z_w \end{bmatrix} + T = \begin{bmatrix} r_{11} & r_{12} & r_{13} \\ r_{21} & r_{22} & r_{23} \\ r_{31} & r_{32} & r_{33} \end{bmatrix}\begin{bmatrix} X_w \\ Y_w \\ Z_w \end{bmatrix} + \begin{bmatrix} X_{wo} \\ Y_{wo} \\ Z_{wo} \end{bmatrix} \quad (2\text{-}50)$$

Where,

$$
\begin{aligned}
r_{11} &= \cos\varphi\cos\kappa, \\
r_{12} &= \sin\omega\sin\varphi\cos\kappa - \cos\omega\sin\kappa, \\
r_{13} &= \cos\omega\sin\varphi\cos\kappa + \sin\omega\sin\kappa, \\
r_{21} &= \cos\varphi\sin\kappa, \\
r_{22} &= \sin\omega\sin\varphi\sin\kappa + \cos\omega\cos\kappa, \\
r_{23} &= \cos\omega\sin\varphi\sin\kappa - \sin\omega\cos\kappa, \\
r_{31} &= -\sin\varphi, \\
r_{32} &= \sin\omega s\cos\varphi, \\
r_{33} &= \cos\omega\cos\varphi.
\end{aligned}
$$

2.4.2 Camera calibration technique

A large amount of research (Heikkilä & Silvén, 1997; Tsai, 1987; Zhang, 1999) has been done in camera calibration. Tsai (1987) proposed a two-stage calibration technique: the first step is to obtain the position and orientation; the second step is to estimate the intrinsic parameters of the camera. Tsai's method does not require an initial guess of parameters. Based on Tsai's method, Heikkilä and Silvén (1997) developed a four-step camera calibration procedure. By adding two steps to compensate for distortion and correcting the distorted image coordinates, the accuracy was improved. The Matlab toolbox for this four-step camera calibration is available online (Heikkilä, 2000). Zhang (1999) proposed a flexible and robust way to calibrate the camera. By photographing a chessboard plane at various angles, the intrinsic and extrinsic parameters can be calculated. A software toolbox to determine these parameters was developed by Zhang (1999)

The camera calibration method used in this thesis is the camera calibration toolbox developed by Jean Yves Bouguet (2010). This method is primarily based on Zhang's method. Bouguet added two tangential distortion coefficients to improve the accuracy of the result.

Zhang uses a closed-form solution to estimate the intrinsic parameters. A chessboard is used as the calibration plane. The calibration grid coordinates must be defined first. It is based on the calibration chessboard and is expressed as (X, Y, Z), as shown in Figure 2-18. Its origin is in a corner of the chessboard. The Z-axis is perpendicular to the calibration plane.

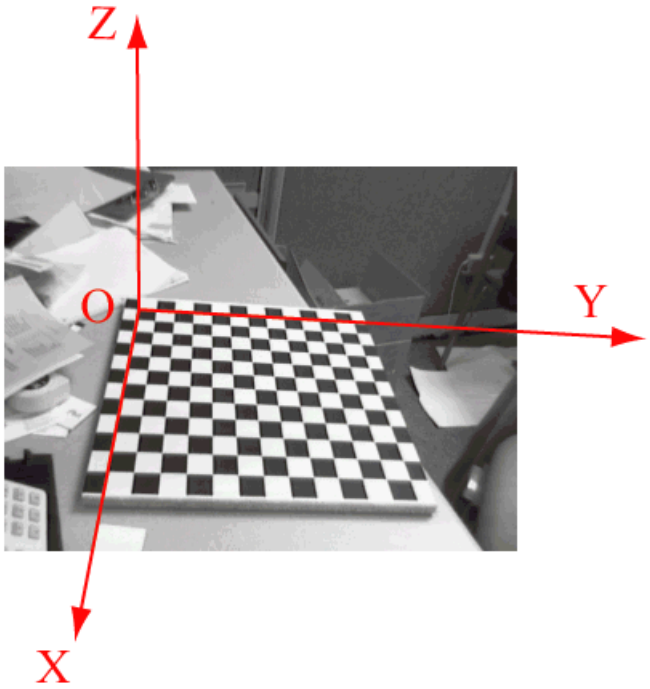

Figure 2-18 Calibration grid coordinates (Bouguet, 2010)

Assume the calibration plane is at Z=0 of the world coordinates. The point in the calibration plane is denoted by M=[X, Y, 0, 1]^T and the corresponding point in the 2D image is denoted by m= [u,v,1]^T. 1 is added as the last element of M and m, because it is required for the later mathematical operations. The intrinsic parameter is denoted by C and the i^{th} column of the rotation matrix R by r_i. Thus, the extrinsic parameters are denoted by (R, t) = (r_1, r_2, r_3, t).

$$m \propto C[r_1, r_2, r_3, t]\begin{bmatrix} X \\ Y \\ 0 \\ 1 \end{bmatrix} = C[r_1, r_2, t]\begin{bmatrix} X \\ Y \\ 1 \end{bmatrix} \propto HM \tag{2-51}$$

H is a scale factor. It relates a model point M to its image point m. It can be obtained using the maximum likelihood criterion, and is designated as $H = [h_1 \ h_2 \ h_3]$. Thus:

$$\lfloor h_1 \ \ h_2 \ \ h_3 \rfloor \propto C \lfloor r_1 \ \ r_2 \ \ t \rfloor \tag{2-52}$$

The elements in the rotation matrix (r_1, and r_2) are orthonormal, giving:

$$h_1^T C^{-T} C^{-1} h_2 = 0 \tag{2-53}$$

$$h_1^T C^{-T} C^{-1} h_1 = h_2^T C^{-T} C^{-1} h_2 \tag{2-54}$$

The above equations are two basic constraints on the intrinsic parameters.

Let

$$B = C^{-T} C^{-1} = \begin{bmatrix} B_{11} & B_{12} & B_{13} \\ B_{12} & B_{22} & B_{23} \\ B_{13} & B_{23} & B_{33} \end{bmatrix} \tag{2-55}$$

B is a symmetric matrix, defined by a 6D vector

$$b = \begin{bmatrix} B_{11} \\ B_{12} \\ B_{22} \\ B_{13} \\ B_{23} \\ B_{33} \end{bmatrix} \tag{2-56}$$

Let the i^{th} column vector of H be $h_i = [h_{i1} \quad h_{i2} \quad h_{i3}]^T$. Then

$$h_i^T B h_j = v_{ij} b = \begin{bmatrix} h_{i1}h_{j1} \\ h_{i1}h_{j2} + h_{i2}h_{j1} \\ h_{i2}h_{j2} \\ h_{i3}h_{j1} + h_{i1}h_{j3} \\ h_{i3}h_{j2} + h_{i2}h_{j3} \\ h_{i3}h_{j3} \end{bmatrix} \begin{bmatrix} B_{11} \\ B_{12} \\ B_{22} \\ B_{13} \\ B_{23} \\ B_{33} \end{bmatrix} \tag{2-57}$$

The two basic constraint Equations (2-53) and (2-54) can be rewritten as two homogeneous Equations (2-58) as follows:

$$\begin{bmatrix} v_{12}^T \\ (v_{11} - v_{22})^T \end{bmatrix} b = 0 \tag{2-58}$$

Each homography provides two constraint equations. In order to solve for *b* with 6 degrees of freedom, at least three images from different perspectives must be used. In practice, more images are taken in camera calibration to increase the accuracy.

2.4.3 Camera calibration procedure

The procedure outlined here was used to conduct the experiments reported in this dissertation.

Step 1: Print a chessboard by a LaserJet printer and attach it to a rigid planar surface.

Step 2: Find the appropriate focus using auto focus with the camera in position, then turn auto-focus off. Keep the lens locked and take a few photographs of the chessboard at various angles by moving the chessboard, as shown in Figure 2–19.

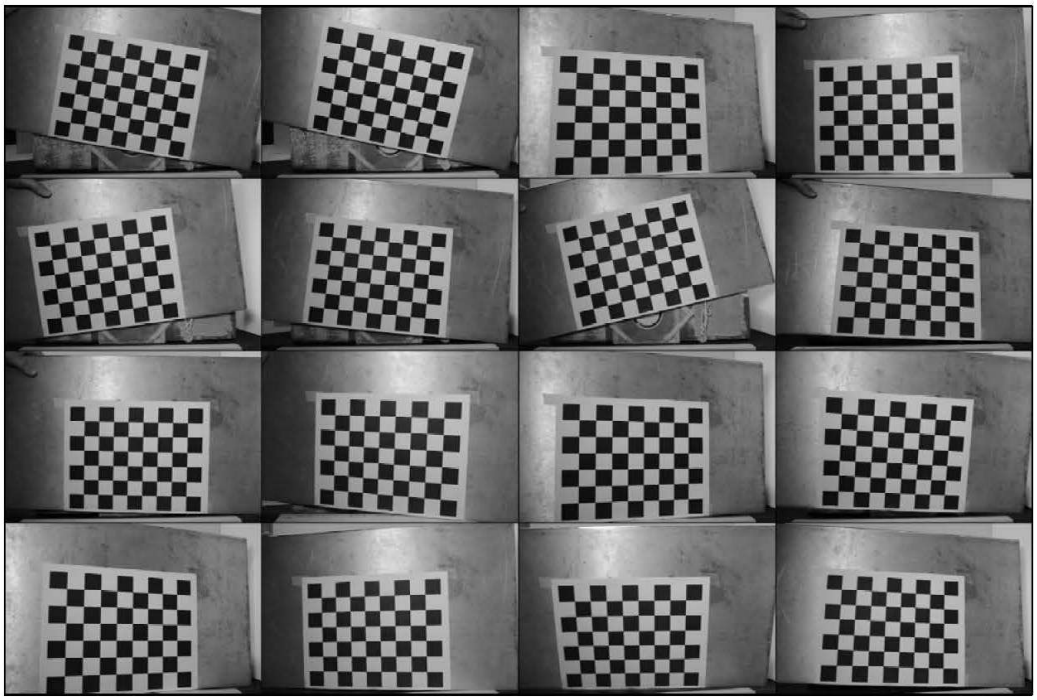

Figure 2-19 Photographs of chessboard at various orientations

Step 3: Use the camera calibration toolbox (Bouguet, 2010) for Matlab to detect the grid corner points in the images and estimate the intrinsic parameters and extrinsic parameters for each image.

Step 4: To decrease the error of the calibration, use the toolbox to recalibrate the intrinsic parameters by using the original intrinsic parameters as an initial guess for the next iteration of the calibration process.

Step 5: Based on the intrinsic parameters of the camera, all the images can be undistorted.

Chapter 3 Optical strain measurement and analysis methods

3.1 Background

Optical strain measurement methods use an optical device to determine the strain. The optical device could be a microscope, laser, or camera. In this thesis, the optical device used is a camera, and the strain is measured by analyzing the digital images it captures.

Digital image correlation (DIC) is a well-known optical strain measurement method. It is also known as particle image velocimetry (PIV) and is a non-contact, optical technology that tracks the movement of chosen targets. A camera is used to capture a series of digital images which are analyzed relative to an initial undeformed state. Images recorded during experimentation or monitoring are processed after the experiment is complete. The images are digitally processed with the help of a computer using gray intensity analysis in the region of interest. The results of the analysis determine displacement and strain.

The digital image technique is applicable to a wide scale range, from as large as a few meters to as small as nanometers. Specimens can be loaded under quasi-static or dynamic conditions. Cameras with high frequencies, capture many images per second, and are readily available. Advances in high-resolution digital cameras and increasing computing performance have improved the accuracy and precision of the DIC technique. As a result, DIC has found extensive applications both in the laboratory and in industry.

In this study, two types of patterns are used for strain measurement: random speckle and a painted rectangle. DIC uses painted speckles as the pattern. By tracking the position of the speckles, the displacement of the specimen can be determined. A new approach developed in this thesis is the use of edge detection of a rectangle painted on the surface. By measuring the position of the rectangles' edges, the displacement can be found. Two computer programs are used for different accuracy levels: ImageJ (National Institutes of Health, 2004) is used for pixel-level, and Matlab for subpixel-level analyses. At the subpixel-level, two algorithms are applied: Gaussian fitting (Shang, Chen, & Tian, 2010) and spline interpolation (Hou & Andrews, 1978; Luu, Wang, Vo, Hoang, & Ma, 2011).

3.2 Digital speckle correlation method

Speckles are widely used as a pattern in the DIC method, which is also called the digital speckle correlation method (DSCM). The speckle may be a naturally occurring pattern on the specimen or it may be painted on. The speckles should be randomly distributed over the surface.

The process of strain measurement by DSCM is as follows: first, an image of the undeformed specimen is taken as a reference image and is divided into several subsets. Each subset should have a unique gray intensity distribution, which functions as a marker for identifying each subset as the deformation occurs. Then, a series of images are taken under loading, as the specimen deforms. These images will be compared with the reference image once the experiment is completed. A correlation criterion is applied to locate the target subsets. This criterion looks for maximum similarity between the deformed and the reference image subset. Displacement, as a vector, is measured from

the center of a reference subset to the center of the deformed subset. A full field displacement map is obtained by determining the displacement each subset experiences, as a vector. A diagram of the DIC method from the test is shown in Figure 3-1.

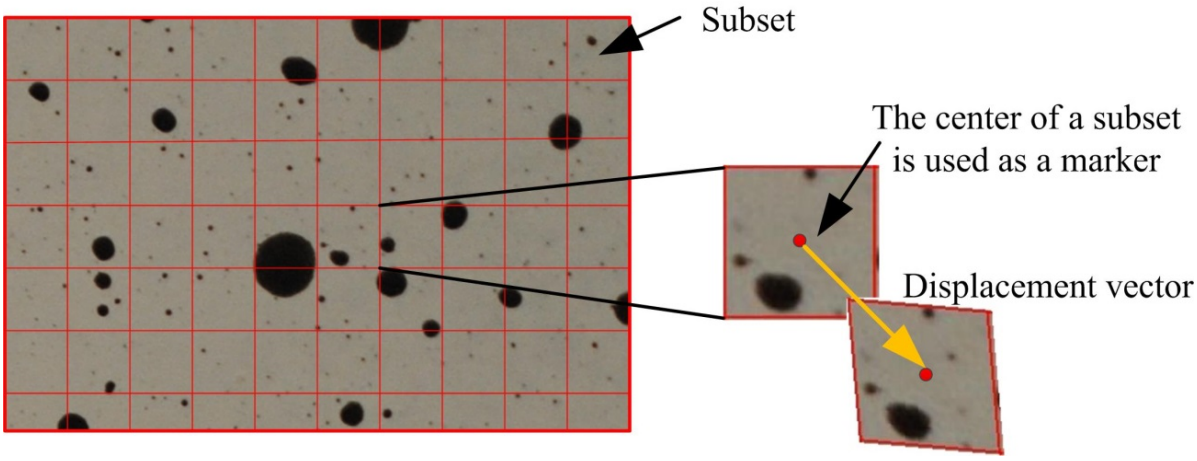

Figure 3-1 The subset and displacement vector for the DIC speckle method

This ability to produce a full field strain measurement map is one of the greatest advantages of DSCM. Prior to the development of this technique, it was very difficult to relate local information to global characteristics such as full field surface strain.

Post-processing of images was completed using Digital Image Correlation and Tracking (Eberl, Thompson, Gianola, & Bundschuh, 2010), which is a Matlab based code. The process of this algorithm is shown in Figure 3-2.

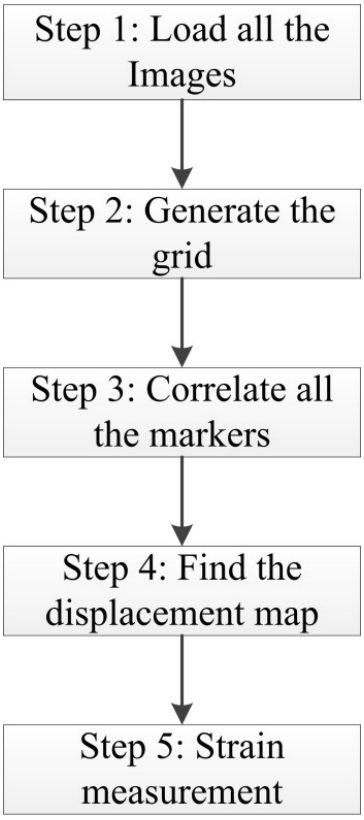

Figure 3-2 Flowchart of digital image correlation and tracking

Step 1: Load all the images. The reference image is the first image, which is used as a baseline for all displacement measurements.

Step 2: Generate the grid. This step asks the user to select a region of interest (ROI) within the reference image, which is then divided into several subsets. The center of each subset serves as a marker for the image correlation. The user selects the desired number of subsets. More subsets provide more markers for the correlation, which may provide more detailed information about the specimen surface and decrease the noise in the measurements. However, a very large number of subsets require much longer processing times and have higher requirements of the computer configuration.

Step 3: Correlate all the markers. This is the core step for DIC. A built-in Matlab function called “cpcorr.m” is used to track the location of markers using cross-correlation

criterion, as shown in Equation (3-1). The resolution of the marker position is as high as 1/1000 pixel, which is subpixel-level. "cpcorr.m " can only track the position of markers by up to four pixels, making it suitable for small displacements. For larger displacements, a reduction factor coefficient is necessary in order to use this function. The image size is first reduced to fall into the range required by the code and then the measuring result is scaled-up for the original image. The markers' positions in the deformed images are recorded.

$$C_{CC} = \sum f_i g_i \tag{3-1}$$

Where f_i is the gray intensity of pixels in the reference image, g_i is the gray intensity of pixels in the deformed image.

Step 4: Find the displacement map. By comparing the positions of markers in the reference and target images, the displacement map is obtained.

Step 5: Strain measurement. From the displacement map, the full field strain map is determined by a pointwise least squares method (Pan, Asundi, Xie, & Gao, 2009).

3.3 Rectangle edge detection method

The rectangle edge detection method calculates strain by locating the edges of a painted rectangle, then calculating the change in size. Deformation of the specimen causes changes in the dimensions of the rectangle. By detecting these changes, strain can be determined. Length is defined by the distance between two parallel edges of the rectangle, such as between the left and right edges or the top and bottom edges. Therefore, strain measurement becomes an edge detection problem. A schematic diagram of the rectangle is shown in Figure 3-3.

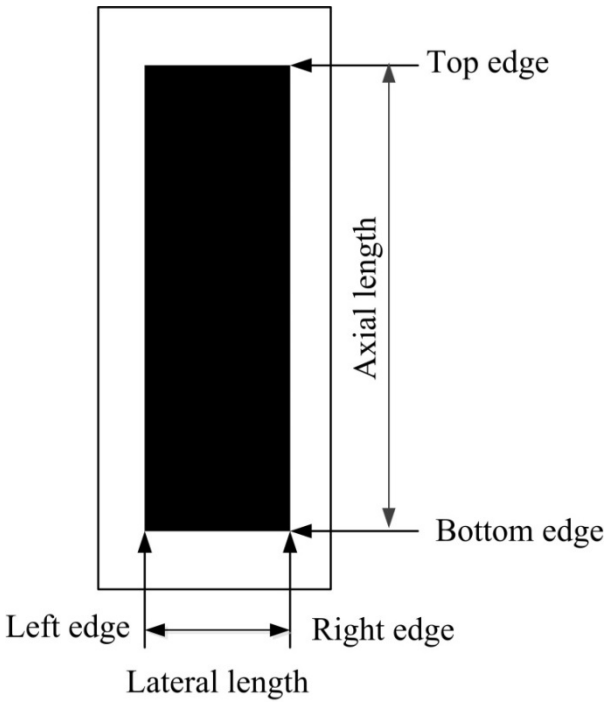

Figure 3-3 Schematic diagram of the rectangle

3.3.1 Pixel-level

The rectangle edge in a digital image must be defined. The edge is determined by a sharp intensity change over a small distance (several pixels) in the image. For the specimens used in this investigation, a black rectangle was painted on a white surface. Therefore, the edge can be readily defined as the boundary between the black pixel and white pixel. However, in the real images, due to lighting conditions and the inherent characteristics of charge-coupled device (CCD) cameras, most pixels are not simply black or white. Rather, they are a shade of gray. Creating a binary image is an option to solve this problem since, in binary, pixels are either black or white. To create binary images, a threshold has to be selected that will mark the boundary between the shades of gray that are binarized to black and white. Then, the strain can be calculated using Equation (3-2).

$$\varepsilon_i = \frac{length\ \ change\ \ in\ \ pixels}{length\ \ in\ \ pixels} = \frac{l_i - l_0}{l_0} \tag{3-2}$$

Where l_i is the length of the rectangle in the image i, and l_0 is the length of the rectangle in the reference image.

High elasticity materials experience large changes in the pixels during deformation, making pixel-level edge detection sufficient. ImageJ is a software used for pixel-level rectangle length measurement in this thesis. The flowchart of the ImageJ macro program is shown in Figure 3-4.

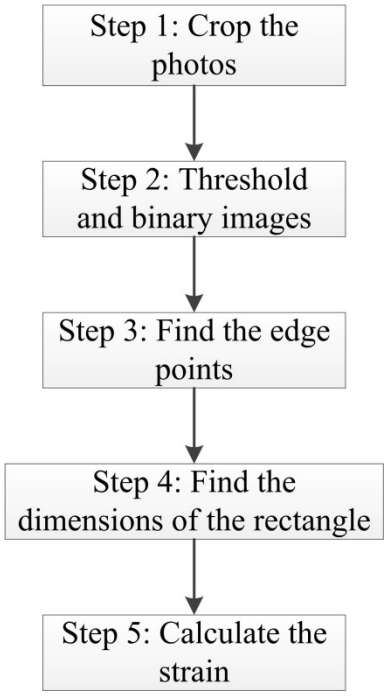

Figure 3-4 Flowchart of ImageJ method

Step 1: Crop all the photos so that only the black rectangle and the white background are visible. By removing the complicated portions of the background, processing becomes simpler.

Step 2: Change the RGB photos to 8-bit grayscale photos, and then threshold the photos to produce binary images. The threshold value for each series of photos is the

same since these photos have the same lighting conditions, in theory. The lighting conditions are kept consistent during the tests to ensure the photos show similar brightness. The principle of selecting a threshold value is such that the binary image should have a clear edge without including too much noise outside the rectangle. Since the cropped photos only contain one object (the rectangle) and one background, the threshold is selected at the average of the distribution means of the all discrete pixels (Wang & Bai, 2003), as shown in Figure 3-5.

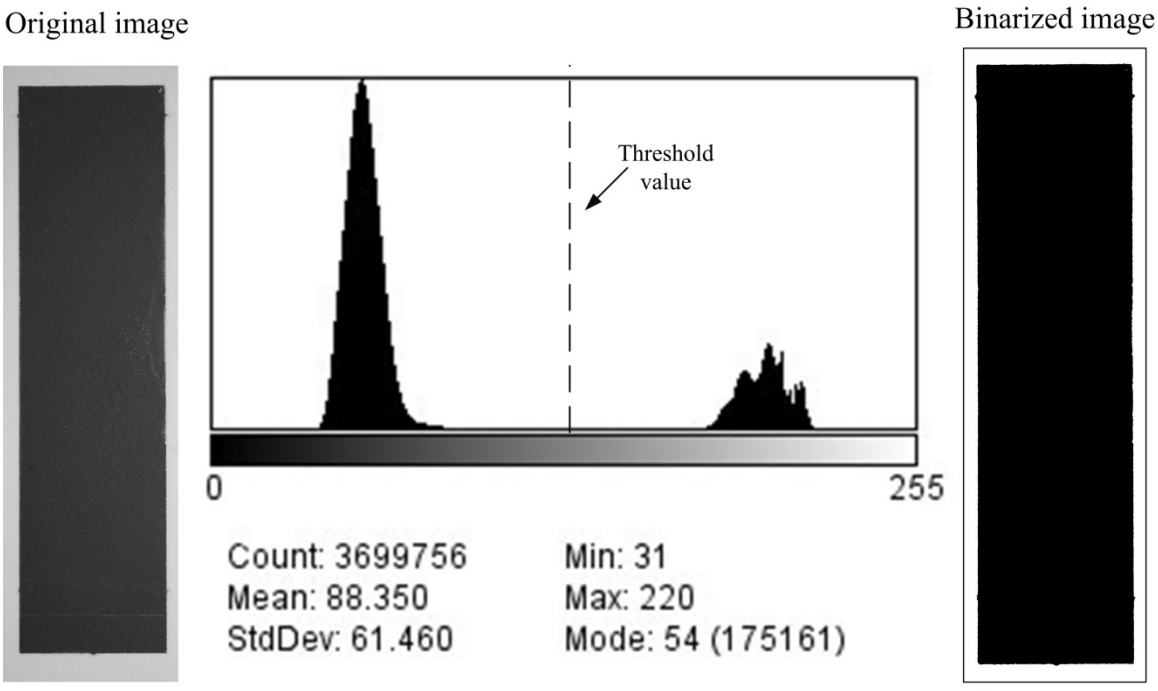

Figure 3-5 Photo threshold by ImageJ

Step 3: Find the edge points. Check the pixel colors, black or white, of each image line by line. If adjacent pixels change, record this location as an edge.

Step 4: The dimensions of the rectangle are obtained for each line and column by detecting the four edges. The height of the rectangle is measured from the top to the

bottom edges, and the width from the left to the right edges. These dimensions are taken as the average value of the length of each line or column.

Step 5: Strain is then calculated using the length change in pixels.

3.3.2 Subpixel-level

Materials with different stiffness experience different deformations under the same load. For more ductile materials, the length change in the image may be several pixels. For brittle materials, the length change may be less than a pixel. Subpixel strain measurement is necessary in order to measure such small deformations.

Subpixel analysis overcomes some of the limitations of pixel-level analysis and provides more detailed information. Subpixels can only be approximated with probability, as their determination requires guessing. These guesses should be based on existing pixel values. Subpixel edge detection algorithms can be classified into three categories: fitting methods, interpolation methods and moment-based methods. The first two methods are studied in this chapter. The moment-based method is not discussed in this thesis, since it is a statistical method.

The edge in an image is defined as the location where sharp gray intensity changes occur. However, due to quality and noise of the image, the largest change in gray intensity at the edge is difficult to detect. Rather than using the gray intensity of pixels, the gradient (change in gray level) is often chosen to detect edges. When using the gradient, the edge is defined as the location where the largest gradient occurs. Since pixel values are discrete, gradients are calculated by subtracting gray intensities of adjacent pixels. The gradient is a vector, having both value and orientation. For the left and right edges, gradient (G_x) is obtained by subtracting the previous column. The lateral

rectangle length is the right edge position minus the left edge position. For the top and bottom edges, the gradient (G_y) is obtained by subtracing the previous row, with the axial rectangle length being the bottom edge position minus the top edge position.

3.3.2.1 Gaussian fitting

Fitting methods attempt to build continuous functions to simulate the edge gradient by fitting curves to real edge points. Using a Gaussian function to fit the edge gradient curve of an image is called Gaussian fitting.

For the rectangle, strain is measured in two directions: axially and laterally. For each direction, neglecting rotation and shear, strain can be simply calculated by $\triangle L/L_0$. Therefore, a 1D Gaussian fitting function (3-3) is used to represent gradients of pixels around the edge in the gradient direction.

$$y = ae^{-\frac{(x-\mu)^2}{2\sigma^2}} \tag{3-3}$$

Where x is the pixel's location, y is the pixel's gradient intensity, μ is the mean of Gaussian function, σ is the standard derivation of Gaussian function, a is the height of the Gaussian curve's peak.

The mean, μ, of a Gaussian function is the location where the function reaches its highest value. It is also considered to be the location of the subpixel edge. The standard derivation, σ, is the width of the Gaussian function.

A Gaussian fitting Matlab program was created to calculate subpixel-level length measurements. The code can be found in Appendix A and the process is described as in Figure 3–6. In this process, the following abbreviations are utilized:

Subscript *l*: left

Subscript r: right

Subscript t: top

Subscript b: bottom

Subscript m: measured

i: image number (0,1, 2, 3…), 0 for the reference image (first image)

l: the length of the rectangle

μ: the mean of the Gaussian function

σ: the standard deviation of the Gaussian function

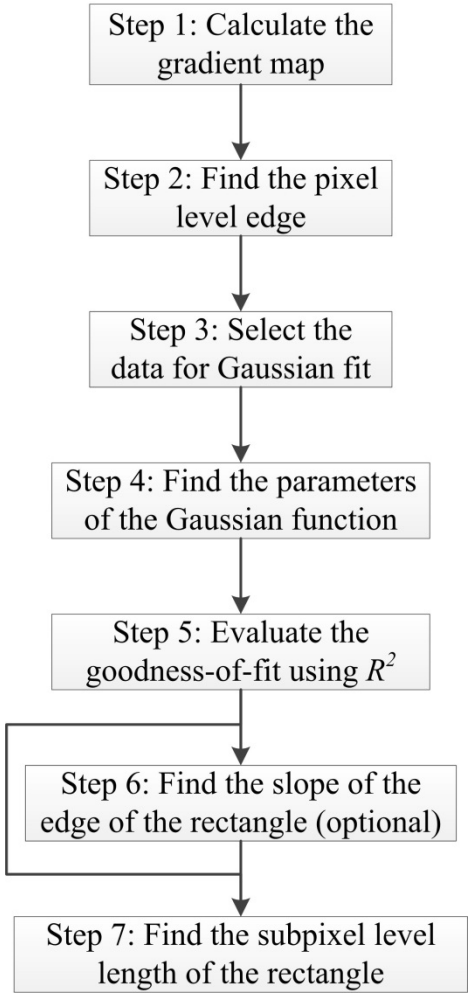

Figure 3-6 Flowchart of Gaussian fit method

Step 1: Calculate the gradient map of each image based on the gray intensity. For axial length, the gradient value is found by subtracting the pixel value of the previous row from the current row. For lateral length, the gradient value is found by subtracting the pixel value of the previous column from the current column.

Step 2: Find the pixel-level edge. The location of the largest gradient is the pixel-level edge.

Step 3: Select the data for the Gaussian fit. Select eight adjacent pixels around the pixel-level edge, with four pixels on each side. These eight pixels plus the pixel with largest gradient gives a total of nine pixels used for the Gaussian fit.

Step 4: Find the parameters of the Gaussian function. Use location (x) and gradient intensity (y) of these nine pixels to fit the Gaussian equation (3-3). The least-squares method is used to find the Gaussian parameters (μ and σ), where μ is the location of the subpixel edge and the convergence condition is 10^{-6} for variations in the Gaussian function.

Step 5: Evaluate the goodness-of-fit using R^2. In order to evaluate the "goodness-of-fit" of the Gaussian function, the coefficient of determination (R^2) is considered.

$$R^2 = 1 - \frac{\sum (y - y_{estimate})^2}{\sum (y - \bar{y})^2} \tag{3-4}$$

Where y is the observed value, $y_{estimate}$ is the predicated values, $\bar{y}$ - is the mean of the observed value.

If R^2 is a small number, the Gaussian curve is not considered suitable for the edge pixel intensity distribution, meaning that the Gaussian model is not reliable. Too high a value of R^2 can filter out too much data reducing the image information. $R^2 \geq 0.9$ is selected as a criterion for finding a good Gaussian fit. To determine the length of the

rectangle, two Gaussian fitting curves, one for each edge, must be fitted. If the coefficients of determination for both sides are greater than or equal to 0.9, then the length is considered reliable. Figure 3-7 shows the Gaussian fitting curves for a row in the black rectangle.

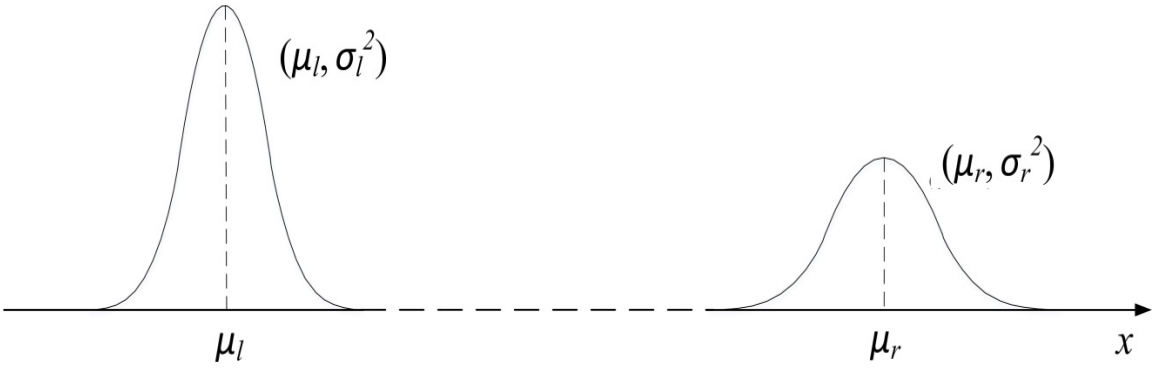

Figure 3-7 Schematic of Gaussian fitting for a row

Step 6: Find the slope of the edges of the rectangle (optional). Rotation occurs if there is some angle between the specimen and the camera. Figure 3–8 shows a schematic diagram of the image taken of a rotated specimen. The measured lateral length is l_m and real lateral length is l. l is calibrated by Equation (3-5). The rotation angle α is the angle between the camera and the specimen. This angle is calculated using the slope of the rectangle edge. Strain after calibrating for this rotation is given in Equation (3-6).

$$l = l_m \cos\alpha \tag{3-5}$$

$$\varepsilon_i = \frac{l_{mi}\cos\alpha_i - l_{m0}\cos\alpha_0}{l_{m0}\cos\alpha_0} \tag{3-6}$$

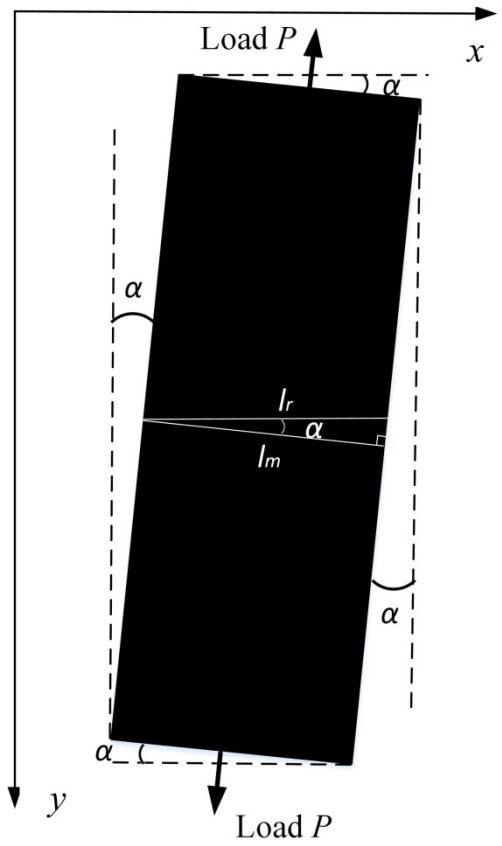

Figure 3-8 Schematic diagram of the rotated specimen image

Under some conditions, rotation occurs during the test. Suppose the first image is straight and the specimen rotates an angle α_i with respect to the camera in the image i. The theoretical length of the rectangle in image i changes from l_i to l_{mi}. These two measurements are related as shown in Equation (3-7).

$$l_{mi} = l_i \cos\alpha_i \tag{3-7}$$

Using Equation (3-7) in the strain calculation Equation (3-2), gives the measured strain in image i, ε_{mi}, which becomes:

$$\varepsilon_{mi} = \frac{l_{mi} - l_0}{l_0} = \frac{l_i \cos\alpha_i - l_0}{l_0} \tag{3-8}$$

Since the length change is very small, $l_i \approx l_0$, the difference between the real strain and measured value can be calculated by Equation (3-9).

$$\Delta\varepsilon_i = \varepsilon_i - \varepsilon_{mi} = \frac{l_i(1-\cos\alpha_i)}{l_0} \approx 1-\cos\alpha_i \tag{3-9}$$

This step is optional. If the error in the strain measurement caused by rotation during the test is small (< 1°) and can be neglected, then this step is not necessary. Several errors caused by rotation are calculated in Table 3-1.

Table 3-1 Error in strain caused by rotation

Angle α_i (degree)	0.5	1	2	3
Error $\Delta\varepsilon_i$	3.8×10^{-5}	1.5×10^{-4}	6.1×10^{-4}	3.8×10^{-3}

Step 7: Find the subpixel-level length of the rectangle. Axial length is calculated by subtracting the top location, μ_t, from the bottom location, μ_b. Lateral length is calculated by subtracting the left location, μ_l, from the right location, μ_r.

3.3.2.2 Spline Interpolation

Interpolation, another subpixel image analysis method, constructs new data points within the range of known data. This makes it easy to apply since it does not need to consider the goodness of fit. A spline interpolation is a special type of piecewise polynomial. It uses low-degree (n < 4) polynomials to connect each known data point, and chooses the sectional polynomial that can smoothly fit all these points together. Interpolation methods construct a set of new data points within the range of known data points. For an image, it is like inserting many pixels between existing pixels to increase resolution. The values of these pixels are computed using interpolation of the pixels in the neighborhood of the edge pixels of the original image. Many interpolation methods have been developed (Pang, Tan, & Chen, 2013; Xu, Wang, & Gu, 2013), such as linear,

bilinear and bicubic interpolation. A spline interpolation function is considered to be highly accurate for subpixel edge detection (Hou & Andrews, 1978; Luu, Wang, Vo, Hoang, & Ma, 2011) and is studied in this thesis. The cubic spline interpolation function is given in Equation (3-10).

$$y = \sum_{m=0}^{3} \alpha_m x^m \tag{3-10}$$

Where x is the pixel's location, y is the pixel's gradient intensity, α is the coefficient of the cubic spline function.

A spline interpolation Matlab program was created to calculate subpixel-level length measurement. The code is presented in Appendix B and the process is described in Figure 3-9.

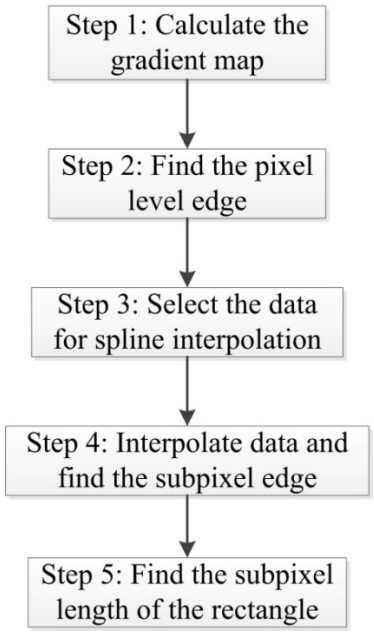

Figure 3-9 Flowchart of spline interpolation method

Step 1: Calculate the gradient map of an image using gray intensity. For axial length, the gradient value is found by each row's gray intensity minus the previous row's.

For the lateral length, the gradient value is found by each column's gray intensity minus the previous column's.

Step 2: Find the pixel-level edge. Find the location where the largest gradient occurs, which is the pixel-level edge.

Step 3: Select the data for the spline interpolation: eight adjacent pixels around the pixel-level edge, with four adjacent pixels on each side. The eight pixels plus the pixel with largest gradient (a total of nine pixels) are selected as known points to find a cubic spline function.

Step 4: Interpolate from the known points to find the subpixel edge. Interpolate using the known pixels to create new points with a 0.01 pixel step size. 0.01 is also the precision chosen for this specimen. For different accuracy requirements, a different step size may be chosen. Find the new location where the maximum gradient occurs, which is the subpixel-level edge, E.

Step 5: Find the subpixel length of the rectangle. Axial length is calculated as the location of the bottom edge minus the location of the top edge, E_b-E_t. Lateral length is the location of right edge minus the location of the left edge, E_r-E_l.

3.4 Experiments

3.4.1 Specimen details

An A36 steel bar was used to evaluate a variety of strain measurement methods, including the algorithms discussed previously. The dimensions and mechanical properties of the specimen are shown in Table 3-2. The dimensions of both the specimen and the painted rectangle were measured using an digital calipers. The dimensions of the rectangle are not used in the analysis.

Table 3-2 Specimen properties

Dimensions of the specimen			Dimensions of the painted rectangle		Mechanical properties	
Thickness (mm)	Width (mm)	Length (mm)	Width (mm)	Height (mm)	Nominal yield strength (MPa)	Nominal ultimate tensile strength (MPa)
3.05	25.25	609.6	15.5	58.4	250	400

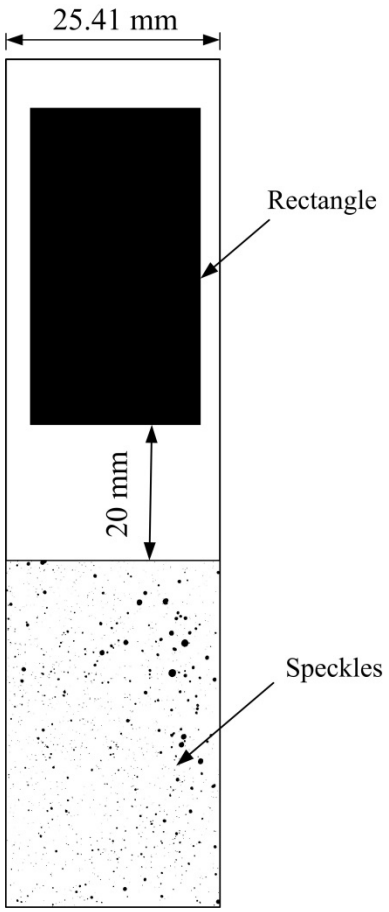

Figure 3-10 Schematic diagram of paintings on the specimen

The two ends of the specimen were bonded with four 26×38 mm aluminum tabs to protect the specimens from damage by the mechanical grips. Strain gages and reflective tapes for laser extensometry were bonded to one side of the specimen. On the

other side of the specimen, two patterns (speckles and a rectangle) were painted. The patterns were located in the middle of the specimen and were separated by 20 mm, as shown in Figure 3-10.

Prior to painting, the specimen surface was cleaned with acetone to remove surface debris. For the speckle pattern, the specimen was first painted white as a background. Once the white paint was dry, black speckles were sprayed onto the white surface using a spray paint. The sizes of the speckles should have a wide distribution. During painting, the rest of the specimen was covered by tape to protect it from stray paint marks. For the rectangle pattern, a rectangle template was drawn on the surface of the specimen and tape was used to protect the area outside of the rectangle. Black paint was then sprayed evenly onto the rectangle. When the paint was completely dried, the tape was removed, leaving a black rectangle on a white background. The paintings on the specimen are shown in Figure 3-11.

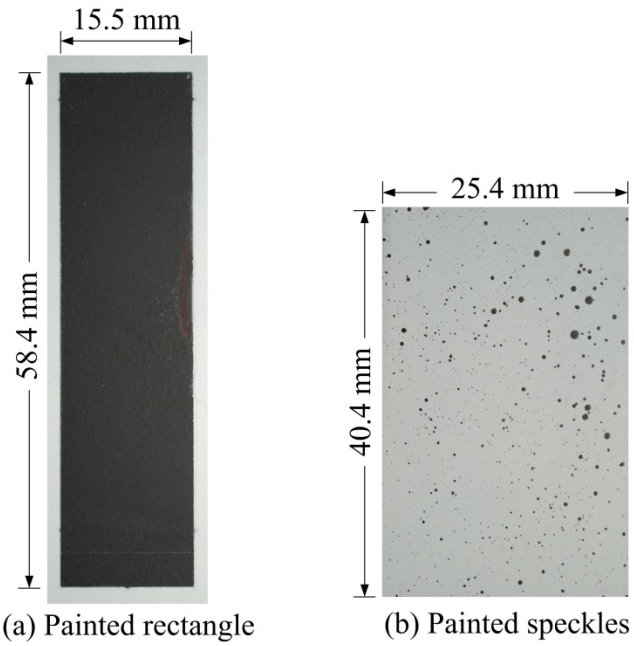

Figure 3-11 Rectangle and speckles painted on the specimen

3.4.2 Test setup

The steel specimen was tested in uni-axial tension using a 53 kN test frame with a 9.8 kN capacity load cell to record the load data. Laser extensometry and a strain gage system were used during testing as reference strain measurement methods. The laser extensometer (MTS Inc., Model: LX500) was mounted on a rigid frame, 305 mm from the specimen. Two reflective tapes approximately 90 mm apart along the axial direction were used as the gage length for the laser extensometer. Two strain gages (Omega SGD-4/120-LY13) were also bonded to the specimen, orthogonal to each other. One was along the axial direction and the other was along the lateral direction. These strain gages were connected to a quarter-bridge circuit. Each strain gage was calibrated before each test to determine the calibration factors used in the equation, describing the relationship between strain and electric current. The schematic diagram of instrument setup on specimen is shown in Figure 3-12.

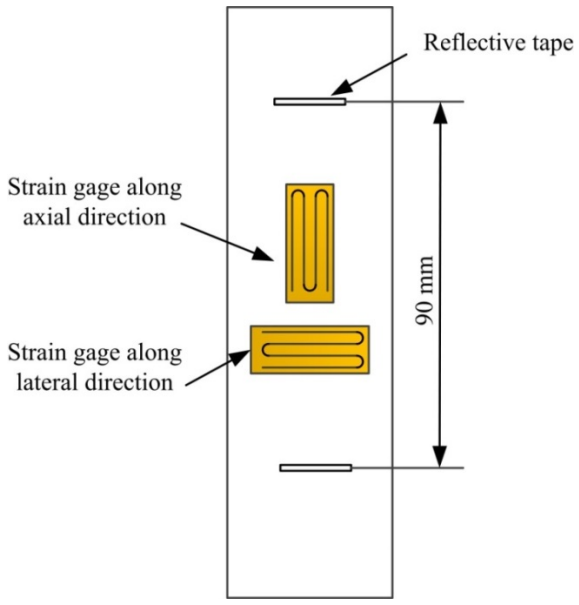

Figure 3-12 Specimen instrumentations set up

Throughout testing, a lighting source was supplied by a 35 Watt bulb producing 1050 Lumens to ensure even and consistent lighting conditions for image capture. A Nikon D3000 10-megapixel digital camera with a 40-mm micro lens was used to record the digital images. The camera lens was aimed directly at the patterns on the specimen, and the resolution of the images was 3872×2592 pixels. The camera shutter speed and aperture were set manually. Based on the lighting condition, the fastest shutter speed was chosen. A remote control was used for this camera to avoid movement of the camera during operation. An iPhone 4S with 1080p HD video was also used during the test to capture images. These images have a resolution of 1920×1080.

The laser extensometer and strain gage system data were collected by a data acquisition system. The test was programmed to run under load control. Initially, a 44 N preload was applied to align the grips. Then, load increased incrementally by 2.2 kN until the load reached about 17.8 kN. Following this loading, the specimen was unloaded until stress reached zero using the same increment of 2.2 kN. Following each incremental load increase or decrease, the load was held stable for three minutes to record the images. The diagram of load increment versus time is shown in Figure 3–13.

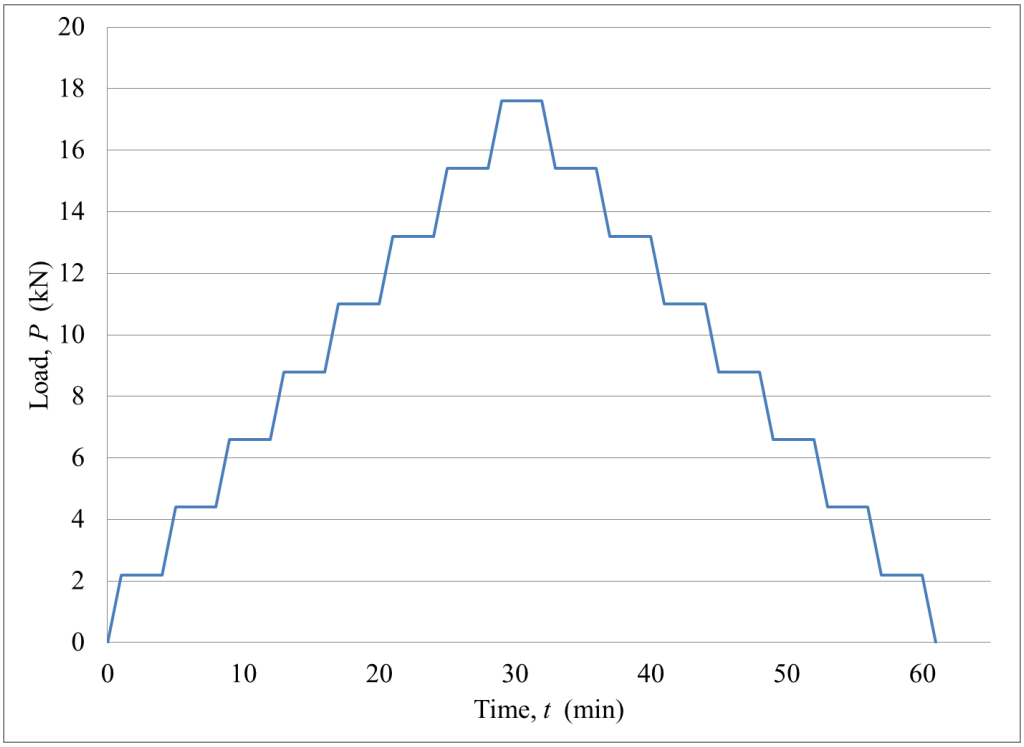

Figure 3-13 Load increment versus time

The specimen was tested three times using different digital imaging techniques as shown in Table 3-3. Test 1 used the Nikon camera to capture the rectangle pattern, Test 2 used the iPhone camera to capture the rectangle pattern, and Test 3 used the Nikon camera to record the speckle pattern. The laser extensometer and the electronic strain gages were used in all three tests. The test setup is shown in Figure 3-14.

Table 3-3 Test matrix

Test	Camera	Pattern	Laser	Strain gage	
			Extensometry	Axial	Lateral
Test 1	Nikon D3000	Rectangle	√	√	√
Test 2	iPhone 4S	Rectangle	√	√	√
Test 3	Nikon D3000	Speckle	√	√	√

The maximum stress during the test, 218 MPa, is below the yield stress of 248 MPa. Therefore, the strain is within the proportional range. This means that the deformation of the specimen is elastic and recoverable.

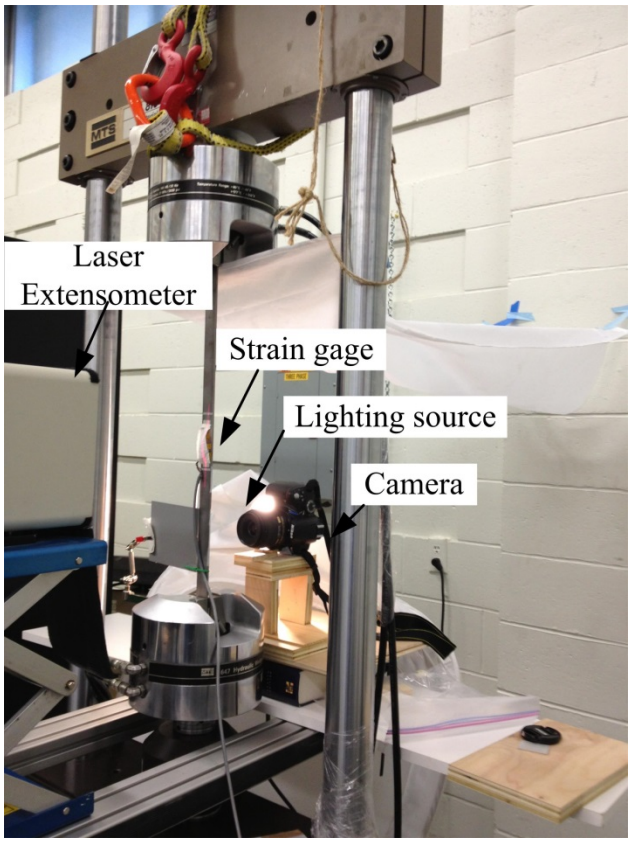

Figure 3-14 Test setup

3.4.3 Calibration of test equipment

3.4.3.1 Strain calibration equations

Prior to using the strain gages for measurement, the strain calibration equation for each gage was found. The calibration equations describe the relationship between electrical signals measured in *Volts* and strain (ε). The strain gage calibration equation used in this study is based on four known resistors.

For axial strain, the calibrated strain ranges from 6×10^{-4} to 3.318×10^{-3}. The calibration equation is shown in (3-11) with R^2= 99.99%.

$$\varepsilon = (-1.05\times10^{-3})*Volts \quad +1.63\times10^{-6} \tag{3-11}$$

For the lateral strain, the calibrated strain ranges from 4×10^{-4} to 2.73×10^{-3}. The calibration equation is shown in (3-12) with R^2= 99.99%.

$$\varepsilon = (1.16\times10^{-3})*Volts \quad -4.31\times10^{-6} \tag{3-12}$$

3.4.3.2 Camera calibration

Camera calibration is an essential step in image analysis. In this thesis, the camera was calibrated by Zhang's method (1999). The purpose of camera calibration is primarily to decrease the distortion caused by the lens. The calibration results are shown in Table 3–4.

Table 3-4 Calibration result of instinct parameters

Test	Focal length $f(\alpha, \beta)$ (unitless)	Principal point (μ_0, v_0) (unitless)	Skew (s) (unitless)	Distortion (kc) (unitless)
Test 1	[14574.26, 14301.40]	[4154.35, 804.14]	0.00	[0.22, -0.12, -0.029, 0.028, 0.00]
Test 2	[2243.54, 2183.98]	[1396.20, 563.49]	0.00	[0.055, -0.087, 0.005,0.014,0.00]
Test 3	[9361.78, 9336.87]	[1760.94, 662.57]	0.00	[0.004, 1.70,-0.01, -0.01, 0.00]

3.4.3.3 Camera setting

Test 1 and Test 3 used a Nikon D3000 camera to record images. The camera settings are shown in the Table 3-5. Test 2 used an iPhone 4S camera to record images,

with no manual setting parameters available. In order to ensure consistency between images, AF (Autofocus) and AE (automatic exposure) were locked on the iPhone 4S camera.

Table 3-5 Camera settings

Test	White balance	Shutter time (sec)	Aperture (unitless)
Test 1	Incandescent	1/40	*f*/3.2
Test 3	Incandescent	1/50	*f*/3.5

3.5 Data analysis

The images taken during Test 1 were processed using three different data analysis methods: pixel-level analysis using ImageJ, and subpixel-level analysis using both Gaussian fitting and spline interpolation. The Test 2 images were analyzed using the subpixel Gaussian fitting method. The images taken during Test 3 were analyzed using the subpixel speckle correlation method. The details of these analyses are described in the following sections.

3.5.1 Nikon camera with rectangle data analysis: Test 1

3.5.1.1 Pixel-level method using ImageJ

The results of the pixel-level image analysis for axial and lateral length strain are shown in Table 3-6 and Figure 3-15. ImageJ uses pixels as the unit to calculate the strain change by detecting the edges of the rectangle, which was painted on the surface of the specimen. The reported axial lengths are the average values of more than 500 columns of the rectangle and the lateral lengths are the average values of more than 3000 rows. The values keep one decimal place.

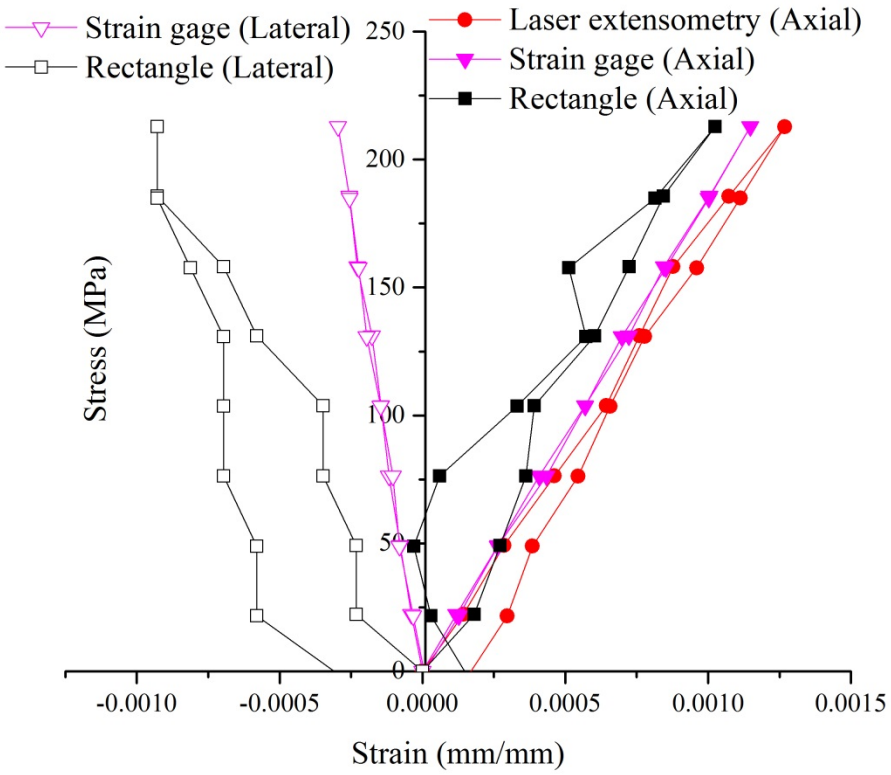

Figure 3-15 Comparison of strain measurements using pixel-level edge detection (rectangle) method

From Table 3-6, it can be seen that since the strain is very small (on the order of 10^{-4}), it is difficult for the ImageJ software to detect these small changes in length. This is particularly noticeable in lateral strain measurements. Lateral strain is much smaller than axial strain, so it requires a higher accuracy method. For sequential (consecutive) images, the ImageJ pixel-level method could not detect very small changes in length. No change in length is observed between images 2 and 3, and between images 4 and 5 for example. For this material, pixel-level strain measurement is not accurate enough.

Table 3-6 ImageJ (pixel-level) axial and lateral length of the rectangle using edge detection

Image number	Axial length (pixels)	Axial strain $\varepsilon\times10^{-4}$	Lateral length (pixels)	Lateral strain $\varepsilon'\times10^{-4}$
1	3317.9	0.00	861.9	0.00
2	3318.5	1.81	861.7	-2.32
3	3318.8	2.71	861.7	-2.32
4	3319.1	3.62	861.6	-3.48
5	3319.2	3.92	861.6	-3.48
6	3319.9	6.03	861.4	-5.80
7	3320.3	7.23	861.3	-6.96
8	3320.7	8.44	861.1	-9.28
9	3321.3	10.25	861.1	-9.28
10	3320.6	8.14	861.1	-9.28
11	3319.6	5.12	861.2	-8.12
12	3319.8	5.73	861.3	-6.96
13	3319.0	3.32	861.3	-6.96
14	3318.1	0.60	861.3	-6.96
15	3317.8	-0.30	861.4	-5.80
16	3318.0	0.30	861.4	-5.80
17	3318.5	1.81	861.7	-2.32

3.5.1.2 Subpixel measurement: One line data analysis

When high accuracy is required, pixel-level image analysis is not sufficient. For this reason, subpixel-level image methods were developed. There are two primary methods, which are presented here: Gaussian fitting and spline interpolation. First, the procedure and results for one row of pixels are presented. Later, the macro results are also studied.

1) Gaussian fitting

One line of data from an image is used as an example to describe this data analysis process. First, the position of the largest gradient must be located. Then, four pixels to the left (Pixels 1-4), four pixels to the right (Pixels 6-9) and the pixel with highest gradient (Pixel 5) are selected to represent the edge. Thus, nine pixels are used for Gaussian fitting. For each line, there are two edges: left and right or top and bottom. Therefore, two Gaussian fittings must be considered.

The parameters of the Gaussian equation were calculated by the least squares method (Shang, Chen, & Tian, 2010). The mean value is the subpixel-level location of the edge. The distributions of gradient values for the left and right sides are shown in Table 3-7 and Table 3-8, respectively.

Table 3-7 Distribution of gradient values for Gaussian fitting of the left edge

Pixel number	1	2	3	4	5	6	7	8	9
x (location)	181	182	183	184	185	186	187	188	189
y (gradient values)	-3	-10	-2	34	76	25	3	-2	1
$y_{estimate}$ (Gaussian values)	0.00	0.02	2.07	33.27	76.27	24.89	1.16	0.01	0.00

Table 3-8 Distribution of gradient values for Gaussian fitting of the right edge

Pixel number	1	2	3	4	5	6	7	8	9
x (location)	976	977	978	979	980	981	982	983	984
y (gradient values)	14	5	17	15	24	11	21	12	4
$y_{estimate}$ (Gaussian values)	7.92	11.57	15.16	17.80	18.73	17.68	14.96	11.34	7.71

Figure 3-16 and Figure 3-17 show two Gaussian fitting curves for two different fitting conditions. The left edge seems to have a good fit since the gradients present a sharp peak. However, the right edge appears to be a very poor fit since the gradients present a broad peak. The coefficient of determination (R^2) needs to be calculated in order to evaluate the fit of these curves. If both the left and right edges have a reasonably good fit, $R^2 > 0.9$, then the subpixel length is considered reliable. The curve fit method is only applicable to edge data that presents a Gaussian distribution. If there is a lot of noise in the data around the edges, the data may not fit the selected curve distribution, causing a poor fit.

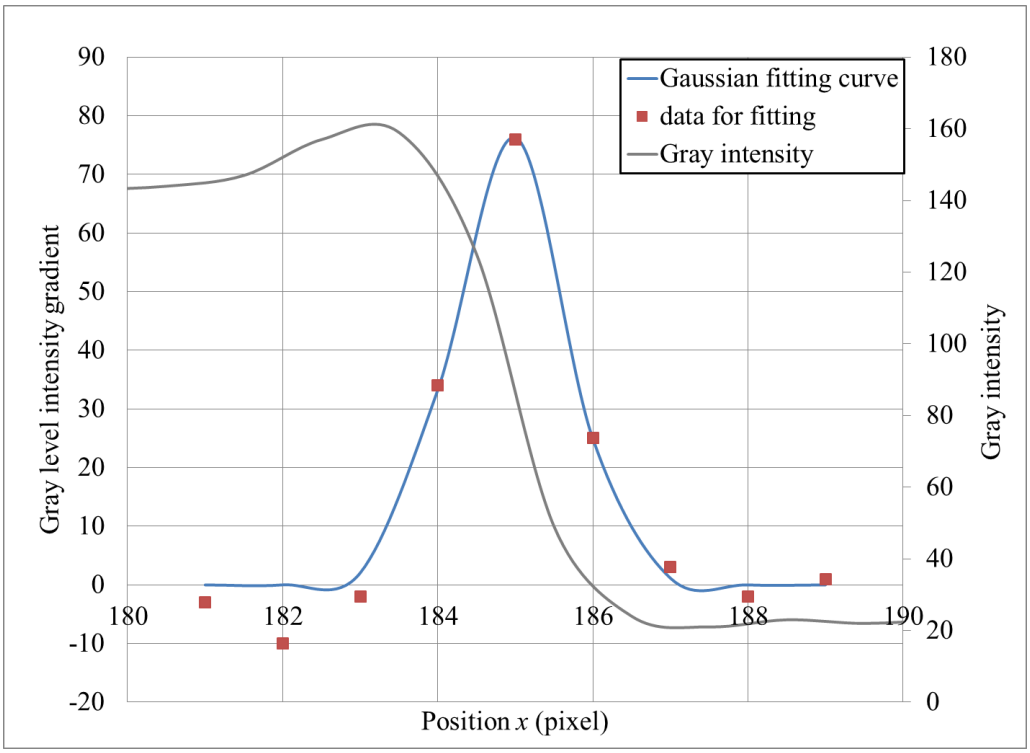

Figure 3-16 Gaussian fitting curve for the left edge

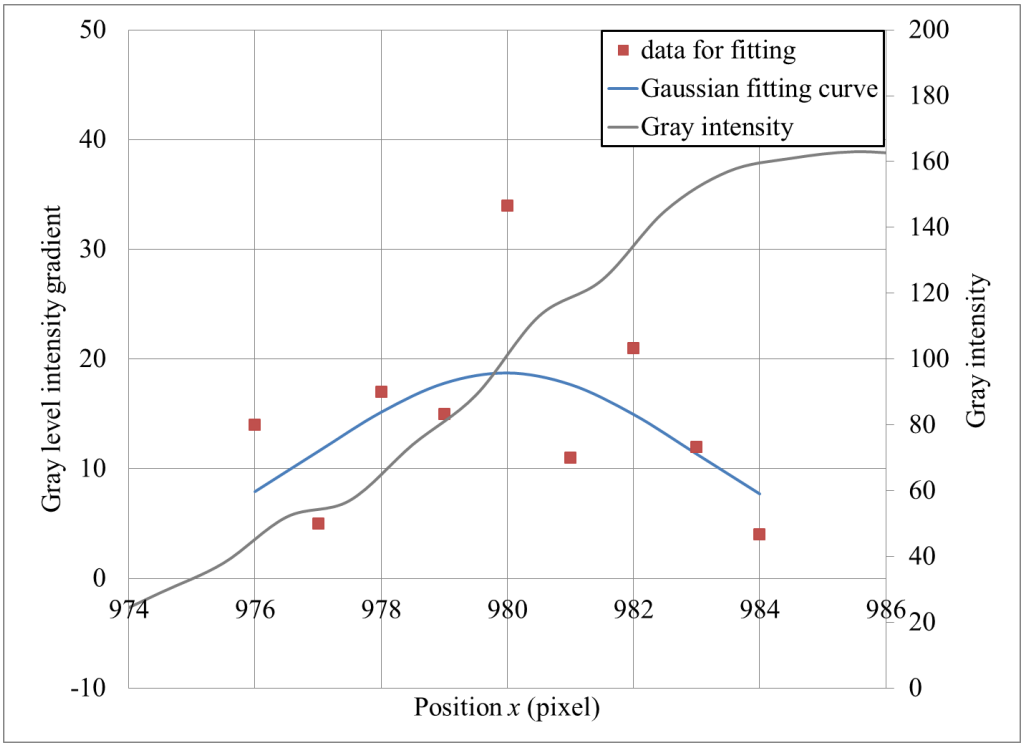

Figure 3-17 Gaussian fitting curve for the right edge

From Figure 3-17 it can be seen that there is not a sharp change in the gray intensity for the right edge. Therefore, it is difficult to find the edge using the gray intensity method presented here. Instead, the gradient can be used to find the edge.

2) Spline interpolation

The process of the spline interpolation method involves first finding the pixel-level edge location by finding the largest gradient. Then eight adjacent pixels are selected (four pixels to the left and four pixels to the right of the largest gradient pixel) for the interpolation. New data are interpolated based on the spline function with a step size of 0.01 pixels. Then, the new location of the largest gradient is the subpixel-level edge.

The lengths of the rectangle are about 3300 pixels in the axial direction and 860 pixels in the lateral direction based on pixel-level edge detection. A 0.01 pixel step size can provide very high accuracy in the strain measurement, with 3.0×10^{-6} pixel accuracy in the axial direction and 1.1×10^{-5} pixel accuracy in the lateral direction. This is high enough for the strain measurements in the test, which are on the order of 10^{-4}.

The spline interpolation function consists of several piecewise polynomial functions. For each pair of points, there is a spline interpolation function. Since nine points are selected for spline interpolation, eight spline interpolation segments are created. The coefficients of the spline interpolation function Equation (3-10) are calculated and listed in Table 3-9 and Table 3-10 for the left and right edge, respectively.

Table 3-9 Coefficients of spline interpolations for the left edge

Function No.	1	2	3	4	5	6	7	8
α_0	2.0	2.0	3.1	-36.3	43.1	-14.0	1.0	1.0
α_1	1.5	7.5	13.5	22.7	-86.2	43.0	1.0	4.0
α_2	-10.5	-1.5	19.5	55.6	-7.9	-51.0	-7.0	-2.0
α_3	-3.0	-10.0	-2.0	34.0	76.0	25.0	3.0	-2.0

Table 3-10 Coefficients of spline interpolation for the right edge

Function No.	1	2	3	4	5	6	7	8
α_0	-9.5	-9.5	12.7	-16.3	19.7	-17.3	7.5	7.5
α_1	39.1	10.5	-18.1	20.0	-29.0	30.0	-21.9	0.5
α_2	-38.6	11.0	3.4	5.3	-3.7	-2.7	5.4	-16.0
α_3	14.0	5.0	17.0	15.0	24.0	11.0	21.0	12.0

Unlike the Gaussian fitting, the spline interpolation method connects all the known data points. Since it relies completely on the known data, the noise in the data can lead to poor results. Figure 3–18 shows the spline interpolation for the left edge of the rectangle. This data has one peak, and is very similar to the Gaussian fit. Figure 3-19 shows the spline interpolation for the right edge. This data has more than one peak, which is caused by irregular data (noise) around the right edge.

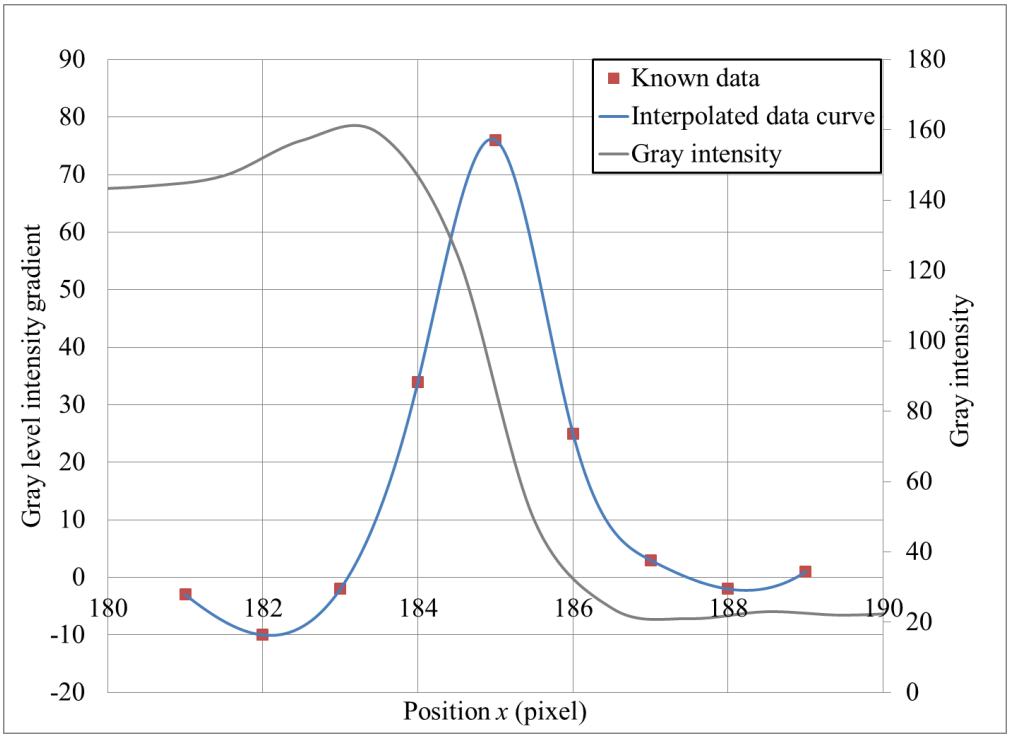

Figure 3-18 Spline interpolation for the left edge

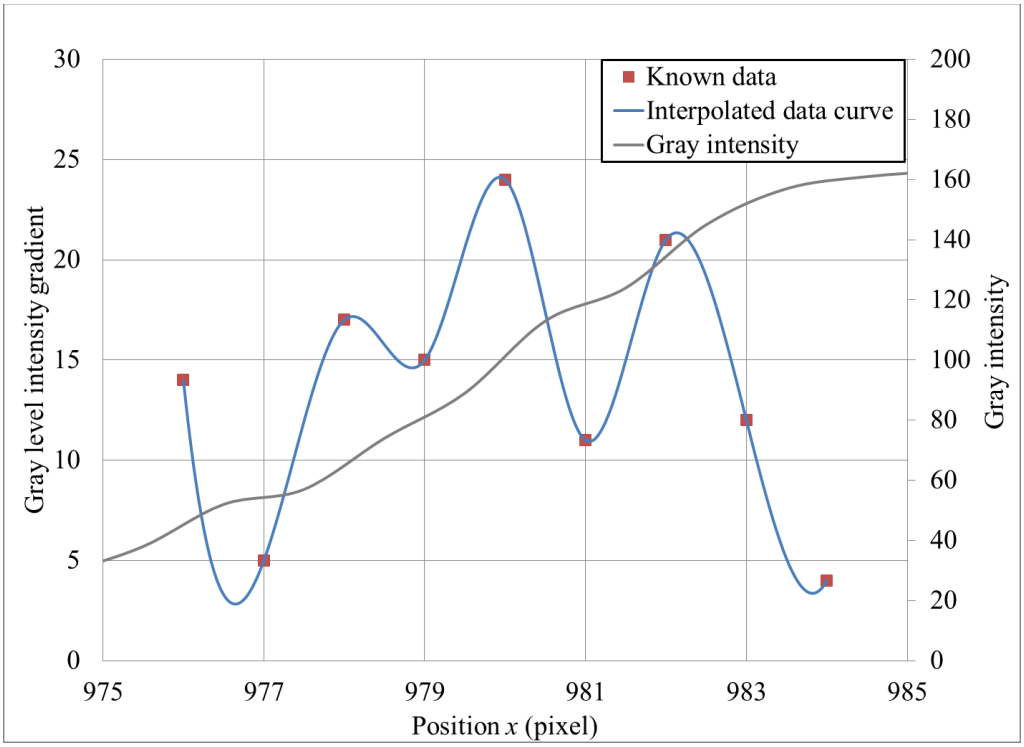

Figure 3-19 Spline interpolation for the right edge

3) Comparison of subpixel methods

Comparison of the two studied subpixel edge detection methods for one row of data is shown in Table 3-11. The left edge position varies by of 0.02 pixels and the right edge position varies by 0.04 pixels.

Table 3-11 Comparison of the two subpixel methods for one line of data

Subpixel methods	Left edge position (pixels)	Right edge position (pixels)
Gaussian fitting	184.93	979.97
Spline interpolation	184.95	979.93
Difference	0.02	0.04

In order to compare these two methods of subpixel edge detection, more data must be considered. The edge locations of 50 lines are shown in Figure 3-20. The differences between these two subpixel methods are calculated by subtracting the values calculated using spline interpolation from those calculated using the Gaussian fitting method, and are shown in Figure 3-21. The *x*-axis shows the pixel number and the *y*-axis shows the subpixel location of the edge. From these figures, most of the data falls within the range of 184 to 186 pixels for the edge location. The maximum difference between the two methods is 1.50 pixels and minimum is 0.01 pixels. The average difference between the methods is 0.25 pixels. The spline interpolation method gives a wider range of edge locations than the Gaussian fit method.

The Gaussian fit and interpolation methods both use the known data to estimate the unknown edge location. Both can realize subpixel-level analysis in digital image processing. The fitting method approximates a function to represent the variation in the data. This approximate function is not necessary in the interpolation method. The fit

method also considers the error existing in the known data by not requiring that every known data point satisfy the fit function. The interpolation method does not consider the error in the known data, rather it relies solely on the known data.

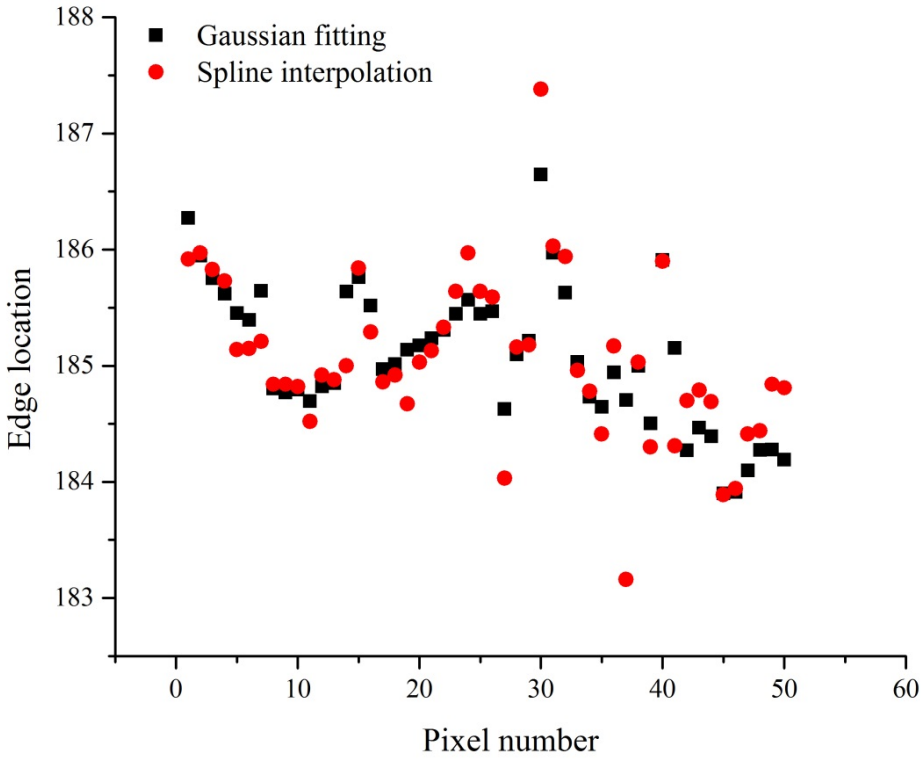

Figure 3-20 Left edge locations using two subpixel-level methods

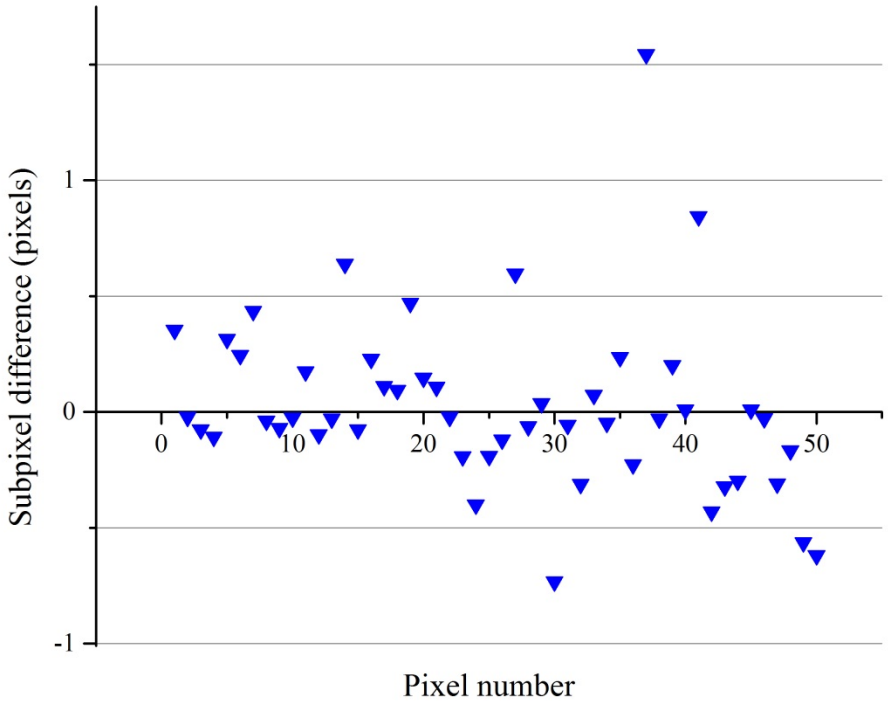

Figure 3-21 Variations between the Gaussian fit and interpolation subpixel methods

3.5.1.3 Macro strain measurement results

The rectangle edge detection method was compared to the laser extensometer and strain gage system. The axial strain measurement results are listed in Table 3–12 and the lateral results in Table 3–13. Figure 3-22 shows a graph comparing the various strain measurement methods.

Table 3-12 Comparison of axial strain measurement results with subpixel rectangle edge detection

Image number	Stress (MPa)	Laser Extensometry $\varepsilon\times10^{-4}$ (mm/mm)	Strain Gage $\varepsilon\times10^{-4}$ (mm/mm)	Rectangle using Gaussian fitting $\varepsilon\times10^{-4}$ (Pixel/Pixel)	Rectangle using Spline Interpolation $\varepsilon\times10^{-4}$ (Pixel/Pixel)	Difference between laser and strain gage	Difference between Gaussian fitting and strain gage	Difference between Spline Interpolation and strain gage
1	0	0.00	0.00	0.00	0.00	0.00%	0.00%	0.00%
2	24	1.44	1.19	0.64	0.26	21.01%	46.24%	78.52%
3	52	2.85	2.64	2.34	4.34	7.91%	11.57%	63.92%
4	81	4.62	4.09	3.38	5.68	13.02%	17.23%	38.89%
5	110	6.43	5.69	5.94	6.60	13.12%	4.56%	16.00%
6	139	7.59	7.22	7.27	7.07	5.14%	0.60%	2.09%
7	168	8.77	8.45	8.51	9.02	3.82%	0.71%	6.74%
8	197	10.73	10.05	9.64	8.82	6.78%	4.01%	12.20%
9	226	12.68	11.48	11.13	10.27	10.49%	3.06%	10.56%
10	196	11.12	10.02	9.39	9.50	11.00%	6.35%	5.19%
11	167	9.60	8.52	9.09	8.69	12.68%	6.69%	1.97%
12	139	7.78	6.98	7.91	7.01	11.45%	13.32%	0.45%
13	110	6.57	5.70	6.42	5.64	15.20%	12.50%	1.09%
14	81	5.45	4.34	5.25	4.56	25.56%	21.06%	5.19%
15	52	3.85	2.64	3.85	2.52	46.13%	46.17%	4.30%
16	23	2.97	1.28	2.59	1.81	132.33%	102.89%	41.39%
17	-6	1.33	-0.25	3.34	2.35	624.58%	1413.39%	1025.10%

Table 3-13 Comparison of lateral strain measurement results with subpixel rectangle edge detection

Image number	Stress (MPa)	Strain Gage $\varepsilon' \times 10^{-4}$ (mm/mm)	Rectangle using Gaussian fitting $\varepsilon' \times 10^{-4}$ (Pixel/Pixel)	Rectangle using Spline interpolation $\varepsilon' \times 10^{-4}$ (Pixel/Pixel)	Difference between Gaussian fitting and strain gage	Difference between spline interpolation and strain gage
1	0	0.00	0.00	0.00	0.00%	0.00%
2	24	-0.39	-1.33	-2.55	240.18%	554.33%
3	52	-0.78	0.33	-0.62	142.42%	20.74%
4	81	-1.17	0.46	-2.57	139.42%	119.33%
5	110	-1.45	-1.93	-2.16	32.75%	48.88%
6	139	-1.77	-5.38	-1.84	204.08%	3.85%
7	168	-2.28	-4.41	-4.57	93.38%	100.57%
8	197	-2.56	-4.10	-1.63	60.04%	36.22%
9	226	-2.96	-5.88	-6.37	98.69%	115.53%
10	196	-2.55	-4.15	-0.03	62.94%	98.81%
11	167	-2.23	-3.04	-1.24	36.49%	44.56%
12	139	-1.96	-3.69	-4.93	88.94%	151.86%
13	110	-1.47	-2.14	-1.80	45.65%	22.54%
14	81	-1.04	-2.43	-1.30	133.57%	24.95%
15	52	-0.80	-1.59	-0.30	97.70%	62.77%
16	23	-0.33	-2.97	1.50	812.97%	562.25%
17	-6	0.16	-0.25	0.08	253.75%	52.53%

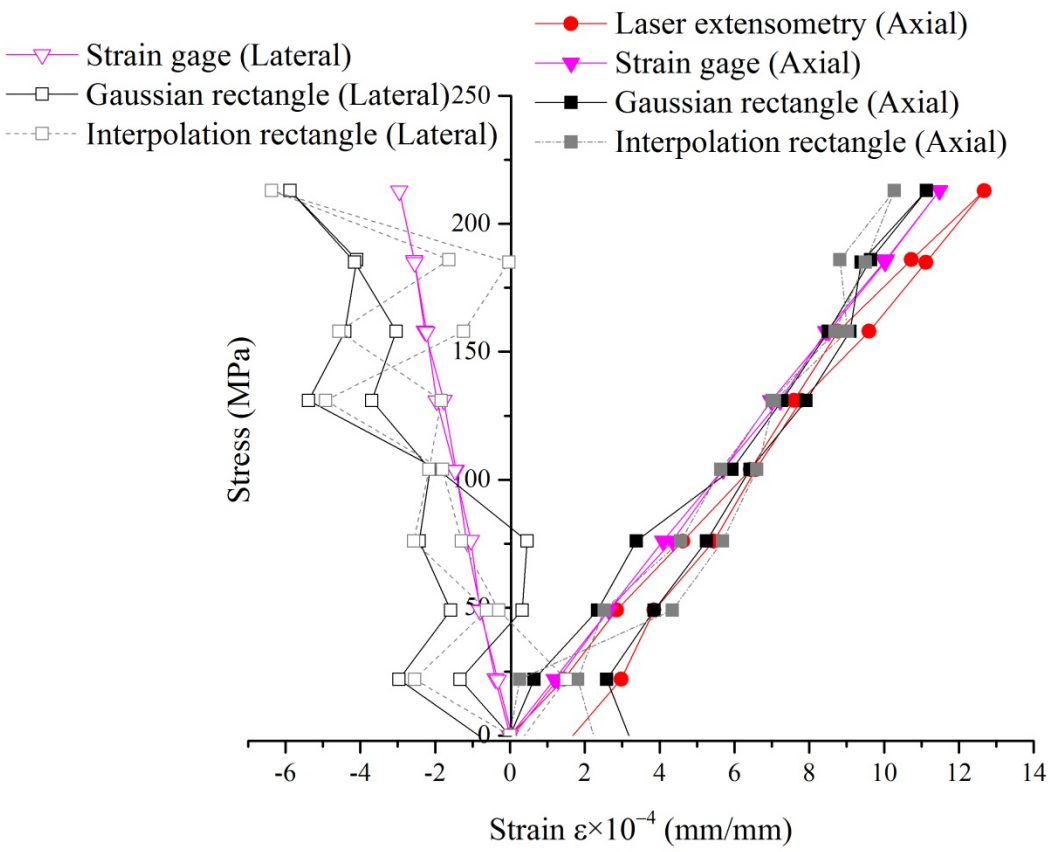

Figure 3-22 Comparison of axial strain measurement methods

The strain measurement is on the order of 10^{-4}. The stress-strain curves of the specimen are limited to the elastic region. Using the strain results obtained from the strain gage as the reference data, the other methods are compared, and the differences are shown in the last three columns of Table 3-12 for the axial strains and last two columns of Table 3-13 for the lateral strains. The differences are calculated based on Equation (3-13).

$$Difference = \frac{\varepsilon^{*} - \varepsilon\ (strain\ \ gage)}{\varepsilon\ (strain\ \ gage)} \tag{3-13}$$

Where, ε^{*} is the strain measured by laser extensometry and two rectangle methods.

Image 1 is used as the baseline from which the strain is measured for the digital image methods and is captured after the specimen is installed in the loading system. Images 1 through 9 were captured as stress increased. The stress reached its maximum value at Image 9, and then decreased back to the initial value (-6 MPa in this test).

For the axial strain, the four strain measurement methods show similar stress-strain curves with similar slopes. However, these methods cannot provide exactly the same strain measurement results. All methods give approximate values for strain. Laser extensometry and strain gages are known to be reliable strain measurement techniques with high accuracy. There is still about a 20% difference between these two techniques. The difference between the two subpixel rectangle methods is similar (18%). Variation in the strain is larger for the highest and lowest stresses and smaller in the middle range stresses.

For the lateral strain, measurements using the two rectangle methods have a large deviation from the strain gage measurements. Therefore, the stress-strain curves have a large gap for increasing and decreasing stress. The average differences between the Gaussian fitting and spline interpolation methods to the strain gages are 149% and 119%, respectively.

The strain measured in Images 2 and 17 shows the largest deviation from the reference methods. As loading is applied, mechanical noise is introduced and is most evident between static and loaded states, such as Images 2 and 17, when loading starts and ends, respectively.

The difference in strain measurements between these methods can be attributed to noise from the machines, resolution of the instruments, limitations of image resolution, and analysis algorithms.

Table 3-14 Axial strain measurements from Image 3

Strain Gage	Rectangle using Gaussian fitting	Rectangle using Spline interpolation
$\varepsilon\times10^{-4}$ (mm/mm)	$\varepsilon\times10^{-4}$ (mm/mm)	$\varepsilon\times10^{-4}$ (mm/mm)
2.64	2.34	4.34

Table 3-15 Lateral strain measurements from Image 8

Strain Gage	Rectangle using Gaussian fitting	Rectangle using Spline interpolation
$\varepsilon'\times10^{-4}$ (mm/mm)	$\varepsilon'\times10^{-4}$ (mm/mm)	$\varepsilon'\times10^{-4}$ (mm/mm)
-2.56	-4.10	-1.63

The axial strain measurements from Image 3 are listed in Table 3–14. The lateral strain measurements from Image 8 are listed in Table 3–15. These two tables show a similar magnitude for the strain gage measured values. The rectangle method using Gaussian fitting shows similar results for axial strain as the strain gage, but very different lateral strain results. The rectangle method using spline interpolation shows a large deviation from the strain gage results in both the axial and lateral directions.

For the axial strain measurement of Image 3, the difference between the two rectangle methods can be attributed to some noise in the data existing around the edge of the painted rectangle. The Gaussian fitting method can filter out the noise data and

achieve results close to those of the strain gage. The spline interpolation method uses the noise data and therefore has a much larger deviation from the accepted strain gage results.

For the lateral strain measurement of Image 8, the two rectangle methods have large deviations from the strain gage. These deviations could be the result of lighting differences between images. The lighting source was on one side of the specimen. For the lateral direction, the lighting distribution for the left and right edges is not even. At the subpixel level, very small lighting changes can cause large differences in strain results.

When comparing strains of the same magnitude in the axial and lateral directions, the lateral strains obtained from the DIC methods deviate from the strain gage measurements much more than the axial strains. This observation is primarily due to the blurriness on the vertical edges and the shorter dimension of the rectangle in the lateral direction. Since the rectangle's lateral dimension (about 860 pixels) is about 25% of the length of the axial dimension (about 3300 pixels), the same blurriness on all edges of the rectangle leads to a much higher error for lateral. As a result, the errors due to blurriness on the vertical edges have a magnified effect (about 4×) on the change in the lateral strain between images.

Figure 3-23 shows a portion of the gradient values of the right edges of Image 3 and Image 8. The highest value in these cells represents the highest pixel value change from neighboring pixels. The darkest color represents the greatest gradient and is considered as the edge. Both images are of the same position along the right edge. A lighting change caused the position of the highest gradient to change. In Image 3, the edge is sharp since the highest gradient is clear based on neighboring cells. In Image 8, the edge is blurred since several cells have similar gradient values. Similar gradient

values around the edge can cause multiple peaks in the interpolation method and cause error in lateral strain results.

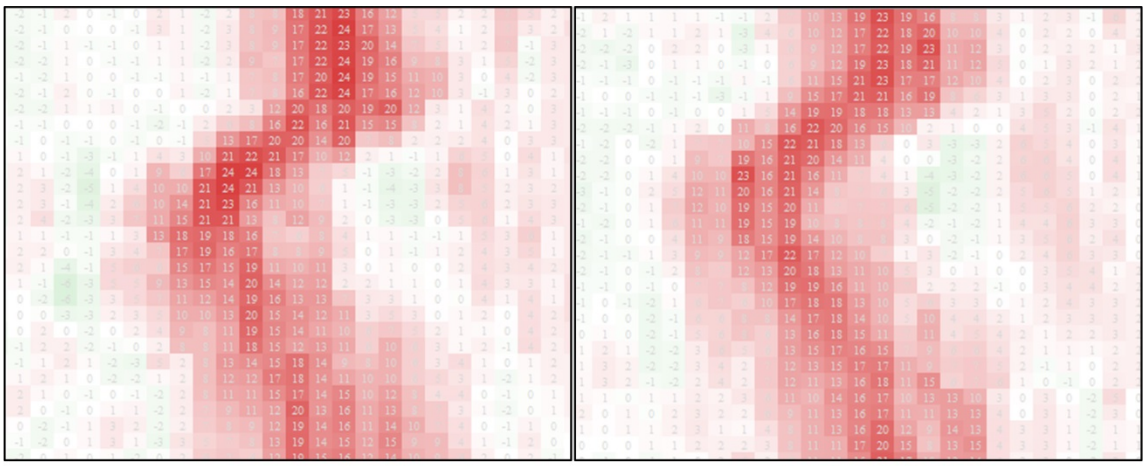

Image 3 Image 8

Figure 3-23 Part of the gradient map of the right edge of the painted rectangle from image 3 and image 8

Since the maximum load applied to the specimens is smaller than the nominal yield stress — the stress-strain diagrams appear linear. From the slope of the line, the modulus of elasticity (E) of the specimen can be obtained (ASTM E111-04). Table 3–16 lists the calculated moduli of elasticity, which are found using the slope of the stress-strain curve (loading part) for each strain measurement method. The modulus of elasticity of A36 steel should be approximately 200 GPa (ASTM A36/A36M-12, 2012). Except for laser extensometry, the measured modules for the other strain measurement methods are close to 200 GPa. The modulus as measured by laser extensometry has about a 10% difference from the theoretical value. This difference is likely attributed to slipping or sliding of the reflective tapes during the tension tests. This observation is supported by Figure 3-22, which shows that the axial strain measured by the laser extensometer does not return to the initial strain of 0 at the start of loading. This belief is

also confirmed by the axial strain measured by the strain gage, which does return to 0. In addition, the maximum stress did not exceed the yield strength during the tension test.

Table 3-16 Modulus of elasticity of the specimen as calculated from the different strain measurement methods

	Laser Extensometry	Strain Gage	Rectangle using Gaussian fitting	Rectangle using spline interpolation
Modulus of elasticity *E* (GPa)	182.65	196.11	193.40	203.88
Difference between Strain Gage (%)	6.86%	N/A	1.38%	3.97%
R^2	0.9969	0.9997	0.9923	0.9215

3.5.1.4 Discussion

A36 steel is a homogenous ductile material and the stress applied during the test is less than the yield stress. Therefore, the stress-strain responses are approximately linear, as expected. Axial strain results show a similar trend for all measurement methods. However, the lateral strain results have a large deviation.

Laser extensometry and strain gages can realize real-time data collection. The digital image methods collect data for post-processing. All the strain measurement methods are discrete.

Poisson's ratio of A36 steel is 0.26. Therefore, in theory, the lateral strain is about one fourth of the axial strain. The width of the rectangle is about 1000 pixels and the height of the rectangle is about 3500 pixels. This difference in the initial reference lengths of the rectangle may cause the differences in the accuracy of strain results in the

lateral and axial direction. For example, for the same amount pixel changes, the accuracy of the axial strain is about 3.5 times of the lateral strain. In addition, the lighting source used in the test was directed at the center of the specimen. Since the shape of the specimen is long and narrow, this lighting arrangement can provide relatively similar lighting for both the top and bottom edges of the painted rectangle. For the left and right edges, the lighting is not evenly distributed. Since the middle of the left and right edges is brighter than the rest of the specimen, this may induce a large deviation in the lateral strain measurements.

A camera with higher resolution or a zoom function, which increases the pixels per unit length in the image, may improve the accuracy in strain measurement. Ideally, the painted rectangle should have the same width to height ratio as the image taken by the camera (4:3 or 16:9). The dimensions of the specimen limit the size of the painted rectangle. In this test, the rectangle size is about 862×3318 pixels, as shown in Figure 3-24, which corresponds to a ratio of approximately 1:4.

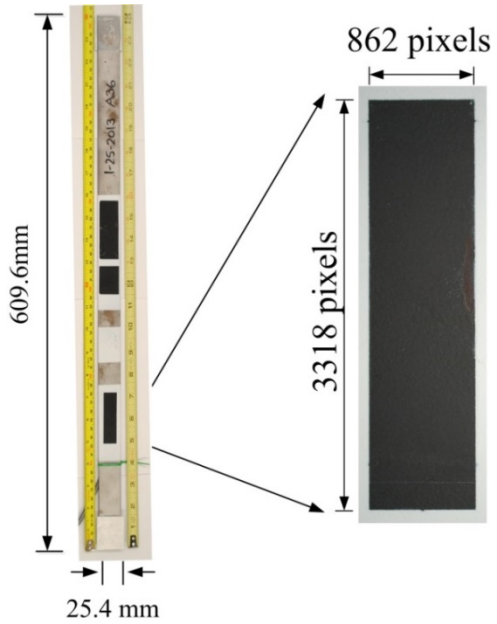

Figure 3-24 Specimen with paint rectangle

For the rectangle edge detection method, the strain measurement is based on the average length change of the painted rectangle. The local deformation of the specimen is not been considered. Therefore, the behavior near stress concentrations cannot be captured.

The modulus of elasticity (E) can be easily calculated by finding the slope of the trend line from the stress-strain curve. From Table 3–16, we can see that the differences between elastic moduli are within 10%, which is a small variation. The R^2 values for all the methods except spline interpolation are greater than 0.99. The value for the spline interpolation method is above 0.90. This indicates that the stress-strain response does show a strong linear trend. Of the two digital image methods, the Gaussian fitting method shows stronger linearity than the spline interpolation method.

The interpolation method solely depends on known data. Thus, if the data are reliable, interpolation can give very good results. However, if there is considerable noise in the data, the interpolation data may be very poor. The Gaussian fit method is also based on known data, but it includes regression to evaluate the trend in the data. Fitting methods will filter some data, which have a large variation from the given model resulting in a low coefficient of determination. Therefore, choosing a suitable model is vital for success of this method. Additionally, a good initial guess for curve parameters is very important. Based on the results of the two rectangle subpixel digital image methods, the Gaussian fitting method shows better results.

3.5.2 IPhone with rectangle data analysis: Test 2

In comparison to the Nikon D3000 camera, the iPhone 4S camera has limited manual settings and low image quality. This camera does not provide detailed settings,

such as shutter time, aperture, and white balance. The images from the iPhone camera are of a lower quality than those from the Nikon D3000. The iPhone image resolution is 1920×1080, while, the Nikon D3000 image resolution is 2872×2592. However, the iPhone camera is very convenient and easy to use. If the strain results obtained from the iPhone images closely match those from the laser extensometer and strain gages, it could be a very useful tool for strain measurement. Test 2 used the iPhone 4S to capture the images that are used to measure the length changes of the rectangle dimensions. All the images are processed using the Matlab Gaussian fitting method to obtain the subpixel-level length of the rectangle.

Figure 3-25 and Table 3–17 compare the strain measurement results using iPhone images to the other strain measurement techniques used. The iPhone axial strain measurement results fall to the left of the other two strain measurement methods. The first five axial strain measurements from the iPhone images roughly increase with the same trend as the laser and strain gage methods. Later measurements read a smaller axial strain than the other methods. For lateral strain measurement, the iPhone results vary greatly and have a large deviation from the strain gage results. The two rectangle methods show a large variation with increasing and decreasing stress, but both methods show a similar stress-strain response.

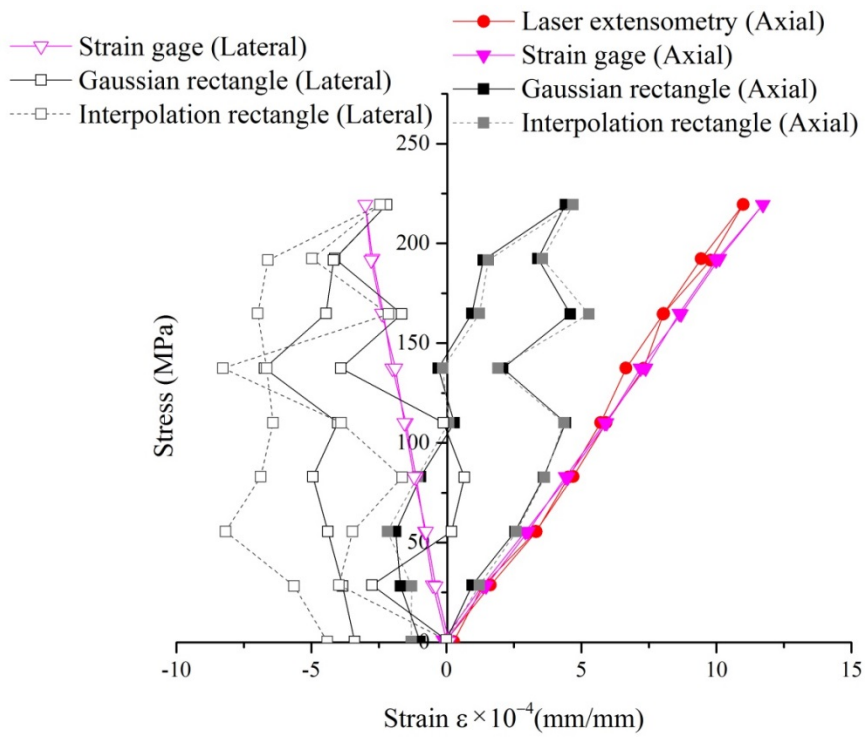

Figure 3-25 iPhone with rectangle axial strain comparison for Test 2

Table 3-17 Strain measurement comparison with iPhone 4S for Test 2

Image number	Stress (MPa)	Laser extensometry (Axial) $\varepsilon\times10^{-4}$ (mm/mm)	Strain gage (Axial) $\varepsilon\times10^{-4}$ (mm/mm)	Gaussian fitting (Axial) $\varepsilon\times10^{-4}$ (pixel/pixel)	Spline interpolation (Axial)) $\varepsilon\times10^{-4}$ (pixel/pixel)	Strain gage (Lateral) $\varepsilon\times10^{-4}$ (mm/mm)	Guassian fitting (Lateral) $\varepsilon\times10^{-4}$ (pixel/pixel)	Spline interpolation (Axial) $\varepsilon\times10^{-4}$ (pixel/pixel)
1	0	0.00	0.00	0.00	0.00	0.00	0.00	0.00
2	29	1.63	1.45	0.96	1.23	-0.50	-2.76	-3.98
3	55	3.33	3.03	2.54	2.59	-0.80	0.19	-3.47
4	83	4.52	4.60	3.60	3.63	-1.12	0.67	-1.63
5	110	5.71	6.05	4.41	4.35	-1.50	-0.11	-3.90
6	137	6.65	7.30	2.09	1.91	-2.00	-3.91	-8.27
7	165	8.03	8.80	4.59	5.27	-2.33	-1.66	-2.14
8	192	9.44	10.23	3.38	3.55	-2.73	-4.13	-4.98
9	219	10.99	11.83	4.41	4.69	-3.00	-2.21	-2.46
10	192	9.79	10.10	1.37	1.56	-2.79	-4.17	-6.61
11	165	8.04	8.74	0.94	1.22	-2.39	-4.45	-6.98
12	137	7.31	7.49	-0.30	-0.14	-1.89	-6.73	-6.66
13	110	5.92	5.98	0.29	0.08	-1.56	-4.02	-6.42
14	83	4.69	4.53	-0.95	-1.06	-1.20	-4.95	-6.87
15	56	3.31	3.14	-1.88	-2.18	-0.75	-4.38	-8.18
16	28	1.34	1.58	-1.70	-1.29	-0.40	-3.84	-5.64
17	0	0.27	0.08	-0.98	-1.30	0.10	-3.40	-4.41

The large deviation between the two rectangle methods can be attributed to the low resolution of the images from the iPhone camera. Small deformations are more difficult to detect in images of lower resolution. The rectangle pixel measurement of the axial length in the iPhone image is about 1365 pixels, which is about one third of the Nikon D3000 at 3327 pixels. This means that in order to detect the same strain change, the iPhone images require three times the accuracy of the Nikon images. For the lateral strain, which is only about one-third the value of the axial strain, much higher accuracy is needed.

The iPhone 4S camera uses complementary metal-oxide-semiconductor (CMOS) as the image sensor. CMOS uses transistors at each pixel to move the charge through traditional wires, so each pixel is treated individually. Compared to the CCD camera, CMOS cameras create images with higher noise. In addition, CMOS requires a higher lighting level to create the same quality image as a CCD camera.

The Gaussian fitting method is based on the CCD image sensor camera. Therefore, due to the limitations of the image quality and noise, the images from the iPhone 4S have a larger variation in strain measurement.

3.5.3 Nikon camera with speckle data analysis: Test 3

Speckles have been used in digital image correlation (DIC) as a pattern for many years as a full field strain measurement method. Compared to the rectangle pattern, which uses only two edges of the rectangle, the DIC method tracks every speckle's position change. Therefore, the DIC method can provide a strain measurement map for the whole specimen surface. The DIC method is, however, very sensitive to vibrations since it uses the relative movement of the speckle to measure strain.

The photographs from the Nikon D3000 are cropped to a resolution of 1468×2320 (3,405,760) pixels, showing only the speckle patterned portion of the images. The selected subset size is 21×21 pixels (about 0.28 × 0.28 mm). This generates 6060 subsets for the correlation, which includes 2,672,460 (= 6060×21×21) pixels. In Figure 3-26, the intersections of the red grid mark the center of each subset. These intersections are used as markers for the correlation.

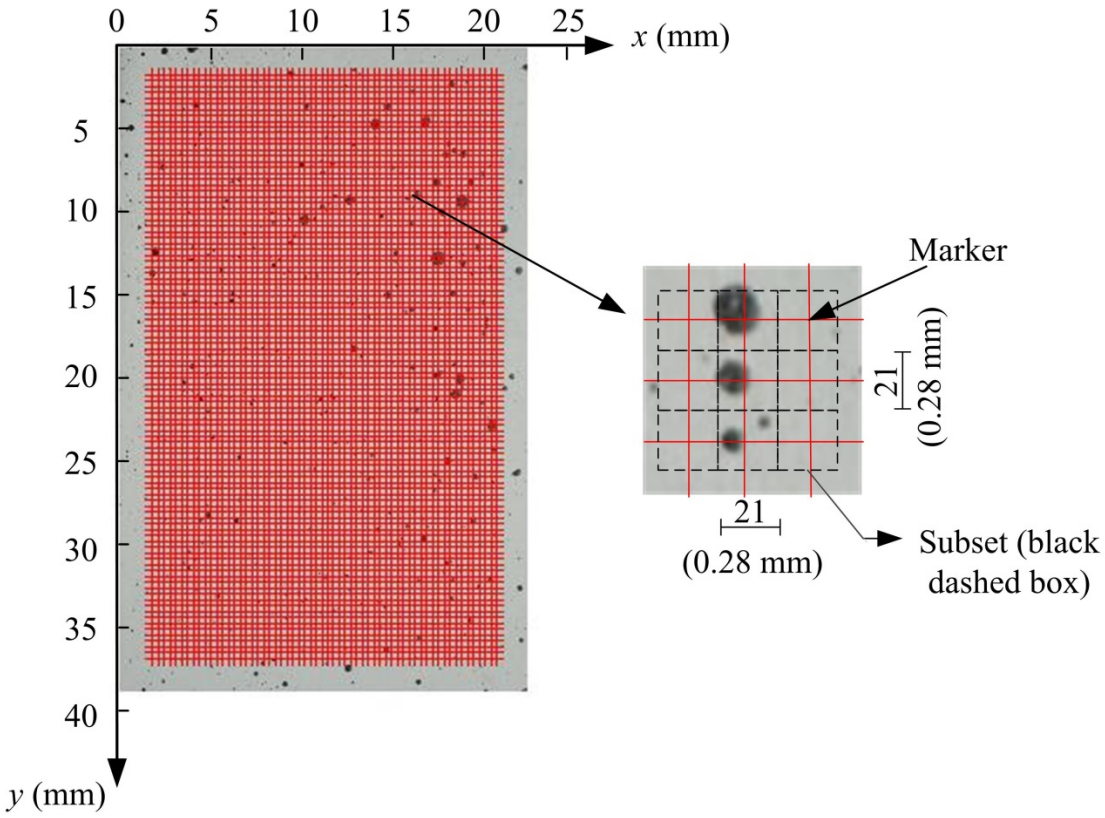

Figure 3-26 Grid with 6060 subsets

The displacement map for the DIC method is a vector map. Displacements are calculated based on the new position of a marker minus the original position of that marker. The length of the displacement vector represents the magnitude of the

displacement and the arrow represents its direction. A portion of a displacement map from Image 6 is shown in Figure 3-27.

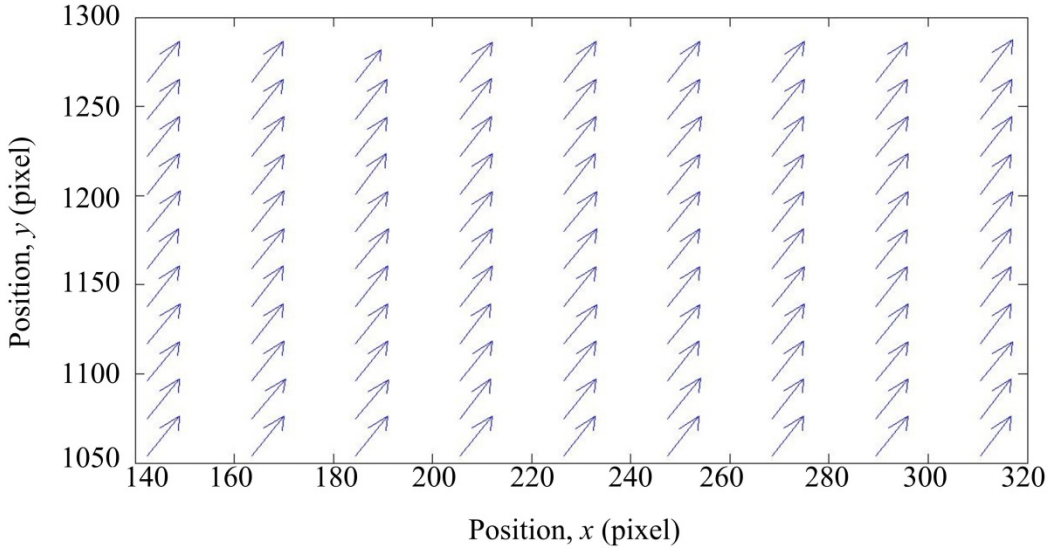

Figure 3-27 Part of a displacement map for Image 6

The displacement vectors in this map all present similar magnitudes and orientations. This means the displacements of the markers of the specimen have a high degree of homogeneity. Since the specimen is a homogeneous material and the shape is rectangular, the specimen should not have a stress concentration region in the center of the specimen. No such stress concentration was observed, as expected. Shear strain is not measured in this test.

The results of the DIC method are listed in Table 3–18. Figure 3-28 shows that the results of strain measurement using the DIC speckle method have a large variation when compared to the other two strain measurement methods both in the axial and lateral directions. The axial strain measurements by DIC speckle method have smaller values than the other two methods and the lateral measurements have larger values than the strain gage. From the displacement map, we can see that the displacement shows a

deviation from the expected vertical direction. If a horizontal force component causes the divergence, the same strain measurement results should be obtained from both laser extensometry and the strain gages. If the location of the specimen or camera changes during the course of the test, the strain results from DIC will have a large deviation from the other two methods.

Table 3-18 Strain comparisons with DIC speckle method for Test 3

Image Number	Stress (MPa)	Laser extensometry (Axial) $\varepsilon\times10^{-4}$ (mm/mm)	Strain gage (Axial) $\varepsilon\times10^{-4}$ (mm/mm)	DIC speckle (Axial) $\varepsilon\times10^{-4}$ (pixel/pixel)	Strain gage (Lateral) $\varepsilon\times10^{-4}$ (mm/mm)	DIC speckle (Lateral) $\varepsilon\times10^{-4}$ (pixel/pixel)
1	0	0.00	0.00	0.00	0.00	0.00
2	28	1.63	1.57	0.21	-0.44	-0.89
3	54	3.24	3.15	1.22	-0.73	-1.58
4	82	3.95	4.59	1.96	-1.15	-2.59
5	109	5.85	6.09	2.77	-1.47	-2.78
6	137	6.86	7.39	3.68	-1.99	-3.99
7	163	8.19	8.83	4.56	-2.32	-4.72
8	191	9.45	10.34	4.37	-2.68	-5.98
9	218	10.65	11.89	4.33	-2.99	-5.15
10	191	9.37	10.24	3.48	-2.73	-4.41
11	164	8.78	8.96	3.04	-2.27	-4.24
12	136	6.80	7.43	2.27	-1.97	-4.09
13	109	5.79	6.17	0.67	-1.46	-3.21
14	82	4.35	4.76	0.18	-1.07	-2.72
15	54	2.46	3.06	0.50	-0.82	-0.36
16	27	1.47	1.69	4.15	-0.36	3.86

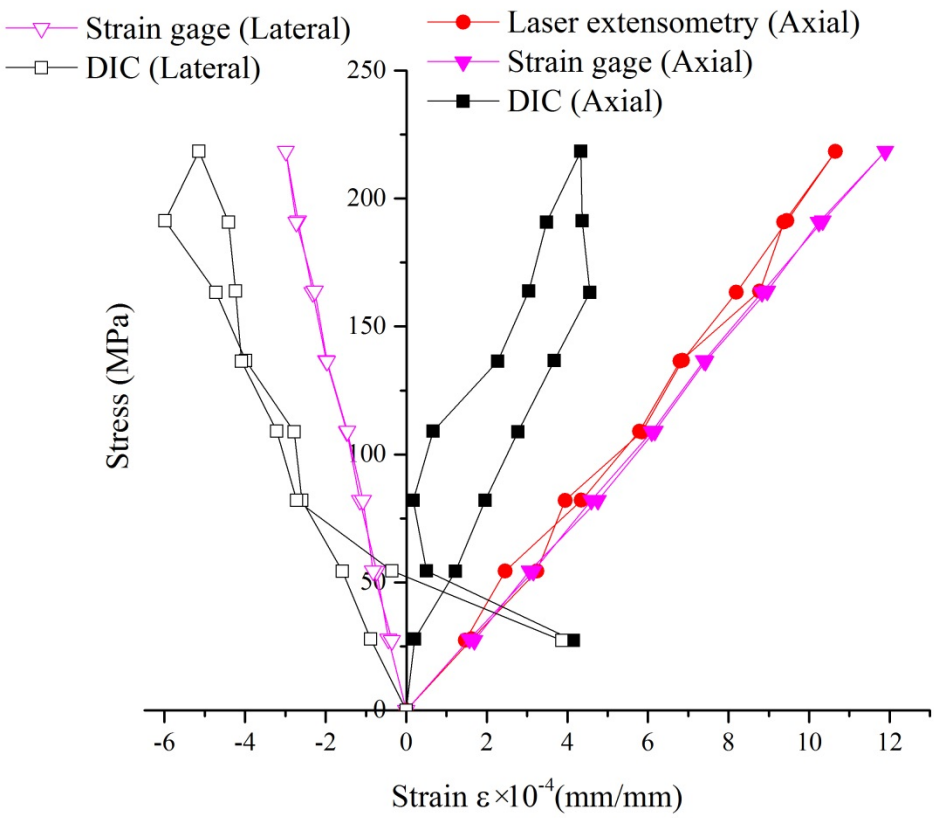

Figure 3-28 Strain comparisons with DIC using Nikon camera

The error in the location change measured by the DIC method can be attributed to the following two reasons. First, the change in location of the camera or specimen caused the poor correlation. A good correlation will result if many conditions are satisfied, including a high image quality, suitable lighting condition, and suitable speckle size and distribution. It is difficult to meet all of these requirements for a good correlation. The Matlab code used for the speckle DIC finds matching markers near to the original location of that marker. If the location changes too much, it is difficult to match the correct markers. The mismatches of markers lead to a poor correlation. Second, the displacement components in the horizontal direction can decrease the axial strain results and increase the lateral strain results. If the camera rotates by a small

amount, it causes divergence of the measured displacements. The axial strain is based on the vertical component of the displacement and the lateral strain is based on the horizontal component of the displacement. Therefore, the measured axial strain is smaller than the real value and lateral strain is larger than the real value.

The full-field axial strain measurement results from images 1, 8, and 16 are shown in Figure 3-29. Each subset works as a unit in these full-field strain measurement maps. The first image in this series serves as the baseline. Each pixel in the full-field strain measurement map represents a 21×21 pixel subset from the original specimen image. In other words, the size of the full-field strain measurement map is 60×101 pixels, which represent 1260 ×2100 pixels in the original image. The color of each pixel in the full-field maps represents the strain magnitude measurement at that position. Image 1 is the reference image and is taken as the baseline strain measurement. Steel is a homogeneous material and the images are recorded in the middle part of the specimen. Therefore, the axial strain field is expected to be uniform in the images, but the color of each pixel in Image 8 and Image 16 is not uniform. This can be attributed to vibrations in the test system and poor correlation in the digital image processing.

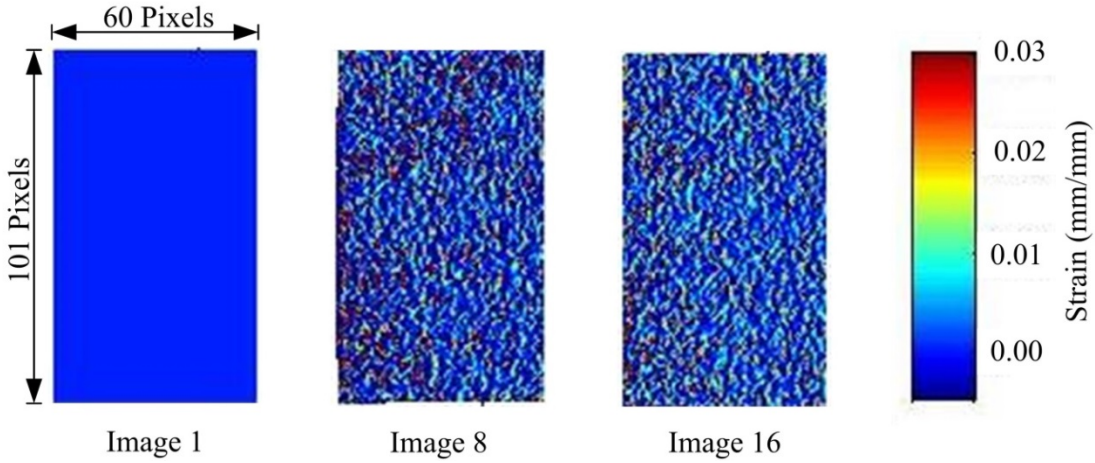

Figure 3-29 DIC full-field strain measurement result

For the DIC method, the size, quantity, and diversity in intensity of the speckles can affect the correlation. Figure 3-30 shows the speckles used for the DIC method. The quantity of speckles is not sufficient to provide enough diversity for good correlation. Additionally, in the bottom left corner of the figure, the speckles are too small to correlate accurately. For this area, detailed local deformation is difficult to determine.

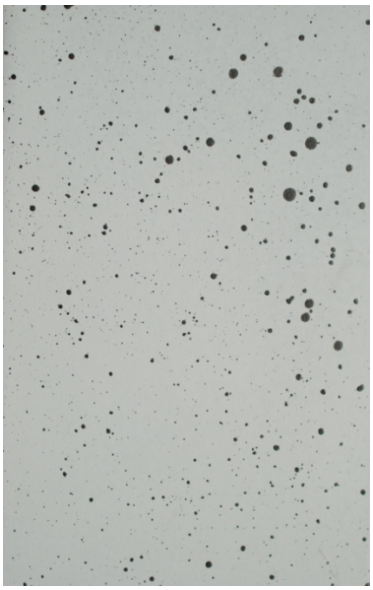

Figure 3-30 Speckles for DIC method

3.6 Conclusions

A new digital image strain measurement method was established by using a painted rectangle pattern. Two accuracy levels, pixel-level and subpixel-level, were implemented using ImageJ and Matlab, respectively. Two different subpixel-level algorithms, Gaussian fitting and spline interpolation were also evaluated using Matlab. The results using the painted rectangle pattern were compared to the DIC (speckle) method, and traditional strain measurement methods including laser extensometry and strain gages.

The rectangle edge detection method is a target-based deformation method, which explicitly considers the deformation of the target (rectangle) to calculate strain. The DIC method uses the relative displacement change of subsets to determine the strain. However, the deformation of the subsets themselves is neglected.

The pixel-level strain measurement method using ImageJ is not suitable for materials with very small strain capacities (in this study, $\varepsilon \approx 10^{-4}$). For micro strain measurement, the subpixel-level strain measurement method must be used.

A rectangle can be a suitable pattern to achieve subpixel-level accuracy of strain measurement. Both the Gaussian fit and the spline interpolation methods provide similar accuracy as laser extensometry and strain gages if the resolution of images is suitable.

In comparing the two subpixel rectangle methods, the Gaussian fitting method gives better results than the spline interpolation method. For the Gaussian fitting method, the coefficient of determination (R^2) is used to evaluate the goodness-of-fit. The Gaussian fitting method can filter out some data by goodness-of-fit (R^2). The data was used only when $R^2 \geq 0.9$. The interpolation method connects all the known data to find the unknown data.

Young's modulus (E) of a specimen was calculated by finding the slope of the axial stress-strain curves. The four strain measurement methods used in this thesis (laser extensometry, strain gages, Gaussian fitting, and spline interpolation) show very similar moduli (difference < 10%). Excluding spline interpolation, the other three methods have a coefficient of determination (R^2) greater than 99%.

The iPhone 4s is not recommended as a strain measurement device, since the results from the iPhone based images show a large deviation from the other methods.

However, with the rapid pace of development in the camera features of the iPhone, strain measurement using the iPhone may be possible soon.

DIC is a full-field strain measurement method. The strain result for each image is the average value of all the subsets. The DIC result in this test has a large deviation from reference methods. Since DIC uses the relative displacement of a subset to calculate strain, any vibration of the test system will decrease the accuracy of the DIC method. Correlation is another factor affecting the accuracy of the DIC method. This method has to find the same subset in all the images. If the correlation is poor, it will cause errors in the result.

Image quality is a critical factor in the digital image method. To obtain high quality images, a high-resolution camera, stable lighting, and vibration-free supports are required.

Chapter 4 Measuring paint removal efficacy by digital image analysis

4.1 Background

With the widespread repair and strengthening of concrete structures, surface preparation of the parent concrete substrate has become a vital factor in the subsequent bond and long-term performance of specialized coatings and repair materials (International Concrete Repair Institute, 2008). These preparation activities typically involve the removal of existing coatings and paints (ASTM D4258-05, 2012; Schmidt, Li, & Spencer, 2001). In some cases, only an aesthetic change is desired, which is often the case for graffiti removal from building façades (Gómez, Costela, García-Moreno, & Sastre, 2006).

Quantifying the effectiveness (or efficiency) of contaminant removal has not been established, nor has its relationship to the mechanical properties of the concrete substrate. The only approach to gage cleaning efficiency is a qualitative visual inspection, which is highly subjective, unstandardized, and unrepeatable. A potential approach for quantifying the cleaning efficiency of any surface preparation method lies in the field of digital image processing. Over the past decade, the analysis of digital photographs has seen increasing use in civil infrastructure applications. For example, Hutchinson and Chen (2006) formulated statistical-based methods to identify and evaluate concrete damage, especially surface cracks. Zhu and Brilakis (2010) automated the digital imaging methods to rapidly identify concrete surface flaws. Breul *et al.* (2008) demonstrated a field-based approach to measure concrete homogeneity and to control

concrete particle size distribution, all performed using digital image processing techniques. No formal approach exists to measure the cleaning effectiveness of infrastructure surface preparation processes such as dry ice blasting, water jetting, and sandblasting. While methods do exist to quantify the abrasive characteristics of these processes (such as scanning electron microscopy and profilometry), they do not measure the amount or fraction of paint removed.

The study in this chapter investigates the efficacy of dry ice blasting to remove paint coatings bonded to flat concrete substrates. Quantitative assessment of the cleaning efficiency is accomplished using gray-level thresholding and binary image conversion. Two threshold value selection methods are established here: histogram-based and edge-based.

This study is the first to offer a simple and repeatable image analysis approach that permits a quantitative assessment of cleaning effectiveness and paint removal. This approach could allow future researchers to quantify coating removal and also measure the extent of surface spalling. The research is also significant in that it utilizes software originally developed for medical imaging.

4.2 Experimental Design

4.2.1 Objectives

The primary objective of this study was to develop a repeatable image processing method to quantify the paint removal efficacy of abrasive blasting.

To simulate existing paint contamination on a concrete substrate (due to either graffiti or a prior aesthetic or protective paint coating), concrete prisms were manufactured under controlled conditions with discrete paint stripes.

4.2.2 Variables

To investigate the role of concrete substrate properties, three mix designs were formulated with the primary independent variable being water-cement (*w/c*) ratio (Table 4-1), which included 0.42, 0.50, and 0.56. This range was intended to replicate typical *w/c* ratios (and subsequent compressive strengths and elastic moduli) of actual concrete structures.

The primary response variable was cleaning efficiency, measured as the fraction of the total paint pixels removed from the surface of the concrete. As demonstrated later, image thresholding is used to segregate pixels into binary classes to facilitate this measurement.

Table 4-1 Fresh and hardened properties of concrete specimens

Specimen ID	Batch	*w/c* Ratio	Air	Mix Design (% Weight)				Density	Slump	* f'_c	^{+}E	k_c	S_a
			(%)	Water	Cement	Coarse	Fine	(kg/m^3)	(cm)	(MPa)	(GPa)	W/m-K	(mm)
C1-1	C1	0.42	3	9%	21%	32%	38%	2230	10.2	42.4	40.6	1.35	0.08
C1-2											48.4		0.07
C2-1	C2	0.50	3	10%	20%	31%	37%	2206	21.6	30.4	28.7	1.43	0.17
C2-2											37.2		0.16
C3-1	C3	0.56	3	11%	19%	32%	38%	2126	27.9	18.4	28.5	1.24	0.16
C3-2											27.9		0.18

* Compressive strength at 28 days

$^{+}$ Dynamic modulus at 302 days (just prior to dry ice cleaning)

4.2.3 Materials

The constituent materials of the concrete mixes included Type I Portland cement, uniformly graded crushed stone with diameter of 19 mm and unit weight of 2463 kg/m^3 (coarse aggregate), sand with fineness modulus of 2.2 and unit weight of 2627 kg/m^3 (fine aggregate). The five commercially available spray paints used to simulate graffiti were manufactured by Rust-Oleum®, as shown in Table 4-2.

Table 4-2 Paint specifications

ROI #	Abbreviated Color Name	Rust-Oleum® Mfr. #	Paint Type
2	Flat Black	1916830	Specialty Camouflage Aerosol
3	Flat White	1690830	Multi-purpose Enamel
4	Earth Brown	1918830	Specialty Camouflage Aerosol
5	Red Primer	1667830	General Purpose Red Primer
6	Army Green	1920830	Specialty Camouflage Aerosol

4.3 Specimen Preparation

4.3.1 Concrete prisms

Specimens were plain concrete prisms measuring 76×102×406 mm, as shown in Figure 4-1. Since surface roughness affects paint adhesion and subsequent cleaning efficiency, it was necessary to provide consistent surface roughness of the cast prisms. To accomplish this, the formwork was lined with one layer of 120-grit, fine grade sandpaper. One day after casting, the prisms were removed from the formwork and the sandpaper was peeled from the prisms and discarded. The prisms were cured at 22°C and 100% relative humidity (RH) for 27 days, and then remained at ambient laboratory conditions of 20°C and 64% RH for the remainder of the study.

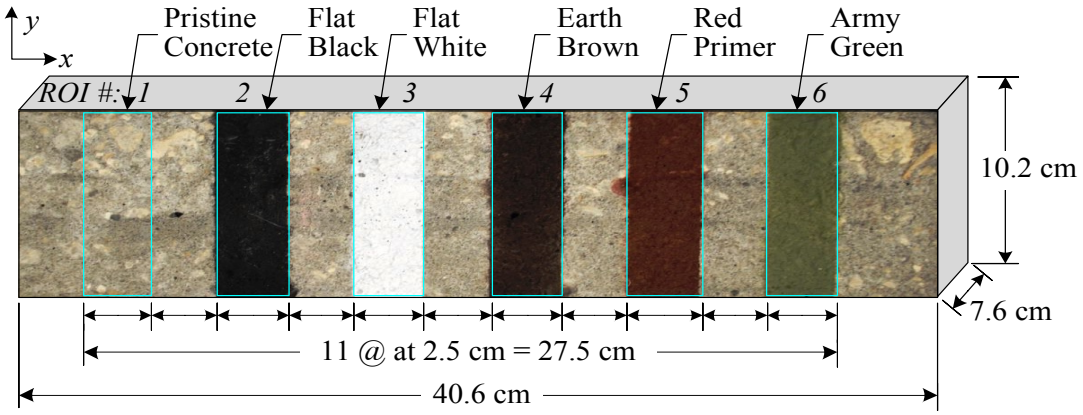

Figure 4-1 Prism dimensions and numbered regions of interest (ROI) (not to scale)

4.3.2 Controlled painting of specimens

Figure 4-1 shows the six regions of interest (ROI # i = 1 to 6) corresponding to the pristine (original) concrete color (i = 1) and the five unique paint stripes (i = 2 to 6) applied to each prism face. During paint application, the remaining ROIs were covered to prevent inadvertent contamination. The spray nozzle was oriented perpendicular to and positioned approximately 15 cm from the specimen surface. Each paint stripe was applied using a constant and continuous spray (3 seconds) along the transverse y-direction of the prism. To provide a relatively uniform thickness and avoid build-up of paint at the start and end of each stripe, the spraying was extended 5 cm beyond both prism edges in the y-direction.

4.4 Test Procedures

4.4.1 Surface roughness via optical profilometry

Since substrate roughness affects adhesion and cleaning effectiveness, the surface roughness of each prism was measured using a Nanovea PS50, 3-D, non-contacting, optical profilometer. Moisture-free, compressed air at 34 kPa was used to remove any

latent dust on the surface prior to scanning. On each prism face, at least three square areas were scanned to calculate a mean value of S_a, the arithmetic average of the surface roughness. Each region measured 44×44 mm, providing a sampling area of 1936 mm^2. The surface elevation of each region was measured at 32,767 points with the sensor's accuracy at 200 nm.

4.4.2 Paint thickness via scanning electron microscopy (SEM)

A Phillips XL30 Environmental Scanning Electron Microscope was used to estimate the thickness of a typical paint coating. A 1-cm cube of specimen C3-2 with Earth Brown paint was excised from the prism and was prepared using a gold sputtering process. Once inside the SEM, the accelerating voltage was 10.0 kV, while the working distance was 12 μm.

4.4.3 Photography system

Photographs of the concrete prism faces were recorded using a Nikon D3000 10-megapixel digital camera. The centroid of the camera's 18-mm lens was aligned with the centroid of the prism face at a distance of 53 cm. The lighting conditions consisted of two 30-Watt fluorescent lamps with 2000-Lumen output and a color temperature of 5000°K. Each color photograph was taken without flash, measured 3872×2592 pixels, and was saved in tagged image file (TIF) format.

4.4.4 Surface cleaning using abrasive blasting

The details of the abrasive blasting system are not presented here since they are not relevant to the image processing method. However, they can be found in the study reported by Millman and Giancaspro (2014) (Millman, 2013).

4.5 Image analysis and results

4.5.1 Image analysis method and results

Before analyzing the images, calibration was conducted using the previously applied method first develop by Zhang (1999). The calibration parameters are shown in Table 4-3.

Table 4-3 Camera calibration parameters

Focal length		Principal point		Skew	Distortion				
f (α, β)		(μ_0, v_0)		(s)	kc(1)	kc(2)	kc(3)	kc(4)	kc(5)
4062.26	4064.30	1939.47	1328.16	0.00	-0.06	-0.12	0.00	0.00	0.00

Prior to the abrasive blasting treatment, each painted ROI (shown earlier in Figure 4-1 contained only the paint color. After blasting, the cleaned ROIs contained the colors of both the paint and the underlying concrete substrate where the paint was removed. Therefore, the premise of the analytical approach was to apply binary image conversion to transform the pixel colors of the two materials (concrete and paint) into either black (binary value of 0) or white (binary value of 1). The relative quantities of the black and white pixels can then be utilized to measure the fraction of paint removed (cleaned). This approach circumvents the need for calibrating the length or setting a measurement scale in the ROI images of the cleaned prisms. The sequence of analysis steps consisted of:

1. Determine mean gray level intensities of the ROIs

   The 24-bit RGB color images have to be converted to 8-bit gray scale format. 8-bit gray scale has 256 different gray intensities.

2. Establish gray level threshold values to separate each ROI paint color from the concrete color.
3. Establish gray level classification ranges for each concrete batch and paint color.
4. Apply thresholding to convert each ROI image into a binary representation.
5. Count black and white pixels to calculate cleaning efficiency.

All image analysis was conducted using ImageJ software, available online for free from the United States' National Institutes of Health (NIH) (National Institutes of Health, 2004). The analysis is based on each pixel of an image so it is a pixel-level analysis. Each ROI has at least 10^6 pixels. The theoretical accuracy of pixel-level can be calculated by 1 pixel/10^6 pixels, which is 10^{-6}. This accuracy is high enough for measurement. Sub-pixel-level accuracy is not necessary for this measurement. In this analysis, the following abbreviations are utilized:

Subscript $_P$: paint,

Subscript $_C$: concrete,

i: ROI # ranging from 1 to 6,

Cj: concrete batch identification where

j = 1 to 4.

Step 1: Determine mean gray level intensities of the ROIs

The RGB (Red-Green-Blue) color photographs of the painted prisms were converted to 8-bit grayscale. Accordingly, the gray level intensity along the face of each prism could vary from a minimum of 0 (black) to a maximum of 255 (white). Figure 4-2

shows the grayscale image and plot of gray level intensity along the length of a typical specimen after painting. The *Set Scale* feature was used to calibrate the length scale in each specimen's photograph using the specimen length measured prior to photographing. Although this step is unnecessary for the image analysis, it was simply used to determine the concentration of pixels of the ROIs. Next, each specimen's ROIs (the concrete color and five paints) were extracted as separate images and saved in TIF format (6 grayscale ROI images per specimen, yielding 36 images). As shown in Table 4-4, the average ROI area was 22.5 cm^2 or 119,665 pixels.

The mean gray level intensities, $\overline{I}_{Pi}$, and standard deviations, σ_{Pi}, of each paint type were calculated using the *Measure* function, then tabulated as shown in Table 4-4. Because water-cement ratio affects the color of concrete, the mean gray level intensity ($\overline{I_{Cj}}$) and standard deviation (σ_{Cj}) were computed separately for each concrete batch. The "darker" paints were considered those whose mean gray level intensity was less than (darker than) that of the concrete batch colors. Thus, the darker paints included Flat Black, Earth Brown, Red Primer, and Army Green. The mean gray level intensity of the Flat White paint was 231, which was greater than (brighter than) that of the concrete batch colors.

The probability density functions (PDFs) were plotted for each concrete batch and each paint color. To statistically account for the color variations in the paints and concrete batches, it was assumed that the overall color range of each ROI was captured within six standard deviations (±3σ) of its mean gray level intensity, as shown in Figure 4-3. Therefore, it was called 3σ. This equates to 99.74% of the area under each PDF. The lower "*L*" bounds of each PDF were calculated using:

$$\text{Concrete: } I_{Cj_L} = \overline{I_{Cj}} - 3\sigma_{Cj} \tag{4-1}$$

$$\text{Paint: } I_{Pi_L} = \overline{I_{Pi}} - 3\sigma_{Pi} \tag{4-2}$$

While the upper "U" bounds were computed using:

$$\text{Concrete: } I_{Cj_U} = \overline{I_{Cj}} + 3\sigma_{Cj} \tag{4-3}$$

$$\text{Paint: } I_{Pi_U} = \overline{I_{Pi}} + 3\sigma_{Pi} \tag{4-4}$$

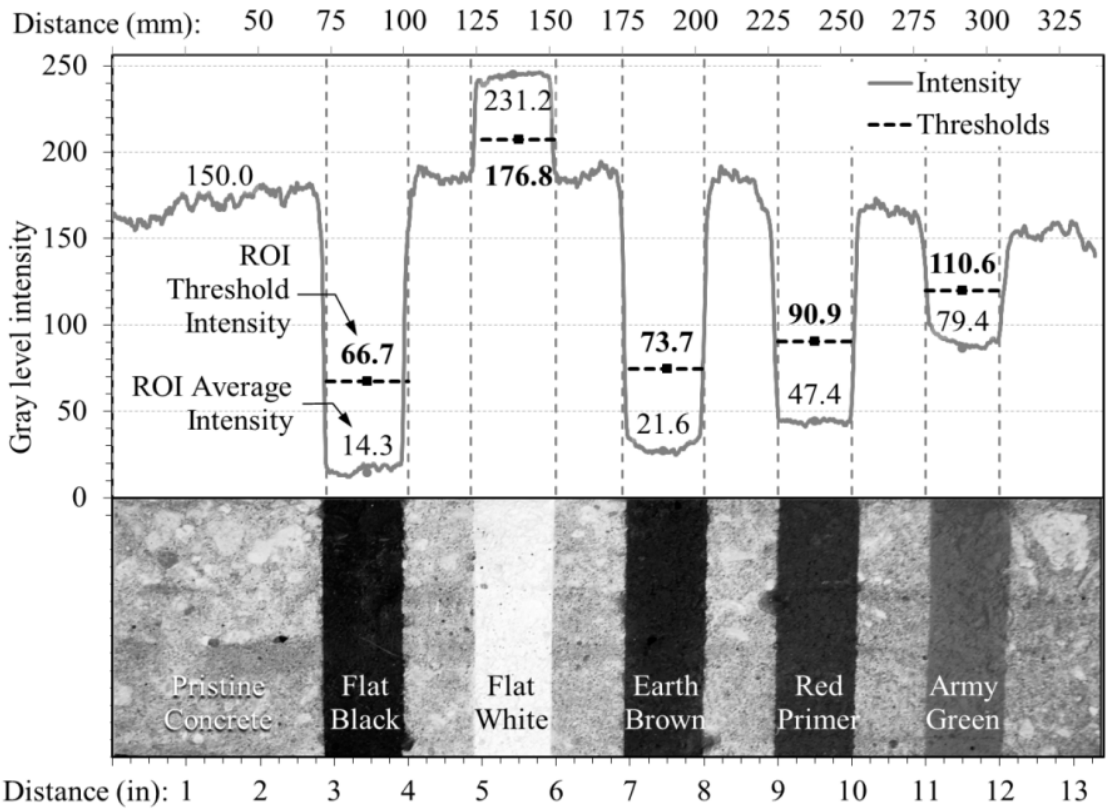

Figure 4-2 Gray level intensity versus distance along prism (prior to cleaning)

Table 4-4 ROI properties and gray level intensity statistics based on 3σ

ROI #, *i*	ROI Color	Average ROI Area			Gray Level Intensity Parameters			
		(pixels)	(cm^2)	(pixels/cm^2)	Mean	St. Dev., σ	Lower Bound	Upper Bound
1	Concrete C1 (*j* =1)	105,034	19.2	5,468	150.0	12.7	111.8	188.2
1	Concrete C2 (*j* =2)	107,488	20.4	5,261	152.3	10.2	121.7	183.0
1	Concrete C3 (*j* =3)	102,316	19.7	5,189	170.8	11.4	136.6	205.0
2	Flat Black	131,364	24.8	5,302	14.3	2.5	6.9	21.6
3	Flat White	131,463	24.8	5,306	231.2	6.7	211.1	251.2
4	Earth Brown	131,050	24.6	5,317	21.6	4.7	7.7	35.6
5	Red Primer	126,224	23.7	5,316	47.4	7.6	24.6	70.1
6	Army Green	122,381	22.8	5,374	79.4	10.0	49.5	109.4
	Average:	119,665	22.5	5,317				

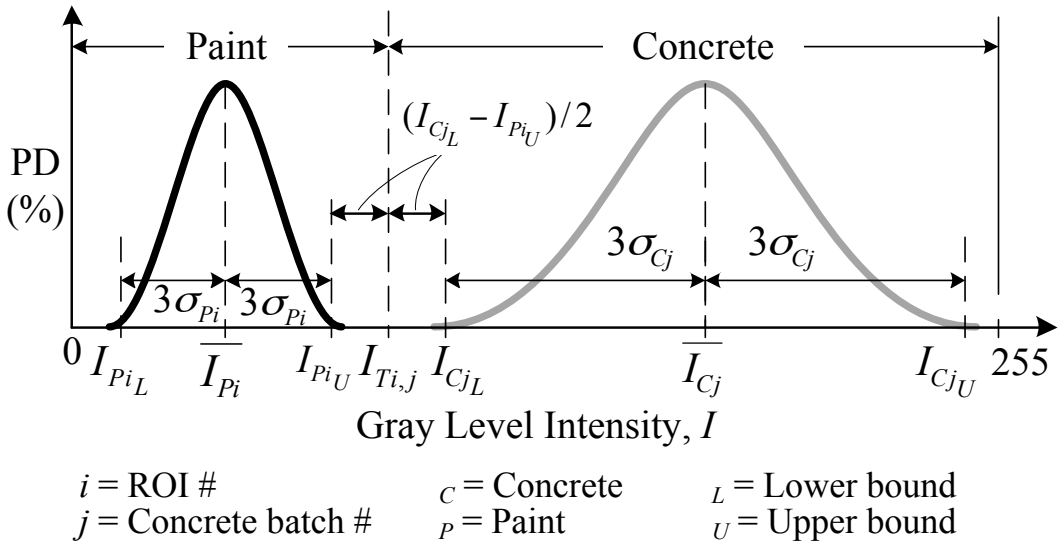

Figure 4-3 Probability density functions (PDFs), identifying thresholds and standard deviations for paint and concrete

Step 2: Establish gray level threshold values to separate each ROI paint color from the concrete color

In the photographs taken after abrasive blasting, it was necessary to numerically classify each pixel as either paint or concrete by defining gray level intensity thresholds, $I_{T\,i,\,j}$. Since each concrete batch had a unique mean gray level intensity, a total of 15

threshold values were calculated to distinguish each concrete batch color from each of the five paint colors. For the darker colored paints, each threshold was calculated as the intensity halfway between the upper bound of the paint PDF (I_{P_U}) and the lower bound of the concrete PDF (I_{C_L}):

$$\text{Dark Paints: } I_{Ti,j} = I_{Pi_U} + \frac{I_{Cj_L} - I_{Pi_U}}{2} \tag{4-5}$$

For the Flat White paint (ROI #3, $i = 3$), the PDF distribution was to the right of the concrete PDF shown earlier in Figure 4-3. Hence, the threshold was calculated as:

$$\text{White Paint: } I_{Ti,j} = I_{T3,j} = I_{Cj_U} + \frac{I_{P3_L} - I_{Cj_U}}{2} \tag{4-6}$$

Step 3: Establish gray level classification ranges for each concrete batch and paint color

The mean gray level intensities for the dark paint colors (ROI #2, 4, 5, 6; all except Flat White) were lower than those of the four concrete batch colors. Therefore, it is assumed that pixels with an intensity less (darker) than the threshold, $I_{Ti,j}$ represent paint, while those pixels with an intensity greater (brighter) than the threshold represent concrete. For classifying dark paints, the threshold intensity computed from Equation (2-17) represents the upper limit of the paint range, while the lower limit equals 0 (pure black). The classification ranges become:

$$\text{Dark Paints: } \underbrace{[0, I_{Ti,j}]}_{\text{Paint Range}} \quad \text{and} \quad \underbrace{[I_{Ti,j}, 255]}_{\text{Concrete Range}} \tag{4-7}$$

Next, consider the lighter paint color of ROI #3 (Flat White). Pixels with an intensity greater (brighter) than the threshold, $I_{T3,j}$, are assumed to represent white paint,

while those pixels with an intensity less (darker) than the threshold represent concrete. The classification ranges become:

$$\text{White Paint:} \quad \underbrace{[0, I_{T3,j}]}_{\text{Concrete Range}} \quad \text{and} \quad \underbrace{[I_{T3,j}, 255]}_{\text{Paint Range}} \tag{4-8}$$

The classification ranges for the five paint colors within each of the three batches are compiled in Table 4-5.

Table 4-5 Gray level thresholds and classification range for binary conversion based on 3σ

ROI # i	Concrete:	C1	C2	C3	C1	C2	C3
	j:	1	2	3	1	2	3
	Paint	Threshold, I_{Tij}			Gray Level Classification Ranges for Paints		
2	Flat Black	66.7	71.7	79.1	[0, 66.7]	[0, 71.7]	[0, 79.1]
3	Flat White	176.8	168.9	201.9	[176.8, 255]	[168.9, 255]	[201.9, 255]
4	Earth Brown	73.7	78.6	86.1	[0, 73.7]	[0, 78.6]	[0, 86.1]
5	Red Primer	90.9	95.9	103.4	[0, 90.9]	[0, 95.9]	[0, 103.4]
6	Army Green	110.6	115.5	123.0	[0, 110.6]	[0, 115.5]	[0, 123]

Step 4: Apply thresholding to convert each ROI image into a binary representation

For any pixel, p, in an ROI image, its gray level intensity (I_p) was evaluated for binary conversion based on the classification ranges determined in the previous step. Pixels with an intensity less (darker) than the threshold were converted to black ($I_{p\,Bin} = 0$), while pixels with an intensity equal to or greater (lighter) than the threshold were converted to white ($I_{p\,Bin} = 1$). The conditional statements used in the algorithm were:

$$\text{Dark Paints: } I_{p\,Bin} = \begin{cases} 0 & \text{if } 0 < I_p < I_{Ti,j} \Rightarrow \text{[Paint range]} \\ 1 & \text{if } I_p \geq I_{Ti,j} \Rightarrow \text{[Concrete range]} \end{cases} \quad (4\text{-}9)$$

$$\text{White Paint: } I_{p\,Bin} = \begin{cases} 0 & \text{if } 0 < I_p < I_{T3,j} \Rightarrow \text{[Concrete range]} \\ 1 & \text{if } I_p \geq I_{T3,j} \Rightarrow \text{[Paint range]} \end{cases} \quad (4\text{-}10)$$

Figure 4-4 shows the binary conversion of the ROI images for specimen C3-2, including the gray level intensity histograms. The vertical dashed lines in each ROI histogram correspond to the thresholds calculated earlier using Equation (4-5) and (4-6). To the left and right of each histogram are the RGB and binary image representations, respectively.

Figure 4-4 Image analysis example for Earth Brown paint on C3-2

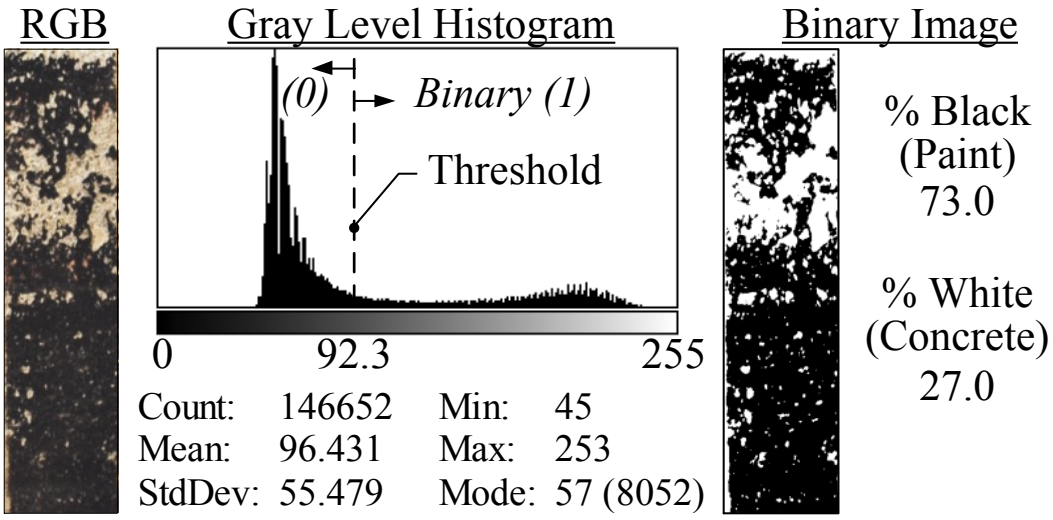

Step 5: Count black and white pixels to calculate cleaning efficiency

For each binary ROI image, the *Overlay.size* function in ImageJ was used to count the black and white pixels. The relative amounts of pixels were used to determine the paint removal effectiveness as shown in equations (4-11) and (4-12).

$$\text{Dark Paints: } e_{Clean} = \frac{Count[I_{p\ Bin=1}]}{Count[I_{p\ Bin=0}] + Count[I_{p\ Bin=1}]} \tag{4-11}$$

$$\text{Light Paints: } e_{Clean} = \frac{Count[I_{p\ Bin=0}]}{Count[I_{p\ Bin=0}] + Count[I_{p\ Bin=1}]} \tag{4-12}$$

The arithmetical mean height (or mean surface roughness), S_a, was calculated using ISO 25178-2 (International organization for standards, 2011):

$$S_a = (1/A)\iint_A |Z_k - Z_{mean}|dA \tag{4-13}$$

Where A is the area of the scanned region (μm^2), Z_k is the height or elevation (μm) at each discrete sampling location k, and Z_{mean} is the average of all Z_k measurements over the scanned area.

The mean surface roughness values are shown in Table 4-1. Table 4-4 presents the mean gray level intensities as well as the lower and upper bounds for the five paint colors. Table 4-5 includes the gray level threshold values, $I_{Ti,j}$, and the corresponding classification ranges for binary conversion. Table 4-6 and Figure 4-5 present the cleaning results.

Table 4-6 Image analysis results for cleaning effectiveness based on 3σ

Specimen ID	Cleaning effectiveness, e (%)					
	Flat Black	Flat White	Earth Brown	Red Primer	Army Green	Average
C1-1	20.5	7.9	48.1	24.7	25.5	25.3
C1-2	17.7	5.2	27.6	45.1	29.0	24.9
C2-1	29.7	8.7	22.9	11.1	16.2	17.7
C2-2	3.2	2.4	13.0	15.5	27.7	12.4
C3-1	25.4	8.5	19.7	27.0	33.9	22.9
C3-2	30.0	7.7	24.7	14.2	7.4	16.8

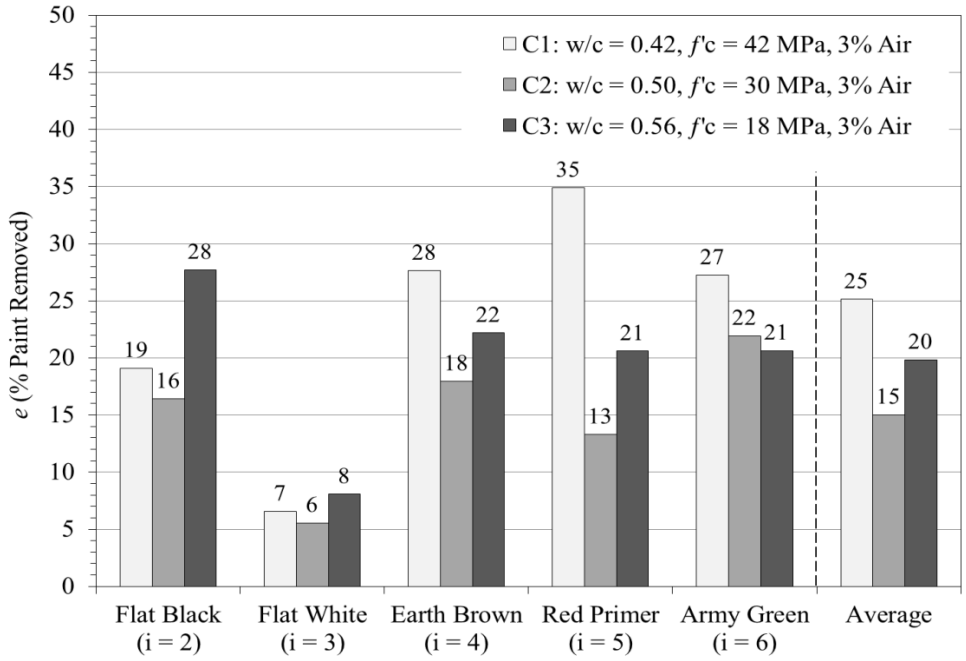

Figure 4-5 Comparison of paint removal efficiency for all concrete batches based on 3σ

4.5.2 Comparison with different threshold values

The threshold value used in this chapter is based on the ±3σ from the mean intensity which is covered by 99.74% area of the PDF. In order to compare the effect of threshold values on the result of the cleaning effectiveness, different threshold values are studied. With 95.44% area of the PDF, there is ±2σ from the mean intensity (shown in Figure 4-6). The threshold values based on 2σ are listed in Table 4-7. The corresponding cleaning effectiveness is shown in Table 4-8. The threshold values based on 1σ (with 68.26% coverage in the PDF) are listed in Table 4-9. The corresponding cleaning effectiveness is shown in Table 4-10. The comparison of cleaning effectiveness for each paint using different threshold values is shown in Figure 4-7 to 4–11. Figure 4-12 compares binary images of C2-1 flat white paint with different threshold values. Figure 4-13 compares binary images of C1-1 red primer with different threshold values.

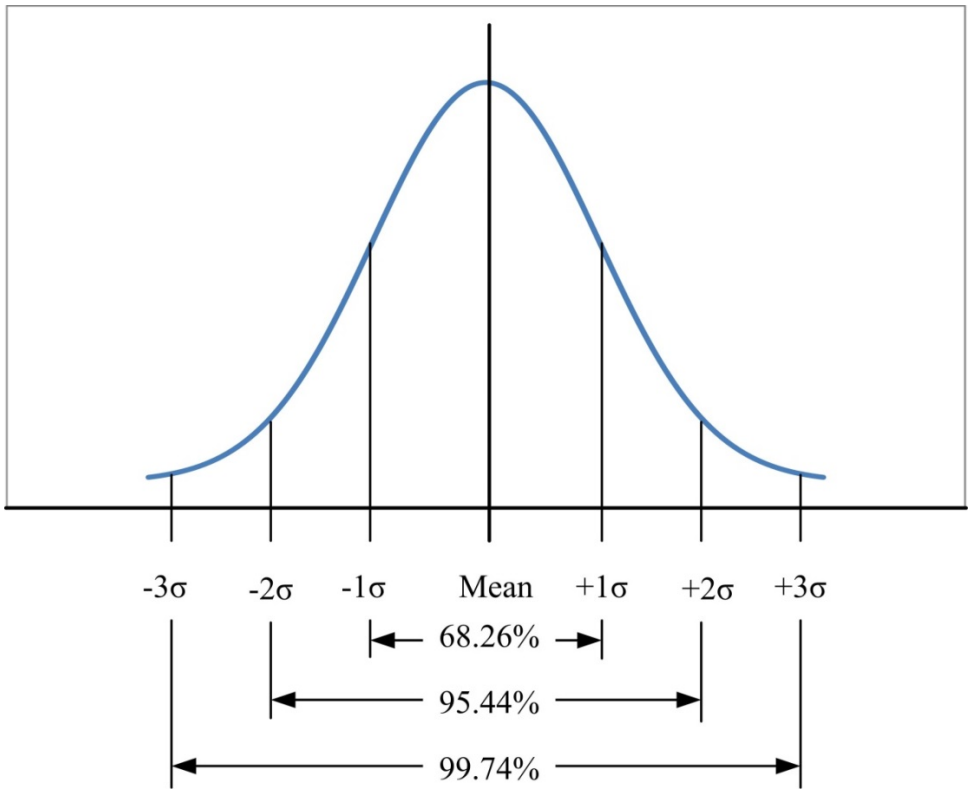

Figure 4-6 Probability density function (PDF) and standard deviations

Table 4-7 Thresholds and classification ranges for binary thresholding based on 2σ

ROI # i	Concrete:	C1	C2	C3	C1	C2	C3
	j :	1	2	3	1	2	3
	Paint	Threshold, I_{Tij}			Gray Level Classification Ranges for Paints		
2	Flat Black	71.8	75.5	83.6	[0, 71.8]	[0, 75.5]	[0, 83.6]
3	Flat White	154.0	150.2	181.5	[154.0, 255]	[150.2, 255]	[181.5, 255]
4	Earth Brown	77.7	81.4	89.5	[0, 77.7]	[0, 81.4]	[0, 89.5]
5	Red Primer	93.5	97.2	105.3	[0, 93.5]	[0, 97.2]	[0, 105.3]
6	Army Green	112.0	115.6	123.7	[0, 112.0]	[0, 115.6]	[0, 123.7]

Table 4-8 Cleaning effectiveness based on 2σ

Specimen ID	Cleaning effectiveness, e (%)					
	Flat Black	Flat White	Earth Brown	Red Primer	Army Green	Average
C1-1	18.8	4.0	46.1	23.2	23.6	23.1
C1-2	16.3	3.9	26.6	43.1	27.7	23.5
C2-1	28.9	4.9	22.5	10.7	16.2	16.6
C2-2	2.9	1.9	12.4	14.9	27.7	12.0
C3-1	24.7	2.9	19.3	26.5	33.9	21.4
C3-2	29.3	3.0	24.3	13.9	7.4	15.6

Table 4-9 Thresholds and classification ranges for binary thresholding based on 1σ

ROI # i	Concrete:	C1	C2	C3	C1	C2	C3
	j:	1	2	3	1	2	3
	Paint	Threshold, I_{Tij}			Gray Level Classification Ranges for Paints		
2	Flat Black	77.0	79.4	88.1	[0, 77.0]	[0, 79.4]	[0, 88.1]
3	Flat White	131.9	131.6	161.1	[131.9, 255]	[131.6, 255]	[161.1, 255]
4	Earth Brown	81.8	84.2	92.9	[0, 81.8]	[0, 84.2]	[0, 92.9]
5	Red Primer	96.1	98.5	107.2	[0, 96.1]	[0, 98.5]	[0, 107.2]
6	Army Green	113.3	115.8	124.4	[0, 113.3]	[0, 115.8]	[0, 124.4]

Table 4-10 Cleaning effectiveness based on 1σ

Specimen ID	Cleaning effectiveness, e (%)					
	Flat Black	Flat White	Earth Brown	Red Primer	Army Green	Average
C1-1	17.1	2.1	44.2	21.8	22.9	21.6
C1-2	14.8	3.0	25.7	41.2	27.0	22.3
C2-1	28.2	2.8	22.1	10.5	16.2	16.0
C2-2	2.6	1.5	11.8	14.7	27.7	11.7
C3-1	23.9	1.2	18.9	26.0	33.4	20.7
C3-2	28.5	1.3	23.9	13.6	7.3	14.9

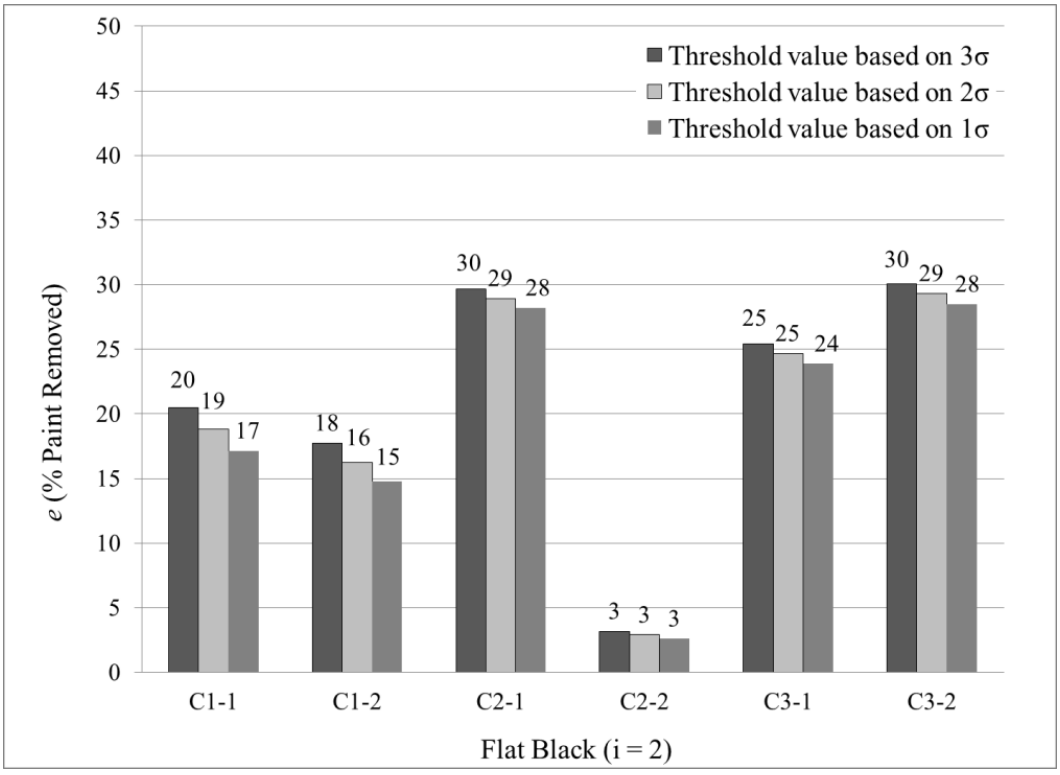

Figure 4-7 Comparison of flat black cleaning effectiveness with different threshold values

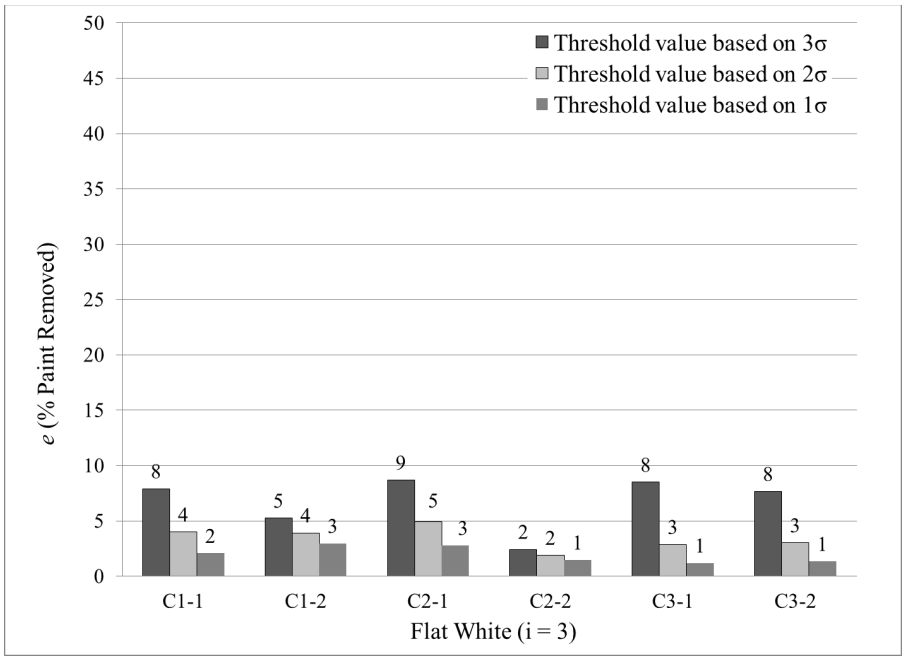

Figure 4-8 Comparison of flat white cleaning effectiveness with different threshold values

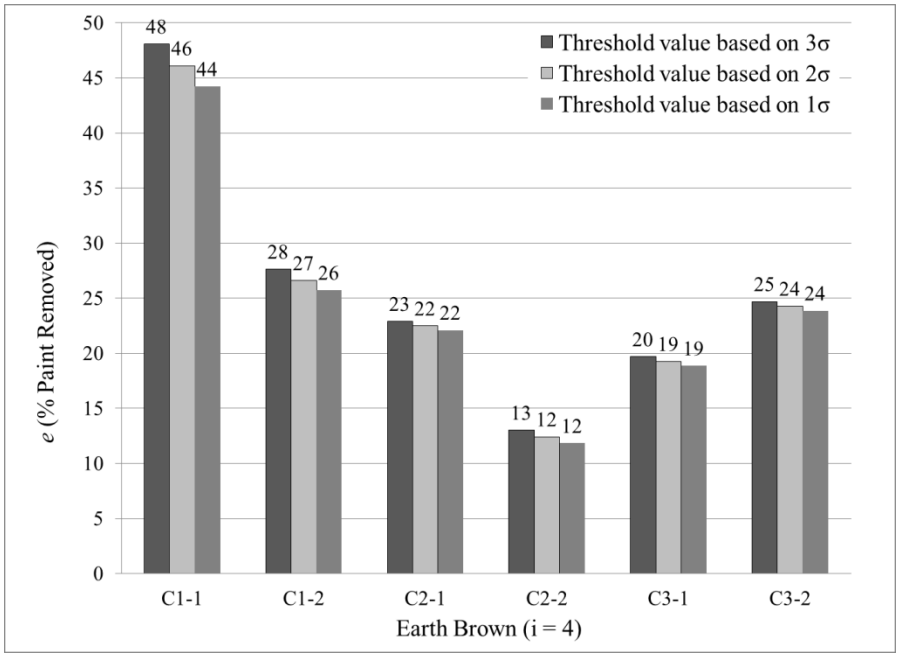

Figure 4-9 Comparison of earth brown cleaning effectiveness with different threshold values

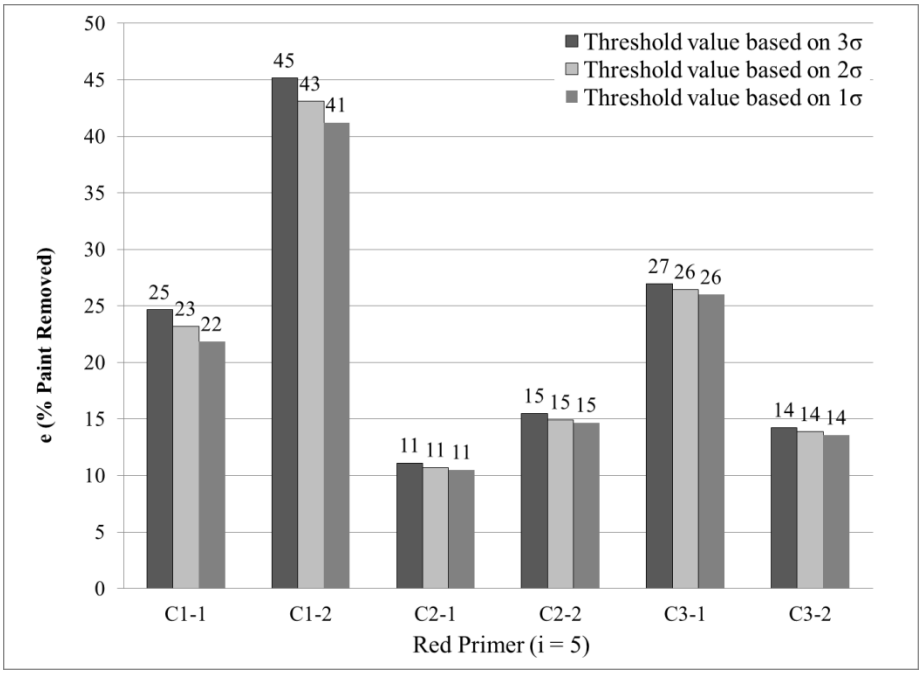

Figure 4-10 Comparison of red primer cleaning effectiveness with different threshold values

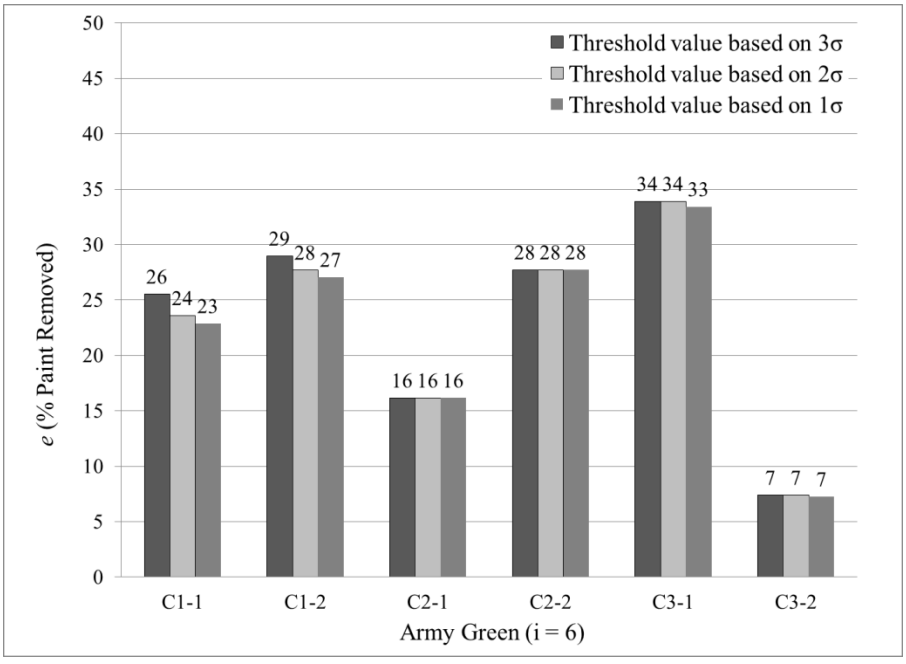

Figure 4-11 Comparison of army green cleaning effectiveness with different threshold values

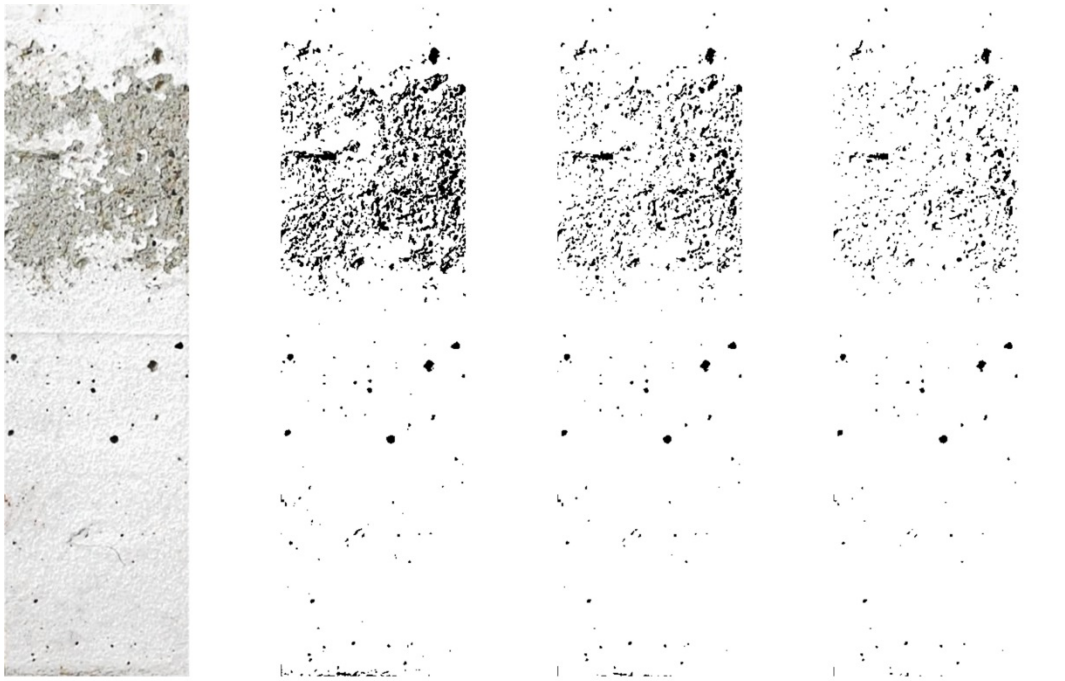

Figure 4-12 Binary image of the white paint ROI of C2-1

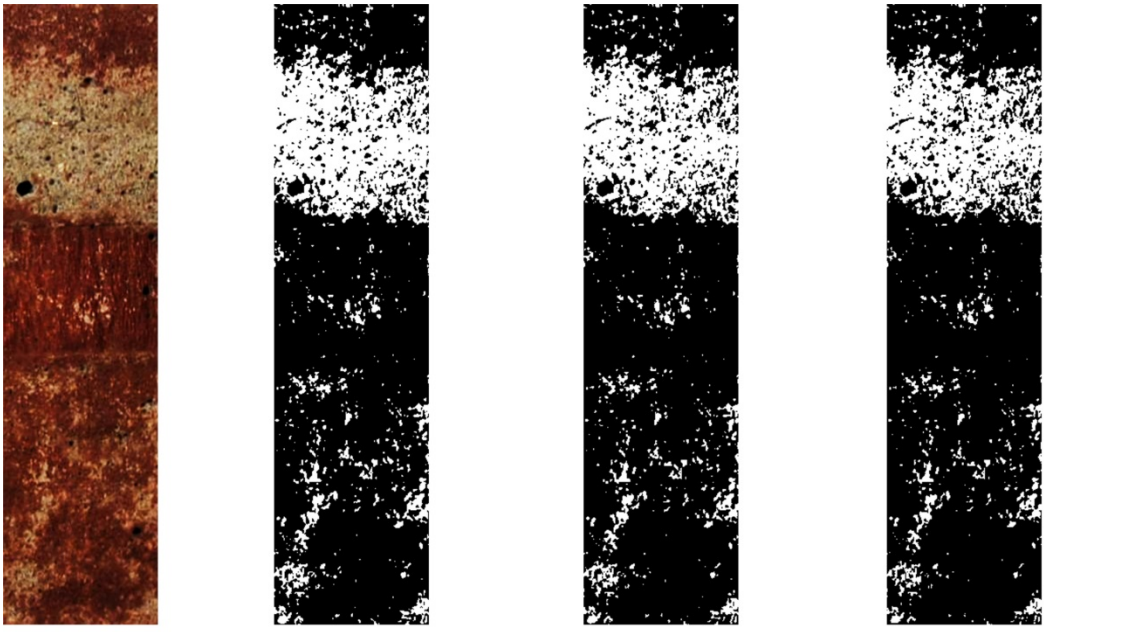

A

Figure 4-13 Binary image of the red primer paint ROI of C1-1

4.5.3 Threshold selection by gray levels of boundary

The threshold values calculated in the previous section are the histogram-based, which is based on the histogram of the whole image or image selection to determine the threshold value. In this section, another threshold selection method is studied: gray levels of the boundary (edge between paint and concrete). This method selects the threshold values based on the gray intensity of the boundary in the digital image.

The edge pixels in the digital images have a phenomenon called "double responding" (Wang & Bai, 2003). This is because edge pixels come from two parts: one belongs to the object and has a similar gray intensity as the object; the other belongs to the background and has a similar gray intensity as the background. Therefore, edge pixels of an object in the digital images have two peaks in the histogram. One peak represents the gray intensity of the object and another represents the gray intensity of the background. The histogram of the true boundary (subpixel edge) falls between these two peaks, shown in Figure 4-14. By finding the gray intensity of the true boundary, the threshold value can be determined. Since the threshold value of this method is based on the gray intensity of the edge, it is called an edge-based threshold value selection method.

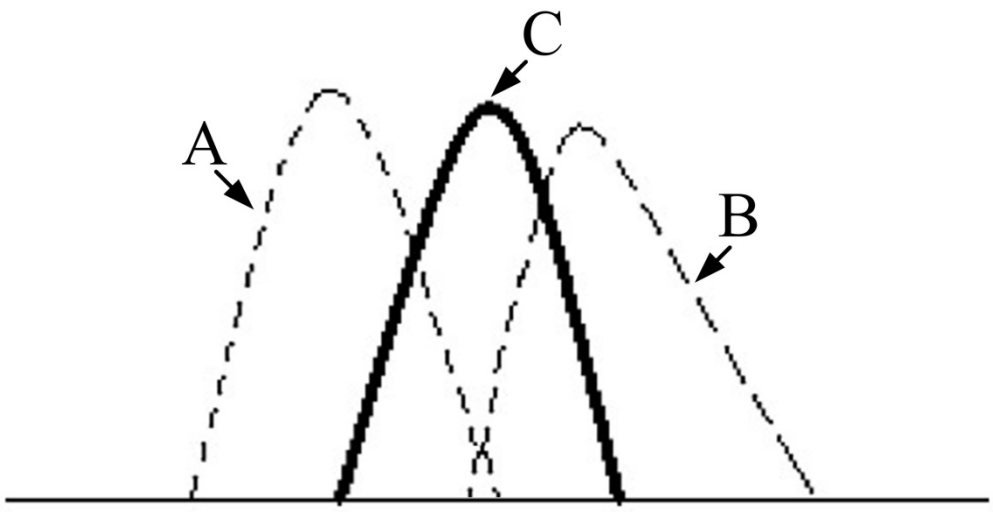

Figure 4-14 Histogram of gray intensity of the true boundary (peak C) and histogram of "double-responding" edge points (peak A and peak B) (Wang & Bai, 2003)

Since the digital images in this study only contain paint and concrete, the gray intensity of the real edge is selected as the threshold value. The Gaussian fitting method introduced in Chapter 3 is used here to find the real edge (subpixel-level) and then an interpolation method is used to find the gray intensity of the real edge. The analysis process for the gray levels of this boundary method is as follows:

Step 1: Use the Gaussian fitting method to find the real edge of the paint.

Crop the images so each paint and some of the concrete surface are visible and then covert the RGB image to 8-bit gray scale format, which contains 256 gray intensities. For each ROI, observe the images and select an area with a clear edge between the paint and concrete, as shown in Figure 4-15. Use the Gaussian fitting method, which is introduced in Chapter 3, to find the real (subpixel) edge of this area.

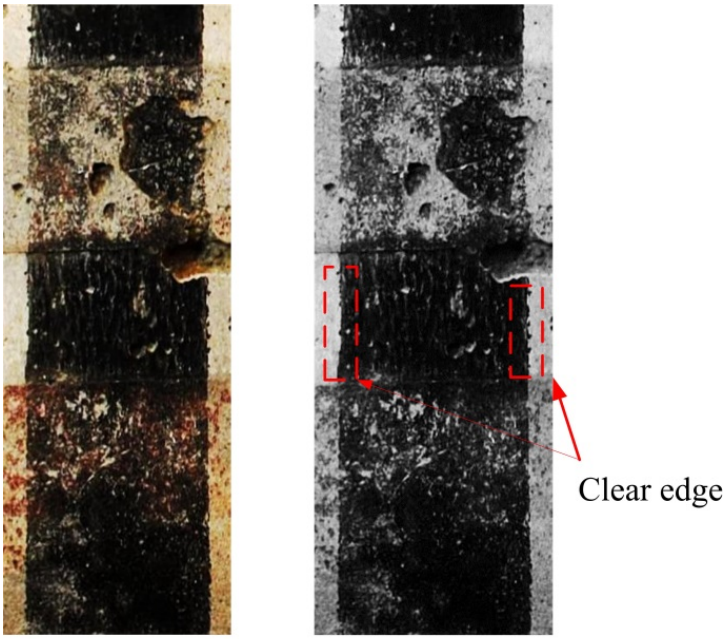

Figure 4-15 RGB and gray image of C1-1

Step 2: Find the gray intensity of the true edge by the spline interpolation method.

In reality, the subpixel edge is not located at a discrete pixel, but between the existing pixels. Therefore, the corresponding gray intensity of the true edge cannot be found directly from a digital image. The pixels near the edge are used to find the gray intensity, as shown in Figure 4-16. Eight pixels near the edge (four on each side) are selected for the interpolation. Spline interpolation is used to find the gray intensity of the true edge.

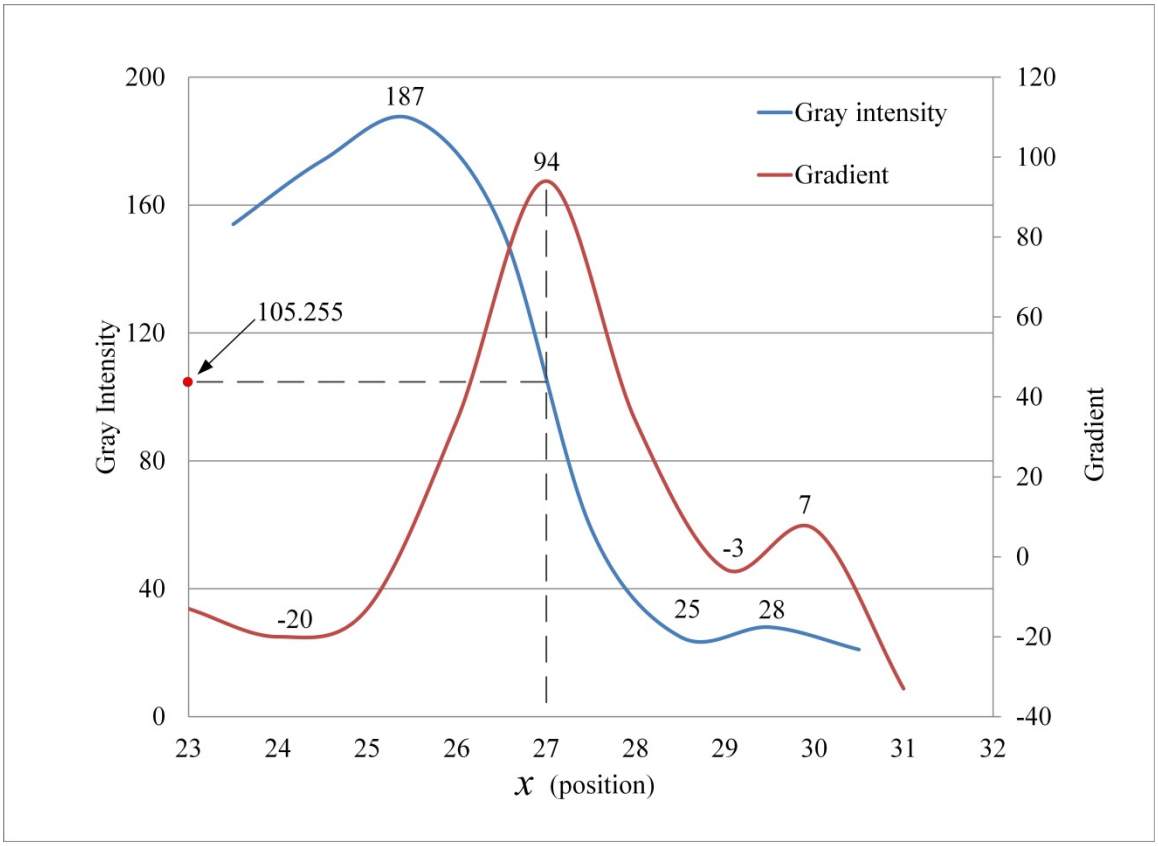

Figure 4-16 Gradient and gray intensity around the edge for flat black

Step 3: The gray intensity of the true edge is the threshold value.

Repeat steps 1 and 2 to find more edge locations on more rows and the corresponding gray intensities. The average of these gray intensities is the threshold value. The threshold value for each concrete and paint is listed in Table 4-11.

Table 4-11 Threshold values based on the gray levels of boundary

ROI # i	Concrete:	C1		C2		C3	
	j:	1	2	1	2	1	2
	Paint	Threshold, I_{Tij}					
2	Flat Black	106.1	106.3	99.4	86.7	113.9	114.7
3	Flat White	205.8	208.0	193.3	184.4	209.6	224.4
4	Earth Brown	84.4	109.9	80.7	107.3	106.4	103.4
5	Red Primer	98.6	121.6	80.6	122.9	110.9	107.9
6	Army Green	101.6	115.3	102.8	123.9	117.2	105.1

The cleaning effectiveness of each concrete specimen is based on the gray levels of the boundary as shown in Table 4-12.

Table 4-12 Cleaning effectiveness based on the gray levels of boundary

Specimen ID	Cleaning effectiveness, e (%)					
	Flat Black	Flat White	Earth Brown	Red Primer	Army Green	Average
C1-1	10.2	15.0	42.8	20.9	33.4	24.5
C1-2	9.2	8.8	19.3	28.4	25.6	18.3
C2-1	25.1	17.2	22.5	14.6	21.0	20.1
C2-2	2.1	3.2	8.7	9.3	22.1	9.1
C3-1	20.4	14.7	17.2	25.1	37.0	22.9
C3-2	24.9	19.3	22.5	13.4	10.8	18.2

4.5.4 Comparison of the two threshold selection methods

The comparison of the two studied threshold selection methods for each paint is shown in Figures 4-17 to 4-21. Figure 4-22 compares binary images of C2-1 white paint with different threshold values. Figure 4-23 compares binary images of C1-1 red primer with different threshold values.

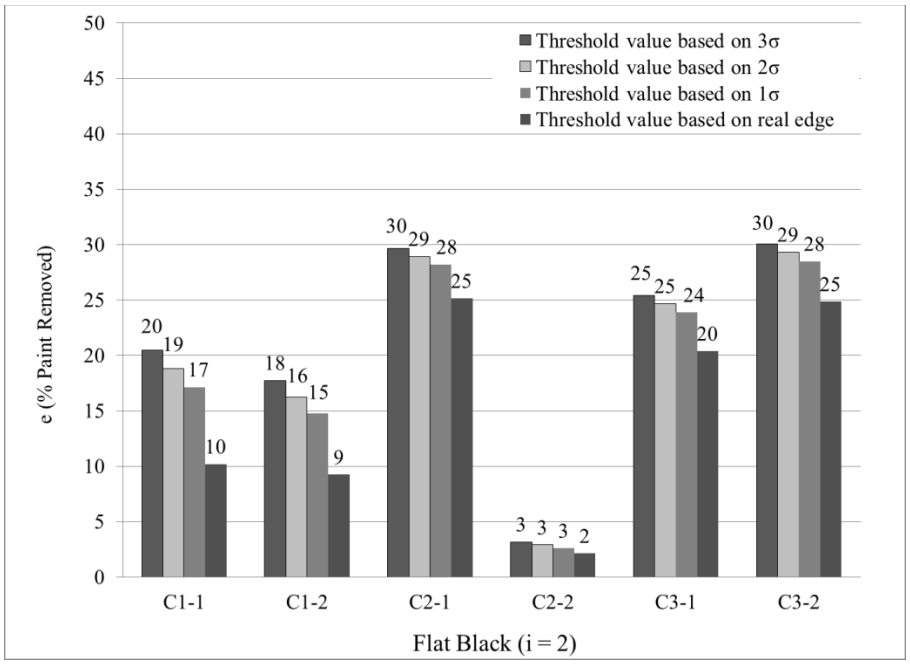

Figure 4-17 Comparison of flat black cleaning effectiveness with different threshold values

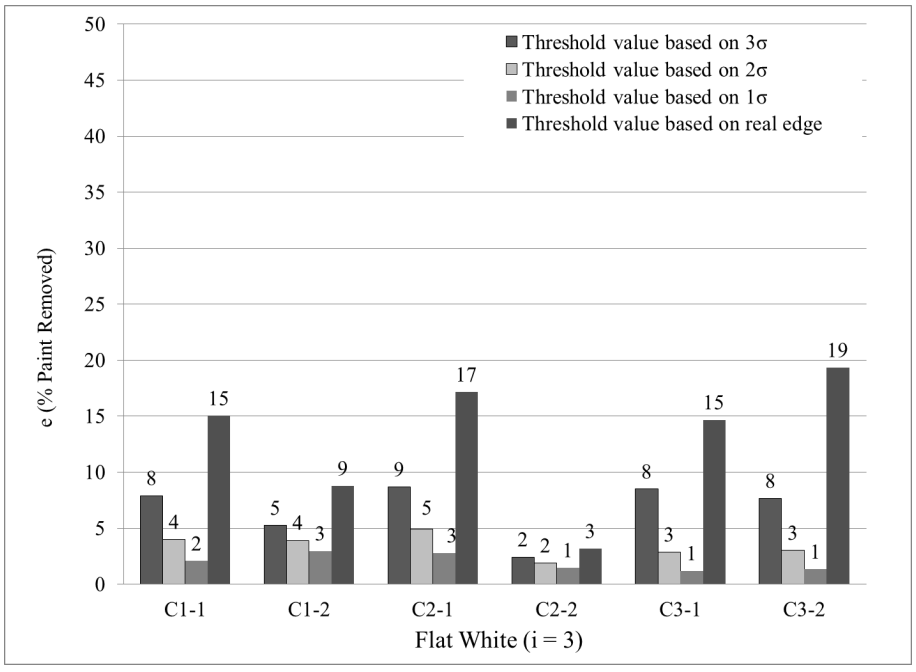

Figure 4-18 Comparison of flat white cleaning effectiveness with different threshold values

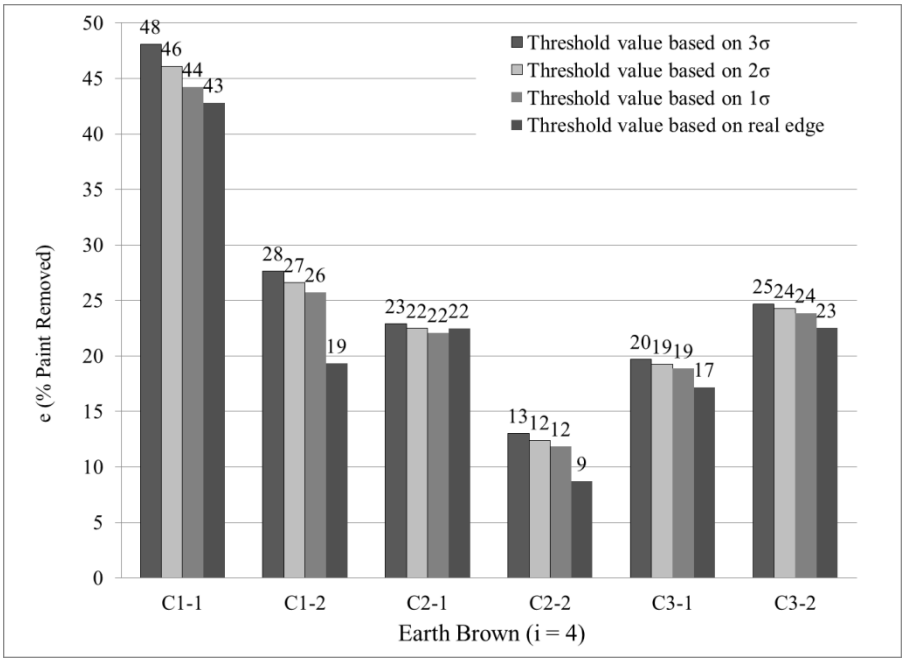

Figure 4-19 Comparison of earth brown cleaning effectiveness with different threshold values

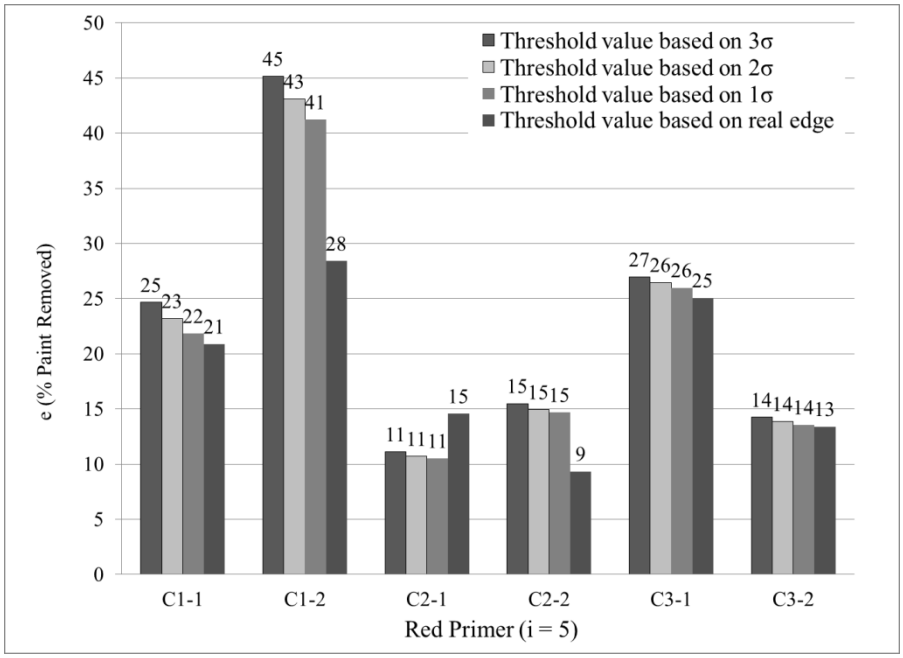

Figure 4-20 Comparison of red primer cleaning effectiveness with different threshold values

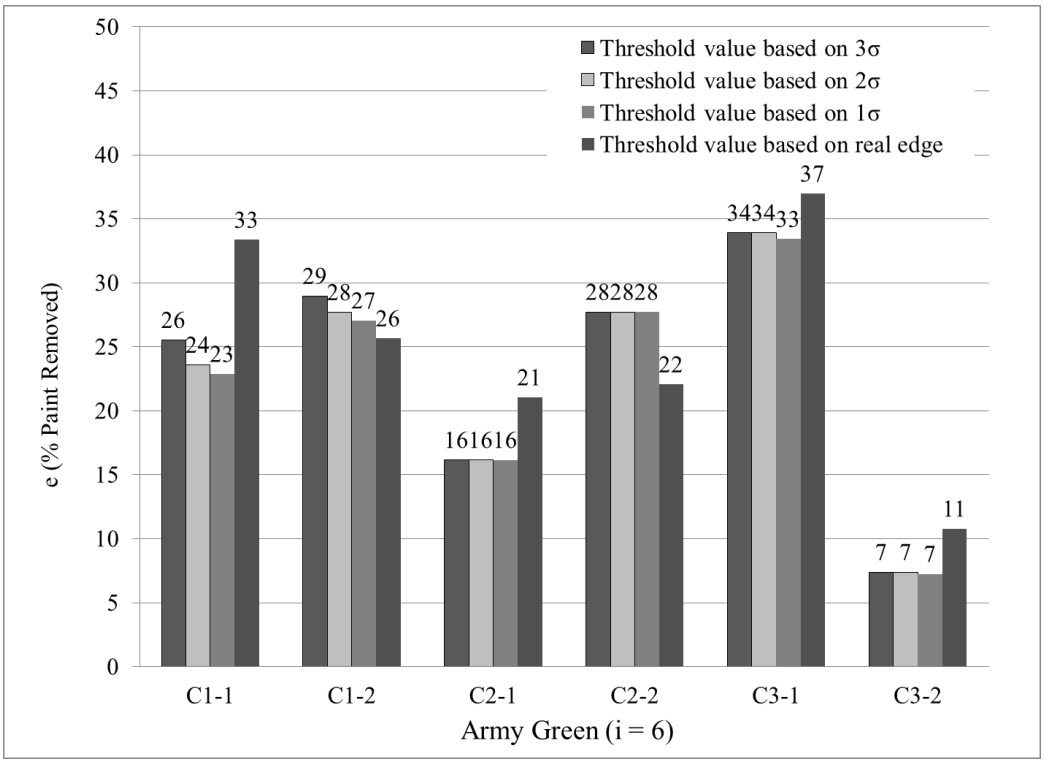

Figure 4-21 Comparison of army green cleaning effectiveness with different threshold values

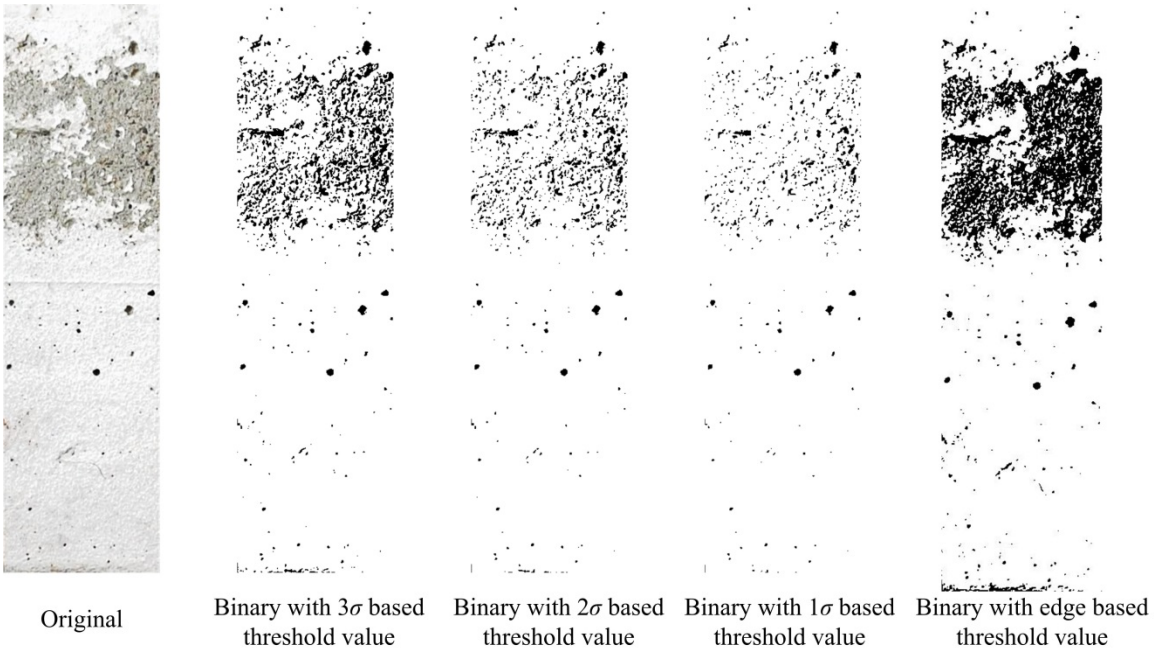

Figure 4-22 Binary image of white paint of C2-1 with different threshold values

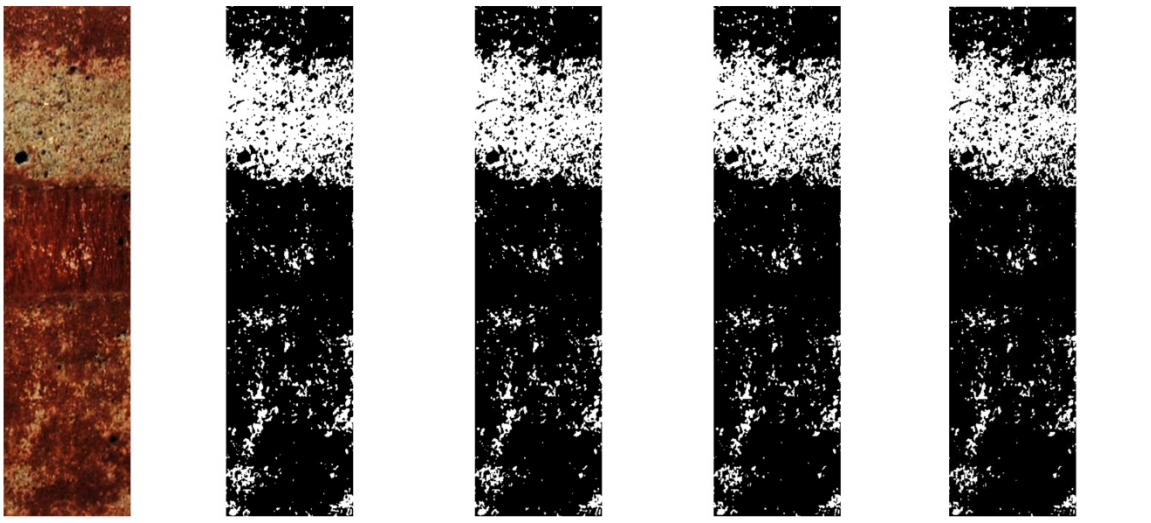

Figure 4-23 Binary image of red primer of C1-1 with different threshold values

4.6 Discussion

4.6.1 Baseline color measurements

The mean gray level intensities of the three concrete batches (C1 through C3) were 150.0, 152.3, and 170.8, respectively. In all three batches, the relative quantities of water, cement, coarse aggregate, and sand remained nearly equal to 10, 20, 31.5,and 37.5% respectively. Although the mix designs had nearly the same proportions, it is well known that slight differences in *w/c* ratio can produce color differences in the concrete. As expected, the lowest *w/c* ratio (0.42 for C1) had the darkest mean intensity (150.0), while the highest *w/c* ratio (0.56 for C3) had the brightest mean intensity (170.8). To simplify the analysis, one could consider using an average gray level intensity of all three concrete batches in lieu of three individual values. However, the aforementioned results demonstrate the sensitivity of the color to changes in *w/c* ratio. Accordingly, three mean intensities were used (Table 4-4).

Although the lighting conditions were held constant in this study, slight variations in lighting would not be expected to substantially change the threshold values of the darker paints since their gray scale intensities differed greatly from that of the pristine concrete. However, increasing the lighting intensity could produce reflections from lighter paints such as the Flat White.

4.6.2 Surface roughness and paint thickness

The average surface roughness, S_a, of all specimens in this study was 0.14 mm, which is relatively smooth. For comparison purposes, the typical surface roughness of sandblasted concrete is 0.70 mm. The typical paint thickness determined using scanning electron micrographs was approximately 1 μm.

4.6.3 Effect of histogram-based threshold value

As expected, the threshold value for each paint is decreased since the confidence interval of the PDF is narrower. As the confidence of the PDF decreases from 99.74% to 95.44% and 68.26%, the gray level classification ranges for the paints become larger (e.g. C1-1 flat black range changes from [0, 66.7] to [0, 71.8] and [0, 77.0] respectively). This change progressively retains more pixels as paint during the binary process. In other words, the cleaning effectiveness appears lower (e.g. C1-1 flat black clean effectiveness is 20.5% based on 3σ, 18.8% based on 2σ and 17.1% based on 1σ). However, the cleaning effectiveness trend between batches is similar. For example, C1-1 has the highest cleaning effectiveness in earth brown (48.1% based on 3σ , 46.1% based on 2σ and 44.2% based on 1σ), which is unchanged compared to the other paints.

The difference in the cleaning effectiveness (e) is small for dark paints but significant for the white paint. The threshold value of the white paint is very close to the

gray intensity of the concrete. For example, the mean gray level intensity of the concrete C1-1 is 150.0 and the threshold value for white paint is 176.8 based on 3σ, 154.0 based on the 2σ and 131.9 based on 1σ. In this condition, e is sensitive to the threshold value. Observation of the binary images of the white paint with two threshold values helps determine which threshold value better represents the figure of the concrete surface. In this study, the threshold value based on 3σ is the best. For the dark paint, for example C1-1 red primer (Figure 4-13), the changes in threshold values (90.9 based on 3σ, 93.5 based on 2σ, and 96.1 based on 1σ), do not significantly change in the binary images.

4.6.4 Comparison of two different threshold value selection methods

Two threshold value selection methods were introduced: histogram-based and edge-based. The histogram-based threshold value selection uses the gray intensity distribution of the paint and concrete to determine the threshold value. In order to differentiate the gray intensity of the concrete from the paint in ROIs, the average gray intensities of all concrete images are considered. The edge-based method used the gray intensity of the real edge as the threshold value. The object (paint) and background (concrete) are distinguished by the gray intensity of the edge.

Here, the 3σ histogram-based threshold value is used in comparison with the edge-based method. The threshold values for most paints (excluding army green) based on the edge method are larger than the histogram-based method (e.g. the flat black for C1-1 is 106.1 based on the edge, and 66.7 based on the histogram). For the army green, the average threshold values from the edge-based method are 108 for C1, 113 for C2 and 111 for C3. These values are similar to the values from the histogram-based method which are 111 for C1, 116 for C2 and 123 for C3, respectively. The cleaning

effectiveness is lower for the most of the dark paints (excluding army green) and higher for the white paint in the edge-based method.

The threshold value is determined from the boundary of the object and the background. In the histogram of the ROIs, it is difficult to tell the regions of paint and background apart. Therefore, the average gray intensity of many concrete images is used as the baseline in the histogram-based method. Therefore, a batch of concrete has the same threshold value (e.g. the threshold value of flat black for C1-1 and C1-2 is the same, 79.4). The threshold values can be selected using one, two or three standard deviations from the gray intensity distribution in the histogram, giving a similar cleaning effectiveness values.

In the edge-based method, the boundary is found directly. Each image in a batch has a different threshold value (e.g., the threshold value of flat black for C2-1 is 99.4 and C2-2 is 86.7). Since the edge points are located between the paint and concrete, the gray intensities of the edge points are also around the average of the gray intensities of the paint and concrete.

By observing the binary images, histogram-based threshold values are more suitable to use with dark paints and edge-based threshold values are more suitable to use with the white paint. However, the differences are not significant.

4.7 Conclusions

In this study, digital image processing was undertaken to quantify the extent of paint removal from a concrete substrate during abrasive blasting. Statistical analysis of the gray level intensities of the images was used to determine varying thresholds for

subsequent binary conversion. Based on the results and observations made in this study, the following conclusions may be drawn:

It is expected that measuring the extent of paint removal becomes more accurate as the contrast between the concrete and paint colors increase. Accordingly, it may be beneficial if an inert dye is added to the concrete batch during mixing. Judicious selection of the dye color could increase the contrast between the paint and underlying concrete, which would simplify the image analysis and generate more accurate and repeatable results.

With increasing gray level classification ranges for the paint, more pixels are designated as paint are retained during the binary process. The corresponding cleaning effectiveness decreases, but the overall trend remains similar. Comparing the binary images with the original image allows for selection of the best binary image to represent the surface topography, allowing for determination of the corresponding threshold value.

For the histogram-based threshold method, each batch of concrete had the same threshold value for the same paint. For the edge-based threshold method, each image has a different threshold value for the same paint. For the histogram-based method, the threshold value is based on the gray intensity of the paint and concrete, and their standard deviation. For the edge-based method, the threshold value is close to the average of gray intensities of the paint and concrete.

Chapter 5 Comparison of strain measurement techniques for FRCM materials

5.1 Background

In this chapter, five strain measurement techniques for a fabric reinforced cementitious matrix (FRCM) are compared: clip-on extensometry, electrical strain gages, laser extensometry, and two digital images strain measurement techniques. The two digital image strain measurement methods are speckle correlation and rectangle edge detection, which is the novel approach developed during graduate study.

A clip-on extensometer is a contacting, mechanical strain measurement technique. It uses knife-edges directly attached to the specimen to track strain. The gage length of the clip-on extensometer is usually fixed and is not suitable for small and delicate specimens, which can be damaged by the knife-edges.

Electrical strain gages are a disposable strain measurement method. The resistance of the strain gage changes corresponding to the deformation of the specimen. During the test, a strain gage is connected to a quarter-bridge electrical circuit. When the specimen deforms, variation of the electric current can be detected. The electric current change corresponds to the strain.

Laser extensometry is a non-contacting method with high accuracy (resolution of 0.001 mm). A laser extensometer illuminates the specimen surface and receives reflections from two reflective tapes, which are attached to the specimen. The distance between the two reflective tapes is the gage length.

Digital image correlation (DIC) strain measurement techniques are non-contacting, optical methods intended to measure surface deformation. There are two techniques studied in this chapter: speckle image correlation (DIC speckle) and rectangle edge detection. The speckle image method correlates the changes in location of a series of painted surface speckles before and after deformation to determine the displacement field of the surface. The rectangle edge method tracks the length change of a painted surface pattern to quantify the strain.

5.2 Experimental Investigation

5.2.1 Specimen preparation

The test material is a fabric reinforced cementitious matrix (FRCM) (Arboleda, Yuan, Giancaspro, & Nanni, 2013; Arboleda, 2014). The FRCM system consists of two primary materials: a cementitious matrix and a dry fiber network. The matrix is a Portland cement-based mortar system with a small amount (< 5% in weight) of dry polymers. The reinforced fiber network is PBO (polyparaphenylene benzobisoxazole) fabric. The PBO fabric has a 0.046 mm nominal thickness and approximately 5 mm clear spacing in the warp direction, and 0.011 mm nominal thickness and approximately 15 mm clear spacing in the weft direction. The roving spacing is about 10 mm and 20 mm in the warp and weft direction, respectively.

Tensile coupons measuring 500×50×10 mm were cut from larger panels. The larger panels were 410×563 mm, and were manufactured using a manual impregnation technique in a rectangular mold. In this process, a 5 mm thick layer of the cementitious matrix was placed, followed by a layer of the fabric, which was manually wetted with the wet cementitious material. The top layer of matrix was then applied to form the surface

of the specimen. The panels were cured for 28 days at 20°C and 70% relative humidity before cutting. Individual coupons were cut using a diamond-tipped wet saw using a rigid fixture to ensure consistent specimen width. 100×50×2 mm steel tabs were bonded with a polyurethane construction adhesive to each specimen 24 hours prior to testing.

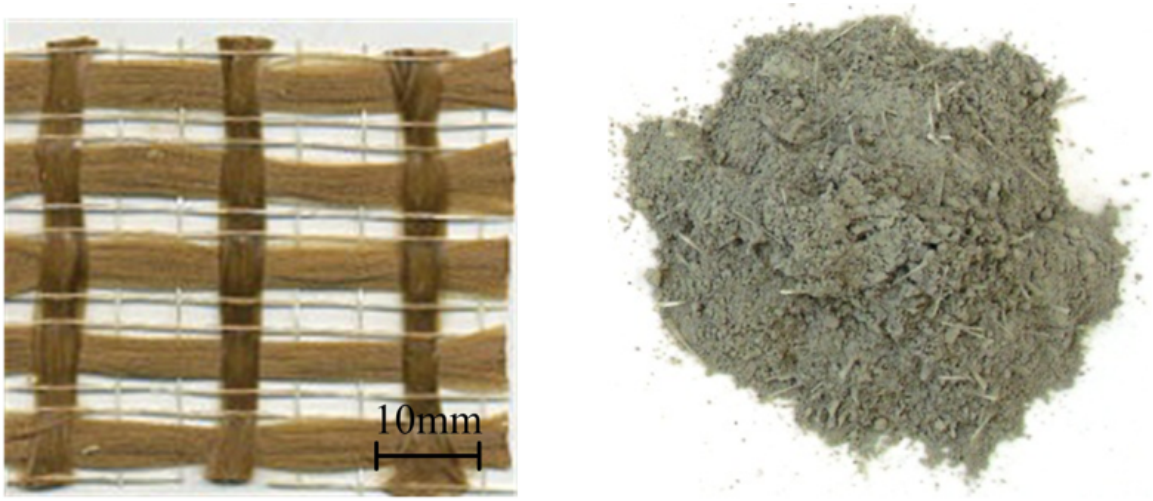

Figure 5-1 PBO- FRCM system: PBO fabric (left), Mortar (right)

5.2.2 Test matrix

Seven specimens were tested using the five strain measurement methods. The instrumentation configuration for each specimen is shown in Table 5-1.

The laser extensometer was used in all seven tests. The strain gages were applied to three specimens (FRCM-1, FRCM-3, and FRCM-4). Four specimens were painted with a rectangle (FRCM-1, FRCM-2, FRCM-3, and DRCM-6) and the other three specimens were painted with speckles. The image of all the specimens are shown in Appendix D. A linear variable differential transformer (LVDT) was used for five specimens (FRCM-1, FRCM-2, FRCM-3, FRCM-4, and FRCM-7) to detect the out-of-plane displacement. The pattern (rectangle and speckles) painting method was previously introduced in Chapter 3.

Table 5-1 Test matrix with instrumentation configuration for each specimen

Specimen name	Laser gage length (mm)	Strain gage length (mm)	Digital image pattern (mm)	LVDT
FRCM-1	102.215	150	Rectangle 101×35	√
FRCM-2	104.346	N/A	Rectangle 55 ×35	√
FRCM-3	196.060	150	Rectangle 55×35	√
FRCM-4	102.700	150	Speckle	√
FRCM-5	105.758	N/A	Speckle	N/A
FRCM-6	104.838	N/A	Rectangle 52×35	N/A
FRCM-7	101.105	N/A	Speckle	√

5.2.3 Test setup

A 49 kN test frame was used to apply the tensile load, which was recorded using a load cell with a 9 kN capacity. A clevis grip set up was used to provide sufficient degrees of freedom in order to minimize secondary moment or torsional loading conditions at the supports due to specimen geometry. The test specimens were aligned with the grips and preloaded to 50 N.

To directly compare the studied strain measurement techniques, the strain measurement devices were strategically arranged as shown in Figure 5-2 The reflective tapes (for the laser extensometer), clip-on extensometer, and the strain gages were arranged on one side of the specimen, while the patterns (speckles or rectangle) were

painted on the other side. For porous surfaces such as concrete, the bleeding edges of the rectangle must be avoided. The rectangle edge detection method uses the Gaussian fitting method to detect the length change of the rectangle to track strain. This method is based on the gradient distribution around the edge represented as a Gaussian distribution. Bleeding creates a blurry localized edge and may change the gradient distribution curve near the edge. White paint is used as a base before the black rectangle is painted, which improves contrast at the edges of the rectangle.

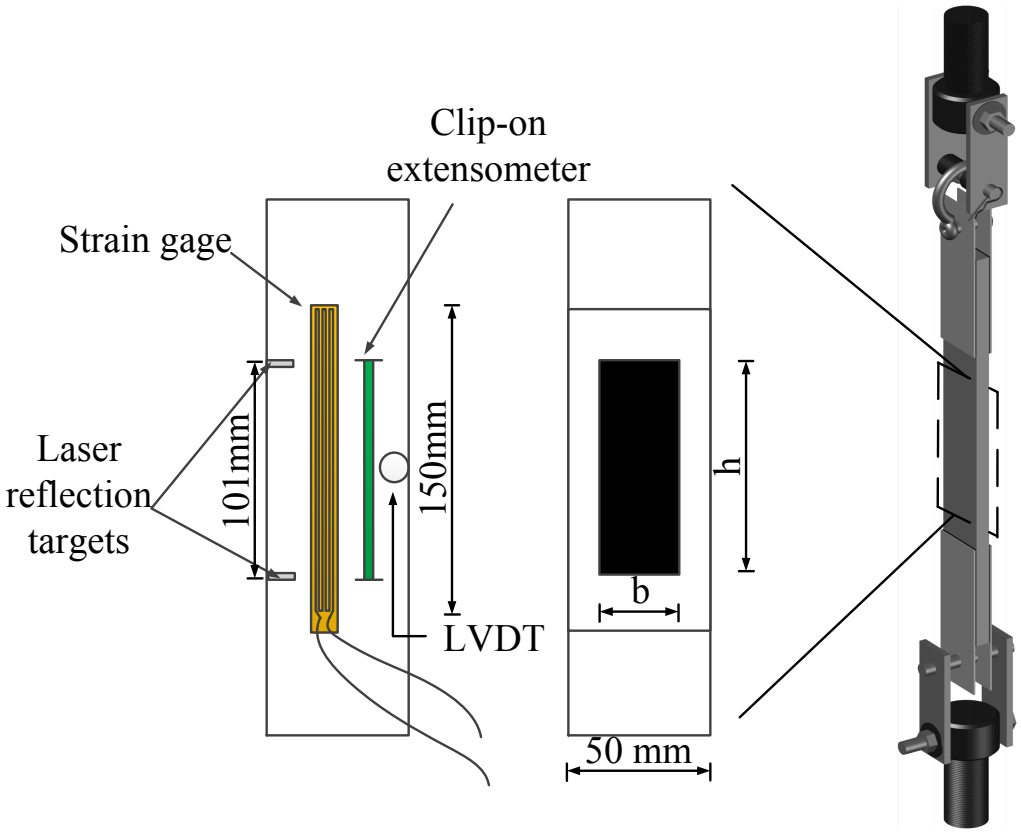

Figure 5-2 Specimen instrumentation set up

The mechanical clip-on extensometer was made by Epsilon with an initial gage length of 101 mm. The clip-on extensometer was mounted directly on the test specimen using knife-edges to measure axial strain. The laser extensometer used in the tension

tests was manufactured by MTS Inc. with a 1/256 frequency setting for data reading. It was mounted on a rigid frame, as shown in Figure 5-3, and directed perpendicular to the specimen at a distance of 300 mm from the specimen face. The two reflective tapes, with a 3 mm width, were attached to the specimen with a gage length of 101 mm. An Omega 240- ohm strain gage with a 150 mm gage length was used in the tension tests. The strain gage was bonded along the axial direction of the specimen and was connected to a quarter-bridge circuit. The models of the devices are listed in Table 5-2.

Table 5-2 Strain measurement devices

Strain measurement device	Manufacturer and model
Mechanical clip-on extensometer	Epsilon, Model: 3542L-0400-050T-ST
Laser extensometer	MTS Inc., Model: LX500
Strain gage	Omega, SGD-150/240-LY40

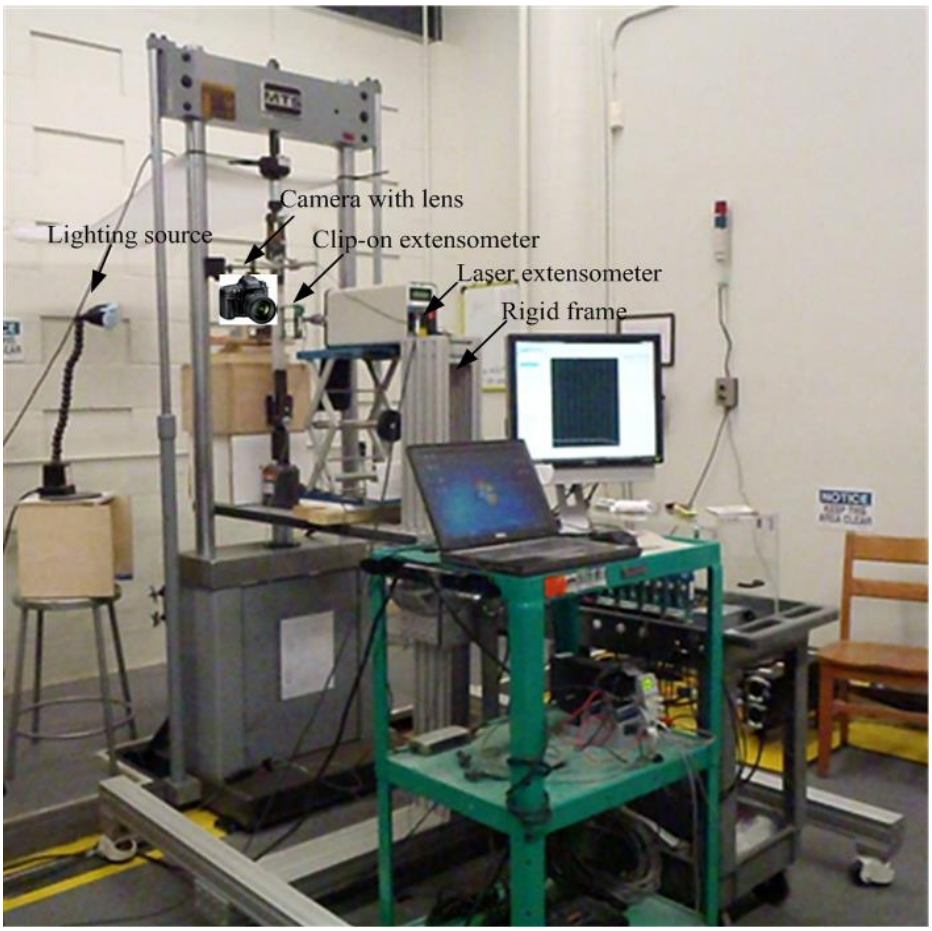

Figure 5-3 Equipment set up

Digital images were recorded using a charge coupled device (CCD) camera with a 40 mm micro lens. The image resolution is 3872×2592 pixels. The camera was mounted on a rigid frame as shown in Figure 5-3, directed at the pattern on the specimen. The camera was calibrated by taking images of a chessboard pattern of known dimensions at many different angles (Zhang 1999). The camera shutter speed and focal ratio for each test is shown in Table 5–3. The parameters in Table 5–3 were previously defined in Chapter 2. Shutter speed and aperture were manually selected based upon the lighting conditions, which were controlled by using a lamp with a 35-Watt bulb supplying 1050 Lumens. In order to ensure a clear photo, the fastest shutter speed was selected based on

the lighting conditions. After executing the first two tests on specimens FRCM-5 and FRCM-6, it was noted that the specimen experienced out-of plane displacement due to specimen curvature. This movement caused loss of focus of the camera, which greatly affected the accuracy of the digital image correlation method. A linear variable differential transformer (LVDT) was added to the test system to record this out-of-plane displacement of the specimen. The LVDT was placed at the midsection of the specimen where the maximum displacement occurred. Positive LVDT data values mean the distance from the specimen to camera decreased and negative LVDT data values mean the distance from the specimen to the camera increased. In order to get clear photos, the camera needed to be kept at a fixed distance from the specimen. Thus, the camera was placed on a movable, frictionless platform resting on stainless steel balls bearing. The platform was connected to the middle of the specimen so it could move freely as the specimen deflected.

Table 5-3 Camera calibration results of internal parameters and camera setting for each specimen

Specimen name	Focal length $f(\alpha, \beta)$ "unitless"	Principal point (μ_0, v_0) "unitless"	Skew coefficient (s) "unitless"	Distortion (kc) "unitless"	Camera shutter speed (sec) and aperture ("unitless")
FRCM-1	[8731.67, 8747.72]	[1951.01, 737.46]	0.00	[-0.23, -0.41, 0.01, 0.01, 0.00]	1/10, *f*/3.2
FRCM-2	[22098.07, 22309.65]	[1400.78, 2700.56]	0.00	[0.52, -2.09, 0.05, -0.03, 0.00]	1/8, *f*/3.2
FRCM-3	[10546.50, 10560.79]	[1401.63, 2026.76]	0.00	[0.29, -1.34, 0.02, -0.02, 0.00]	1/6, *f*/3.3
FRCM-4	[7049.38, 7075.68]	[1792.06, 1402.75]	0.00	[-0.11, 0.53, 0.00, 0.00, 0.00]	1/40, *f*/3.2
FRCM-5	[9108.08, 9064.18]	[1605.21, 1191.45]	0.00	[-0.45, 9.10, -0.01, -0.01, 0.00]	1/80, *f*/3.2
FRCM-6	[7440.08, 7416.66]	[1541.28, 1407.28]	0.00	[0.06, -0.48, -0.00, -0.00, 0.00]	1/15, *f*/3.2
FRCM-7	[12821.96, 13350.98]	[452.77, 1206.79]	0.00	[-1.26, 4.09, -0.00, 0.11, 0.00]	1/40, *f*/3.2

5.2.4 Test procedure

All the data, including laser extensometer, clip-on extensometer, strain gage, load cell and LVDTs were collected using a data acquisition (DAQ) system. The test was programmed to run under displacement control at a rate of 0.25 mm/min with measurements recorded continuously at a rate of 1 Hz. To synchronize the digital images with the DAQ system, the test was paused every 0.25 mm of crosshead (stroke) displacement to take a series of images for subsequent DIC analysis.

There were five strain measurement methods applied during testing. Three of these, including the clip-on extensometer, laser extensometer and strain gage system were synchronized through the DAQ system. The two digital image methods (speckles and rectangle) collected data during the test and were analyzed for strain measurement after the test was complete. A series of consecutive photos of each specimen were taken during the tension tests. All the photos were undistorted using the intrinsic parameters of the camera to remove any distortion caused by the lens of the camera.

5.3 Analytical methods

The digital images collected from the tests were processed using the Matlab codes introduced in Chapter 3. The specimens with the speckle pattern were processed using the DIC speckle Matlab code. The specimens with the rectangle pattern were processed using the Gaussian fitting subpixel Matlab code. The details of the procedures for these two image analysis methods were introduced in Chapter 3.

5.4 Test results

The data results of all the specimens (FRCM 1 to FRCM 7) are presented in Table 5–4 to Table 5–10. For FRCM-2 and FRCM-6, since there was a large out-of-plane displacement, the digital images from these tests were very blurred. Therefore, the Gaussian fitting method could not be applied, so the rectangle edge detection method failed to provide results for these two specimens. For FRCM-1, FRCM-3, and FRCM-4, the strain gages fail to provide data after several stress increments.

Figure 5-4 to Figure 5-10 shows a comparison between the DIC method (rectangle or speckle) and the other strain measuring methods in a dual axis graph with a stress-strain curve for each axial strain instrument on the primary axis (on the left) and LVDT data for out-of-plane displacement versus strain on the secondary axis (on the right). Positive LVDT data indicates that the distance from the specimen to the camera decreases during testing. Negative LVDT data indicates that the distance from the specimen to the camera increases during testing. For FRCM-5 and FRCM-6, the LVDT was not applied.

Table 5-4 Axial strain test results for FRCM-1

Stress (MPa)	Laser Extensometer $\varepsilon\times10^{-3}$ (mm/mm)	Clip-on Extensometer $\varepsilon\times10^{-3}$ (mm/mm)	Strain Gage $\varepsilon\times10^{-3}$ (mm/mm)	Rectangle edge detection $\varepsilon\times10^{-3}$ (pixel/pixel)
0.00	0.00	0.00	0.00	0.00
0.29	-0.04	-0.14	-0.13	-0.22
0.66	-0.10	-0.26	-0.32	-1.22
0.98	-0.03	-0.31	-0.40	-2.23
1.67	0.18	-0.20	-0.29	-2.77
2.25	0.55	0.34	0.05	-1.25
2.50	1.19	0.91	0.56	-0.06
2.95	2.38	2.00	N/A	0.95
3.02	4.26	3.73	N/A	2.16
3.29	5.13	4.45	N/A	2.44
3.65	5.69	5.08	N/A	2.63
3.96	6.22	5.57	N/A	2.90
4.30	6.59	6.03	N/A	3.30
4.69	7.23	6.68	N/A	3.62
5.01	7.78	7.19	N/A	4.29
5.38	8.46	7.82	N/A	4.66
5.78	9.06	8.43	N/A	4.96
6.12	9.69	8.97	N/A	5.43
6.40	10.16	9.40	N/A	5.79
6.49	10.39	9.50	N/A	5.97
6.65	10.73	9.71	N/A	6.45
6.57	10.74	9.64	N/A	6.38
6.20	10.53	9.45	N/A	6.41

Table 5-5 Axial strain test results for FRCM-2

Stress (MPa)	Laser Extensometer $\varepsilon\times10^{-3}$ (mm/mm)	Clip-on Extensometer $\varepsilon\times10^{-3}$ (mm/mm)	Rectangle edge detection $\varepsilon\times10^{-3}$ (pixel/pixel)
0.00	0.00	0.00	N/A
1.07	0.03	-0.01	N/A
1.93	0.41	0.29	N/A
2.43	0.91	0.86	N/A
2.73	2.52	2.44	N/A
3.07	3.50	3.29	N/A
3.22	3.78	3.66	N/A
3.53	4.23	4.25	N/A
3.84	5.54	5.29	N/A
4.26	6.23	5.90	N/A
4.67	6.87	6.49	N/A
5.03	7.52	6.97	N/A
5.42	8.05	7.48	N/A
5.78	8.67	7.95	N/A
6.08	9.12	8.31	N/A
6.36	9.53	8.66	N/A
6.55	9.83	8.89	N/A
6.63	10.14	9.03	N/A
6.59	10.41	9.05	N/A
6.06	10.47	8.77	N/A

Table 5-6 Axial strain test results for FRCM-3

Stress (MPa)	Laser Extensometer $\varepsilon\times10^{-3}$ (mm/mm)	Clip-on Extensometer $\varepsilon\times10^{-3}$ (mm/mm)	Strain Gage $\varepsilon\times10^{-3}$ (mm/mm)	Rectangle edge detection $\varepsilon\times10^{-3}$ (pixel/pixel)
0.00	0.00	0.00	0.00	0.00
0.54	-0.06	-0.10	-0.11	0.96
0.99	-0.12	-0.25	-0.26	1.73
1.40	-0.07	-0.24	-0.26	0.52
1.92	0.07	-0.14	-0.16	-1.41
2.52	0.53	0.18	0.17	-3.77
2.81	1.49	1.18	N/A	-6.84
3.16	2.29	2.08	N/A	-8.86
3.47	3.19	3.33	N/A	-9.83
3.68	4.31	4.19	N/A	-7.25
3.93	5.07	4.80	N/A	-5.14
4.27	5.61	5.21	N/A	-2.49
4.57	5.94	5.63	N/A	-1.01
4.92	6.38	6.03	N/A	-0.19
5.14	6.68	6.36	N/A	0.26
5.33	7.02	6.75	N/A	0.69
5.61	7.39	7.15	N/A	0.94
5.89	7.67	7.50	N/A	1.79
6.16	8.01	7.87	N/A	2.82
6.37	8.27	8.09	N/A	3.07
6.59	8.51	8.40	N/A	3.92
6.64	8.58	8.64	N/A	4.19
6.75	8.59	8.75	N/A	4.29
6.74	8.55	8.81	N/A	4.08
5.83	8.05	8.57	N/A	2.44
3.56	6.34	7.16	N/A	-1.40

Table 5-7 Axial strain test results for FRCM-4

Stress (MPa)	Laser Extensometer $\varepsilon\times10^{-3}$ (mm/mm)	Clip-on Extensometer $\varepsilon\times10^{-3}$ (mm/mm)	Strain Gage $\varepsilon\times10^{-3}$ (mm/mm)	DIC Speckle $\varepsilon\times10^{-3}$ (pixel/pixel)
0.00	0	0	0	0
0.57	-0.1	-0.1	-0.21	0.03
1.23	-0.13	-0.13	-0.22	0.23
2.61	0.41	0.41	0.3	1.36
3.02	0.89	0.89	N/A	5.38
3.08	2.84	2.84	N/A	6.19
3.49	4.46	4.46	N/A	6.72
3.24	5.27	5.27	N/A	7.17
3.75	5.11	5.11	N/A	7.99
4.24	5.51	5.51	N/A	8.67
4.68	6.04	6.04	N/A	9.33
5.10	6.74	6.74	N/A	9.99
5.46	7.52	7.52	N/A	10.65
5.91	8.27	8.27	N/A	11.22
6.33	9.08	9.08	N/A	11.77
6.69	9.68	9.68	N/A	12.27
6.99	10.13	10.13	N/A	12.64
7.26	10.48	10.48	N/A	12.93
7.35	10.63	10.63	N/A	13.23
7.31	10.59	10.59	N/A	13.3
6.89	10.19	10.19	N/A	14.67
5.70	8.94	8.94	N/A	15.64
4.52	8.11	8.11	N/A	16.42

Table 5-8 Axial strain test results for FRCM-5

Stress (MPa)	Laser Extensometer $\varepsilon\times10^{-3}$ (mm/mm)	Clip-on Extensometer $\varepsilon\times10^{-3}$ (mm/mm)	DIC Speckle $\varepsilon\times10^{-3}$ (pixel/pixel)
0.00	0.07	0.00	0.00
1.29	0.30	0.12	0.65
2.22	0.71	0.43	4.32
2.59	2.01	1.49	8.01
2.91	3.76	2.74	8.76
3.15	4.47	3.41	11.14
3.47	5.11	4.11	12.03
3.38	5.00	4.37	12.03
3.74	4.98	4.47	13.50
4.05	5.27	4.92	15.06
4.18	5.46	5.17	15.16
4.53	5.81	5.60	16.98
4.83	6.26	6.11	17.58

Table 5-9 Axial strain test results for FRCM-6

Stress (MPa)	Laser Extensometer $\varepsilon\times10^{-3}$ (mm/mm)	Clip-on Extensometer $\varepsilon\times10^{-3}$ (mm/mm)	Rectangle edge detection $\varepsilon\times10^{-3}$ (pixel/pixel)
0.00	0.19	0.00	N/A
0.15	0.13	-0.06	N/A
0.66	-0.10	-0.29	N/A
1.05	-0.36	-0.56	N/A
1.77	-0.03	-0.23	N/A
2.03	0.35	0.00	N/A
2.25	1.70	1.20	N/A
2.64	2.73	2.33	N/A
3.03	3.34	3.04	N/A
3.32	3.61	3.42	N/A
3.20	3.41	3.20	N/A
3.56	3.76	3.48	N/A
3.95	4.14	3.76	N/A
4.32	4.59	4.14	N/A
4.69	5.17	4.56	N/A
4.94	5.60	4.87	N/A

Table 5-10 Axial strain test results for FRCM-7

Stress (MPa)	Laser Extensometer $\varepsilon\times10^{-3}$ (mm/mm)	Clip-on Extensometer $\varepsilon\times10^{-3}$ (mm/mm)	DIC Speckle $\varepsilon\times10^{-3}$ (pixel/pixel)
0.00	-0.03	0.00	0.000
0.46	0.16	0.25	0.018
1.23	0.24	0.57	0.006
2.32	0.23	0.53	0.030
2.70	1.73	1.68	0.030
3.16	3.05	2.84	0.064
3.47	4.45	3.88	0.17
3.56	5.87	5.10	0.20
3.92	6.67	5.82	0.32
4.25	7.42	6.52	0.56
4.38	8.06	7.26	0.67
4.85	8.86	7.74	0.84
5.25	9.58	8.38	1.06
5.68	10.34	9.00	1.30
6.10	10.94	9.47	1.57
6.52	11.63	10.04	1.88
6.94	12.27	10.60	2.12
7.23	12.82	10.98	2.70
6.78	13.16	11.02	3.42

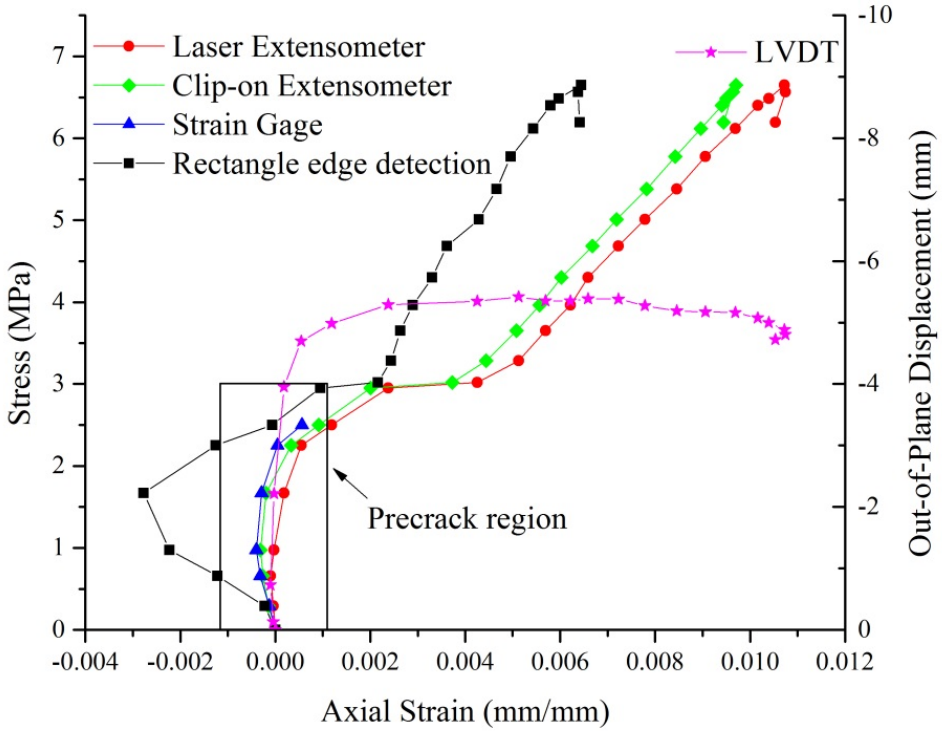

Figure 5-4 Comparison of axial strain measurements for FRCM 1

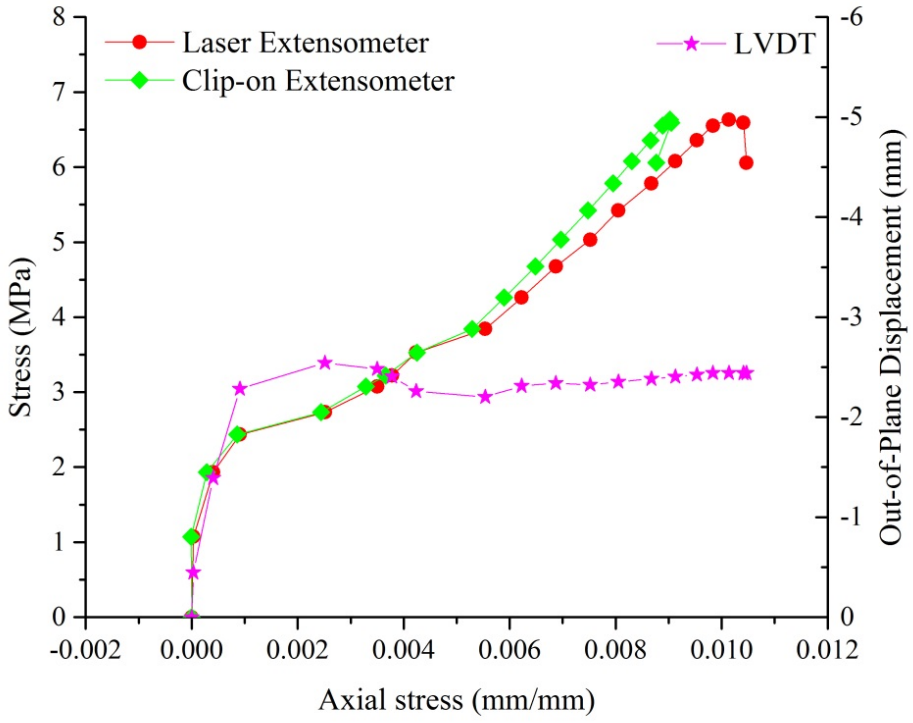

Figure 5-5 Comparison of axial strain measurements for FRCM-2

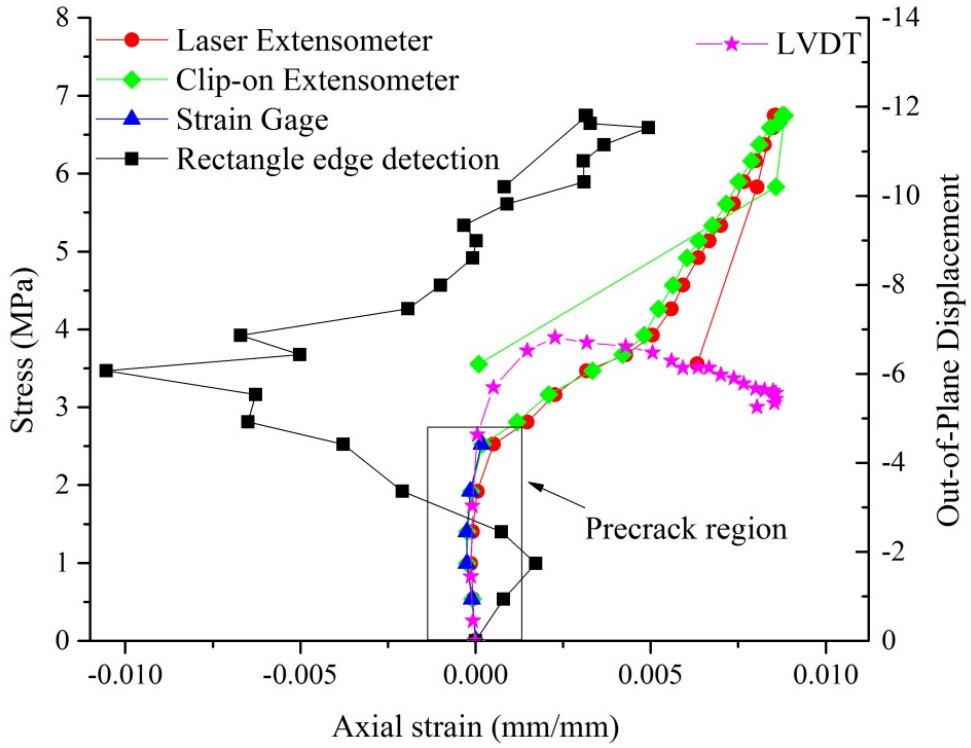

Figure 5-6 Comparison of axial strain measurements for FRCM 3

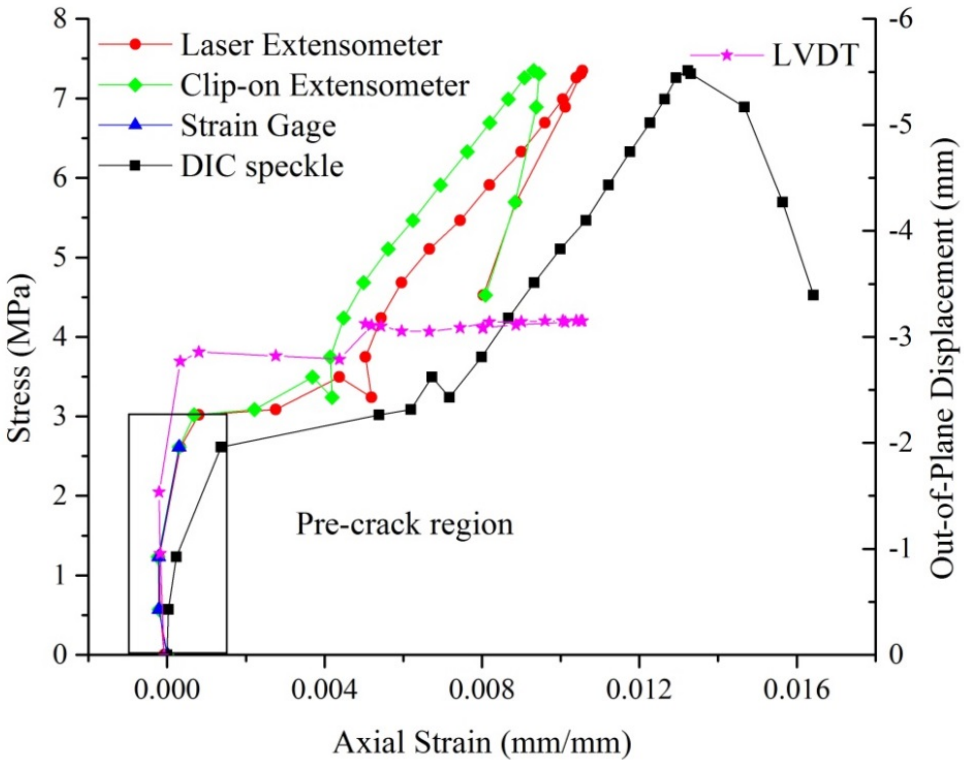

Figure 5-7 Comparison of axial strain measurements for FRCM 4

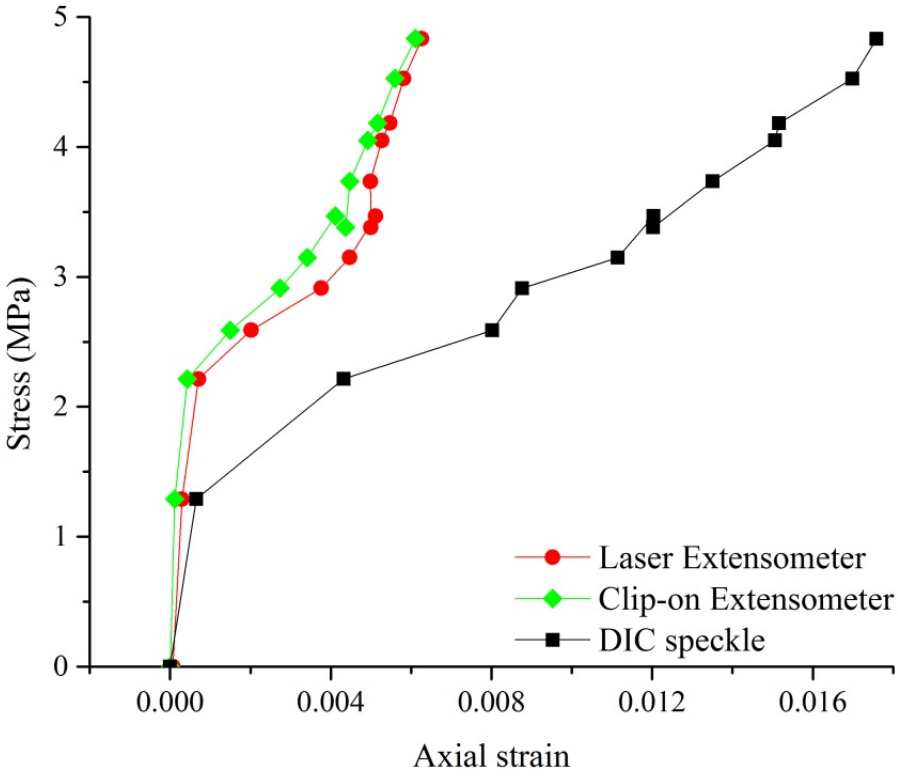

Figure 5-8 Comparison of axial strain measurements for FRCM 5

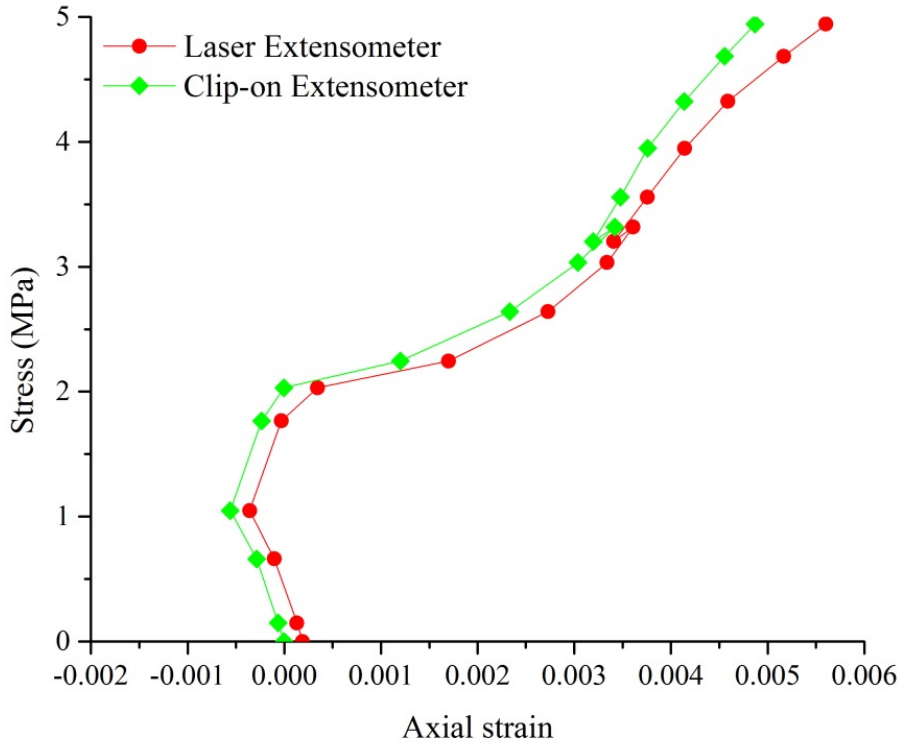

Figure 5-9 Comparison of axial strain measurements for FRCM 6

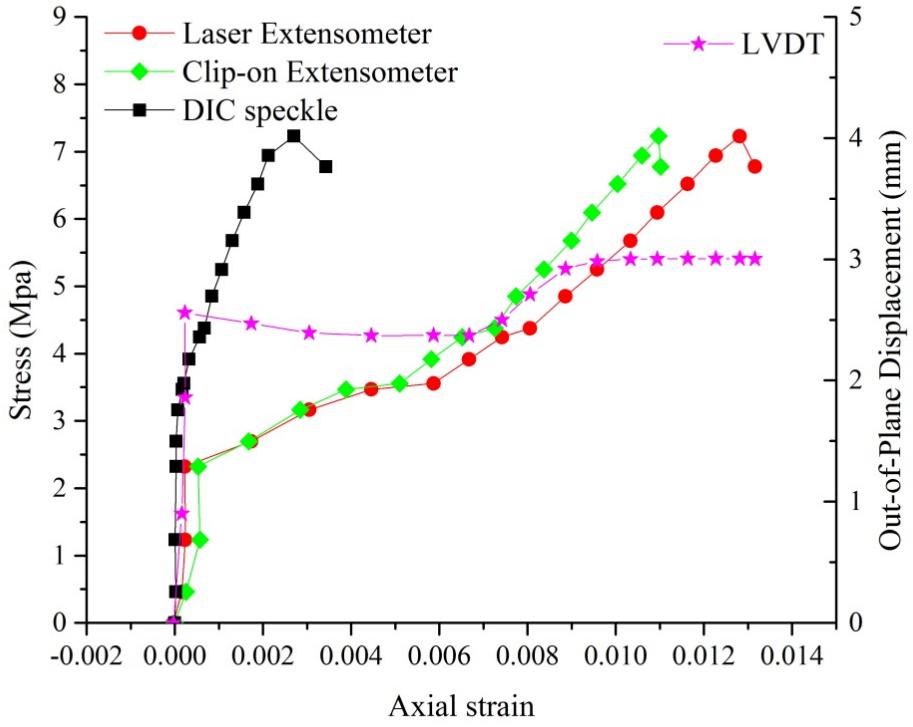

Figure 5-10 Comparison of axial strain measurements for FRCM 7

5.5 Discussion

5.5.1 Comparison of the strain measurement methods

From Figure 5-4, Figure 5-6 and Figure 5-7, the laser, clip-on extensometer and strain gage give coherent strain measurement results initially (when axial strain $\varepsilon < 0.001$). At the same time, the out-of-plane displacement increases rapidly. After that, the strain gage fails and the out-of-plane displacement response becomes flat. $\varepsilon < 0.001$ is the pre-crack region. When tensile stress is applied to the specimen, the specimen presents out-of-plane displacement, as indicated by the LVDT data. For any displacement beyond a certain point (5 mm for FRCM-1, 4.5 mm for FRCM-3 and 3 mm for FRCM-4), a crack occurs, absorbing the strain energy. When the crack occurs within the gage area, the strain gage circuit fails and no further data can be recorded. The laser,

clip-on extensometer, and DIC method show a plateau after the specimen cracks and then the strain increases again. When the composite was in a state of saturated cracking (near 3 MPa), the matrix failed, the fabric has been straightened and took most of the load. Specimen failure occurred when the fabric delaminated from the matrix and the composite material could not support any load.

Laser extensometry and the clip-on extensometer showed similar strain measurement results for the full duration of the tension tests. These results may be considered as the real strain of the specimen. The strain gage can only be used in the beginning of the tension test, until the specimen cracks. Before cracking, the strain gage, laser extensometry, and clip-on extensometer gave similar strain measurement results. When the crack crosses the region covered by the strain gage, it is broken and cannot provide correct strain measurement results. Initially, the matrix of the composite material deforms as tensile stress is applied (pre-crack region). Strain beyond the elastic deformation of the matrix causes cracking to occur. These cracks manifest as a plateau in the stress-strain curve. The specimen undergoes substantial deformation with only a small increase in stress. The strain continues to increase as stress increases.

From the stress-strain curves, the failure modes of the specimens can be deduced. However, it is difficult to use only one strain measurement method to characterize the failure. The strain gages failed near the beginning of the test, so without digital images processed using the DIP method, it is difficult to explain unexpected data from the strain gages after cracking. Since all the stress-strain curves present the same trend, any strain measurement method can be used in the deduction of failure modes.

5.5.2 Comparison of two DIC methods

The two DIC methods show very different strain measurement results in comparison to the other methods. This difference could be attributed to the out-of–plane displacement experienced by the FRCM specimens. Results from the LVDT show that the specimen experienced large out-of-plane displacement. This out-of-plane displacement may be caused by several factors. One possibility is that the specimen was cast while the fabric was initially curved; upon loading, the fabric straightens and the entire composite material deforms out-of-plane. Another possibility is that the entire composite specimen was initially curved prior to loading. Upon loading, the specimen straightened out, which resulted in a change in out-of-plane displacement. Another possibility is that the matrix cracked asymmetrically on the two sides of the specimen. This out-of-plane movement has a significant effect on the digital image strain measurement techniques. The digital image methods measure the deflection of the specimen at the subpixel-level. This requires that each photo captured by the camera have a clear image of the specimen at a high resolution. For this reason, maintaining a constant focal distance from the camera lens to the specimen is critical during the test.

For the rectangle edge detection method, the deformation in real space can be represented by pixels in the images. All the images must have the same scale. The strain measurement was based on the change in the pixels of the digital image. The photos captured during tension tests were blurred and had different scales, as seen in Figure 5-11, which caused many errors in edge detection. For specimens FRCM-2 and FRCM-6, the edges of the rectangle were too blurred to analyze. The Gaussian fitting method could not be applied since the gradient intensities around the blurred edges do not present a

Gaussian distribution. For specimens FRCM-1 and FRCM-3, the out-of-plane displacement caused a change in scale. The axial length of the rectangle should increase as tensile loading is applied. However, since the distance from the specimen to the camera increases, the measured axial length appears to decrease in these images. When the out-of-plane displacement changes slowly, the distance between the specimen and camera is relatively constant.

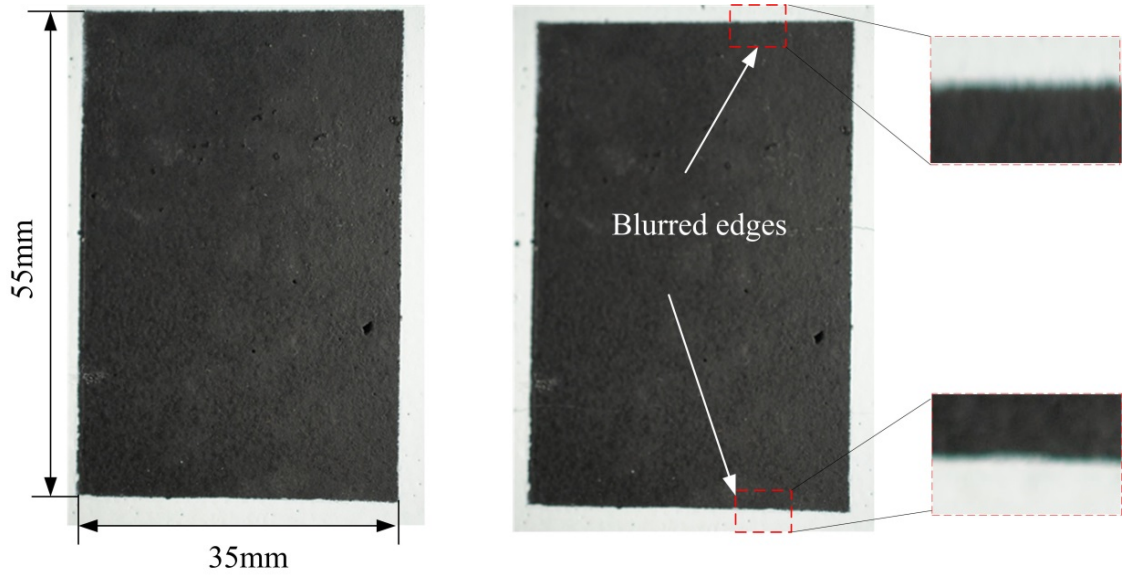

(a) Original image (b) Blurred image

Figure 5-11 Comparison of original and blurred images of FRCM-2

The DIC speckle method measures the strain by correlating the images before, during, and after loading to generate a displacement map. Then, the displacement map is used to find the strain map. Changes in scale also cause errors in this correlation. In DIC speckle, a grid is generated over the image to divide it into subsets for correlation. The grid is superimposed on the later images by searching nearby to maximize matching. Mismatching introduces a bias in the measurement, which may cause larger or smaller measurements. The specimens FRCM-4 and FRCM-5 show larger strain measurement

results compared to other methods. The specimen FRCM-7 shows a smaller strain measurement result.

5.6 Comprehensive comparison

To comprehensively compare these five strain measurement methods, all factors related to measurement should be considered. These include requirements for specimen preparation, set up of devices used in the experiment and relative costs. The primary comparisons are given in Table 5–11, Table 5–12, and Table 5–13.

Table 5-11 Comparison of methods: Requirements for specimen preparation

Strain measurement methods	Requirements for specimen preparation	Evaluation
Clip-on extensometer	Relative flat surface	Simple
Laser extensometry	Apply reflective tape on the specimen surface No high laser reflective surface	Simple
Strain gage system	Need to bond strain gage to the specimen surface	Difficult
DIC (Natural texture)	Nothing	Simple
DIC (Speckles)	Paint speckles on the specimen surface	Simple
Rectangle edge detection	Paint a rectangle on the specimen surface	Simple

Table 5-12 Comparison of methods: Experimental set up for strain measurement devices

Strain measurement method	Primary set up requirement	Evaluation
Clip-on extensometer	Directly mount on the specimen	Simple
Laser extensometry	Mount on a rigid frame with 305 mm distance from specimen	Simple
Strain gage system	Perform a calibration before test for each strain gage	Difficult
Digital image methods (DIC and Rectangle edge detection)	Calibrate camera if the setting of the system changed Stable, vibration-free supports Stable and evenly distributed lighting	Difficult

Table 5-13 Comparison of methods: Relative cost

Strain measurement method	Device and relative cost	Evaluation
Clip-on extensometer	Clip-on extensometer (100sg)	Expensive, reusable
Laser extensometry	Laser extensometer and reflective tape (750sg)	Very expensive, reusable
Strain gage system	Bridge circuit and strain gage (1sg)	Inexpensive, not resuable
Digital image methods (DIC and Rectangle edge detection)	Camera, lens and Matlab software (125sg)	Inexpensive, reusable

"sg": the cost of 1 strain gage is used as a baseline

These tables show a comparison of the three primary factors to consider: requirements for specimen preparation, set-up of the device in the experiment and relative cost. In the cost comparison, the price of one strain gage was used as the unit and the cost for other methods were compared with that cost.

The clip-on extensometer is directly mounted on the specimen without any specimen preparation. Sufficient tension must be provided to prevent slippage of the knife edges or clip-on wire forms mounted on the specimen. DAQ allows for real-time data collection during the test. It was easy to setup, had high accuracy and relatively low cost. However, for very brittle or soft specimens, the knife-edge can easily damage the specimen.

Laser extensometry also has a low requirement for specimen preparation. Reflective tape can be directly applied to the specimen with various gage lengths, up to 100mm. Specimen with mirror-like surface must be avoided since they may cause redundant laser reflection. These spurious reflections lead to incorrect readings of the laser extensometer. Additionally, laser extensometry has high accuracy with non-contact features. However, high price limits the usefulness of this method.

The strain gages have high requirements for specimen surface preparation. A smooth surface free of large discontinuities, voids, and elevations is necessary. Surface preparation is extensive and includes removal of dust and other foreign debris particles, and neutralization of chemical residue on the surfaces of the specimen and strain gage. Gage alignment, adhesive bonding, and wire soldering can be a time-consuming, delicate procedure requiring prior training and ample experience. Each strain gage also needs to be calibrated before testing to determine the relationship between electric current and

strain. The strain gages are also highly sensitive to ambient temperature, which means calibration must be conducted in the same room as the test.

The digital image method requires patterns on the specimen as marks to track. If the specimen has a natural texture, preparation of the specimen is not necessary. For other surfaces, painting a pattern is required. A rigid base and frame are needed to support the equipment and maintain alignment of the camera with the specimen. Calibration of the camera is also needed. DIC is not a real-time method and software for image analysis is a necessity. The accuracy is based on the quality of images and experimental conditions. The device for the digital image method serves multiple functions such as photography, which enormously lowers the cost.

5.7 Conclusions

For FRCM materials, clip-on and laser extensometry are recommended options for strain measurement since they can provide accurate results and are easy to implement. With an initial investment, these two methods can be reused for strain measurements.

Strain gages are not ideal for this kind of material since the strain gages may fail to provide strain measurement results once cracking begins. For more ductile materials, strain gages can be useful. Additionally, it is important to consider that strain gages are sensitive to temperature. In environmental studies, strain gages can be used if the change in temperature is considered during calibration.

The DIC methods evaluated in this study are 2D (in plane) methods which are difficult to apply to specimens that show out-of-plane displacement or straightening behavior during the test. 3D DIC should be applied to study strain measurement for these types of materials.

Chapter 6 Conclusions and Recommendations

6.1 Overview

In this thesis, a new digital image strain measurement method was established by using a painted rectangle pattern and is termed as "rectangle edge detection" (RED). Two accuracy levels, pixel-level and subpixel-level, were implemented using ImageJ and Matlab, respectively. For subpixel-level, two algorithms: Gaussian fitting and spline interpolation were also studied.

The rectangle edge detection method has some advantages and disadvantages compared with traditional strain measurement methods such as strain gages, clip-on extensometry and laser extensometry.

As a digital image processing (DIP) method, RED does not contact the specimen during testing and has no influence on the specimen. Additionally, RED is applicable to a wide range of specimen dimensions. From bridges to a micro size material, if digital images can be consistently recorded, RED can be applied. In addition, RED could provide field measurements, which are important in many applications in civil engineering.

RED also has some limitations. It is a surface and in-plane strain measurement method. Its application in the composite (FRCM) material studies in this thesis indicated that, for the specimens showing out-of-plane displacement, it is difficult to record consistent images. Using these images for data analysis causes large deviations in strain results. For the RED method, analysis is based on the digital images and, therefore, the image quality is critical.

In this dissertation, RED is applied to two kinds of materials, A36 steel as a ductile material and FRCM composite as a brittle material. If there is no out-of-plane displacement, RED method is suitable for both of these materials. For brittle material, which is not suitable to use strain gage, RED method can be used as an alternative method in strain measurement.

The algorithms in RED can also be used to evaluate paint removal effectiveness on concrete surfaces. It provides a threshold value selection method in DIP and it is named edge-based threshold selection method.

6.2 Conclusions

By comparing the RED strain measurement with digital image correlation (DIC) and other strain measurement methods, several conclusions can be drawn:

The rectangle edge detection method is a target-based deformation method, which explicitly considers the deformation of the target (rectangle) to calculate strain. DIC uses the relative displacement change of subsets to determine the strain. However, the deformation of the subsets is neglected.

A painted rectangle can be a suitable pattern to achieve subpixel-level accuracy in surface strain measurement. Both the Gaussian fitting and the spline interpolation methods provide similar accuracy as laser extensometry and strain gages if the resolution of the images is high enough.

In comparing the two subpixel rectangle methods, the Gaussian fitting method gives better results than the spline interpolation method. The Gaussian fitting method can filter out some data by goodness-of-fit (R^2) and converged data. The interpolation

method connects all the known data to find the unknown data, which neglects any noise in the known data.

The iPhone 4s is not recommended as a strain measurement device for now since the resolution and camera setting for iPhone cannot ensure consistency in recording images. However, with the rapid pace of development in the camera features of the iPhone, accurate strain measurement using the iPhone may be possible soon.

DIC is a full-field strain measurement method. The strain result for each image is the average value of all the subsets. Since DIC uses the relative displacement of subset to calculate strain, any vibration of the test system will decrease the accuracy of DIC method. Correlation is another factor in determining the accuracy of DIC method. The DIC method must find the same subset in all the images. If the correlation is poor, it will cause errors in the result.

In digital image processing, image quality is the most critical factor. Consistent and high quality images must have similar brightness, suitable exposure, high resolution and good focus. To obtain high quality images, a high resolution camera, stable lighting, and vibration-free supports are required.

The digital image strain measurement methods (RED and 2D DIC) discussed in thesis are only suitable for in-plane strain measurement. For the material with out-of-plane displacement in tension tests, RED and 2D DIC methods will fail since the out-of-plane displacement changes the focus length in images. 3D DIC can be used to measure out-of-plane displacement.

DIP methods characterize the behavior of the visible domain on the surface of the specimen. A combination of technologies (both traditional and emerging) may be

necessary to fully characterize the mechanical response of a material or structure subjected to loading.

There is no specific way to determine the reliability of all the strain measurement methods. When different strain measurement methods are used and give different results, there is no way to find which method is better without introducing a control strain measurement method that is assumed to be the true strain measurement.

The rectangle edge detection method can also be applied in finding threshold value in digital image processing. By selecting a suitable threshold value to separate the paint and concrete color, the paint removal effectiveness can be determined.

6.3 Future work

Further study in digital image processing in civil engineering could be undertaken. The most important advantage of the DIC method is that it can relate local deformation to global behavior. However, this feature is not developed in RED method in this thesis. The reason DIC can measure full-field strain is that it divides the images into small subsets. If many small rectangles are painted on the specimen surface, such as Figure 6-1, then full-field strain measurement can also be realized by the RED method.

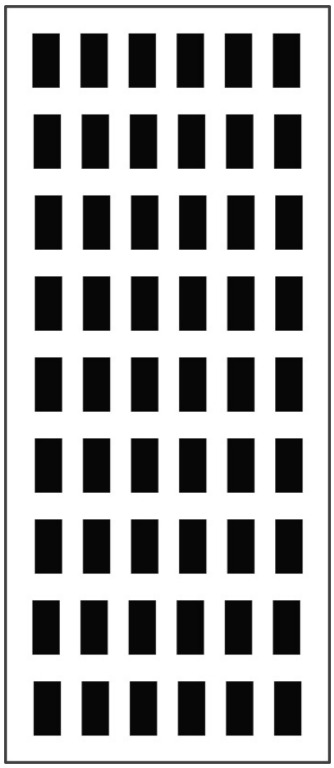

Figure 6-1 Pattern for full-field strain measurement in RED

The materials studied in this thesis are steel and brittle matrix composite, which are commonly used in civil engineering. In other research fields, different materials can be investigated, such as polymer-based composites. The required resolution of images for each strain range can also be studied.

The strain discussed in this study does not include shear strain. Shear strain could be measured by RED by calculating the angle change of the painted rectangle.

References

American Concrete Institute. (2002). Guide to thermal properties of concrete and masonry systems. Farmington Hills: American Concrete Institute.

American Concrete Institute. (2003). Concrete repair manual. Farmington Hills: American Concrete Institute.

ASTM A36/A36M-12. (2012.). Standard Specification for Carbon Structural Steel. *ASTM International*, West Conshohocken, PA, 2012, DOI: 10.1520/A0036_A0036M-12, www.astm.org.

ASTM D4258-05. (2012). Standard practice for surface cleaning concrete for coating. *ASTM International*, West Conshohocken, PA, 2012, DOI: 10.1520/D4258-05R12, www.astm.org.

ASTM E111-04. (2010). Standard test method for Young's modulus, tangent modulus, and chord modulus. *ASTM International*, West Conshohocken, PA, 2010, DOI: 10.1520/E0111-04R10, www.astm.org.

Arboleda, D., Yuan, S., Giancaspro, J., & Nanni, A. (2013). Comparison of strain measurement techniques for the characterization of brittle, cementitious matrix composites. In A. Zingoni (Ed.), *Research and Applications in Structural Engineering, Mechanics and Computation* (pp. 1567-1572). Cape Town: CRC Press.

Arboleda, D. (2014). Fabric reinforced cementitious matrix (FRCM) composites for infrastructure strengthening and rehabilitation: characterization methods (Dissertation). University of Miami, Coral Gables, FL.

Archbold, E., Burch, J., & Ennos, A. (1970). Recording of in-plane surface displacement by double-exposure speckle photography. *Optica Acta: International Journal of Optics*, 17(12), 883-898.

Asundi, A., & North, H. (1998). White-light speckle method – current trends. *Optics and Lasers in Engineering*, 29(2-3), 159-169.

Basu, M. (2002). Gaussian-based edge-detection methods-a survey. *IEEE Transactions on Systems, Man and Cybernetics, Part C (Applications and Reviews)*, 32(3), 252-260.

Becker, B., & Dripke, M. (2011). Choosing the right extensometer for every material testing application. *Advanced Materials & Processes*, 169(4), 17-21.

Bin, T., Lei, A., Cui, J., Kang, W., & Liu, D. (2008). Subpixel edge location based on orthogonal Fourier-Mellin moments. *Image and Vision Computing*, 26(4), 563-569.

Bouchara, F., Bertrand, M., Ramdani, S., & Haydar, M. (2007). Sub-pixel edge fitting using B-spine. In A. Gagalowicz & W. Philips (Eds.), *Proceedings of the 3rd International Conference on Computer Vision / Computer Graphics Collaboration Techniques* (pp. 353-364). Berlin: Springer

Bouguet, J. (2010, July 9). Camera Calibration Toolbox for Matlab. Retrieved July 25, 2012, from http://www.vision.caltech.edu/bouguetj/calib_doc/

Breder, R., Estrela, V., & de Assis, J. (2009). Sub-pixel accuracy edge fitting by means of B-spline. *Multimedia Signal Processing, MMSP'09. IEEE International Workshop on* (pp. 1-5). Rio De Janeiro: IEEE

Breul, P., Geoffray, J., & Haddani, Y. (2008). On-site concrete segregation estimation using image analysis. *Journal of Advanced Concrete Technology*, 6(1), 171-180.

Bruck, H., McNeill, S., Sutton, M., & Peters, W. (1989). Digital image correlation using Newton-Raphson method of partial differential correction. *Experimental Mechanics*, 29(3), 261-267.

Bulut, S. (2009). Strain measurement under the minimal controller synthesis algorithm and an extensometer design. *Journal of Materials Processing Technology*, 209(1), 194-201.

Burch, J., & Tokarsk, J. (1968). Production of multiple beam fringes from photographic scatters. *Optica Acta*, 15(2), 101-111.

Canal, L.P., González, C., Molina-Aldareguía, J.M., Segurado, J., & LLorca, J. (2012). Application of digital image correlation at the microscale in fiber-reinforced composites. *Composites Part A: Applied Science and Manufacturing*, 43(10), 1630-1638.

Canny, J. (1983). *Finding edges and lines in images* (AL-TR-720). Artificial Intelligence Laboratory of the Massachusetts Institute of Technology. Retrieved from ftp://publications.ai.mit.edu/ai-publications/pdf/AITR-720.pdf.

Canny, J. (1986). A computational approach to edge detection. *IEEE Transactions on Pattern Analysis and Machine Intelligence*, PAMI-8(6), 679-698.

Chasiotis, I., & Knauss, W. (2001). A new microtensile tester for the study of MEMS materials with the aid of atomic force microscopy. *Experimental Mechanics*, 42(1), 51-57.

Chen, M., Huang, C., & Lee, W. (2005). A fast edge-oriented algorithm for image interpolation. *Image and Vision Computing*, 23(9), 791-798.

Cheng, P., Sutton, M., Schreier, H. & McNeill, S. (2002). Full-field speckle pattern image correlation with B-spline deformation function. *Experimental Mechanics*, 42(3), 344-352.

Cheng, S., & Wu, T. (2005). Subpixel edge detection of color images by principal axis analysis. *Pattern Recognition*, 38(4), 527-537.

Chew, K., & Zarrabi, K. (2011). Non-contact displacements measurement using an improved particle swarm optimization based digital speckle correlation method. *2011 International Conference on Pattern Analysis and Intelligent Robotics* (pp. 53-58). Putrajaya: IEEE.

Chiang, F., & Asundi, A. (1979). White light speckle method of experimental strain analysis. *Applied Optics*, 18(4), 409-411.

Cho, S., Chasiotis, I., Friedmann, T., & Sullivan, J. (2005). Young's modulus, Poisson's ratio and failure properties of tetrahedral amorphous diamond-like carbon for MEMS devices. *Journal of Micromechanics and Microengineering*, 15(4), 728-735.

Coimbra, K., & Greenwood, R. (2000). Tensile testing of ceramic fibers by video extensometry. *Journal of Materials Science*, 35(13), 3341-3345.

Da, F., & Zhang, H. (2010). Sub-pixel edge detection based on an improved moment. *Image and Vision Computing*, 28(12), 1645-1658.

Dandliker, R. (1980). Holograohic interometry and speckle photography for strain measurement: A comparsion. *Optics and Lasers in Engineering*, 1(1), 3-19.

Daniels, A., Kominsky, J., & Clark, P. (2001). Evaluation of two lead-based paint removal and waste stabilization technology combinations on typical exterior surfaces. *Journal of Hazardous Materials*, 87(1-3), 117-126.

Davis, C., & Freeman, D. (1998). Statistics of subpixel registration algorithms based on spatiotemporal gradients or block matching. *Optcial Engineering*, 37(4), 1290-1298.

Dawson, A., Bless, S., Levinson, S., Pedersen, B., & Satapathy, S. (2008). Hypervelocity penetration of concrete. *International Journal of Impact Engineering*, 35(12), 1484-1489.

Dong, S., Song, B., Hansz, B., Liao, H., & Coddet, C. (2011). Improvement in the properties of plasma-sprayed metallic, alloy and ceramic coatings using dry-ice blasting. *Applied Surface Science*, 257(24), 10828-10833.

Dripke, M., & GmbH, Z. (2009, February 9). Materials Testing: Choosing the Right Extensometer. Retrieved November 28, 2011, from Laboratory Equipment: http://www.laboratoryequipment.com/article-the-right-extensometer-0902.aspx.

Du, M., & Chiang, F. (1998). The effect of static tensile strain on fatigue – An experimental study using laser speckles. *International Journal of Fatigue,* 20(5), 331-338.

Eberl, C., Thompson, R., Gianola, D., & Bundschuh, S. (2010, Novmber 19). Digital image correlation and tracking. Retrieved Novermber 20, 2012, from http://www.mathworks.com/matlabcentral/fileexchange/12413-digital-image-correlation-and-tracking.

Elbing, F., Anagreh, N., Dorn, L., & Uhlmann, E. (2003). Dry ice blasting as pretreatment of aluminum surfaces to improve the adhesive strength of aluminum bonding joints. *International Journal of Adhesion and Adhesives*, 23(1), 69-79.

Figliola, R. S., & Beasley, D. E. (2011). Theory and design for mechanical measurements (5th ed). Hoboken: John Wiley & Sons, Inc.

Fu, Z., Shi, J., & Wu, S. (1997). A theoretical study of the optimum linearity conditions of the structure of an axial extensometer. *Journal of Materials Processing Technology*, 69(1-3), 152-154.

Garbacz, A., Courard, L., & Kostana, K. (2006). Characterization of concrete roughness and its relation to adhesion in repair systems. *Materials Characterization*, 56(4-5), 281-289.

Gere, J. M. (2001). Mechanics of materials (5th ed). Stanford: Bill Stenquist.

Giancaspro, J., Millman, L., & Goolabsingh, R. (2011). Concrete surface preparation using dry ice bombardment. Retrieved December 30, 2013, from http://www.youtube.com/watch?v=TpYa5_YHCjQ.

Gómez, C., Costela, A., García-Moreno, I., & Sastre, R. (2006). Comparative study between IR and UV laser radiation applied to the removal of graffiti on urban buildings. *Applied Surface Science*, 252(8), 2782-2793.

Grellmann, W., Bierögel, C., & König, S. (1997). Evaluation of deformation behavior in polyamide using laser extensometry. *Polymer Testing*, 16(13), 225-240.

Gruen, A. W. (1985). Adaptive least squares correlation: a powerful image matching technique. *Journal of Photogrammetry, Remote Sensing and Cartography*, Vol.14, 175-187.

Guo, L., Sun, W., He, X., & Xu, Z. (2008). Application of DSCM in prediction of potential fatigue crack path on concrete surface. *Engineering Fracture Mechanics*, 75(3-4), 643-651.

Haddadi, H., & Belhabib, S. (2008). Use of rigid-body motion for the investigation and estimation of the measurement errors related to digital image correlation technique. *Optics and Lasers in Engineering*, 46(2), 185-196.

Hagara, M., & Kulla, P. (2011). Edge detection with sub-pixel accuracy base on approximation of edge with Erf function. *Radioengineering*, 20(2), 516-523.

Hannah, R., & Reed, S. (1992). Strain gage user's handbook. Cambridge: Springer.

Heikkilä, J. (2000, Oct 17). Camera calibration toolbox for Matlab. Retrieved July 25, 2012, from Camera calibration toolbox for Matlab: http://www.ee.oulu.fi/~jth/calibr/.

Heikkilä, J., & Silvén, O. (1997). A four-step camera calibration procedure with implicit image correction. *1997 IEEE Computer Society Conference on Computer Vision and Pattern Recognition* (pp. 1106-1112). San Juan: IEEE.

Helm, J., McNeill, S., & Sutton, M. (1996). Improved three-dimensional image correlation for surface displacement measurement. *Optical Engineering*, 35(7), 1911-1920.

Hild, F., & Roux, S. (2006). Digital image correlation: from displacement measurement to identification of elastic properties- a review. *Strain*, 42(2), 69-80.

Hoffmann, K. (1989). An introduction to measurements using strain gages. Pfungstadt: Hottinger Baldwin.

Horgnies, M., Willieme, P., & Gabet, O. (2011). Influence of the surface properties of concrete on the adhesion of coating: characterization of the interface by peel test and FT-IR spectroscopy. *Progress in Organic Coatings*, 72(3), 360-379.

Hou, H., & Andrews, H. (1978). Cubic splines for image interpolation and digital filtering. *IEEE Transactions on Acoustics, Speech and Signal Processing*, 26(6), 508-517.

Hu, Z., Xie, H., Lu, J., Hua, T., & Zhu, J. (2010). Study of the performance of different subpixel image correlation methods in 3D digital image correlation. *Applied Optics*, 49(21), 4044-4051.

Hutchinson, T., & Chen, Z. (2006). Improved image analysis for evaluating concrete damage. *Journal of Computing in Civil Engineering*, 20(3), 210-216.

Hwang, S., Horn, J., & Wang, H. (2008). Strain measurement of SU-8 photoresist by a digital image correlation method with a hybrid genetic algorithm. *Optics and Lasers in Engineering*, 46(3), 281-289.

Hyde, P., & Davis, L. (1983). Subpixel edge estimation. *Pattern Recognition*, 16(4), 413-420.

International Concrete Repair Institute. (2008). Selecting and specifying concrete surface preparation for coatings, sealers, and polymer overlays. Rosemont: ICRI.

International Organization for Standards. (2011). ISO 25178-2 Geometrical product specifications surface texture: areal. Geneva: ISO.

Jennings, H., Bullard, J., Thomas, J., Andrade, J., Chen, J., & Scherer, G. (2008). Characterization and modeling of pores and surfaces in cement paste: correlations to processing and properties. *Journal of Advanced Concrete Technology*, 6(1), 5-29.

Jensen, K., & Anastassiou, D. (1995). Subpixel edge localization and the interpolation of still images. *IEEE Transactions on Image Processing*, 4(3), 285-295.

Jerabek, M., Major, Z., & Lang, R. (2010). Strain determination of polymeric materials using digital image correlation. *Polymer Testing*, 29(3), 407-416.

Jin, H., & Bruck, H. (2005). Theoretical development for pointwise digital image correlation. *Optical Engineering*, 44(6), 1-14.

Kaufmann, J. (2004). Experimental identification of ice formation in small concrete pores. *Cement and Concrete Research*, 34(8), 1421-1427.

Kihm, K. (1997). Laser speckle photography technique applied for heat and mass transfer problems. *Advances in Heat Transfer*, Vol.30, 255-311.

Knauss, W., Chasiotis, I., & Huang, Y. (2003). Mechanical measurements at the micron and nanometer scales. *Mechanics of Materials*, 35(3-6), 217-231.

Kyowa Electronic Instruments. (2010, November 8). Introduction to strain gages. Retrieved November 28, 2011 from KYOWA sensor system solutions: www.kyowa-ei.co.jp/english/pdf/whats.pdf.

Lagattu, F., Bridier, F., Villechaise, P., & Brillaud, J. (2006). In-plane strain measurements on a microscopic scale by coupling digital image correlation and an in situ SEM technique. *Materials Characterization*, 56(1), 10-18.

Lagattu, F., Brillaud, J., & Lafarie-Frenot, M. (2004). High strain gradient measurements by using digital image correlation technique. *Materials Characterizaion*, 53(1), 17-28.

Lamond, J., & Pielert, J. H. (2006). Significance of tests and properties of concrete and concrete-making materials. Philadelphia: ASTM.

Lecompte, D., Smits, A., Bossuyt, S., Sol, H., Vantomme, J., Dan Hemelrijck, J., & Habraken, A. (2006). Quality assessment of speckle patterns for digital image correlation. *Optics and lasers in engineering*, 44(11), 1132-1145.

Leendertz, J. (1970). Interferometric displacement measurement on scattering surfaces utilizing speckle effect. *Journal of Physics E: Scientific Instruments*, .3(3), 214-218.

Li, C., & Xu, G. (2009). Sub-pixel edge detection based on polynomial fitting for line-matrix CCD image. *Second International Conference on Information and Computing Science* (pp. 262-264). Manchester: IEEE.

Liu, K., & Ding, J. (1993). A mechanical extensometer for high temperature tensile testing of ceramics. *Journal of Testing and Evaluation*, 21(5), 406-413.

Lu, H., & Cary, P. (2000). Deformation measurements by digital image correlation: implementation of a second-order displacement gradient. *Experimental Mechanics*, 40(4), 393-400.

Luu, L., Wang, Z., Vo, M., Hoang, T., & Ma, J. (2011). Accuracy enhancement of digital image correlation with B-spline interpolation. *Optics Letters*, 36(16), 3070-3072.

Lyvers, E., & Mitchell, O. (1988). Precision edge contrast and orientation estimation. *Transactions on Pattern Analysis and Machine Intelligence*, 10(6), 927-937.

Maini, R., & Sggarwal, H. (2009). Study and comparison of various image edge detection techniques. *International Journal of Image Processing*, 3(1), 1-12.

Marr, D., & Hildreth, E. (1980). Theory of edge detection. Proc.R.Soc.Lond.B, 187-217.

Martin, D. (1977). Laser holographic and speckle photography methods for defect detection and strain evaluation in pressure vessels. *Nuclear Engineering and Design*, 43(1), 227-236.

Millman, L. (2013). Surface assessment and modification of concrete using abrasive blasting (Dissertation). University of Miami, Coral Gables, Florida.

Mitchell, M. (1998). An introduction to genetic algorithms. Cambridge: MIT Press.

Motoie, K., Sakane, M., & Schmidt, J. (1983). An extensometer for axial strain measurement at high temperature. *Mechanics of Material*, 2(2), 179-182.

National Institutes of Health. (2004, 11 17). Image processing and analysis in Java. Retrieved December 30, 2013, from ImageJ: http://rsb.info.nih.gov/ij/.

National Instruments. (2006, September 6). Choosing the right strain-gauge for your application. Retrieved August 17, 2012, from National instruments: http://www.ni.com/white-paper/3092/en.

National Instruments. (2011, March 18). Strain measurements with strain gages: how-to guide. Retrieved November 28, 2011, from National instruments: http://zone.ni.com/devzone/cda/tut/p/id/7130.

Noh, J., La, J., Youm, W., Chulsoo, K., & Kyihwan, P. (2003). A new optical laser extensometer using a position sensitive detector (PSD). *Proceedings of the 2003 IEEE/ASME International Conference on Advanced Intelligent Mechatronics* (pp. 1178-1181). Kobe: IEEE.

Noh, S., & Yamaguchi, I. (1992). Two-dimensional measurement of strain distribution by speckle correlation. *Japanese Journal of Applied Physics*, 31(9A), 1299-1301.

Omega. (2014). The strain gage. Retrieved November 15, 2011, from Omega: http://www.omega.com/literature/transactions/volume3/strain.html.

Oskoei, M., & Hu, H. (2010). A survey on edge detection methods. Colchester: University of Essex.

Paciornik, S., Martinho, F., de Mauricio, M., & d'Almeida, J. (2003). Analysis of the mechanical behavior and characterization of pultruded glass fiber–resin matrix composites. *Composites Science and Technology*, 63(2), 295-304.

Pan, B., & Li, K. (2011). A fast digital image correlation method for deformation measurement. *Optics and Lasers in Engineering*, 49(7), 841-847.

Pan, B., Asundi, A., Xie, H., & Gao, J. (2009). Digital image correlation using iterative least squares and pointwise least squares for displacement field and strain field measurements. *Optics and Lasers in Engineering*,47(7-8), 865-874.

Pan, B., Lu, Z., & Xie, H. (2010). Mean intensity gradient: An effective global parameter for quality assessment of the speckle patterns used in digital image correlation. *Optics and Lasers in Engineering*, 48(4), 469-477.

Pan, B., Qian, K., Xie, H., & Asundi, H. (2009). Two-dimensional digital image correlation for in-plane displacement and strain measurement: a review. *Measurement Science and Technology*, 20(6), 1-17.

Pan, B., Wang, Z., & Xie, H. (2009). Generalized spatial-gradient-based digital image correlation for displacement and shape measurement with subpixel accuracy. *The Journal of Strain Analysis for Engineering Design*, 44(8), 659-669.

Pan, B., Xie, H., & Wang, Z. (2010). Equivalence of digital image correlation criteria for pattern matching. *Applied Optics*, 49(28), 5501-5509.

Pan, B., Xie, H., Wang, Z., Qian, K., & Wang, Z. (2008). Study on subset size selection in digital image correlation for speckle patterns. *Optics Express*, 16(10), 7037-7048.

Pan, B., Xie, H., Xu, B., & Dai, F. (2006). Performance of sub-pixel registration algorithms in digital image correlation. *Measurement Science and Technology*, 17(6), 1615-1621.

Pang, Z., Tan, H., & Chen, D. (2013). An improved low-cost adaptive bicubic interpolation arithmetic and VLSI implementation. *Acta Automatica Sinica*, 39(4), 407-417.

Perusek, G., Davis, B., & Sferra, J. (2001). An extensometer for global measurement of bone strain suitable for use in vivo in humans. *Journal of Biomechanics*, 34(3), 385-391.

Pilch, A., Mahajan, A., & Chu, T. (2004). Measurement of whole-field surface displacements and strains using a genetic algorithm based intelligent image correlation method. *Journal of Dynamic System, Measurement, and Control*, 126(3), 479-488.

Pitter, M., See, C., & Somekh, M. (2001). Fast subpixel digital image correlation using artificial neural networks. Proceedings of 2001 International Conference on Image Processing (pp. 901-904). Thessaloniki: IEEE.

Press, W., Teukolsky, S., Vetterling, W., & Flannery, B. (2007). Numerical recipes (3rd edition): The art of scientific computing. New York: Cambridge University Press.

Rosenberg, B., Yuan, L., & Fulmer, S. (2006). Ergonomics of abrasive blasting: A comparison of high pressure water and steel shot. *Applied Ergonomics*, 37(5), 659-667.

Santos, P., Júlio, E., & Silva, V. (2007). Correlation between concrete-to-concrete bond strength and the roughness of the substrate surface. *Construction and Building Materials*, 21(8), 1688-1695.

Schmidt, M. J., Li, L., & Spencer, J. T. (2001). Removal of chlorinated rubber coating from concrete surfaces using an RF excited CO_2 laser. *Journal of Materials Processing Technology*, 114(2), 139-144.

Schneider, S., J., S., Rupitsch, S., & Zagar, B. (2007, December). Signal processing for laser-speckle strain-measurement techniques. *IEEE Transactions on Instrumentation and Measurement,* 56(6), 2681-2687

Schreier, H., Braasch, J., & Sutton, M. (2000). Systematic errors in digital image correlation caused by intensity interpolation. *Optical Engineering*, 39(11), 2915-2921.

Schwider, J. (1990). IV advanced evaluation techniques in interferometry. *Progress in Optics*, Vol. 28, 271-359.

Shang, Y., Chen, J., & Tian, J. (2010). The study of sub-pixel edge detection algorithm based on the function curve fitting. *Proceedings of 2nd International Conference on Information Engineering and Computer Science* (pp. 1-4). Wuhan: IEEE.

Spur, G., Uhlmann, E., & Elbing, F. (1999). Dry ice blasting for cleaning: process, optimization, and application. *Wear*, Vol. 233-235, 401-411.

Sun, Y., & Pang, J. (2007). Study of optimal subset size in digital image correlation of speckle pattern images. *Optics and Laser in Engineering*, 45(9), 967-974.

Sutton, M., Yan, J., Tiwari, V., Schreier, H., & Orteu, J. (2008). The effect of out-of-plane motion on 2D and 3D digital image correlation measurements. *Optics and Lasers in Engineering*, 46(10), 746-757.

Tabatabai, A., & Mitchell, O. (1984). Edge location to subpixel values in digital imagery. *IEEE Transaction on Pattern Analysis and Machine Intelligence*, PAMI-6(2), 188-201.

Tay, C., Yap, C., Shang, H., & Tay, T. (1995). Plastic strain measurement in polypropylene using laser speckle technique. *Journal of Materials Processing Technology*, 48(1-4), 307-313.

Thévenaz, P., Blu, T., & Unser, M. (2000). Interpolation revisited (medical image application). *IEEE Transactions on Medical Imaging*, 19(7), 739-758.

Tong, W. (2005). An evaluation of digital image correlation criteria for strain mapping application. *Strain*, 41(4), 167-175.

Tsai, R. (1987). A versatile camera calibration technique for high-accuracy 3D machine vision metrology using off-the-shelf TV cameras and lenses. *IEEE Journal of Robotics and Automation*, 3 (4), 323-344.

Vendroux, G., & Knauss, W. (1998). Submicron deformation field measurements: Part 2. Improved digital image correlation. *Experimental Mechanics*, 38(2), 86-92.

Verhulp, E., Rietbergen, B., & Huiskes, R. (2004). A three-dimensional digital image correlation technique for strain measurements in microstructures. *Journal of Biomechanics*, 37(9), 1313-1320.

Wang, H., & Hou, Z. (2010). Application of genetic algorithms in a surface deformation measurement technique. *Proceedings of 2010 Sixth International Conference on Natural Computation* (pp. 2291-2295). Yantai: IEEE.

Wang, L., & Bai, J. (2003). Threshold selection by clustering gray levels of boundary. *Pattern Recognition Letters*, 24(12), 1983-1999.

Wang, X., & Ling, H. (2010). An edge-adaptive interpolation algorithm for super-resolution reconstruction. *Proceedings of 2010 International Conference on Multimedia Information Networking and Security* (pp. 81-84). Nanjing: IEEE.

Watman, C., Austin, D., Barnes, N., Overett, G., & Thompson, S. (2004). Fast sum of absolute differences visual landmark detector. *Proceedings of 2004 IEEE International Conference on Robotics and Automation* (pp. 4827-4832). New Orleans: IEEE.

Wei, G., Tan, Q., Liu, G., & Xiong, L. (2010). A two-dimensional sub-pixel edge detection algorithm based on hyperbolic tangent. *Proceedings of 2nd International Conference on Information Engineering and Computer Science* (pp. 1-4). Wuhan: IEEE.

Wernicke, G., Bouamama, L., Kruschke, O., Demoli, N., Gruber, H., & Kruger, S. (2001). Some investigations in holographic microscopic interferometry with respect to the estimation of stress and strain in micro-opto-electro-mechanical systems (MOEMS). *Optics and Laser in Engineering*, 36(5), 475-485.

Weston, D.P., Shipway, P.H., & Harris, S.J. (2005). Coating removal from an industrial polypropylene blend by cryogenic blasting: the development of substrate damage. *Wear*, 258(1-4), 392-401.

Whiting, D., & Nagi, M. (1998). Manual on control of air content in concrete. Portland Cement Association (PCA).

Wojciechowski, A., Pisarek, J., & Kityk, A. (2010). Non-contact 1D vibration analysis in temporal digital speckle photography. *Optics and Lasers in Engineering*, 48(3), 320-324.

Wolverton, M., Bhattacharyya, A., & Kannarpady, G. (2009). Efficient, flexible, noncontact deformation measurements using video multi-extensometry. *Experimental Techniques*, 33(2), 24-33.

Xu, X., Wang, K., & Gu, G. (2013). An improved method for shape measurement using two-dimensional digital image correlation. *Optik – International Journal for Light and Electron Optics*, 124(20), 4097-4099.

Yamaguchi, I. (1981). Speckle displacement and decorrelation in the diffraction and image fields for small object deformation. *Optica Acta*, 28(10), 1359-1376.

Yamaguchi, I. (2003). Holography, speckle and computers. *Optics and Lasers in Engineering*, 39(4), 411-429.

Yang, H., & Pei, L. (2011). Fast algorithm of subpixel edge detection based on Zernike moments. *Proceedings of 4th International Congress on Image and Signal Processing* (pp. 1236-1240). Shanghai: IEEE.

Yonekawa, M., Ishii, T., Ohmi, M., Takada, F., Hoshiya, T., Niimi, M., Ioka, I., Miwa. Y., & Tsuji, H. (2002). Development of a remote-controlled fatigue test machine using a laser extensometer for investigation of irradiation effect on fatigue properties. *Journal of Nuclear Materials*, 307-311(part 2), 1613-1618.

Zhang, Z. (1999). Flexible camera calibration by viewing a plane from unknown orientations. *Proceedings of the Seventh IEEE International Conference on Computer Vision* (pp. 666-673). Kerkyra: IEEE.

Zhou, P., & Goodson, K. (2001). Subpixel displacement and deformation gradient measurement using digital image/speckle correlation (DISC). *Optical Engineering*, 40(8), 1613-1619.

Zhu, D., Mobasher, B., & Rajan, S. (2012). Non-contacting strain measurement for cement-based composites in dynamic tensile testing. *Cement and Concrete Composites*, 34(2), 147-155.

Zhu, Z., & Brilakis, I. (2010). Machine vision-based concrete surface quality assessment. *Journal of Construction Engineering and Management*, 13(2), 210-218.

Appendix A: Gaussian fitting subpixel-level rectangle length calculation (Part of Matlab code)

```
% This code uses Gaussian fitting method to find the subpixel-level rectangle
% length in axial direction for multiple photos
% The data will save in an Excel file
 close all;
clear all;
clc
%%%%%%%%%%%%%%%%%%%%%%%%%%%%%%%%%%%%%%%%%%%%%%%%%%%%%%%%%%%%%%%%%%%%%%%%%%%%
% Measurement range setting
% This part has to change according to the photos
height=200;
halfwidth=250;
halfpixelnumber=4;
foldername='test 1 axial(r2-0.8)';
%%%%%%%%%%%%%%%%%%%%%%%%%%%%%%%%%%%%%%%%%%%%%%%%%%%%%%%%%%%%%%%%%%%%%%%%%%%%
files=dir('*.jpg');%
tn=size(files);
```

```
for t=(1:tn)   % loop for picture
imageName=files(t).name;
 aa=imread(imageName);
aagray=double(rgb2gray(aa));
[r,c]=size(aagray);
aagray_flip=255-aagray;
grad_axial=diff(aagray);
grad_axial_flip=diff(aagray_flip);
 % divide the picture into two parts: top and bottom
grad_axial_top=grad_axial_flip(1:height,(round(c/2)-
halfwidth):(round(c/2)+halfwidth));
grad_axial_bottom=grad_axial((r-height):(r-1),(round(c/2)-
halfwidth):(round(c/2)+halfwidth));
 % find the size of two parts
[rt,ct]=size(grad_axial_top);
ii=1;
 for i=(1:ct)    % loop for each line
% find the postion of maximum y gradient value for each coloum: ymax_t
% notice that for axial direction, the x is coloum, y is the pixel's gray value
        y_axial_top=grad_axial_top(:,i);
        y_axial_bottom=grad_axial_bottom(:,i);
        ymaxpt=find(y_axial_top==max(max(y_axial_top)));
        ymaxpb=find(y_axial_bottom==max(max(y_axial_bottom)));
```

```
% get the 4 pixels' value on the top and 4 pixels on the bottom for Gaussian fitting
    xt=(ymaxpt-halfpixelnumber):(ymaxpt+halfpixelnumber);
    ytop=y_axial_top((ymaxpt-halfpixelnumber):(ymaxpt+halfpixelnumber));
    ytop=ytop';
    xb=(ymaxpb-halfpixelnumber):(ymaxpb+halfpixelnumber);
    ybottom=y_axial_bottom((ymaxpb-
halfpixelnumber):(ymaxpb+halfpixelnumber));
    ybottom=ybottom';
% define the initial fitting parameters (Very important, reflect the result! )
% use the pixel-level position as initial guess
% Use min sum of square to find the parameters of Gaussian function
    beta0t=[y_axial_top(round(ymaxpt)),ymaxpt,1]
    [betat,rest]=lsqcurvefit(@(pp,x)(pp(1)*exp(-((x-
pp(2))./pp(3)).^2)),beta0t,xt,ytop);
    beta0b=[y_axial_bottom(round(ymaxpb)),ymaxpb,1];
    [betab,resb]=lsqcurvefit(@(q,x)(q(1)*exp(-((x-
q(2))./q(3)).^2)),beta0b,xb,ybottom);
% calculate the coefficient of determination
    yestimatet=betat(1)*exp(-((xt-betat(2))./betat(3)).^2);
    ymeant=mean(ytop);
    SStott=sum((ytop-ymeant).^2);
    SSerrt=sum((ytop-yestimatet).^2);
    Rt=1-SSerrt/SStott;
```

```
        yestimateb=betab(1)*exp(-((xb-betab(2))./betab(3)).^2);
        ymeanb=mean(ybottom);
        SStotb=sum((ybottom-ymeanb).^2);
        SSerrb=sum((ybottom-yestimateb).^2);
        Rb=1-SSerrb/SStotb;
if (Rt>=0.8)& (Rb>=0.8)
   % the first column is the position of the top line
axial_length(ii,1,t)=betat(2);
% the second column is the position of the bottom line
axial_length(ii,2,t)=betab(2)+r-height;
% the third column is the axial length
axial_length(ii,3,t)=axial_length(ii,2,t)-axial_length(ii,1,t);
% the fourth column is res of top
axial_length(ii,4,t)=rest;
% the fifth column is the top coefficient of determination Rt
axial_length(ii,5,t)=Rt;
% the sixth column is res of bottom
axial_length(ii,6,t)=resb;
% the seventh column is the bottom coefficient of determination Rb
axial_length(ii,7,t)=Rb;
else
continue
end
```

```
        clear ymaxpt;
        clear ymaxpb;
        clear xt;
        clear xb;
        clear ytop;
        clear ybottom;
        end
        xlswrite(foldername,axial_length(:,:,t),t)
end
```

Appendix B: Spline interpolation subpixel-level rectangle length calculation

(Part of Matlab code)

```
% This code can use 1D spline interpolation method to find the subpixel-level
% rectangle length in the axial direction for multiple photos
% The data will save in an Excel file
 close all;
clear all;
clc;
%%%%%%%%%%%%%%%%%%%%%%%%%%%%%%%%%%%%%%%%%%%%%%%%%%%%%%%%%%%%%%%%%%%%%%%%%%%%
% Measurement range setting
% This part has to change according to the photos
height=200;
halfwidth=250;
halfpixelnumber=4;
foldername='test 1 axial(r2-0.8)';
resolution=0.01;    %  parameter for the accuracy
%%%%%%%%%%%%%%%%%%%%%%%%%%%%%%%%%%%%%%%%%%%%%%%%%%%%%%%%%%%%%%%%%%%%%%%%%%%%
files=dir('*.jpg');%
tn=size(files);
```

```
for t=(1:tn)   % loop for picture
   imageName=files(t).name;
   aa=imread(imageName);
   aagray=double(rgb2gray(aa));
   [r,c]=size(aagray);
   aagray_flip=255-aagray;
   grad_axial=diff(aagray);
   grad_axial_flip=diff(aagray_flip);
  % divide the picture into two parts: top and bottom
   grad_axial_top=grad_axial_flip(1:height,(round(c/2)-
halfwidth):(round(c/2)+halfwidth));
   grad_axial_bottom=grad_axial((r-height):(r-1),(round(c/2)-
halfwidth):(round(c/2)+halfwidth));
  % find the size of two parts
   [rt,ct]=size(grad_axial_top);
   ii=1;
   for i=(1:ct)    % loop for each line
   % find the postion of maximum y gradient value for each coloum: ymax_t
   % notice that for axial direction, the x is coloum, y is the pixel's gray value
        y_axial_top=grad_axial_top(:,i);
        y_axial_bottom=grad_axial_bottom(:,i);
        ymaxpt=find(y_axial_top==max(max(y_axial_top)));
        ymaxpb=find(y_axial_bottom==max(max(y_axial_bottom)));
```

```
% get the 4 pixels' value on the top and 4 pixels on the bottom for Gaussian
fitting
    xt=(ymaxpt-halfpixelnumber):(ymaxpt+halfpixelnumber);
    ytop=y_axial_top((ymaxpt-halfpixelnumber):(ymaxpt+halfpixelnumber));
    ytop=ytop';
    xb=(ymaxpb-halfpixelnumber):(ymaxpb+halfpixelnumber);
    ybottom=y_axial_bottom((ymaxpb-
halfpixelnumber):(ymaxpb+halfpixelnumber));
    ybottom=ybottom';
  % set 0.01 steps
  xtq=(ymaxpt-halfpixelnumber):0.01:(ymaxpt+halfpixelnumber);
  xbq=(ymaxpb-halfpixelnumber):0.01:(ymaxpb+halfpixelnumber);
 % interpolation
  ytq=interp1(double(xt),double(ytop),xtq,'spline');
  ybq=interp1(double(xb),double(ybottom),xbq,'spline');
 % find the subpixel-level edge
  ytopposition=find(ytq==max(max(ytq)));
  ybottomposition=find(ybq==max(max(ybq)));
  [ytopsizer,ytopsizec]=size(ytopposition);
  [Ybottomsizer, ybottomsizec] =size(ybottomposition)

  ytopedge=xtq(1)+ytopposition*0.01;
  ybottomedge=r-roihight+xbq(1)+ybottomposition*0.01;
```

```
    % the first coloumn is the position of the top line
    axial_length(ii,1,t)=ytopedge;
    % the second coloumn is the position of the bottom line
    axial_length(ii,2,t)=ybottomedge;
    % the third coloumn is the axial length
    axial_length(ii,3,t)=ybottomedge-ytopedge;
ii=ii+1;
            clear ymaxpt;
        clear ymaxpb;
        clear xt;
        clear xb;
        clear ytop;
        clear ybottom;
        clear ytopedge;
        clear ybottomedge;
end
    xlswrite(foldername,axial_length(:,:,t),t)
 end
```

Appendix C Images of A36 test specimens

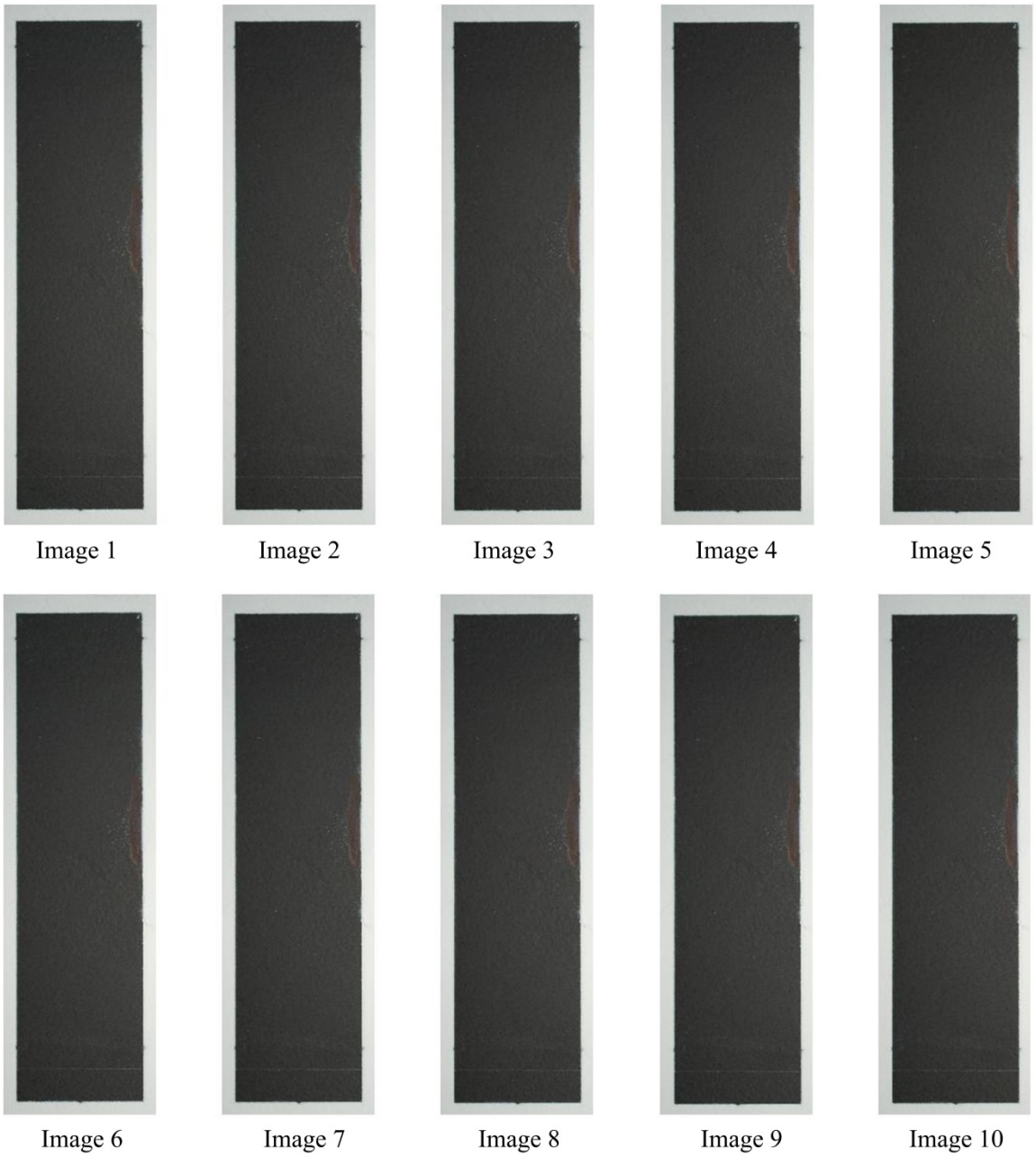

Figure C-1 Test 1: Nikon with rectangle

Image 11

Image 12

Image 13

Image 14

Image 15

Image 16

Image 17

Figure C-1 Test 1: Nikon with rectangle (continued)

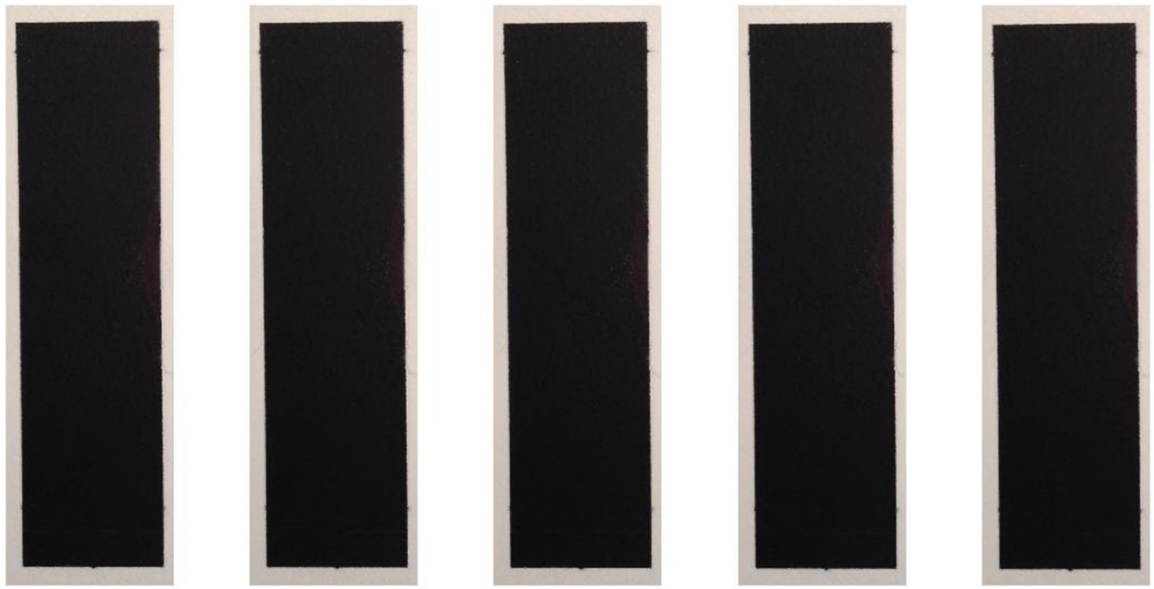
Image 1

Image 2

Image 3

Image 4

Image 5


Image 6


Image 7


Image 8


Image 9


Image 10

Figure C-2 Test 2: iPhone 4s with rectangle

Image 11

Image 12

Image 13

Image 14

Image 15

Image 16

Image 17

Figure C-2 Test 2: iPhone 4s with rectangle (continued)

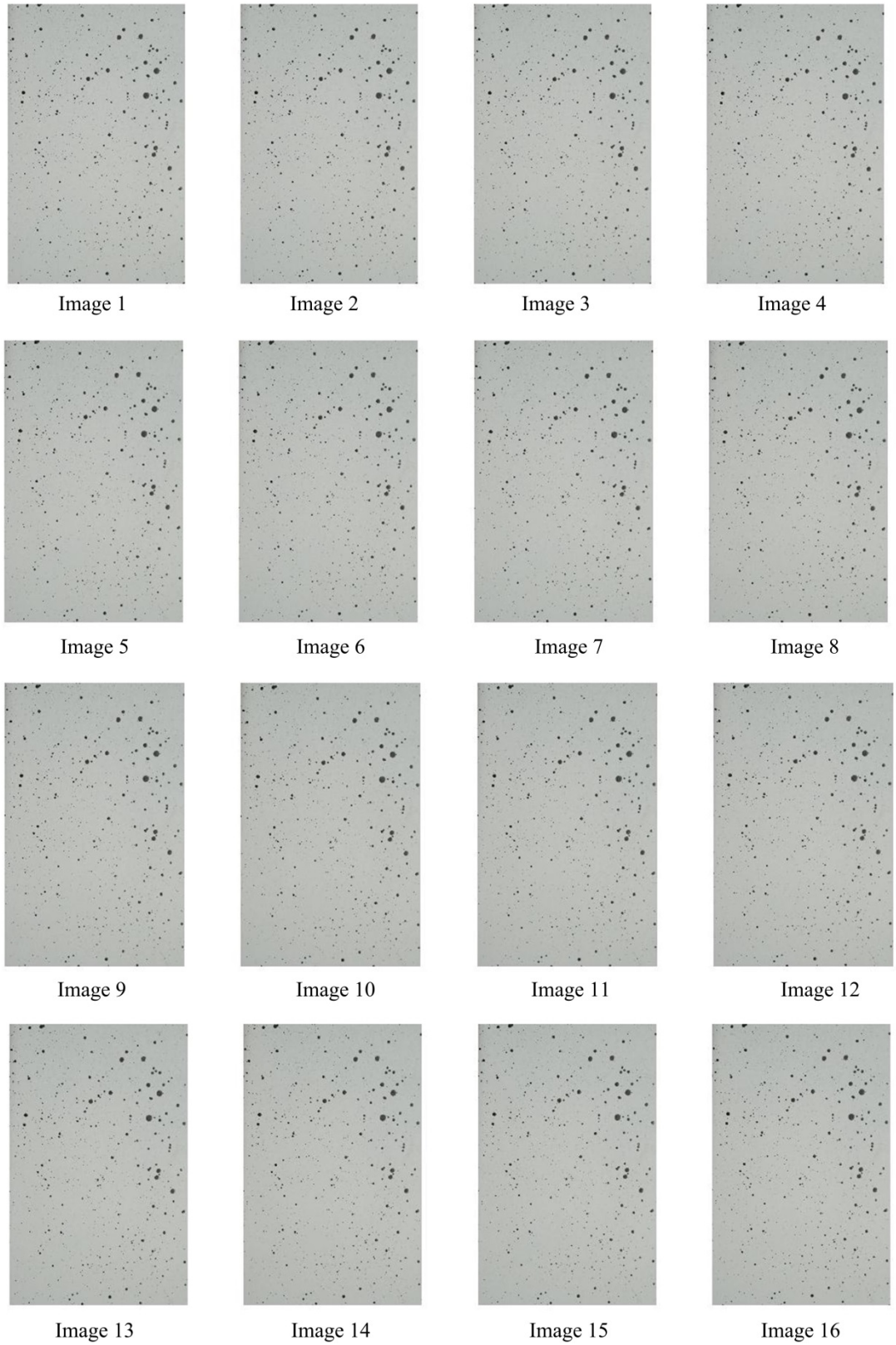

Figure C-3 Test 3: Nikon with speckles

Appendix D Images of FRCM test specimens

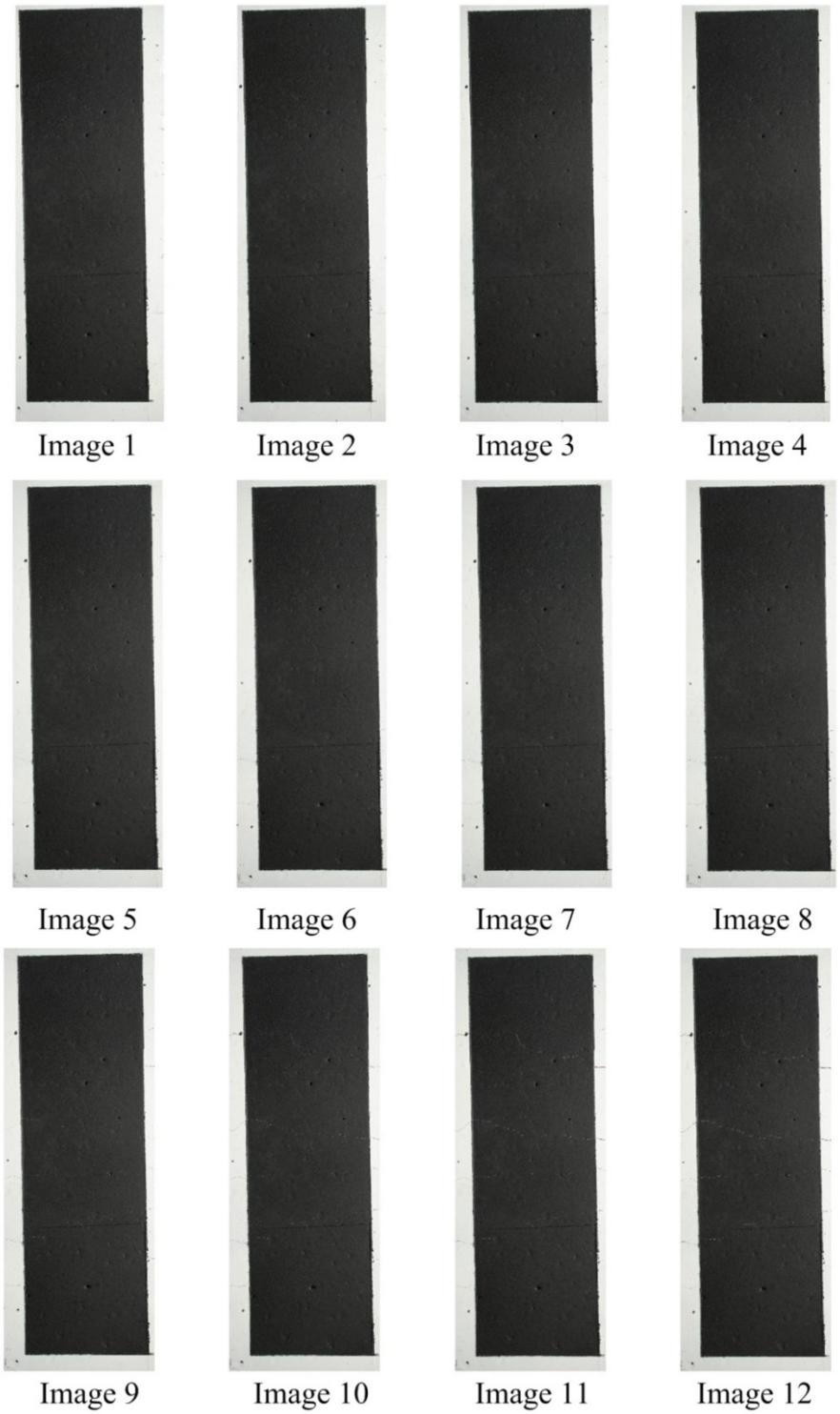

Figure D-1 Images of FRCM-1

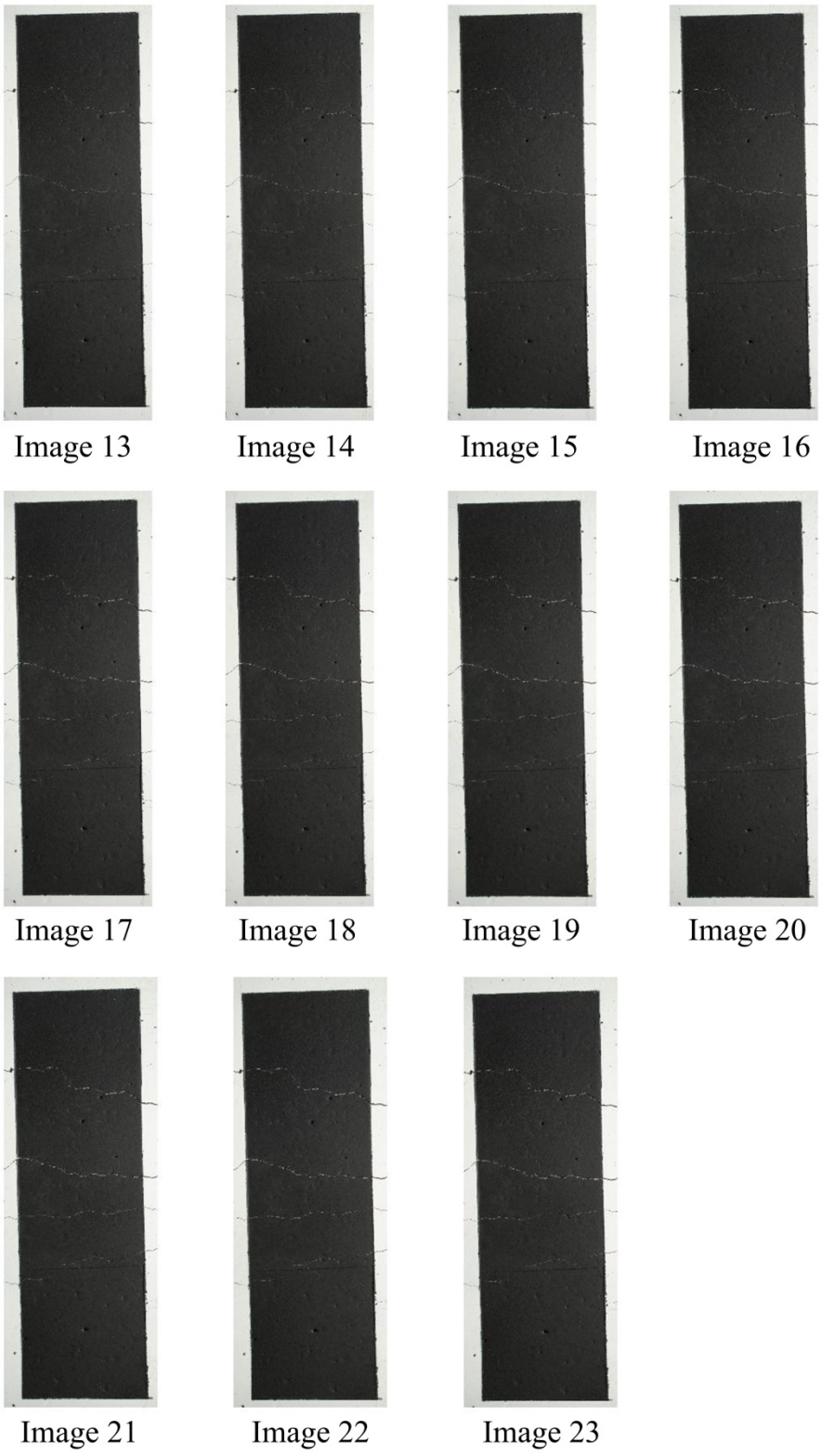

Figure D-1 Images of FRCM-1 (continued)

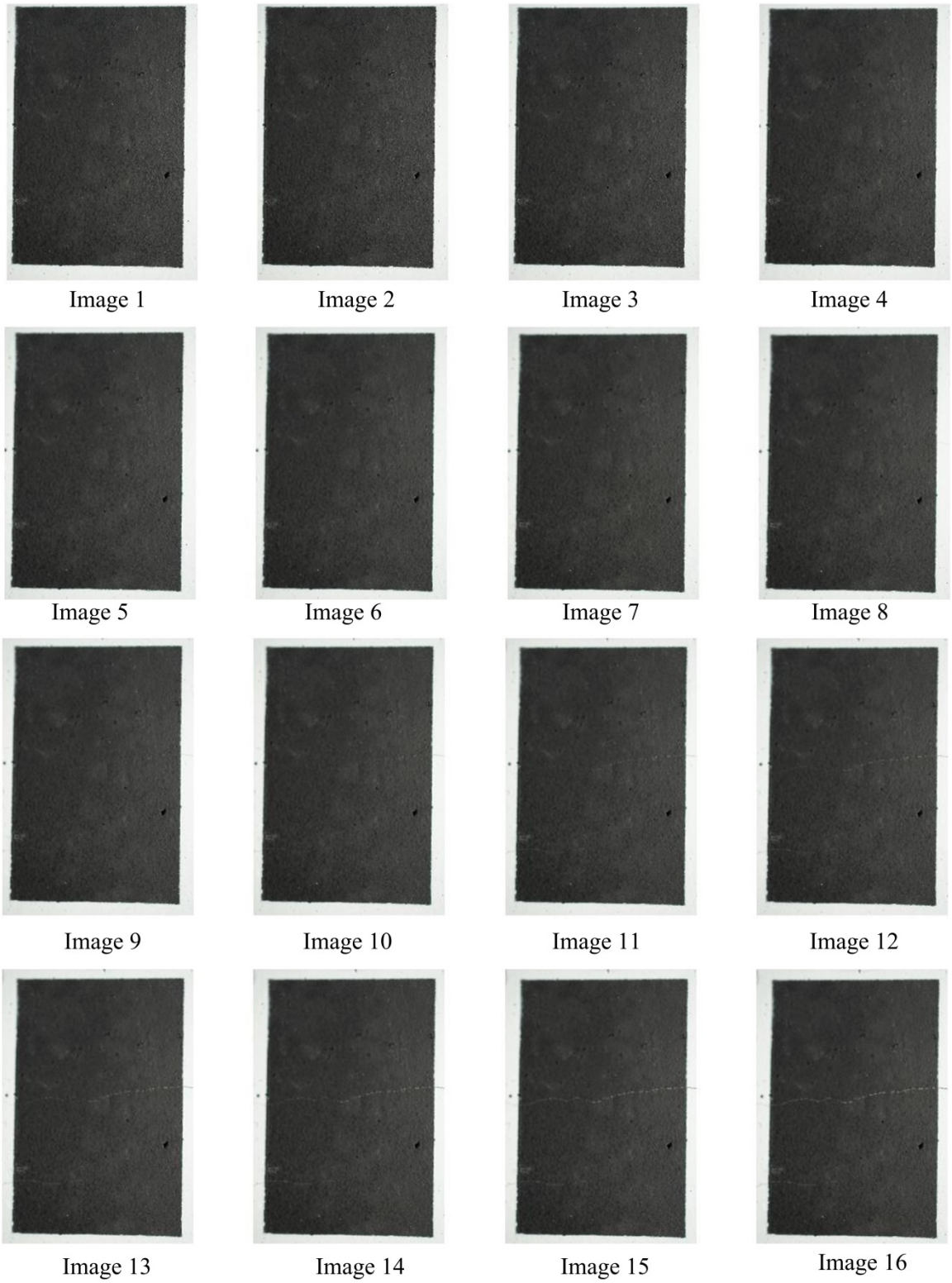

Figure D-2 Images of FRCM-2

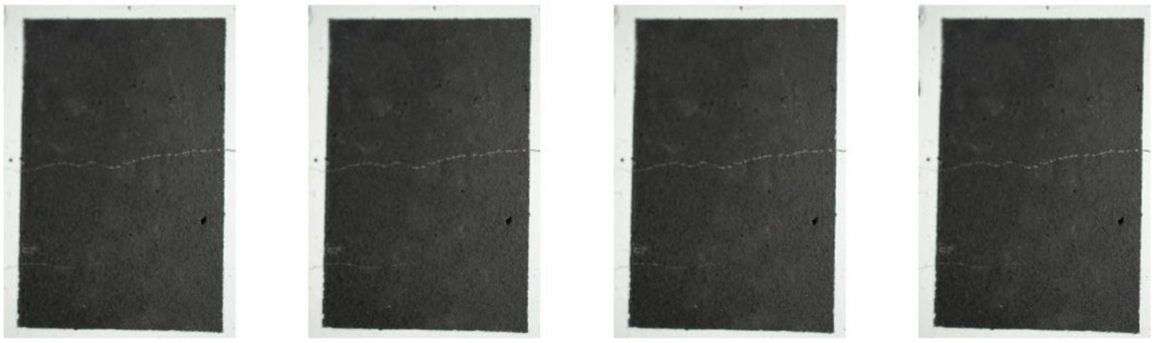

Image 1 Image 2 Image 3 Image 4

Figure D-2 Images of FRCM-2 (continued)

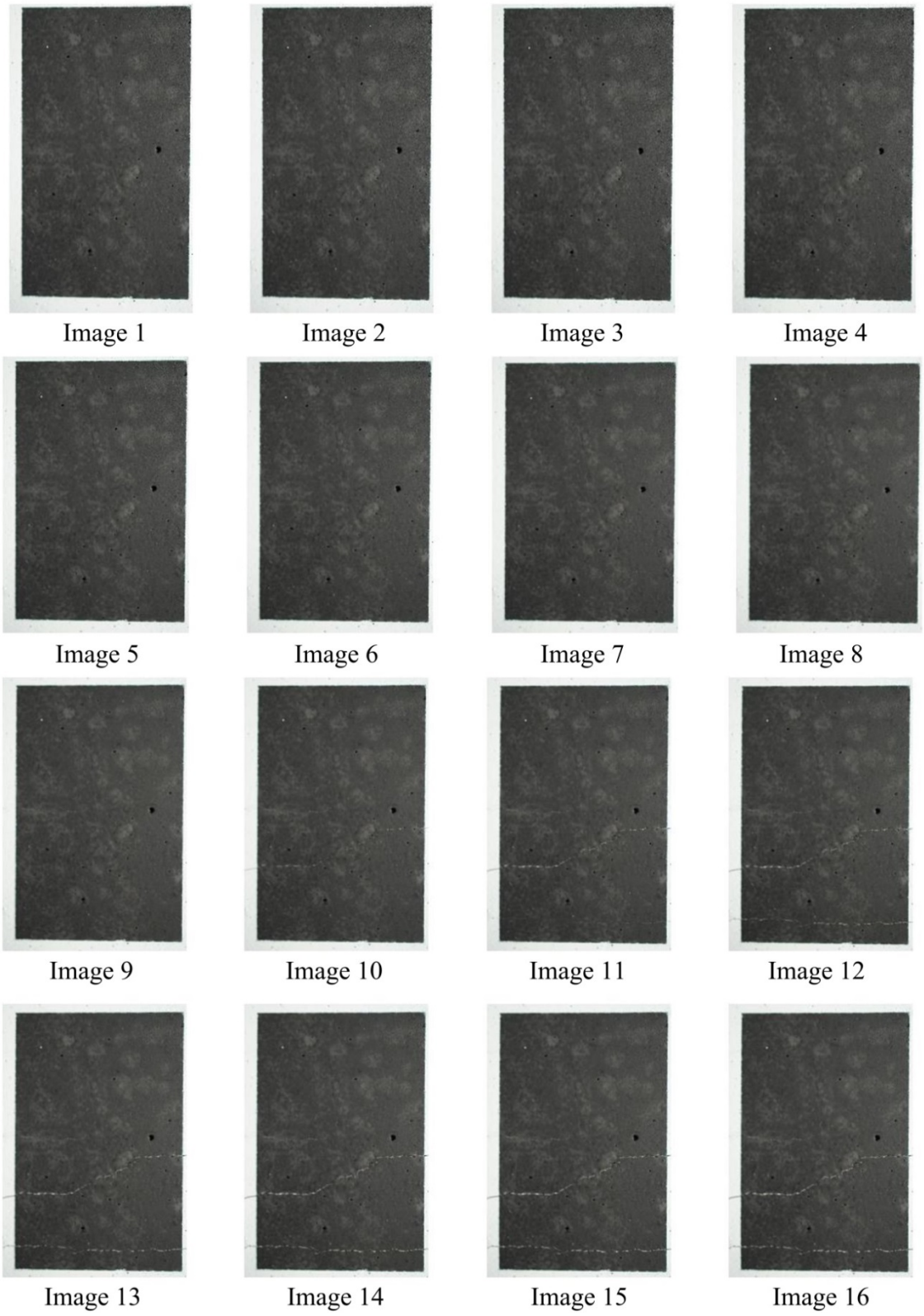

Figure D-3 Images of FRCM-3

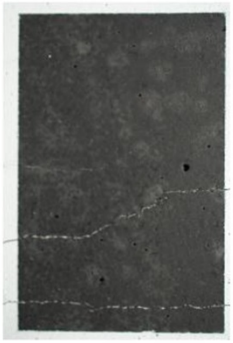

Image 17

Image 18

Image 19

Image 20

Image 21

Image 22

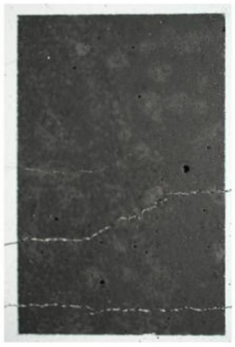

Image 23

Image 24

Image 25

Image 26

Figure D-3 Images of FRCM-3 (continued)

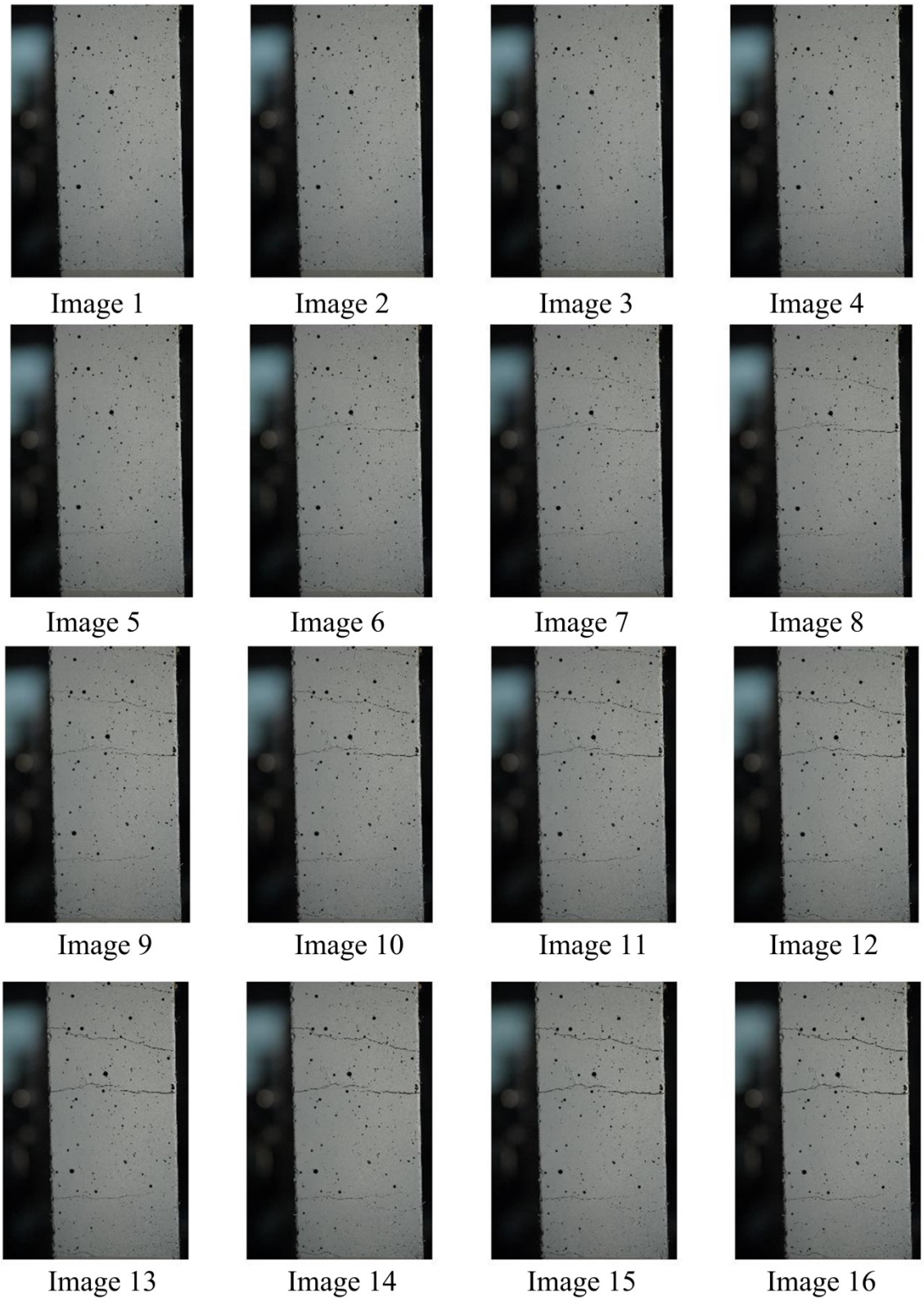

Figure D-4 Images of FRCM-4

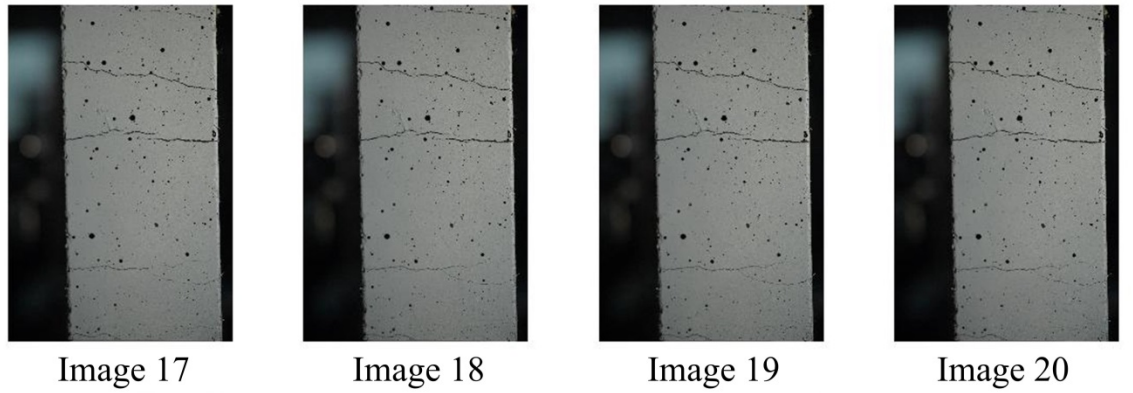
Image 17

Image 18

Image 19

Image 20


Image 21


Image 22


Image 23


Image 24

Figure D-4 Images of FRCM-4 (continued)

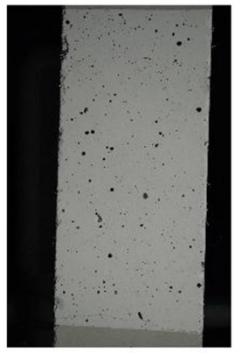
Image 1

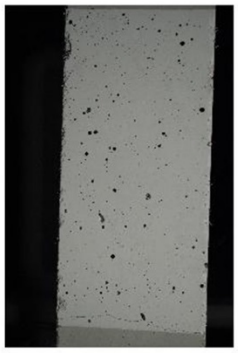
Image 2

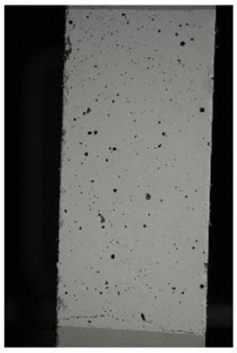
Image 3

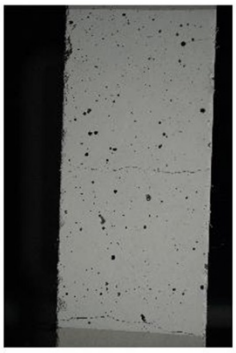
Image 4

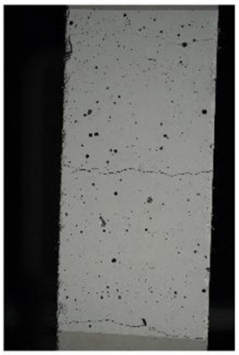
Image 5

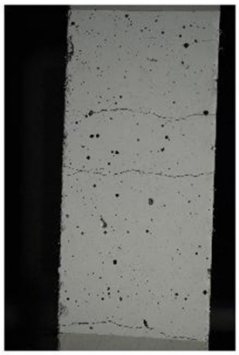
Image 6

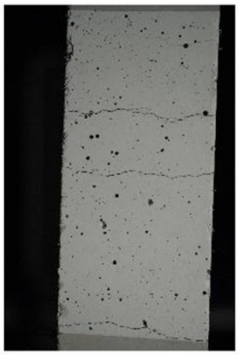
Image 7

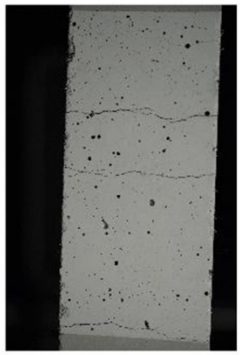
Image 8

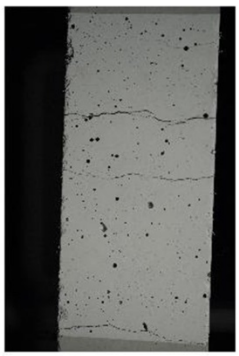
Image 9

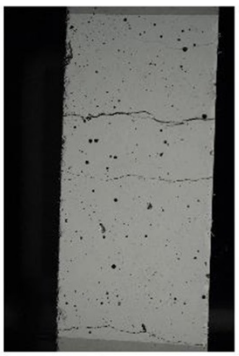
Image 10

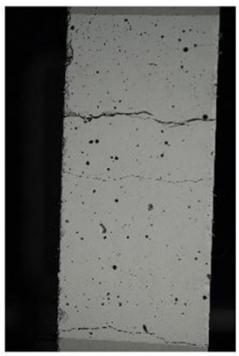
Image 11

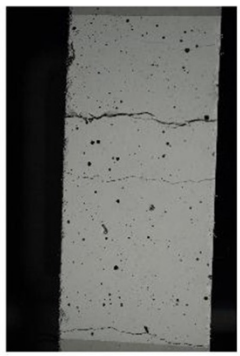
Image 12

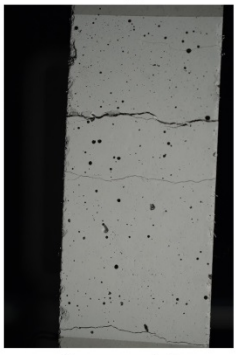
Image 13

Figure D-5 Images of FRCM-5

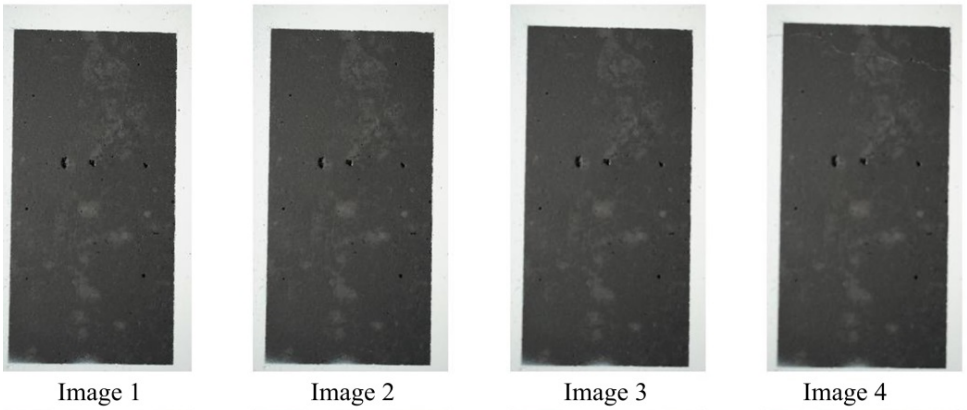
Image 1

Image 2

Image 3

Image 4

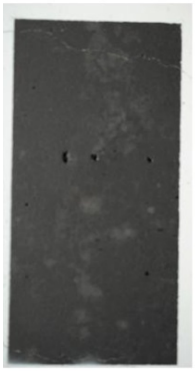
Image 5

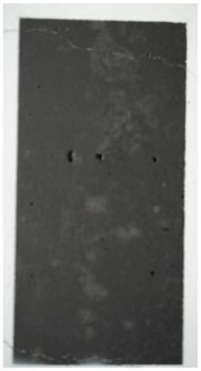
Image 6

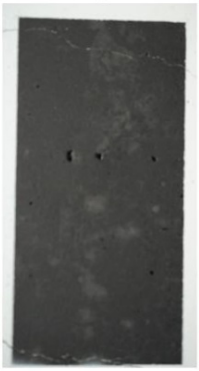
Image 7

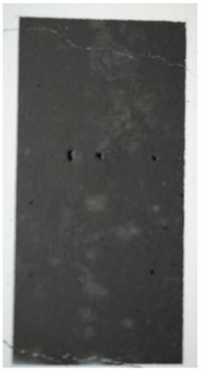
Image 8

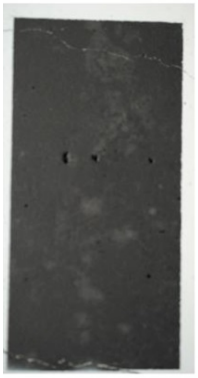
Image 9

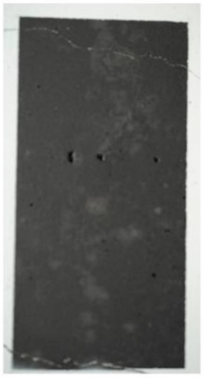
Image 10

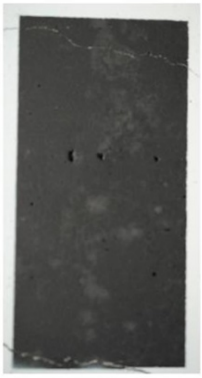
Image 11

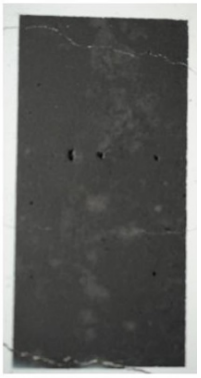
Image 12

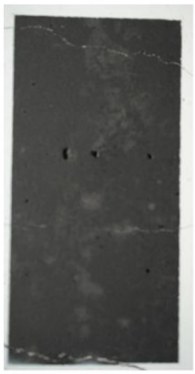
Image 13

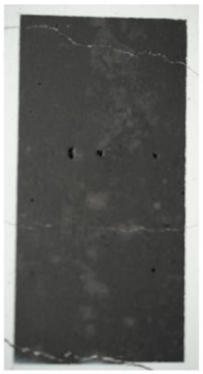
Image 14

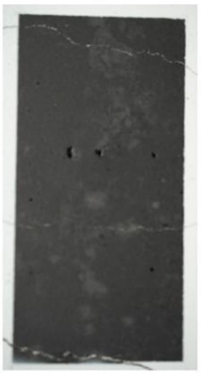
Image 15

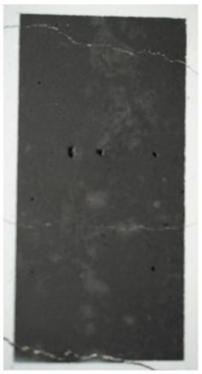
Image 16

Figure D-6 Images of FRCM-6

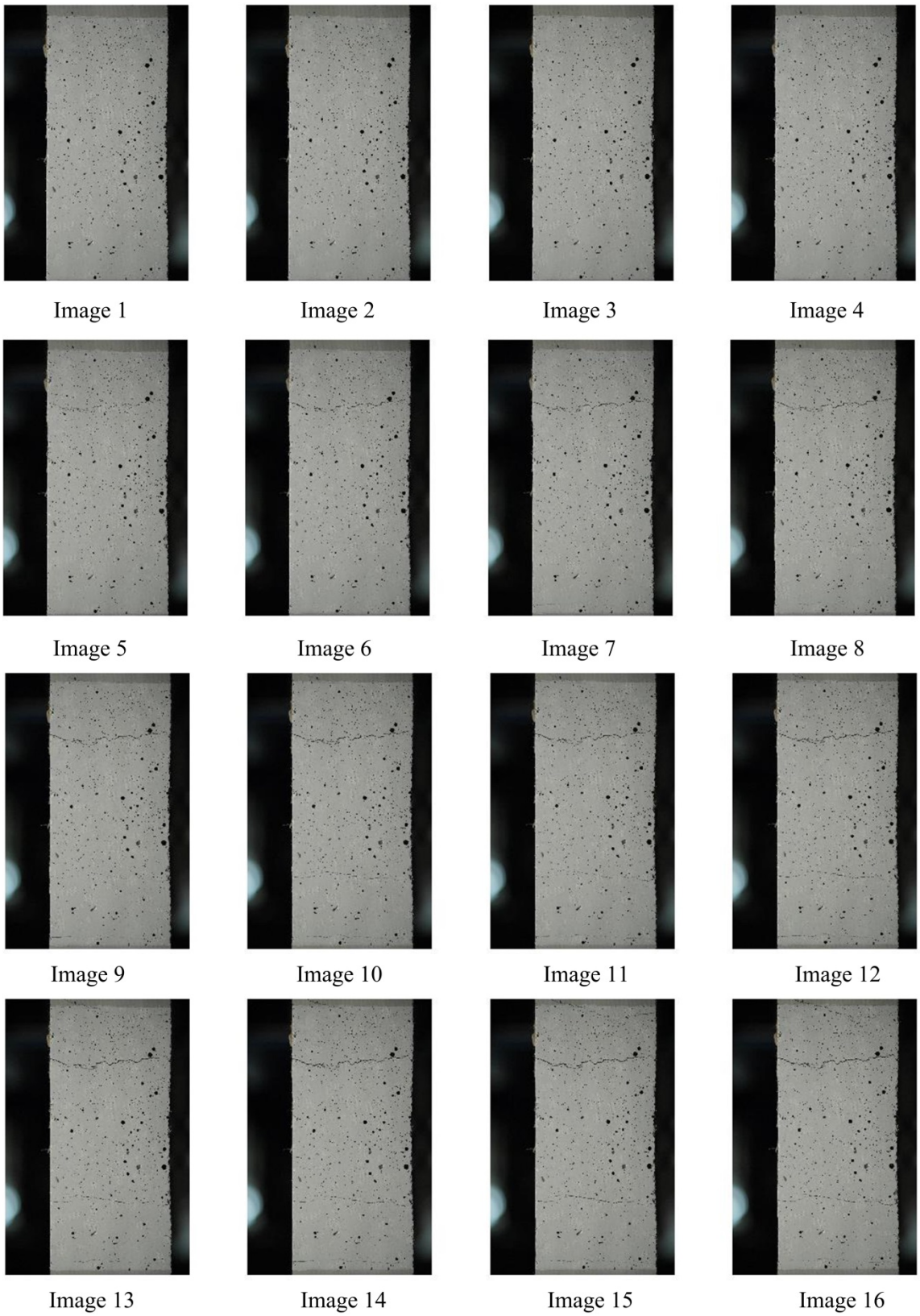

Figure D-7 Images of FRCM-7

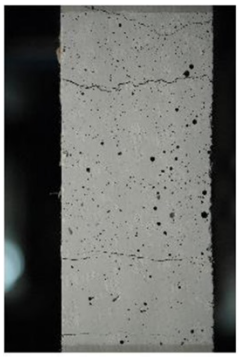

Image 17

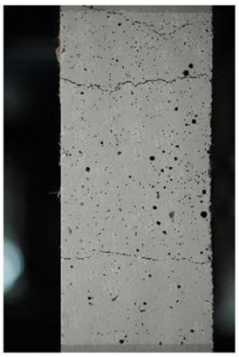

Image 18

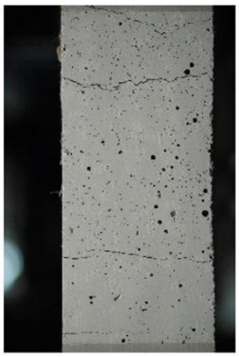

Image 19

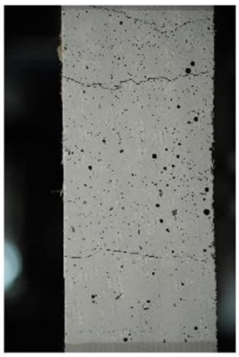

Image 20

Figure D-7 Images of FRCM-7 (continued)